Analysis and optimization of mixed-mode conical adhesively bonded joints under thermo-mechanical loadings

Ophélie Devaux

THESE / UNIVERSITE DE BRETAGNE OCCIDENTALE

sous le sceau de l'Université Européenne de Bretagne

pour obtenir le titre de

DOCTEUR DE L'UNIVERSITE DE BRETAGNE OCCIDENTALE

Mention : Sciences pour l'Ingénieur

Spécialité : Génie Mécanique

Ecole Doctorale EDSM

Présentée par

Ophélie Devaux

Préparée au LBMS [EA 4325]

Laboratoire Brestois de Mécanique et des Systèmes, ENSTA Bretagne / UBO / ENIB

en collaboration avec

- le Centre National d'Etudes Spatiales
- la Direction Générale de l'Armement

Analysis and optimization of mixed-mode conical adhesively bonded joints under thermo-mechanical loadings

Soutenance prévue le 26 octobre 2015
devant le jury composé de :

S. Fontaine
Professeur des Universités, DRIVE EA1859, ISAT - Nevers / *Rapporteur*

Y. Grohens
Professeur des Universités, LIMATB EA4250, UBS - Lorient / *Rapporteur*

T. Aubry
Professeur des Universités, LIMATB EA4250 - Brest / *Examinateur*

T. Vallée
Dr ès Sc, .Architectural Engineering, Civil Engineering, Fraunhofer Institute for Manufacturing Technology and Advanced Materials - Brême / *Examinateur*

A. Bergerot
Ingénieur, AIRBUS Defense and Space - Bordeaux / Invité

F. Lavelle
Ingénieur, CNES Direction des lanceurs - Paris / *Invité*

K. Mathis
Ingénieur, CNES Direction des lanceurs - Paris / *Invité*

B. Mortaigne
Docteur – Ingénieur, Responsable du domaine scientifique « Matériaux, Chimie, Energie », DGA/DS/MRIS - Bagneux / *Invité*

J.Y. Cognard
Professeur des Universités, LBMS EA4325, ENSTA Bretagne - Brest, *Co-encadrant* / *Invité*

R. Créac'hcadec
Maître de Conférences HDR, LBMS EA4325, ENSTA Bretagne - Brest / *Directeur de Thèse*

Contents

INTRODUCTION

Structural adhesive bonding is well-established in various industrial applications that require a significant weight reduction. Besides this advantage, it offers the possibility to innovative design concept and to lead to great design flexibility since this can be easily integrated into industrial sequences. In automotive, aircraft, construction [MOU 11] or spatial applications, bonded joints are generally supplemented by/or compete with mechanical fasteners such as bolts, rivets or welds. In the automotive industry [BUR 11], the main goals associated with the use of bonded joint technology are the lightweight of car-body structures and safety and lower-fuel consumption. In terms of crash resistance, it is also a way to improve energy dissipation. Regarding the aircraft industry, the increasing use of composite materials makes the adhesive bonding an expanding and popular technology.

Despite its potential advantages, there is a lack of confidence from the manufacturers of the spatial industry for replacing mechanical fasteners by adhesively bonded joints. In fact, the structural design of launch vehicles is complex and must take into account lot of constraints. Due to the large-scale of such structures, adhesive joint are manufactured under specific controlled conditions. The pyrotechnic environment and the large scale of the bonded structures imposed to have very low curing temperatures These structures after being manufactured are stored at room temperature. This step can reach several months, until the launch. Thus, the question of the change of the bonded assembly strength during its manufacturing and service life makes industries confused.

The SYLDA structure is considered in this study (Figure 1).

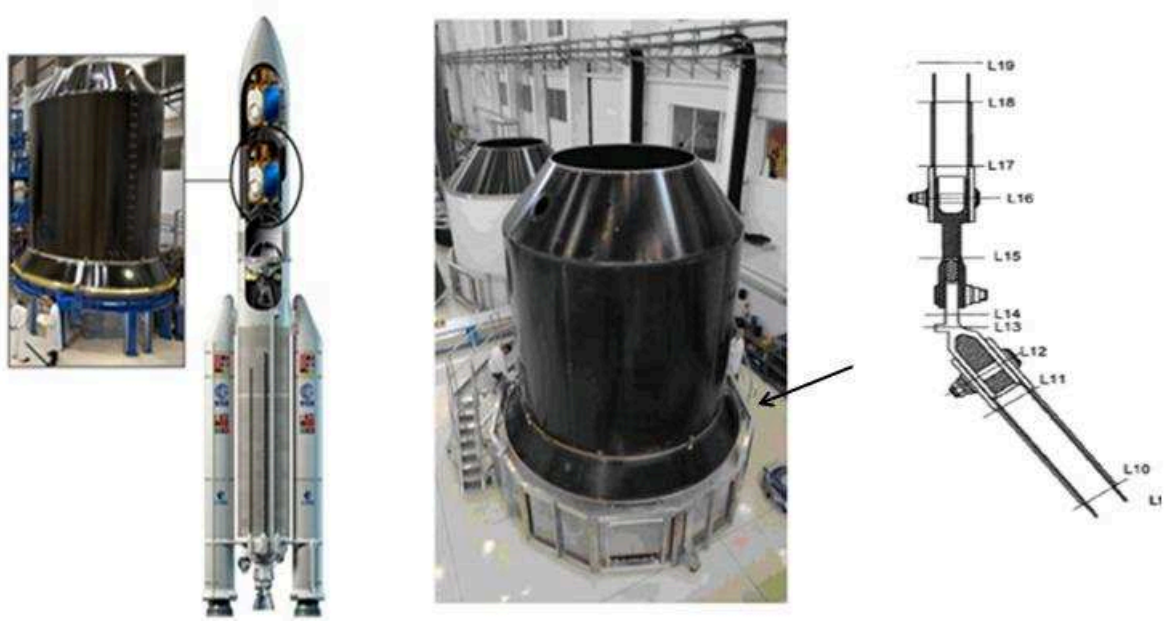

(a) (b)

Figure 1. (a) Illustration of the Ariane 5 spacecraft and the SYLDA structure and (b) bonded connection type on the SYLDA structure.

As shown in Figure 1 (a), the SYLDA structure is housed within the upper part of the launcher fairing and allows launching multiple payloads in only one flight. This is an assembly of two cones with a cylindrical center part made of expanded aluminum honeycomb core and covered by carbon fiber/resin skins. Those parts are assembled by bonded joints and riveted aluminum frames, as presented in Figure 1 (b). In addition, a connection contains a pyrotechnic cordon necessary to separate the SYLDA parts before the payload deployment.

The SYLDA bonded structure is 4.9 m high, has a diameter of 4.5 m and thus cannot be conventionally bonded in an autoclave. Thus, SYLDA is bonded with the cold-curing adhesive Hysol EA-9321. Those adhesives are characterized by an unsteady curing state. During its life cycle, the SYLDA structure is subjected to some thermal, mechanical and coupled thermo-mechanical loadings. As detailed in Figure 2, the life course of the SYLDA structure is made of several steps which are associated with specific loadings:

- A curing and storage step for which only environment stresses are applied. Only thermal effects are considered in this study. Humid aging effects are neglected.
- A transport storage for which the SYLDA structure is carried by boat to the launch center in French Guiana. Thermal and mechanical loadings have to be regarded.
- A storage step for which temperature may have a great impact on the bonded structure since high environmental temperatures are applied on a partially cured bonded joint.
- A launch step for which high temperature and mechanical loads are applied separately or simultaneously.

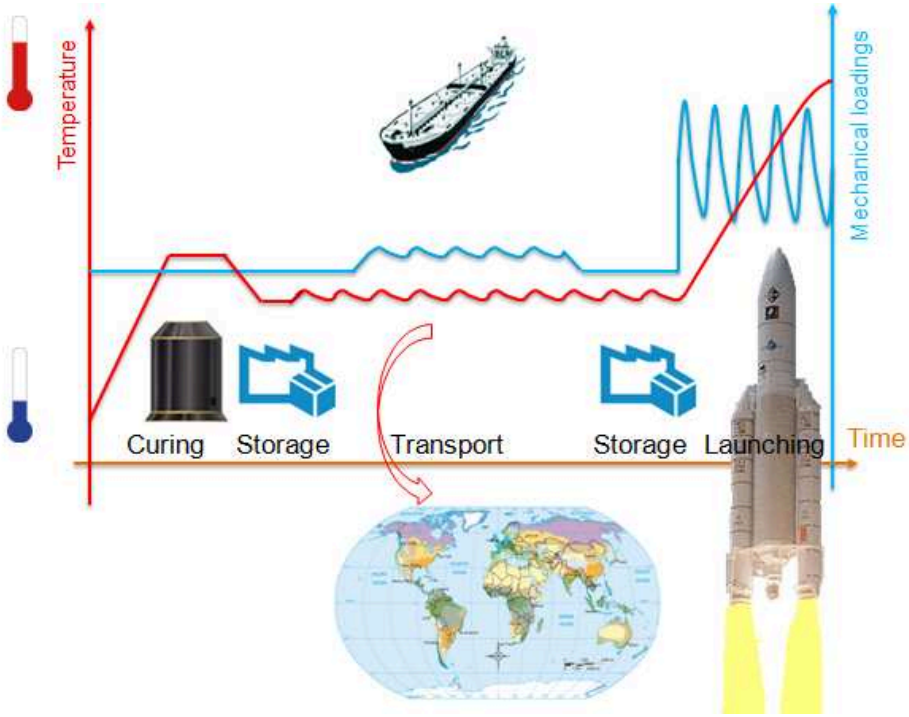

Figure 2. Life course of the SYLDA structure: identification of the loadings applied.

In the view of the different steps identified and the unsteady curing state of the adhesive, the question of the change in the physical and mechanical properties of the cold-curing adhesive Hysol EA-9321 during the service life of the SYLDA structure is extremely relevant to predict the resistance of such structure.

A main objective of this study was to characterize the mechanical behavior of a cold-curing adhesive such that used on the SYLDA structure. This must regard the effect of the curing state of such adhesive on its mechanical behavior. A bonding adhesive/aluminium was considered but the strategy developed will be transposed to composite materials.

A numerical tool for predicting the mechanical behavior of an adhesive in a spatial bonded assembly such the SYLDA structure during its life path would be provided after this work.

This document contains 5 chapters:

- The chapter 1 gives an overview on the use of structural adhesive bonding in the aerospace industry. Some aspects of structural adhesive such as the mechanical properties under specific loadings and environmental conditions are reviewed.

- The chapter 2 is dedicated to the prediction of the curing behavior of an adhesive in a bonded assembly during curing process. To that end, a kinetic model was experimentally investigated, numerically modelled and then, validated through a simple test, namely the curing of cylindrical block of adhesive.

- The chapter 3 focuses on studying experimentally the influence of the curing state of the adhesive Hysol EA-9321 on its mechanical properties via the Arcan Evolution device. The aim was to provide a strong database for the identification of the 3D behavior of the adhesive including curing degree effects.

- The chapter 4 consists in characterizing a partially cured adhesive, such the cold-curing adhesive Hysol EA-9321, in a bonded assembly. Multiple cure-dependent models were developed and split in two steps: a first characterization of the totally cured adhesive behavior and the integration of cure-dependent parameters in such model.

- The chapter 5 is a numerical study to provide a test representative of the adhesive behavior in the SYLDA structure.

References

[BUR 11] B. Burchardt. Handbook of Adhesion Technology. Ed. L.F.M da Silva, A. Öchsner, R.D. Adams. Springer-Verlag Berlin Heidelberg , Vol 2. Chap 46. 2011.

CHAPTER 1 :

STATE-OF-ART

Résumé

Ce chapitre étudie le collage structural dans sa globalité afin de mieux appréhender les éventuels problèmes liés à leur utilisation dans des domaines particuliers, ici l'aérospatial.

Une présentation du collage structural ainsi que son application dans le domaine aérospatial a tout d'abord été effectuée. Les adhésifs étant des polymères, ils présentent des propriétés différentes suivant leur état de réticulation. Ces propriétés interviennent à différentes échelles de l'assemblage collé : le polymère, les surfaces et interfaces ou interphases ainsi que l'assemblage. Tout d'abord, l'adhésif est un polymère dont le degré de polymérisation et le cycle de cuisson sont étroitement liés. Une revue des connaissances liées à la cinétique de réticulation de l'adhésif lors du procédé de cuisson a donc été réalisée. Ensuite, la compréhension des mécanismes d'adhésion et de la résistance mécanique a été développée. Enfin, l'ensemble des étapes liées au dimensionnement des assemblages collés a été recensé. Les modèles de comportement ont d'abord été mis en évidence. Du point de vue des adhésifs structuraux, on trouve des modèles élasto-plastiques avec prise en compte des effets de vitesse. En ce qui concerne la science des polymères, le degré de réticulation est souvent pris en compte dans le comportement des adhésifs. Cependant, celui-ci n'est déterminé que pour l'étape de cuisson dans le but d'évaluer les contraintes résiduelles dans l'assemblage. On trouve néanmoins, une loi de type Mahnken-Shlimmer semblable à celle des adhésifs structuraux. Ces modèles nécessitent ensuite d'être alimentés par des essais mécaniques. L'essai Arcan semble le plus adapté pour notre type d'étude puisqu'il permet de solliciter le joint de colle de manière hors plan.

Summary

This chapter gives an overview on the use of structural adhesive bonding in the aerospace industry. Different aspects of structural adhesives such as the evolution of mechanical properties under specific loadings and in service conditions are reviewed. Foremost, the chemical and physical principles of an adhesive are given. The cross-linking mechanisms evolving during the curing process are studied accurately. In fact, the curing state of the adhesive is critical in the resulting bonded joint performance. Then, constitutive models predicting by the science of polymers and structural adhesives were presented. A specificity of the polymer science is to propose constitutive models with introduction of the curing degree. Both sciences highlighted a similar model based on that of Mahnken-Schlimmer. Finally, a review of test dedicated to identify those models is presented.

Contents

1.1. Structural bonding: generalities

1.1.1. Definition, advantages and drawbacks

"Adhesive bonding" which refers to a joining method of two components together is one of the most innovative processes for joining industrial structures. This is not a novel technology since first discovered adhesive occurred in Egypt to bond papyrus fibers together around 2000-1500 B.C. The arrival of the industrial revolution in 1900 brought about major technological advancements resulting in the use of new materials in formulating adhesives. Over the last 100 years, synthetic plastic and rubbers had been widely developed and thus extended the adhesive bonding technology to numerous industrial fields. Nowadays, adhesive manufacturers offer more than 250, 000 different products for a wide range of applications.

The expression "structural bonding" refers to high performance of a bonded assembly in terms of mechanical resistance. No order of magnitude was given; Jeandreau et al. [JEA 06] qualified an adhesive as structural when it confers to the assembly strength of the same order of magnitude as those of surrounding adherends and does not affect the physical integrity of the bonded structure. This definition is closely related to the durability of a structural adhesive. For instance in spatial industry, the bonded structure SYLDA is a relevant application case since the bonded joint must resist to the life cycle of such structure, i.e. from the manufacturing to the launching stage with the different thermal and mechanical loadings associated to each stage.

In an industrial context, adhesive bonding is one alternative to traditional joining method such as welding, riveting. Table 1 summarizes the features of the commonly joining methods used in industrial applications.

	Welding	**Brazing and soldering**	**Mechanical fastening**	**Adhesive bonding**
	Joint features			
Permanence	Permanent joints	Permanent	Threaded fasteners permit disassembly	Permanent joints
Stress distribution	Local stress	Good stress distribution	High stress distribution at fasteners	Almost unifrom distribution Edge effects
Appearance	Acceptable	Good	Surface discontinuities	Joint almost invisible
Materials joined	Limited to similar materials	Ability to join dissimilar metals	Wide forms and combination of materials	Capability to join dissimilar materials
Temperature resistance	Very high	Limited by filler metal	High	Poor resistance to elevated temperature

Mechanical resistance	Special provision Often necessary to enhance fatigue resistance	Good resistance to vibration	Special provision for fatigue	Excellent mechanical properties Good resistance to environmental conditions

Table 1. Comparison of joining methods [PET 00].

Adhesive bonding produces a continuous connection between surfaces in contact [KIN 97] and thus a more homogeneous/uniform stress distribution and avoids the high stress concentrations encountered in mechanical fasteners such as bolts or rivets. As shown in Figure 3, the stress distribution in the adhesively bonded joint is much more uniform than for welding or riveting joints. The mechanical resistance resulting is then higher for adhesively bonded joints at nearly constant weight. Further, substituting of mechanical fasteners by bonded joints allows lightening the structure.

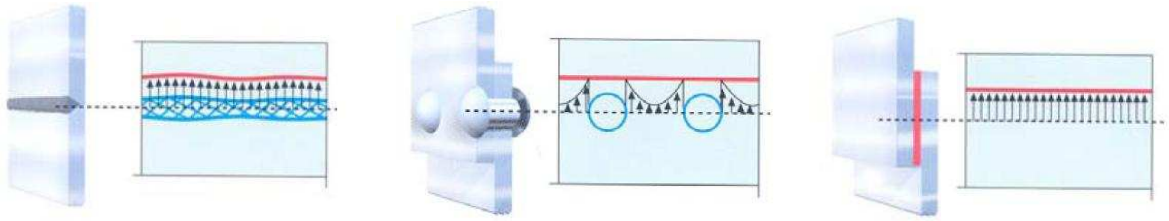

(a) Welding (b) Riveting (c) Bonding

Figure 3. Stress distribution for different joining assemblies under in-plane loading [LOC 95].

Moreover, adhesive bonding enables the design of smooth external surfaces and integrally sealed joints with minimum sensitivity to crack propagation. Adhesive can also bond dissimilar materials. Adhesive bonding provides a stiffening effect compared to riveted, welded joints: bonded joint stiffens the entire bonded area whereas rivets or welds provide only local point stiffening. The bonding process is carried out at temperatures sufficiently low to preserve the mechanical properties and integrity of adherends.

Nevertheless, adhesive bonding recognizes some drawbacks. Most of them concern the preparation stage. Adhesive materials are perishable and must be stored according to the manufacturer's recommend procedures. Once mixed or removed from the freezer, they must be applied and cured within a specific time. Adhesive bonding is much more sensitive to surface preparation than mechanical fastening. A strong and durable bond requires a proper surface preparation [KIN 87]. Some adhesives exhibit important volume shrinkage during the curing process which may influences the bonded assembly resistance [YU 13]. Another hard point is the recycling of bonded joints. Bonded joints can be considered as permanents joint. Thus, disbonding process is complex and often causes damage to the adherends and surrounding structures. This raises the main limit of the use of adhesive bonding: a lack of confidence of industrial partners of the process and designing approaches developed. So, continuous improvements in terms of understanding phenomena, non-destructive controls, characterization and modelling of adhesives must be realized to better predict the durability of bonded assemblies.

1.1.2. Structural adhesives in aerospace industry

Packam et al. [PAC 05] classified structural adhesives into subclasses based on the resin chemistries used in their formulation. Most important categories concern the phenolic adhesives, the polyurethane adhesives, the epoxy adhesives and the acrylic adhesives.

Structural epoxy adhesives are extensively used in the aerospace industry [POL 1990] as paste or film and can be manufactured either with one-part heat cure paste which contains liquid resin instead of solid resins or with two-part ambient temperature cure epoxy paste adhesives (resin and hardener). These adhesives are low-molecular-weight substances characterized by the presence of the epoxy group which is a three-membered oxirane-ring composed of one oxygene atom linked to two carbon atoms, as shown in Figure 4.

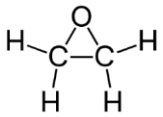

Figure 4. The epoxy group.

Among a wide variety of epoxy resins available commercially, the most group of epoxy resin is produced from the chemical reaction between bisphenol A and epichhlorohydrin resulting in the diglycidyl ether of bisphenol A (DGEBA):

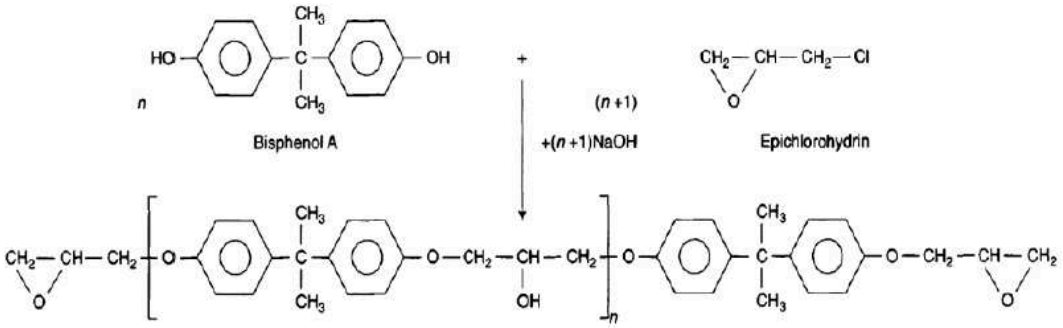

Figure 5. Synthesis of DGEBA: the reaction of bisphenol A with epichlorohydrin [JOA 07].

The DGEBA epoxy resin reacts with the hardener in stoichiometric quantities during the curing process. This is a polymerization reaction made at a curing temperature generally recommanded by the manufacturer. The DETA (dietylenetriamine) is one of the most commonly hardener used with epoxy resins DGEBA. Both species react together according to poly-addition reactions (Figure 6):

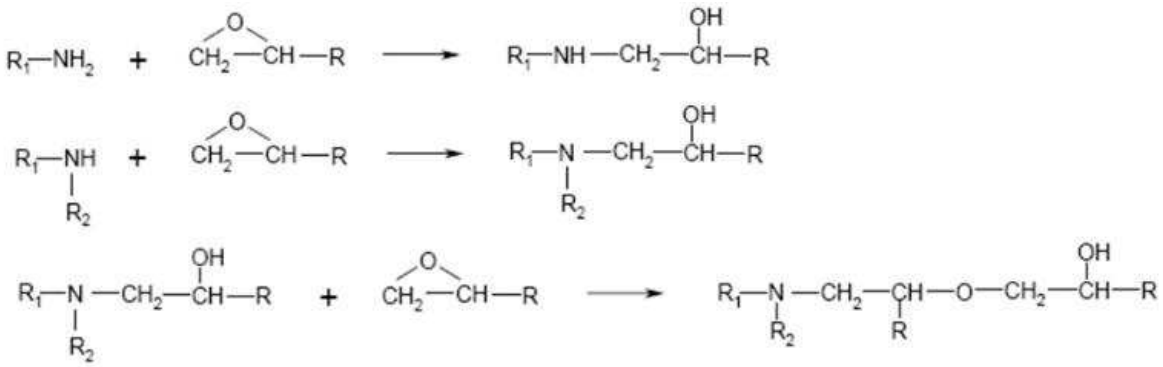

Figure 6. Curing mechanism of epoxies in presence of amines.

The resulting product is a structural epoxy adhesive. These epoxies are much appreciated in aerospace industry as they provide good adhesion to various surfaces, good ageing properties, great resistance to high stresses and a wide range of temperatures. Further, they offer a wide range of cure characteristics and mechanical properties depending on their formulation and curing state. In fact, tough but fragile, their formulation can be modified in order to have higher flexibility while keeping their original mechanical resistance at the same time.

The mechanical strength of current adhesives and sealant available on the market in Figure 7 highlight that epoxy adhesives are significantly more resistant than the others. They achieve easily a tensile strength of 20-35 MPa against 2-15 MPa for other structural adhesives.

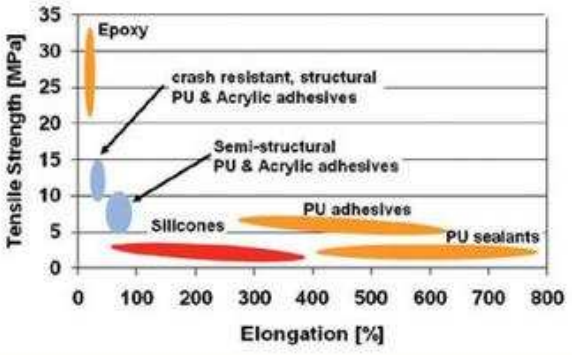

Figure 7. Tensile strength and elongation at fracture of structural adhesives [WAG 11].

The choice of an adhesive is very complex in the spatial field since typical requirements vary and differ widely following the kind of structure and the environment conditions in-service. For instance, the widespread use of cryogenic rocket fuels or pyrotechnic cordons forces the adhesives to maintain adequate properties at low temperatures. At the other extreme, those adhesives must resist to elevated temperature encountered during the rocket launch.

The technology assembly must adjust to such conditions and one can see a tendency to evolve from film adhesive/autoclave bonding to paste/adhesive/cold bonding:

One current technology commonly used in aircraft/aerospace industries uses vacuum-bagging of ambient temperature assembled layups, often in a clean room environment for maximize adhesion in order to produce vibration-resistant and high temperature-resistant structures. However, manufacturers need faster throughput, a reduction of labor costs and a better resistance of adhesives to avoid requirement of rigorous clean room conditions or autoclave curing. Additionally, those manufacturing process and conditions cannot be applied to large-scale structures. Hence, cold-curing adhesives in form of paste were introduced replacing film adhesives. Those adhesives allow storing the bonded structures in outdoor conditions that requires almost maintenance.

As suggested by Moussa et al.[MOU 11], cold-curing adhesives are suitable for large-scale structures which are erected and set-up in outdoor conditions. However, it is associated with a lack of knowledge regarding adhesive behavior during exposure to environmental conditions. In fact, these cold-curing adhesives are partially cured and provide different mechanical properties according to their curing state. Therefore, the accurate prediction of the mechanical behavior of a cold-curing adhesive during its life span remains an existing industrial problematic.

1.2. Chemical and physical properties

Epoxy adhesives are polymeric materials which represent an important class of polymers. High degree of cross-linking and the nature of the chain bonds give to cured epoxies many desirable characteristics. These latter are cure-dependent and induce cure-dependent mechanical properties. Therefore, chemical and physical properties occurring during the curing process of epoxies must be studied to better understand the resulting mechanical behavior.

1.2.1. Curing phenomena

During the curing process of an adhesive, a low-molecular weight liquid is transformed into a cross-linked solid polymer.

1.2.1.1. Major transitions during the adhesive curing

Two main phenomena are involved during adhesive curing: polymerization and cross-linking. There is a competition between these two events all over the curing process. At the early stage, the uncured epoxy resin is mixed with a hardener according to a ratio recommended by manufacturer in order to initiate the curing process. The chemical reaction within the mixture proceeds and polymer chains crosslink to each other. As a result, molecular weight increases, causing an increase in viscosity. The cross-linking is an exothermic reaction; thus, the formation of the polymer network generates heat generation which results in a temperature increase. The molecular weight continues to increase until the gel time. It is the time for which the adhesive transforms from liquid phase to solid phase. This transition is also called the gel point [WAN 93a][WAN 93b]. From this point, the molecular weight increases until forming a fully cross-linked polymer network. Figure 8 summarizes successive steps occurring during the curing process of an adhesive.

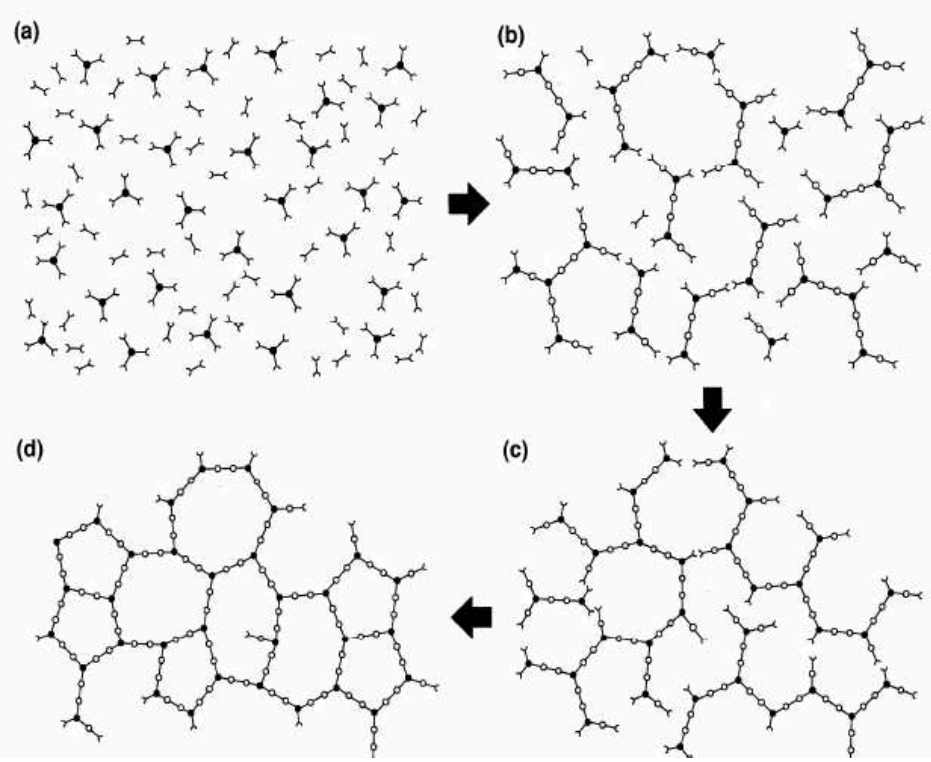

Figure 8. Schematic representation of adhesive-cure: (a) onset of reaction, (b) increase of cross-linking below the gel point, (c) formation of incompletely gelled crosslinked network and (d) fully cured polymer [PRI 97].

Gelation is a critical transition where the molecular weight is almost maximum and tends to form an infinite network. This takes place during the onset of the polymerization reaction at gel time. Gelation is a microscopic phenomenon but is characterized by macroscopic effects. It seems necessary to distinguish the microscopic gelation and its consequence, i.e. macroscopic gelation. Microscopic gelation appears at a gel time which corresponds to a defined point in chemical reaction and, thus, a specified curing degree. This kind of gelation depends on functionality, reactivity and stoichiometry of the reactants and is very difficult to quantify since it corresponds to measure solubility and molecular weight. At macroscopic scale, gelation means in a phase change from a liquid to solid and the change in mechanical properties associated is easier to measure. In addition, beyond the gel time, the molecular weight no longer changes [DUS 88], thus only

macroscopic change can be investigated all over the curing reaction. Macroscopic gelation affects adhesion, elastic properties, viscosity and general processability of adhesives. This gelation time can be experimentally determined with Dynamic Mechanical Analysis (DMA) measurements. The first evidence of this phenomenon appears in the complex modulus, tangent delta and complex viscosity [AST 90]. The gelation time is the time for which tangent delta *tanδ* is at the maximum (Figure 9)[GIL 74][ENN 83]. Menard et al. [MEN 99] defined it as the crossover point of the loss and storage moduli (one major drawback of this method is that some materials do not have a crossover point).

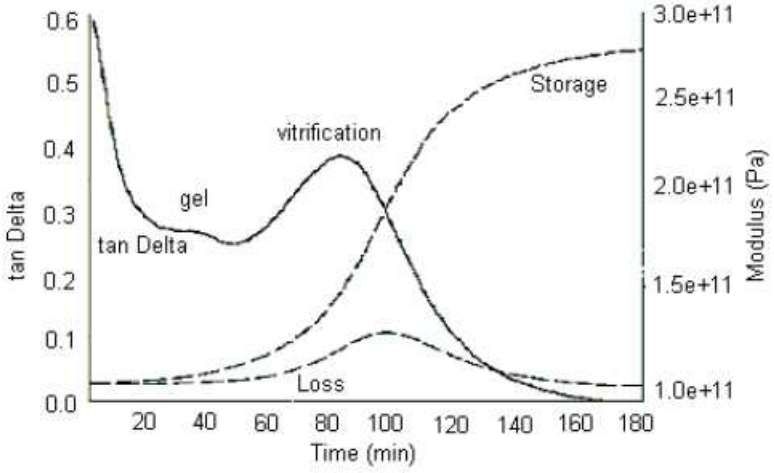

Figure 9. Changes in DMA measurements during isothermal curing [BIL 00].

Vitrification corresponds to the stage of cure at which the curing adhesive transforms in a glassy solid. At this point, the reaction is decelerated due to the reduced mobility of the reactants and the difficulty to diffuse to each other. Contrary to gelation, vitrification is a phase transition from a rubber to glass which can be quantified through Differential Scanning Calorimetry (DSC) and DMA measurements. In DSC analysis, the vitrification is characterized by a decrease in reaction rate around the end of curing. However, it is generally masked by the curing reaction exotherm in classical DSC. Hence, it is preferable to use a modulated-temperature (TMDSC). The curing exotherm appears in the loss heat capacity C_p but vitrification is identified in the storage heat capacity C_p [BIL 98][BIL 99]. A series of isothermal MTDSC measurements in Figure 10 shows a vitrification point as half-height drop of the storage heat capacity C_p.

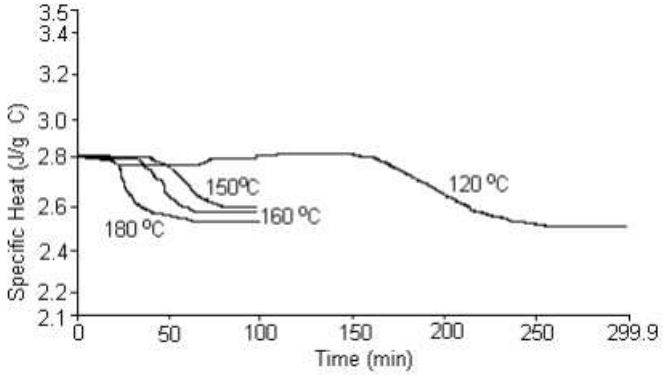

Figure 10. Example of isothermal modulated-temperature DSC scans [BIL 00].

These major phase transformations appearing during the curing process are represented in a Time-Temperature-Transformation (TTT) diagram and a Conversion-Temperature-Transformation (CTT) diagram [ENN 83][WIS 90](Figure 11). In these diagrams, several regions correspond to different physical states of the adhesive during curing. On these diagrams, there are three critical temperatures: T_{g0} is the glass transition temperature of the uncured adhesive, T_{gel} is the glass transition temperature at which gelation

and vitrification occur simultaneously, $T_{g\infty}$ is the glass transition temperature of the fully cured adhesive. At temperatures below and close to the glass transition T_{g0}, the reactive species are immobilized in a glassy state, therefore, reaction is slow to occur. For temperatures ranging from T_{g0} to T_{gel}, the liquid mixture reacts until its glass transition temperature T_g reaches the cure temperature. At temperatures between T_{gel} and $T_{g\infty}$, gelation precedes vitrification and a cross-linked network forms and grows until the glass transition temperature $T_{g\infty}$ reaches the cure temperature. At temperatures close to $T_{g\infty}$, the reaction may be controlled by diffusion. Below this temperature, the adhesive remains in the rubber state when no degradation occurs. Otherwise, the adhesive transforms in a char.

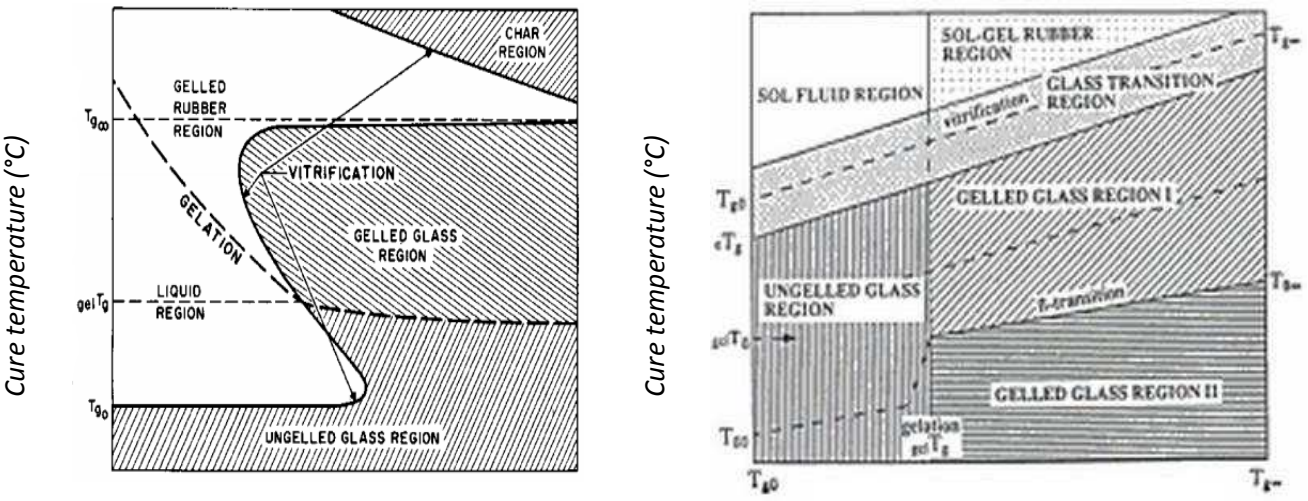

Figure 11. (a) Generalized isothermal cure diagram of Time-Temperature-Transformation and (b) Generalized isothermal diagram of Conversion-Temperature-Transformation.

The evolution of the glass transition T_g shown in the TTT and CTT cure diagram can be described with a relationship with the segmental mobility, the cross-link density and the degree of conversion. Dibenedetto et al. [DIB 87] proposed the following equation:

$$\frac{T_g - T_{g0}}{T_{g0}} = \frac{(\varepsilon_\infty / \varepsilon_0 - c_\infty / c_0)x}{1-(1-c_\infty / c_0)x} \qquad (1.1)$$

where x is the crosslink density, ε_0 the lattice energy of the uncured adhesive, ε_∞ the lattice energy of the fully cured adhesive , c_0 the segmental mobility of the uncured polymer and c_∞ the segmental mobility of the totally cured polymer. A modification of this equation was proposed by Pascault et al. [PAS 90], such as:

$$\frac{T_g - T_{g0}}{T_{g\infty} - T_{g0}} = \frac{\lambda\alpha}{1-(1-\lambda)\alpha} \qquad (1.2)$$

where α is the curing degree, λ a structure-dependent parameter ranging from 0 to 1. This parameter is also equal to the ratio of the differences in heat capacity between the glassy state and rubbery/liquid state at fully cured conversion and uncured conversion [VEN 97]:

$$\lambda = \frac{\Delta C_{p\infty}}{\Delta C_{p0}} \quad (1.3)$$

The value of the parameter λ generally ranges from 0.2 to 0.8 for a DGEBA (epoxy resin)/DETA (hardener) system.

1.2.1.2. Cure monitoring techniques

As shown previously, the curing of an adhesive initiates some processes for which various phase transformations associated to complicated curing kinetics occur. Some different thermal analysis monitoring methods are able to follow the changes in thermal properties of appearing during the curing of adhesives. Among these techniques, there are Differential Scanning Calorimetry (DSC) analysis, Dynamic Mechanical Analysis (DMA), Thermogravimetric analysis (TGA).

Differential Scanning Calorimetry

Differential Scanning Calorimetry is the most common type of cure monitoring technique. It consists in measuring the difference in thermal energy inouts into a sample and a reference as a function of time or temperature when a thermal load is applied. Both isothermal (constant temperature) and dynamic (temperature increases linearly at a constant heating rate) heating conditions can be submitted. The reference is generally an empty pan or an inert material.

DSC is able to measure the phase transitions, such as glass transition, melting and crystallization. Data as specific heat capacity, degree of cure can also be investigated. DSC is often used to identify the curing kinetics of a thermoset, particularly of epoxy polymeric materials. This method has some advantages: it requires small weight samples, high speed of determination, thus reduction of costs of time and production. In addition, DSC is a reliable technique since it provides an accuracy of results better than 1-2%.

Two types of scanning calorimeter can be identified (Figure 12). On one hand, the “heat flux DSC” monitors the heat flux between the sample and the reference using a configuration in a single cell with only one heating source. On the other hand, regarding the “power compensation DSC”, the sample and reference are in separate cells. This kind of DSC measures the difference in power applied to maintain a zero temperature gradient between the sample and reference. This cure monitoring technique made the assumption that the temperature gradient within the sample is negligible.

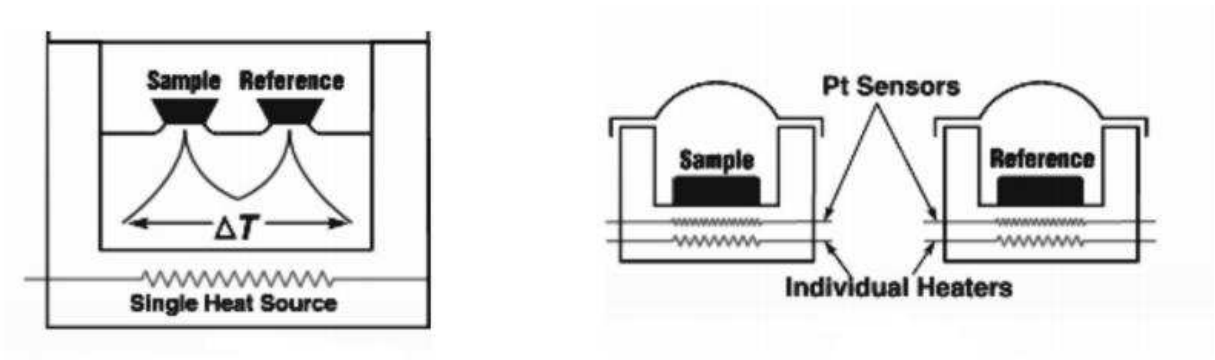

(a) (b)

Figure 12. Schematic representation of two types of DSC: (a) heat flux DSC and (b) power compensation DSC.

Spectroscopy techniques

Spectroscopy techniques, such as Infrared Spectroscopy (IR) and Fourier Transform Infrared Spectroscopy (FTIR) are reliable methods for monitoring the curing process of a thermoset [BAK 93][JOH 92].

Infrared spectroscopy consists in measuring the absorption of the IR radiations in the frequency range for which the molecule vibrates. These vibrations come from the functional groups contained in the polymer chain.

Fourier Transform Infrared Spectroscopy is based on the same principle of infrared spectroscopy. A major difference is that IR used a prism or gratings to separate the individual frequencies of energy emitted from the infrared source. However, FTIR is preferred to IR for many reasons. It is a non destructive method. This technique gives precise measurement without external calibration. Then, it has greater optical throughput. Finally a lack of sensitivity and thus, a lack of reliability is generally observed for the infrared spectroscopy instrumentation.

These measurement techniques are based on the absorption of light due to characteristic vibrations of molecular species in the infrared spectral region and rely on Beer-Lambert law:

$$\mathrm{A} = -\log_{10}\frac{\mathrm{i}}{\mathrm{i}_0} = \varepsilon \cdot \mathrm{l} \cdot \mathrm{c} \tag{1.4}$$

where A is the absorbance, *i* the intensity of transmitted light and i_0 is the intensity of the incident light. *c* (mol.L^{-1}) is the molar concentration of attenuating species in the material, *l* (cm) the path distance of the light through the sample and ε (L.mol^{-1}.cm^{-1}) is the molar absorptivity of the sample. Equation 1.4 shows a linear dependence of the absorption intensity on the molar concentration of the attenuating species. Hence, it is possible to extract some informations. For instance, strong absorptions are observed in the mid-infrared region (almost 915 cm^{-1}) for an epoxy thermoset system. The following relationship normalizes the peak intensity by a reference [SAB 87][SCH 87][MIJ 96]:

$$\mathrm{f}_{915} = \frac{\mathrm{A}_{915,\mathrm{t}}}{\mathrm{A}_{\mathrm{ref},\mathrm{t}}}\frac{\mathrm{A}_{\mathrm{ref},0}}{\mathrm{A}_{915,0}} \tag{1.5}$$

Where f_{915} is the fraction of unreacted species at time *t*, $A_{915,t}$ is the specimen absorbance at 915 cm^{-1} at time *t*, $A_{ref,t}$ is specimen absorbance at reference band at time *t*, $A_{ref,0}$ is specimen initial absorbance at reference band and $A_{915,0}$ is specimen initial absorbance at 915 cm^{-1}. This previous equation is also a way to eliminate differences in sample slippage and in specimen thickness.

The presence of functional groups, such as OH and NH_2 groups can be investigated by monitoring other frequency bands and applying the equation 1.5 for this range of frequencies. Thus, the molar concentrations of different functional groups give an access to the kinetics if the epoxy system.

Dynamic Mechanical Analysis

Thermosets, such as epoxy adhesives, generally exhibit viscoelastic properties [CHO 88][FER 80]. These ones changes during curing process [HOS 10]. Dynamic Mechanical Analysis (DMA) is generally used to characterize a material as a function of time, temperature. It consists in measuring the response of a material that is subjected to oscillating stress. From this stress applied, an oscillating strain is measured. This indicates mechanical properties such as the tendency to flow, i.e. viscosity, and the stiffness modulus. Experimentally, this measures stiffness and damping. These data are expressed through a dynamic modulus E', a dynamic loss modulus E" and a mechanical damping term delta δ (energy dissipation of the material). If the material is purely elastic, there is no phase difference between the stress applied and the strain occurred (δ=0°). If the material is perfectly viscous, a phase angle δ of 90° is observed between the applied

load and the resultant strain. For a viscoelastic material, the phase angle δ is between the maximum values 0° and 90° (Figure 13 (a)) and is mathematically divided into dynamic and dynamic loss modulus (equation 1.6 and equation 1.7, Figure 13 (b)).

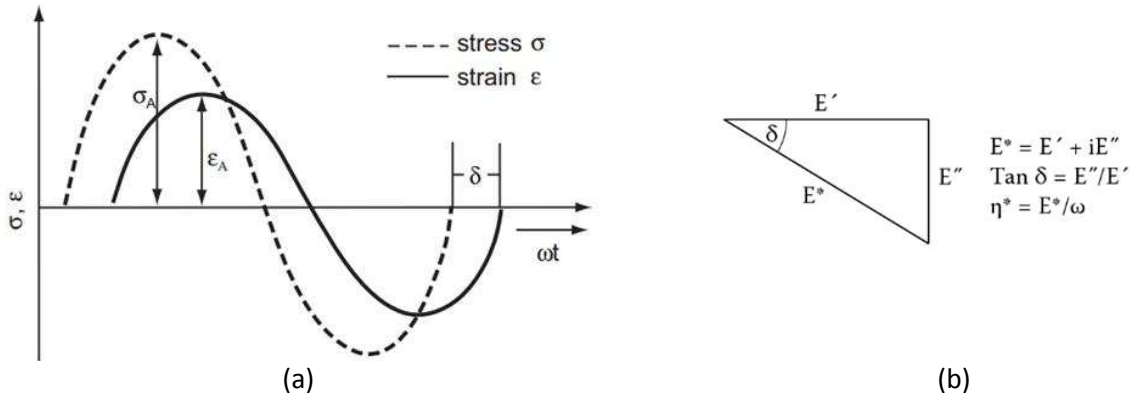

(a) (b)

Figure 13. (a) DMA response of a linear-viscoelastic material and (b) vector triangle representing the relationship between complex *E, dynamic *E'* and dynamic loss *E"* moduli measured by DMA.**

$$E^* = E' + iE'' \tag{1.6}$$

$$\mathrm{Tan}(\delta) = \frac{E''}{E'} \tag{1.7}$$

DMA not only estimates viscosity and modulus but it also provides information about curing process, such as the onset of cure, the glass transition temperature T_g [SIR 96][DIN 91][HUR 83][BAR 93]. Some standards [AST 90a][AST 90b][AST 94] are recommended to measure accurately the T_g using DMA. This temperature is generally the temperature for which the dynamic loss modulus *E"* or the maximum loss factor $tan(\delta_{max})$ is maximum. Some methods define the glass transition temperature as the inflection point or the height value of the drop in dynamic modulus *E'*, the onset of the drop in dynamic modulus, the onset of increase of dynamic loss modulus and the onset of increase in the loss factor *tan(δ)*.

Thermo Gravimetric Analysis

Thermo Gravimetric Analysis is generally used to determine thermal degradation temperature or thermal stability. This technique monitors the weight loss of a thermoset that is subjected to a controlled temperature in a controlled atmosphere. Thus, the weight change is a function of time and temperature. The thermal stability can be investigated by comparing weight change for several thermosets [PRA 04].

1.2.1.3. Cure kinetics

The curing process of adhesives generates lot of thermal gradients inside these materials which are converted from a viscous liquid to a solid. Since, the curing process generates changes in adhesive properties and so does the bonded assembly, it is very important to correctly estimate the ultimate state of the cured adhesive whatever the thermal history or the thermal loads applied on the assembly during the curing process may be. Some mathematical models (Table 2) are used to describe properly the adhesive-curing reactions. Beyond these kinetic models, there are mechanistic [LEE 00][VAL 05][YOU 97] and phenomelogocial models [LIL 05].

Mechanistic models are complex models which are written at microscopic scale. These are made from the balance of reactive species involved in the chemical reactions. So, it requires measurements of concentrations of reactant, intermediates and final species. Phenomenological models are identified at macroscopic scale and assume an overall reaction. These are based on an empirical relation between

reaction kinetics. These models are fitted to experimental kinetic data (as shown later in chapter 2). These kinds of models give little information on the reaction mechanism but are generally preferred to describe the curing behavior of a thermoset in the case of industrial applications.

Since the chemical composition of the adhesive constituents is unknown, phenomenological models were preferred to study the cure kinetics of the adhesive. One drawback of the cure kinetic modelling is that there is no general model to predict the curing behavior of all thermosets. Another one is that, for a given thermoset, kinetic models are generally based on dynamic and isothermal approaches. The first one describes the curing for non-zero curing rate whereas the other one is used for isothermal loadings. Hence, both issues needs to be investigated to predict properly any curing cycle which is a combination of dynamic and isothermal scans. These kinds of problems are really limiting in the case of industrial applications since it generates costs of time and production.

Kinetic model	**Reference**	**Expression**	**Parameters**	
			Nb	**Definition**
1^{rst} Order	[MAR 89]	$\frac{d\alpha}{dt} = k(1-\alpha)$	3	k: Rate constant E_a: Activation energy A: Rate coefficient
n^{th} Order	[KNA 91][CHI 92][RYA 73]	$\frac{d\alpha}{dt} = k(1-\alpha)^n$	4	k: Rate constant E_a: Activation energy A: Rate coefficient n: Reaction order
Autocatalytic - 1	[SUN 02]	$\frac{d\alpha}{dt} = k\alpha^m(1-\alpha)^n$	5	k: Rate constant E_a: Activation energy A: Rate coefficient m, n: Reaction orders
Autocatalytic - 2	[LAN 87]	$\frac{d\alpha}{dt} = (k_1 + k_2\alpha)(1-\alpha)(B-\alpha)$	7	k_1, k_2: Rate constants E_{a1}, E_{a2}: Activation energies A_1, A_2: Rate coefficients B: Stoichiometry factor
Autocatalytic - Horie	[HOR 70]	$\frac{d\alpha}{dt} = (k_1 + k_2\alpha)(1-\alpha)^2$	6	k_1, k_2: Rate constants E_{a1}, E_{a2}: Activation energies A_1, A_2: Rate coefficients

Autocatalytic - Kamal & Sourour	[KAM 73][KAM 76]	$\frac{d\alpha}{dt} = (k_1 + k_2\alpha^m)(1-\alpha)^n$	8	k_1, k_2: Rate constants E_{a1}, E_{a2}: Activation energies A_1, A_2: Rate coefficients m, n: Reaction orders
Self acceleration	[MAL 89]	$\frac{d\alpha}{dt} = k(1-\alpha)(1-C\alpha)$	4	k: Rate constant E_a: Activation energy A: Rate coefficient C: Constant
Mechanistic	[YAN 91]	$\frac{\alpha}{\alpha_{gel}} = f(\text{concentration})$	1	α_{gel}: conversion at gelation

Table 2. Mathematical models to represent the curing behavior of thermosets.

For each model, the data k or k_i (i=1,2) is the time-dependent reaction rate following the Arrhenius law [ARR 89] :

$$k = Ae^{-\frac{E_a}{RT}} \tag{1.8}$$

where A (s^{-1}) is the pre-exponential factor, E_a (J/mol) is the activation energy, R (8.314 J/mol-K) is the universal gas constant and T (K) the temperature.

The parameters of the curing rate models are determined either under isothermal or dynamic DSC experiments [GIL 74][KAM 73][KAM 76][LEE 00][RIC 84]. Indeed, some models are dedicated to describe curing behavior of a thermoset under isothermal conditions and the others are intended to describe it under dynamic conditions. A non linear least-squares regression is generally used to determine the parameters of each model [LEE 82]. A good correlation is often observed between experiment and results predicted by models for identical running conditions. On the contrary, experiment and results predicted by models differ when a dynamic model is applied on experimental isothermal DSC data. A similar observation is done for isothermal predictions of experimental dynamic DSC data. MacCallum et al. [MAC 70] discussed the applicability of isothermal models to describe dynamic conditions.

1.2.1.4. Diffusion-controlled phenomena

As shown previously on the Time-Temperature-Transformation cure diagram explanation, the cure reaction is controlled by chemical kinetics and diffusion. At the early stage of the curing reaction, when the mixture resin/hardener is liquid (low viscosity), the curing reaction is controlled by chemical kinetics. Approaching the glassy state, the reaction become diffusion-controlled and consequently the movement of the reactive species is decelerated and thus, the reaction is slowed down. α_c is the critical curing degree for which this phenomena occurs. Cole at al. [COL 91] proposed a rate constant $k_{diffusion}$, based on free volume theory, to describe the diffusion phenomena:

$$k_{diffusion}(\alpha) = k_{chemical}e^{-C(\alpha-\alpha_c)} \tag{1.9}$$

Where $k_{chemical}$ is the rate constant of the curing reaction controlled by chemical kinetics, C is an empirical constant which is temperature dependent.

Wise et al. [WIS 97] suggested a modification of the WLF equation [WIL 55] to model the diffusion rate constant:

$$k_{diffusion}(T) = k_{diffusion0} e^{\frac{C_1 (T - T_g)}{C_2 + T - T_g}} \quad (1.10)$$

where C_1, C_2 are fitting parameters and T is the cure temperature of the system. T_g is the glass transition of the curing system. $K_{diffusion0}$ is the value of the diffusion rate at the glass transition $(T=T_g)$.

Gillham et al. [SIM 93] proposed a diffusion model based on free volume theory, such as:

$$k_{diffusion}(T) = k_{diffusion0} e^{-\frac{b}{f}} \quad (1.11)$$

where b is an adjustable parameter. f is a free volume parameter described by the following expression:

$$f = 4.8 \cdot 10^{-4} (T - T_g) + 0.025 \quad (1.12)$$

where T is the cure temperature and T_g the glass transition temperature of the system. $k_{diffusion0}$ follows an Arrhenius law [ARR 89].

Considering the overall curing reaction, this latter can be decomposed into distinct mechanisms: chemical-controlled and diffusion-controlled mechanisms. Then, the overall reaction rate constant k, which controls the curing reaction rate, can be written as follows [RAB 37]:

$$\frac{1}{k} = \frac{1}{k_{chemical}} + \frac{1}{k_{diffusion}} \quad (1.13)$$

At the onset of the curing process, the reaction is chemical-controlled. Hence, $k = k_{chemical}$. The chemical rate constant $k_{chemical}$ follows an Arrhenius temperature-dependence law [ARR 89]. Approaching the glassy state, the reaction becomes diffusion-controlled. Thus, the rate constant $k_{diffusion}$ is stronger and needs to be considered in the overall rate constant definition.

Regarding the definition of the diffusion according to Cole et al. [COL 91] (equation 1.10), a combination of equation 1.9 and 1.13 gives the diffusion factor DF:

$$DF(\alpha) = \frac{k}{k_{chemical}} = \frac{1}{1 + e^{C(\alpha - \alpha_c)}} \quad (1.14)$$

Fournier et al. [FOU 96] proposed a diffusion factor on the basis of Cole's diffusion rate contant:

$$DF(\alpha) = \frac{2}{1 + e^{\frac{(\alpha - \alpha_c)}{b}}} - 1 \quad (1.15)$$

where b is an empirical parameter and α_c the critical curing degree for which diffusion appears.

This factor is used to quantify the deceleration effect of diffusion on cure kinetics. If $\alpha << \alpha_c$, the reaction is governed by chemical kinetics. The diffusion factor DF is close to unity and the contribution of diffusion is negligible. When $\alpha \geq \alpha_c$, the diffusion factor DF decreases linearly and tends to zero when the curing reaction stops.

The modified kinetics models are obtained by combining the diffusion factor DF with the curing models defined in Table 2 as the ratio of the experimentally measured curing rate $(d\alpha/dt)_{exp}$ over the predicted

conversion rate (such as models presented in Table 2) at the same degree of cure α without mobility restrictions $(d\alpha/dt)_{models}$:

$$\left(\frac{\mathrm{d}\alpha}{\mathrm{dt}}\right)_{\mathrm{exp}} = \mathrm{DF}(\alpha,\mathrm{T})\left(\frac{\mathrm{d}\alpha}{\mathrm{dt}}\right)_{\mathrm{models}} \tag{1.16}$$

where $k_{chemical}$ and $k_{diffusion}$ are the rate constants of the cure reaction controlled by chemical kinetics and of the same reaction controlled by diffusion, respectively.

1.2.1.5. Determination of kinetic parameters using DSC and errors affecting parameters

Treatment of DSC data

As shown previously, DSC monitoring technique is used to measure the difference in heat flow rate between a sample (a thermoset in our case) and a reference. The reaction kinetics are determined from these measurements by assuming that the heat of reaction at a time *t* is proportional to the overall extent of reaction given by the concentration of reactive groups consumed. Hence, from this assumption, the degree of cure α can be defined such as [KIM 98][RYA 84][WHI 02]:

$$\alpha = \frac{\Delta \mathrm{H_t}}{\Delta \mathrm{H_T}} = \frac{\int_0^{\mathrm{t}} \left(\frac{\mathrm{dH}}{\mathrm{dt}}\right) \mathrm{dt}}{\int_0^{\mathrm{t_f}} \left(\frac{\mathrm{dH}}{\mathrm{dt}}\right) \mathrm{dt}} \tag{1.17}$$

where ΔH_t is the heat of reaction released during isothermal or dynamic scan at an intermediate curing state of the adhesive at time *t*, ΔH_T is the total heat of reaction calculated during dynamic scans, $(dH/dt)_t$ is the heat flow at time *t* and $(dH/dt)_t$ is the heat flow at the end time of reaction t_f measured by isothermal or dynamic scans.

The rate of the curing reaction is obtained as follows:

$$\frac{\mathrm{d}\alpha}{\mathrm{dt}} = \frac{1}{\Delta \mathrm{H_T}} \left(\frac{\mathrm{dH}}{\mathrm{dt}}\right)_{\mathrm{t}} \tag{1.18}$$

DSC measurements can be conducted under isothermal or dynamic conditions. An isothermal DSC analysis consists in measuring the heat flow released (equation 1.17), and then, the heat of reaction released at a constant temperature. Regarding dynamic scanning condition, the previous quantities are measured over a constant heating rate scan. Typical DSC thermograms for a thermoset curing under dynamic and isothermal conditions appear in Figure 14.

These thermograms give an access to the integral quantity of equation 1.17 (ΔH_t) by integrating the area under the curves along a baseline. This baseline is generally defined in two ways: a straight baseline and a sigmoidal baseline. In DSC analysis, baseline is often investigated by realizing a second isothermal heating run on the sample which has already being cured. As shown in Figure 14 (b) for isothermal measurements, this baseline is almost a horizontal line. Hence, the difference between a heat of reaction calculated by integrating the area under a straight baseline and those calculated by integrating along a second-run baseline is negligible. On the contrary, for dynamic scans (Figure 14 (a)), the line along which the area under the curves is integrated is a sigmoidal baseline. Therefore, the use of a straight baseline can affect reliability and accuracy of the data.

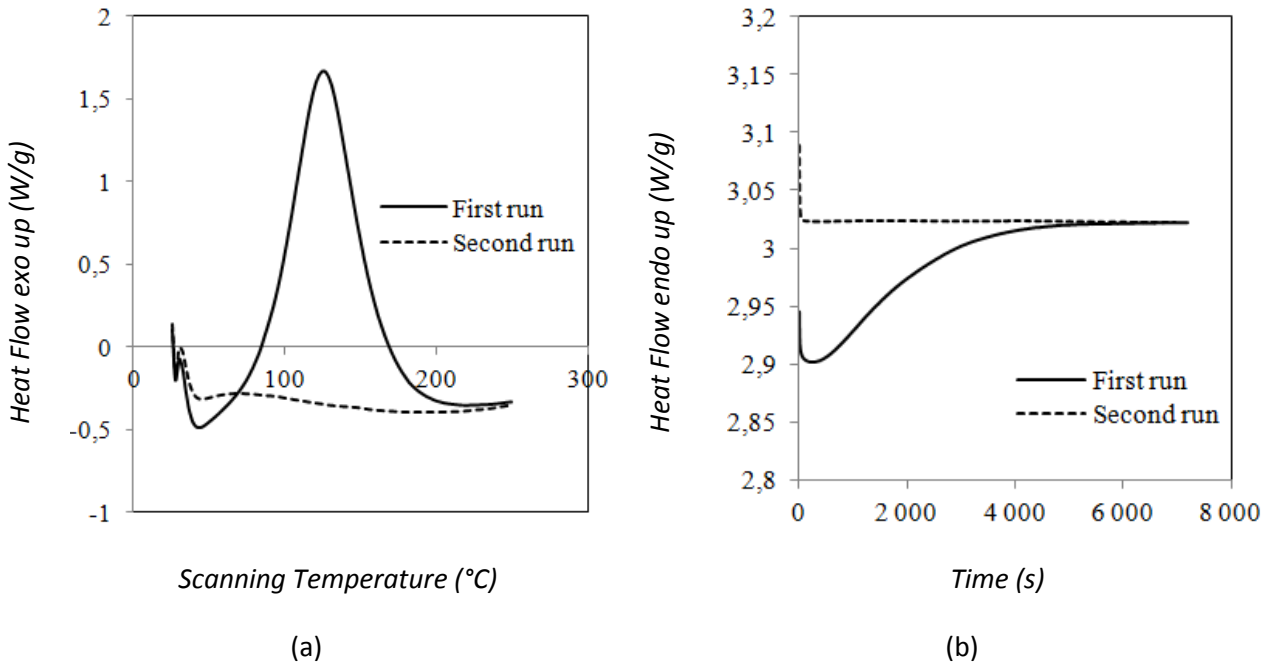

Figure 14. Typical DSC thermograms of a curing thermoset: (a) dynamic scan and (b) isothermal scan.

Bandara et al. [BAN 86] established an iterative algorithm to provide the sample baseline correction for all dynamic scans. In the case of thermoset curing, this algorithm assumes that thermal loadings involve progressive changes in chemical composition and in physical properties, such as specific heat, of uncured and cured thermoset. During the dynamic curing stage, the chemical blend evolves to reach its final state and contains a lot of intermediate species. Thus, the temperature range can be divided into a number of segments S_n and the sample baseline can be written as:

$$S_{baseline}(t) = \sum_{i=1}^{S_N} \alpha \cdot \left[S_f^i(t) - S_0^i(t) \right] + S_0^i \tag{1.19}$$

where α is the curing degree (defined, as previously, in equation 1.17), $S_0^i(t)$ is the DSC heat flow at the onset of the curing reaction and $S_f^i(t)$ is the DSC flux at the end of the dynamic curing reaction. Considering the assumption on the chemical blend, the following conditions are satisfied:

$$S_{baseline}(t) = \sum_{i=1}^{S_N} S_0^i(t) \quad \text{for} \quad \alpha = 0 \tag{1.20}$$

$$S_{baseline}(t) = \sum_{i=1}^{S_N} \alpha \cdot S_f^i(t) \quad \text{for} \quad \alpha = 1 \tag{1.21}$$

An iterative algorithm (Figure 15) must be implemented to measure the curing degree and the sample baseline during the dynamic curing process.

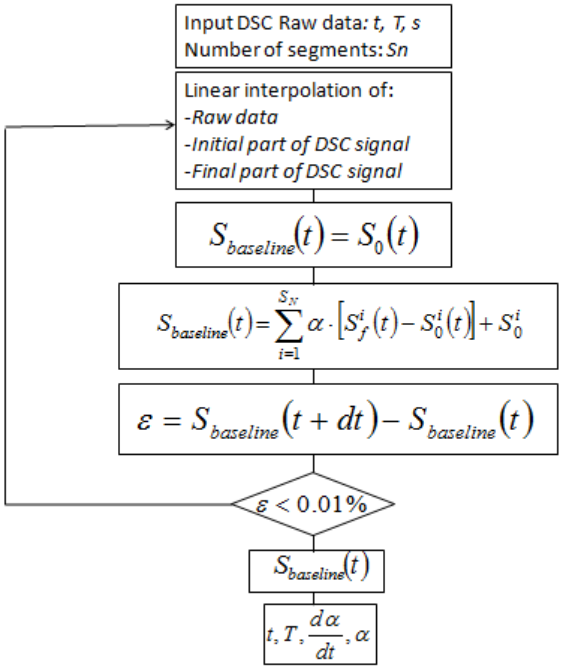

Figure 15. Bandara algorithm: flow chart.

1.2.2. Adhesion theory

Kinloch et al. [KIN 87] defined an adhesive as the material used to create a bonded assembly by holding two substrates together thanks to interfacial forces. The resulting adhesion mechanism is not a generalized and unified phenomena but the addition of various complex adhesion effects. In fact, interfacial adhesion can take place on cell-scale, as bioadhesion, to large-scale, such as space bonded structure. Thus, interfacial forces involved in the bonding mechanism range from intermolecular strengths, like Van der Waal's forces, to mechanical loadings. In the same way, the environment in which the adhesion phenomenon occurs varies from sub-freezing to high temperatures as in aerospace industry. This wide range of conditions has a significant impact on the resulting bond strength and the joint failure. These two quantities provide insight of the success of the bonding process and the level of adhesion reached inside. Joint failures are generally as either "cohesive" or "adhesive". Cohesive failure is a failure in the bulk layer of the adhesive or the adherends away from the interface. Adhesive failure appears when the failure happens at the interface between the adhesive and adherends. A combination of both kinds of failure (cohesive and adhesive) sometimes appears. It is called "mixed failure mode" (Figure 16 (d)).

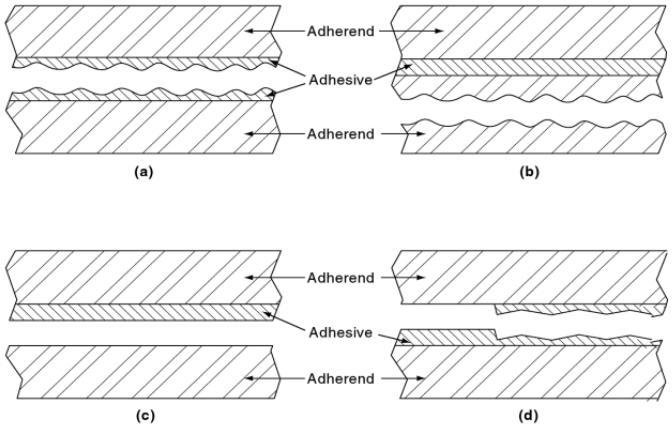

Figure 16. (a) Cohesive failure within the adhesive, (b) cohesive failure within the adherends, (c) adhesive failure and (d) mixed-mode failure. [MES 04]

Some theories of adhesion have been proposed [COG 00][COM][DAR 02][ROC 02] to attempt to describe the phenomenon of adhesion. These latter can be classified into physical and chemical interactions (Figure 17).

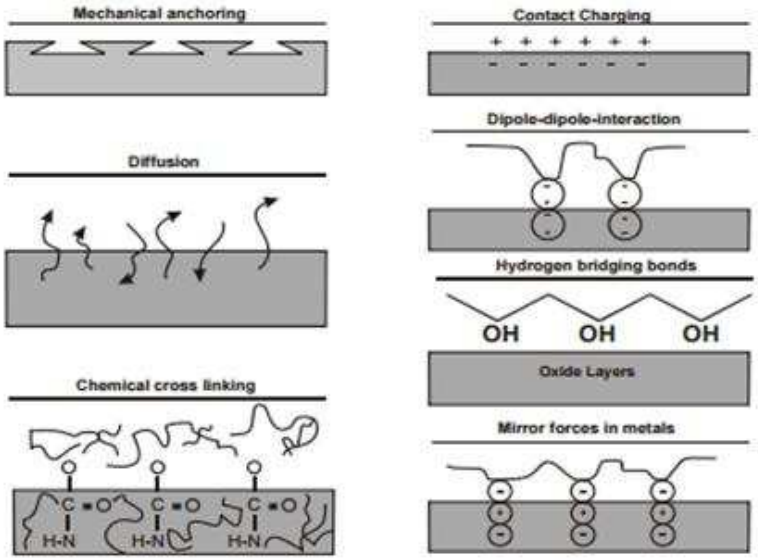

Figure 17. Physical and chemical causes of adhesion [BAS 03].

1.2.2.1. Physical interactions

Mechanical interlocking

This is the oldest theory of adhesion. This was firstly based on the mechanical anchorage of an adhesive in a wood adherend and similar porous materials [MAC 25]. Then, it was extended to other materials such as aluminum. This theory assumes that adhesion occurs by penetration of the adhesive into surface irregularities of the adherend, such as pores, holes or cavities. Hence, a good adhesion is provided by an adherend surface with sufficient microsopic cavities or undercutting. Packam et al. [PAC 83] emphasized the role of mechanical interlocking on the resulting adhesion strength. The mechanical interlocking mechanism is controlled by the roughness. Therefore, mechanical adhesion is surface roughness dependent. Mechanical interlocking can provide a better adhesion process by increasing the area of the surface to be bonded and, then, by increasing of the number of microscopic undercutting or root-like cavities. However, an important roughness can conduct to entrap air bubbles and lead to stress concentrations, crack initiation. Mechanical interlocking can contribute to make stronger adhesive bonds that resist to thermal and hydrolytic degradation [SNO 02]. This is mainly shown in the case of adhesion of polymers to metals or textiles [MIC 87][RIT 98]. Michalske et al. [MIC 93] reported that good bond strength and long term durability for anodized metal bonded assembly require mechanical interlocking. This theory does not explain the good adhesion of polymers with perfectly smooth surfaces (for instance for some glasses).

Diffusion theory

This theory was primarily developed to explain the adhesion of polymer materials to themselves (autohesion) [VOY 63] and states that adhesion is obtained by mutual penetration (interdiffusion) (Figure 18) of adhesive and substrate. Since interdiffusion depends on factors like temperature and contac time, both materials are placed in contact for a significant period and at temperatures ranging above their glass transitions. This theory is based on two fundamentals properties of polymers, namely chains mobility and solubility. In fact, the polymer chains are sufficiently mobile and mutually soluble to diffuse into each other

across the interface. Several mechanisms explain the self-adhesion of a polymer: reptation [BRO 86], entanglement coupling [KLE 79] and cooperativity [EDW 73].

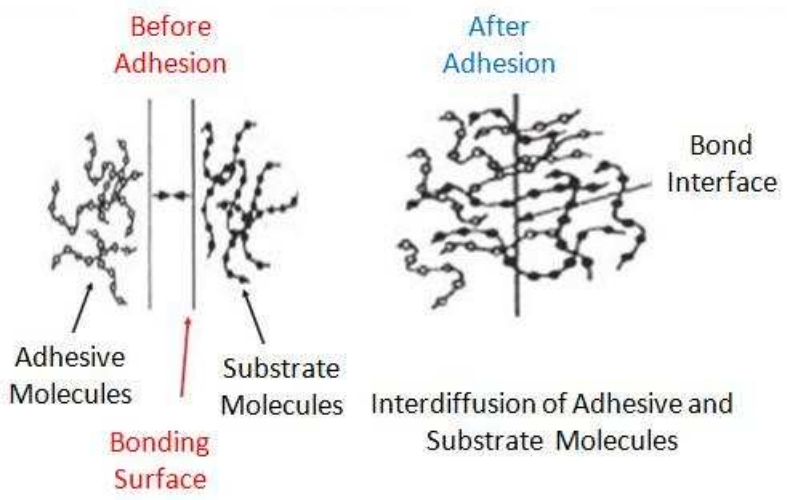

Figure 18. Interdiffusion at the interface adhesive-substrate [CHAP 14].

The validity of this theory is limited for non-soluble polymer and substrate, highly crosslinked polymers or if contact between adhesive and substrate occurs at temperatures ranging far below their glass transition temperatures.

Electrostatic theory

This theory was proposed by Deryagin et al. [DER 48] and is based on the difference in electronegativity of an adherend and an adhesive coming in contact to each other. When an adhesive is placed in contact with an adherend, electrons are transferred from one to the other. For an aluminium substrate, such transfer goes from adhesive to adherend. This forms an electrical double layer at the interface which gives electrostatic attraction forces. Some authors demonstrated that electrical effects have an influence on the adhesive strength. Possart et al. [POS 88] identified experimentally the electrical double layer at the interface without breaking the adhesive bond by using Scanning Electron Microscope (SEM). Horn et al. [HOR 90][HOR 92] revealed and determined charge transfer between glass and mica. One limitation of this theory is the case of non metallic systems for which the contribution of electrostatic mechanisms are negligible compared to that of chemical interactions [ROB 77a][ROB 77b].

Chemical bonding theory

This theory suggests the formation of chemical bonds across the interface between adhesive and adherend. Among these bonds, there are covalent, ionic or hydrogen bonds, Van der Waal's forces or Lewis acid-base interactions. Chemical bonds may have a significant contribution to the adhesive bond strength. Chemical forces are compared in Table 3. Covalent and ionic bonds forces have energies ranging from 60 to 1100 $kJ.mol^{-1}$, significantly higher other weak chemical bonds (around 0.08 to 50 $kJ.mol^{-1}$). Generally, other adhesion mechanisms are added to chemical adhesion (mechanical interlocking, diffusion, wetting). Hence, the chemical composition across the interface depends on functional groups of the adhesive, the chemical composition, surface properties of the adherend surface and, thus, the resulting strength may be different. Furthermore, coupling agents and adhesion promoters can be used to help in fixing the adhesive at the surface by chemical reaction [PLUE 91][HO 85][HAI 88].

Type of Interaction	Strength [kJ/mol]
Van der Waal's	
Induced dipole-induced dipole (dispersion or London forces)	0.08-40
Dipole-induced dipole (Debye forces)	>2
Dipole-dipole (Keesom forces)	4-20
Primary chemical bonds	
Covalent	60-700
Ionic	600-1100
Metallic	110-350
Hydrogen bonds	
Involving fluorine	Up to 40
Not involving fluorine	10-25
Acid-base interactions	
Conventional Bronsted	Up to 1000
Lewis	Up to 80

Table 3. Strengths of chemical forces which may contribute to adhesive resistance [KIN 87].

Weak boundary layer theory

In contrast to previous theories, this approach investigated by Bikerman [BIK 61] does not explain the adhesion of a material to another one, but rather why an adhesive and adherend debond. It is suggested that a failure in a bonded assembly only takes place in a single phase, at the weakest link at the interface between materials. Hence, there is a weak layer at the interphase between adhesive and adherend at which failure occurs. This weak boundary layer may have several origins [PAC 05][PET 07][PIZ 03] and appears at different working stages of the bonded joint. During the application stage of the adhesive along the adherend, air bubbles or impurities may be entrapped. Chemical deterioration or modification of the kinetics of the polymerization or cross-linking reaction may appear at the interface through catalytic effects or the competitive adsorption between reactive species during the curing reaction. Then, the service environment of the bonded joint (moisture exposure, corrosion) can generate weak boundary layers [COG 00].

Adsorption/Wetting theory

Proposed by Sharpe et al. [SHAR 64], this theory describes wetting phenomena of the adherend by the adhesive. Wetting is the ability of a liquid to maintain contact with a solid surface result from a balance between cohesion and adhesion (Figure 19 (a)) [SHU 85]. Cohesion is the result of attraction forces within the adhesive. On the contrary, adhesion is the effect of attraction forces at the interface between adhesive, adherend.

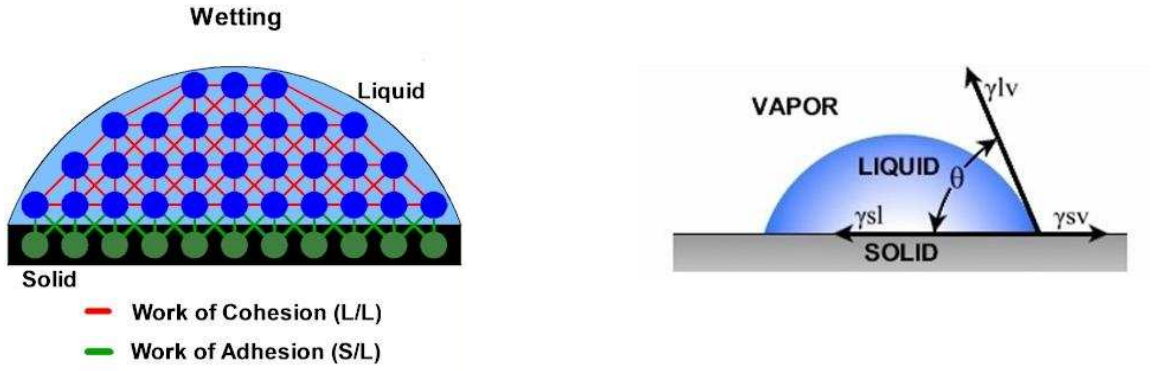

(a) (b)

Figure 19. Wetting phenomena: (a) Cohesion/adhesion and (b) Contact angle θ [BUD 10].

When adhesion forces between the solid and liquid are higher than the cohesive forces within the liquid, the liquid tends to wet the surface. The balance of cohesive and adhesive forces is described by the Young Equation:

$$\gamma_{SV} = \gamma_{SL} + \gamma_{LV}\cos(\theta) \tag{1.22}$$

where γ_{SV} is the surface energy at solid/vapour interface, γ_{SL} is the surface energy at solid/liquid interface, γ_{LV} is the surface energy at liquid/vapour interface. Θ is the contact angle resulting from a tendency of surface tensions to reduce the area of wet surface. Two equilibrium regimes can be identified (Figure 20). For a contact angle ϑ greater than 90°, the liquid does not wet the surface and conducts to a non-wetting. In that case, the surface is hydrophobic. A partial wetting is achieved for a contact angle ϑ ranging from 0 to 90°. Thus, the surface is hydrophilic. A complete wetting is reached for a contact angle θ equal to zero.

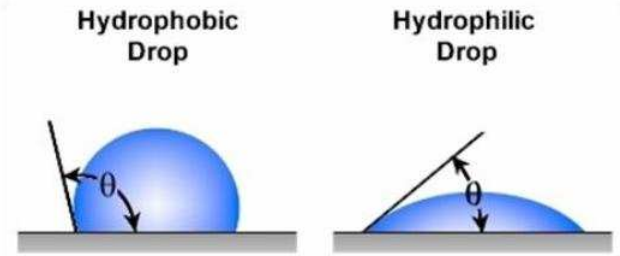

Figure 20. Schematic representation of both equilibrium regimes [BUD 10].

1.2.3. Surface treatments

Surface treatments aim to ensure that adhesion develops to the extent that the weakest link in the bonded assembly is either within in the adhesive or the adherend, i.e., a rupture occurs away from the interface and consists of a cohesive failure of adhesive or adherend rather than at the interface. Specific surface treatment strategies occur at different stages of the curing process (Figure 21). The selection of the surface

treatment for a given application depends on the materials to be bonded, the service environment and the stress applied.

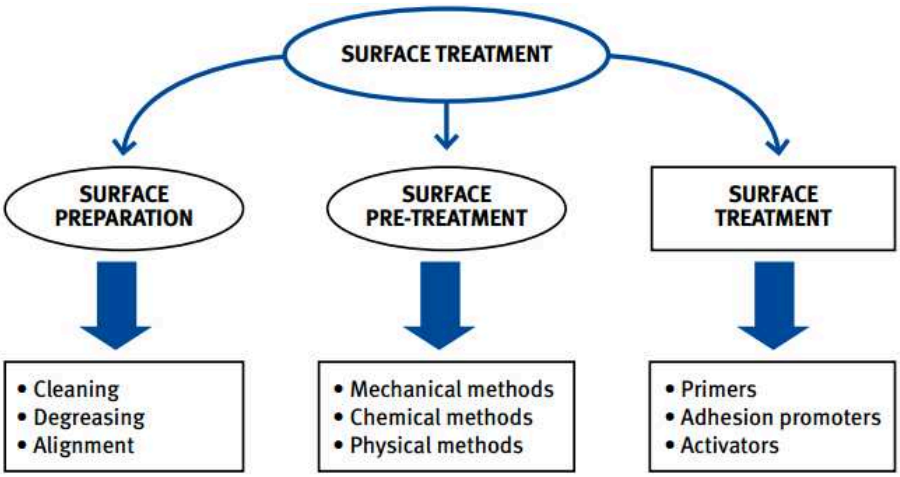

Figure 21. Process steps involved in surface treatment [TAS 09].

Surface preparation

The main purposes of surface preparation are to:

- Remove the contaminated weak boundary layers that prevent the adhesive from spreading properly on the substrate, create weak links at the interface adhesive/adherend. The contaminated layers are made from oils, greases, waxes, oxides (Figure 22)
- Prevent the development of weak boundary layers during working and ageing process
- Optimize the wetting of the adherend. To that end, the contact angle ϑ is reduced by increasing surface tensions at the interface between adhesive and adherend

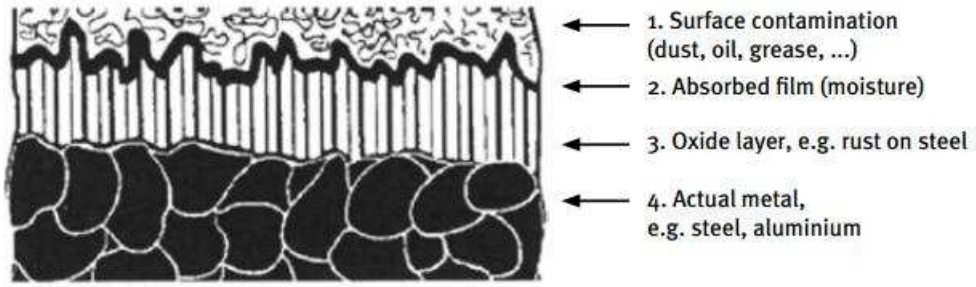

Figure 22. Typical surface layers on a metal substrate [TAS 09].

Optimal surface preparation is achieved on a two steps process which consists in cleaning the substrate and remove weak boundary layers from any kind of contamination.

The first step involves applying a cleaning solvent or a chemical treatment in order to remove contaminants from the surface. The most commonly used cleaning solvents are isopropyl alcohol and acetone. Chemical treatments are widespread to clean polymeric surfaces. This is usually a powerful solvent or a strong acid which is able to modify the chemical composition of the adherend surface. The most frequently used chemical treatments [KNI 97][DAV 89] are silicates, caustics, Phosphates….These treatments have the disadvantage of being adherend specific and require a proper chemical hygiene before application.

The second step is a mechanical process which aims to remove heavy contaminations such as oxide layers, dirt. It includes abrasive blasting, wire brushing and abrasion with sandpaper, metal wool, emery cloth [BIS 89][KIN 81][LEV 77]. The cleaning step is generally required after this kind of process.

Surface pre-treatment

Following the surface preparation, surface pre-treatment consists in removing the soaked weak surface layers of liquid solvent. Then, the inherent surface is activated by transforming its chemistry. This treatment step uses mechanical, chemical and physical methods. Mechanical and chemical methods are the same that those described for surface preparation. Physical methods use the reactivity of polymeric surface to modify its chemical composition by excited charges or species that promotes adhesion. Some techniques of this method are Plasma, Flame, Corona discharge or ion beam etching [MAR 10].

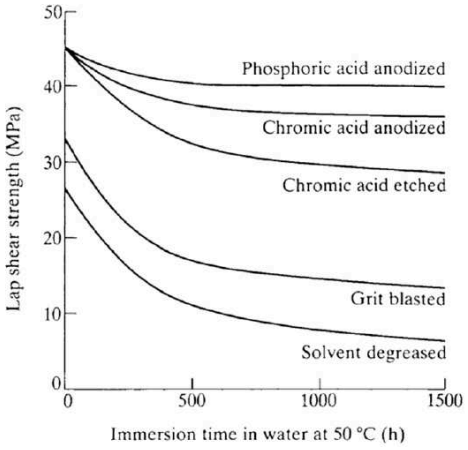

Figure 23. Effect of surface pre-treatment on the Lap shear strength of aluminium joints subjected to water-ageing [KIN 87].

According to Figure 23, phosphoric acid anodized and chromic acid anodized provide very good adhesion resistance.

Surface treatment

Surface treatment refers to the application of adhesion promoters, primers to improve adhesion by introducing an interphase region at which rupture will initiate (silane coupling agents, chromate conversion coatings for instance). In addition, this area may provide surface protection against external aggressions such as corrosion or ageing. Considering its main purposes, it is believed that kind of surface treatment improve the adhesive resistance. However, the introduction of an interphase area may contribute to a gradient of mechanical properties between the different phases. Hence, a modification of the mechanical properties close to the adherend may lead to stress concentrations and the resulting bonded strength may be affected [SCH 90].

The aerospace industry uses a wide variety of adherends in manufacturing bonded structures such as aluminium, stainless steel, titanium alloys or thermosetting/thermoplastic composites. The most commonly used surface preparation methods for metal adherends are chrome-sulfuric acid etching, chromic acid anodizing. For non metallic adherends, they may be sanded, grit blasted, etched with acids/bases, flame treated or plasma etched. Regarding primers, it consists generally in applying a spray, for instance BR®127 primer is used on lap shear specimens of FM®73 bonded to aluminium. Aerospace companies use an accelerated test to verify that surface preparation is suitable to insure durability. In this test, namely the wedge test (Figure 24), a wedge is driven between two strips of bonded adherend material. The specimen is stabilized one hour at room temperature. Then, the crack length is recorded and the specimen is placed

one hour at 140°F, 100 RH. In such conditions, crack growth should be very slight and failure should be mainly cohesive.

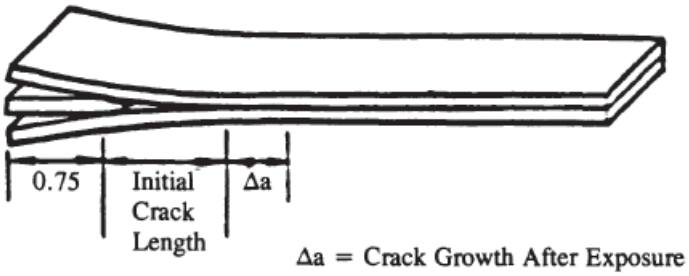

Figure 24. Wedge test specimen [SKE 90].

1.2.4. Mechanical properties of adhesives

In aerospace industry, a large spectrum of conditions and load type is encountered. This may affect the adhesively bonded joint resistance.

Influence of temperature

Structural adhesives are thermosetting polymers which exhibit a wide range of mechanical behavior. During curing process, a low molecular weight liquid is transformed into a cross-linked solid through successive chemical reactions. The temperature at which the adhesive changes from glassy to rubber-like behavior is the glass transition temperature *Tg* and corresponds to a significant change in mechanical properties. Hence, the mechanical behavior of the adhesive is very sensitive to temperature.

-Maurice et al.[MAU 13] shows experimentally the influence of curing temperature on the mechanical responses of an adhesive (Figure 25). In that case, the curing state of the adhesive is fixed following curing process and a specific curing state of the adhesive is associated with each curing temperature. Hence, from these curve, it can be assumed that curing degree has an influence on the mechanical response of an adhesive.

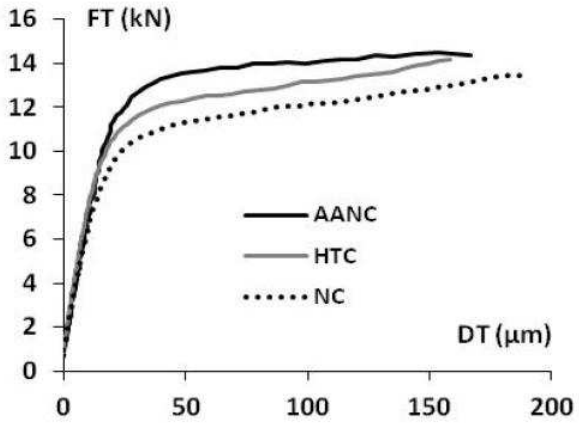

Figure 25. Experimental investigation of the influence of the curing temperature on the mechanical behavior of an adhesive in shear [MAU 13].

- Badulescu et al. [BAD 12] experimentally highlighted this trend by testing, via Modified Arcan device, identical bonded joint having undergone different thermal loads (Figure 26). The curing state of this adhesive is fixed following the curing but evolved with the thermal loads applied.

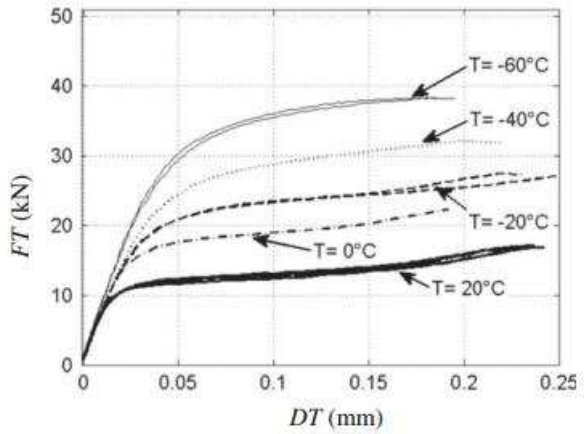

Figure 26. Experimental investigation of the influence of temperature on adhesive behavior using the Modified Arcan test in shear [BAD 12].

Influence of cure shrinkage

Another important feature of the curing process is a dimensional or volume change called "shrinkage". During curing process, the formation of chemical bond between atoms allow them to approach closer than in non-bond situation, thus the adhesive shrinks during curing and increases in density [DEA 78][PLE 90][WEI 79]. Yu et al. [YU 13] shows that the cure shrinkage at higher curing temperature is higher than at ambient temperature for epoxy adhesive DER332/HY951 (Figure 27).

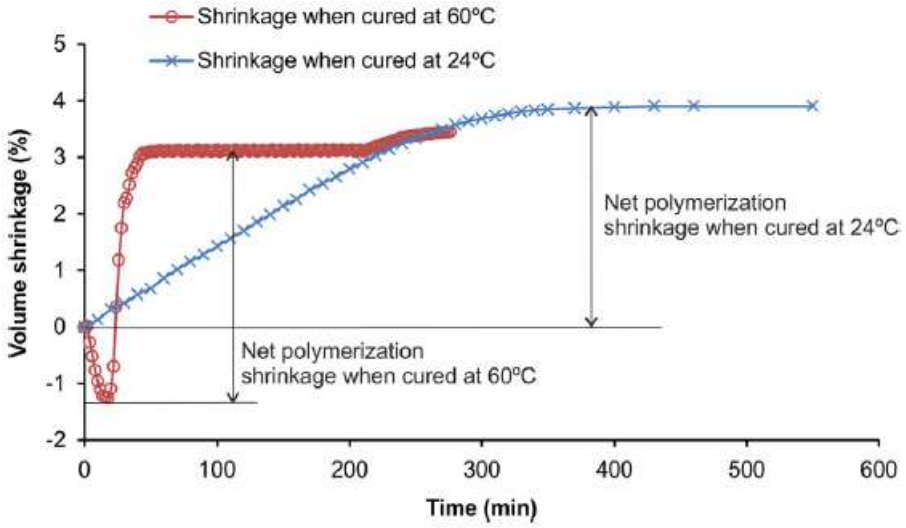

Figure 27. Change with time during the cure process of the volumetric shrinkage of DER332/HY951 cured at 24°C and 60°C [YU 13].

Influence of strain-rate

An adhesive is a viscous material and then is strain-rate dependent. With increasing strain-rates, the adhesive behavior ranges from a rubber to a glassy material and material properties such as strength increase. Créac'hcadec et al.[CRE 08] underlined these rate effects dependence through modified Arcan test in shear for several strain rates, as shown in Figure 28.

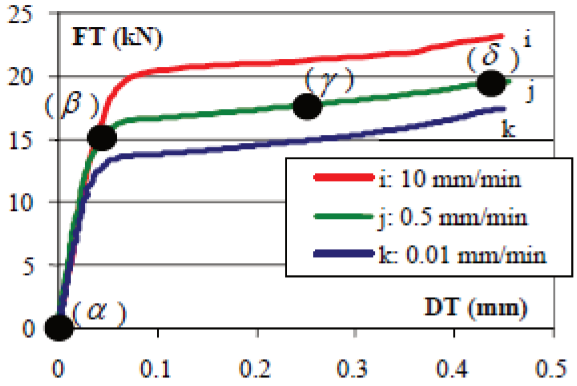

Figure 28. Strain-rate dependent mechanical behavior of Araldite®420 A/B [CRE 08].

Influence of adhesive thickness

The adhesive thickness has a significant influence on its mechanical properties such as critical fracture energy. Cognard et al. [COG 10] showed that an increase of the adhesive thickness increases rupture near the free edges of the adhesive by using a modified TAST specimen. A similar observation was made by Kawashita et al. [KAW 08]. Hence, the adhesive thickness must be accurately controlled and must be representative of the real application case.

Influence of external parameters

Due to their wide application fields, structural adhesives often evolve under specific service conditions. The long term durability of such bonded structures is strongly affected by aggressive environment conditions and is one factors which has limited adhesives application in some domains such as marine and offshore structures [CRO 97][JAR 06]. A first effect occurring in humid conditions is the absorption of water by adhesive, which causes some reversible processes: plasticization, hydrolysis and swelling. Others processes are irreversible and located at the interface adhesive/adherend: cracking, crazing and degradation of interface through corrosion or moisture [BOW 84]. As a result, humid ageing significantly weakens the bonded joint and thus affect the bonded assembly strength. Further studies investigated the performance of an adhesive subjected to humid ageing [ADA 04][BOR 09][ARN 14]. In Figure 29, Arnaud et al. [ARN 14a] showed a deterioration of the adhesive performance with humid ageing. A decrease of the transmitted load is observed with an increase of ageing times ($t_0<t_1<t_2<t_3<t_4$). La Saponara et al. [LAS 10] noted a similar behavior.

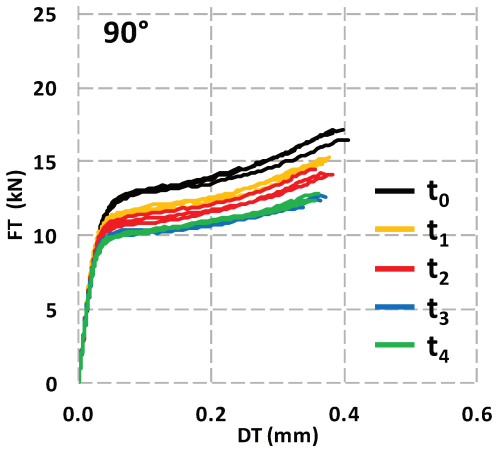

Figure 29. Influence of humid aging on mechanical behavior of Hysol® EA9309.3NA using the modified Arcan test in shear [ARN 14a].

1.2.5. Quality control and assurance in adhesive joints

Widespread use of adhesive bonding technology in aerospace, automotive or in civil-engineering industries has conduct to the development of a reliable testing technology. The use of structural adhesive bonding is associated with the difficulty in predicting the performance in service of the bonded joint. Thus, destructive and non-destructive evaluation techniques were developed to determine the bonded assembly resistance under appropriate environmental and loading conditions.

As highlighted through adhesion theories, the manufacturing process has a major impact on the performance of adhesive bonded joints. This latter can be affected by variations and manufacturing defects in production. Thus, it is fundamental to control process parameters of each production step to check properties of the adhesive with the real substrates. The manufacturing process is made of some successive steps. One of these is the application of a surface treatment on adherend surfaces to optimize the adhesion mechanisms. Then, the adhesive is prepared and is spread on the adherend surfaces. Some defects may occur from mixing, pot-life, tools and applicators, temperature, humidity. The curing of the bonded assembly follows. These process activities show that the quality of a bonding process is highly-dependent on the quality of the personnel. Therefore, reliable tests (destructive and nondestructive) must be completed by staff training. From these precautions, a quality assurance system is developed. The aim of this system is not only related to the knowledge of the adhesive bonding performance but also to the design and manufacturing. Some aspects of this reliability system are detailed in checklists or guidance through international standard such as standard ISO 9000 [ISO 05] and ISO 9004 [ISO 09]. The concept of quality assurance in an industrial context is summarized in Figure 30.

The performance of an adhesive bonded joint can be evaluated either by destructive or non destructive methods. Destructive methods consist in testing destructively a representative sample of the joint. However, this kind of methods is difficult to justify for complex and large scale structures since it represents only a small aspect on the totally adhesively bonded structure and the assumed loadings on the reduced structure can widely differ from these applied in reality. The most commonly destructive tests used in adhesive bonding evaluation is lap shear and peel tests [DAS 01]. Various destructive tests were proposed to investigate the time-dependent behavior of an adhesive in a specific environment [ADA 04][KIN 04]. Non destructive methods involves at different stage of the manufacturing process. Testing prior to bonding refers to the surface treatment of the adherend before spreading the adhesive. Some of non destructive tests are wettability testing, the Fokker contamination test [BIJ 78], reflection of IR beam [EIS 03]. The others non destructive methods occur after the bonding process and are classified into four groups [END 95]: acoustic, radiography, electric and thermal methods. Further details about these methods are provided by Ehrhart et al. [HER 2010]. Compared to destructive tests, the non destructive tests have the advantage to reduce costs. However, none of these tests are really satisfactory and sustaining good control over the manufacturing process increases the achievement of a defect free joint.

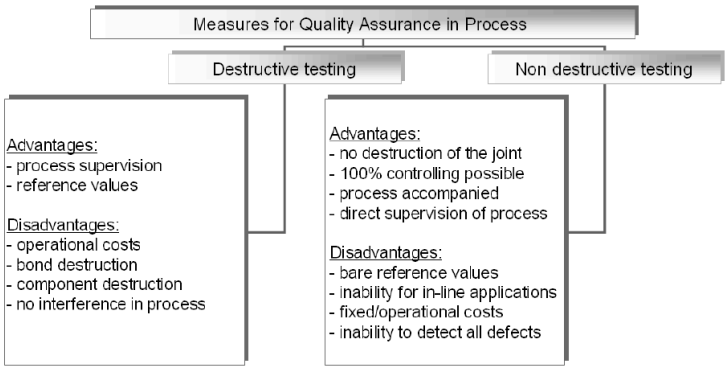

Figure 30. Concept of quality assurance in an industrial context [MIC 05].

1.3. Analysis of bonded joints

An ideal role of bonded joints would be to sustain quasi-static, cyclic or dynamic loads without affecting the performance of the whole bonded structure. However, due to a lack of suitable information on the adhesive behavior and failure criteria, manufacturers tend to take some safety precautions. These latter appear in the form of safety factors or addition of mechanical fasteners such as bolts or rivets. These practices weigh down the structure and increase production costs. Hence, reliable design and predictive methods must be developed to increase the industrial application of adhesives. It consists in determining the failure strengths, stresses/strains for a given loading, prediction of crack initiation and propagation. Analytical and numerical methods allow accessing these quantities.

1.3.1. Modes of loading

Each approach considers different modes of loading of a bonded joint, as shown in Figure 31. The stress distribution in an adhesive layer affects the bonded joint resistance. Hence, a joint is generally designed so that the stress distribution is as uniformly as possible across the entire bonded area. Shear stresses are strong since all of the bonded area involves in the bonded joint resistance. For loadings such as peeling and cleavage, the stress distribution is concentrated at one end of the joint. Thus, peel, cleavage stresses must be minimized and shear stresses must be promoted.

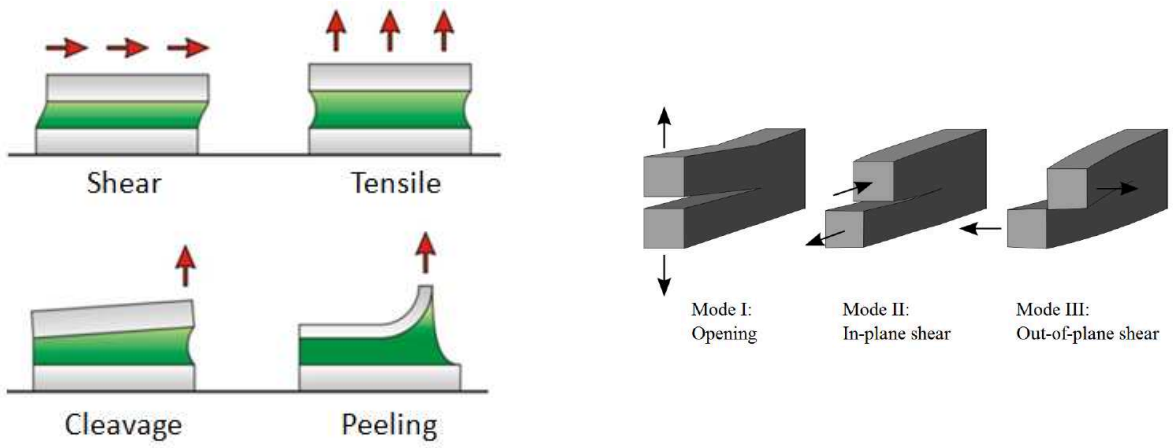

(a) (b)

Figure 31. Adhesive bonding: (a) Basic modes of loading [JOA 07] and (b) basic fracture modes.

1.3.2. Edge-effects in bonded joints

Edge effects are a common feature of most bonded assemblies. They result from a critical area made of “spew fillets” or edges which induce stress concentrations/singularities which can contribute to crack initiation and propagation in the adhesive. This makes experimental and numerical analyses of the mechanical behavior of an adhesive particularly difficult. Hildebrand et al. [HIL 94] investigated experimentally the influence of the “spew fillet” geometry and adherend shape on the joint performance with a Single Lap-Joint specimen (SLJ). Hentinen et al. [ADA 05] showed that the resulting strength and type of failure were highly sensitive to these geometries. Thus, these singularities must be considered to optimize the design of bonded assemblies.

A modified design of the TAST specimen was brought by Créac’hcadec et al. [CRE 08] in order to reduce edge effects. Compared to an original geometry made of straight adherends and straight edges of the free edges of the adhesive, the presence of beaks in the adherence strongly limits the edge effects. From this study, Cognard et al. [COG 08] numerically studied the influence of the local geometry on the edge effects

to use an optimized geometry on the modified Arcan Test, namely with beaks and cleaned edges (Figure 32).The beaks are milled on the full length of the assembly.

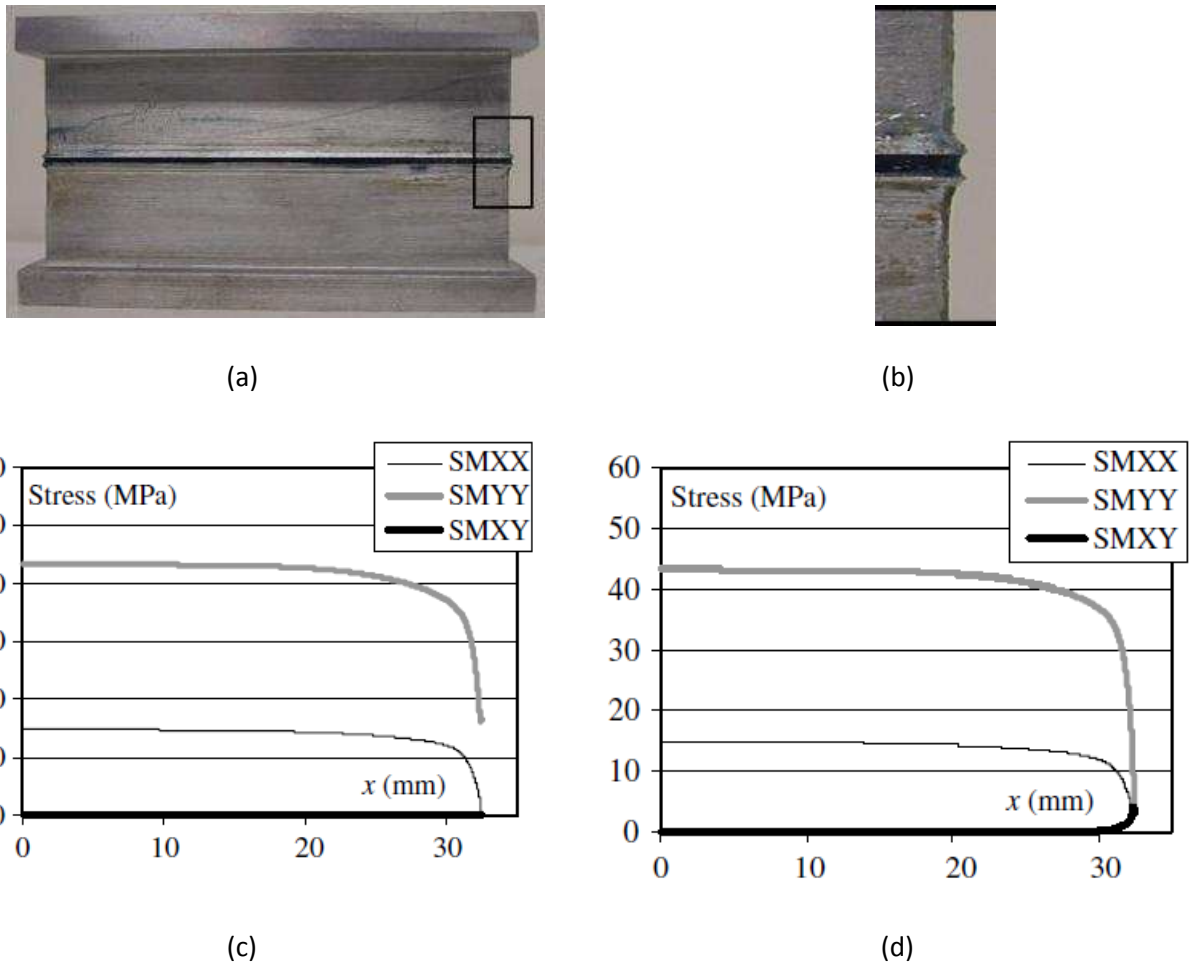

Figure 32. Modified Arcan Test: (a) general view of the test specimen, (b) zoom of the local geometry of the beaks close to the adhesive, (c) stress distribution in the mid-plane of the adhesive along the overlap for tensile-shear test and (d) stress distribution at the interface adhesive/substrate for tensile-shear test [COG 08].

In order to simplify the manufacturing process and to improve the reduction of the edge effects, Créac'hcadec et al. [CRE 15] proposed a new geometry with circular beaks close to the adhesive for Arcan TCS fixture (Figure 33). This improved geometry was brought to the Arcan Evolution specimen. Numerical studies showed that design of beaks is suitable to reduce edge effects [CRE 15].

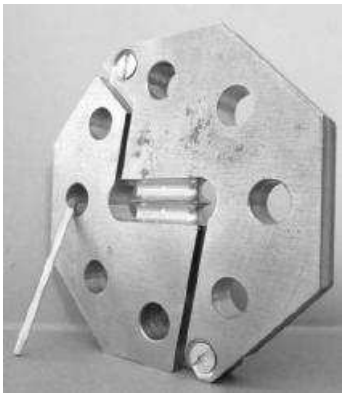

(a)

(b)

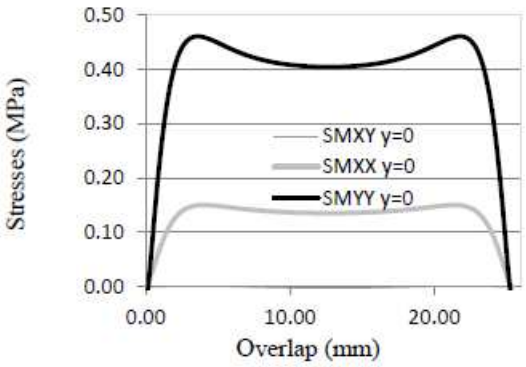

(c)

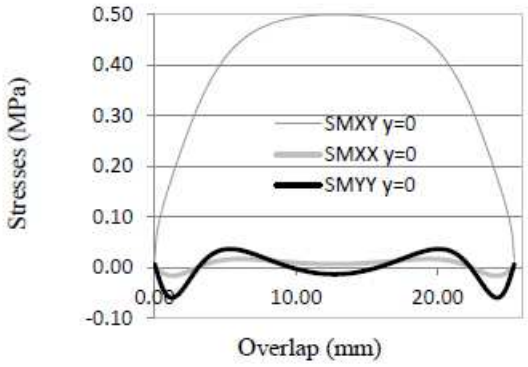

(d)

Figure 33. Tensile/Compression-Shear Test: (a) general view of the test specimen, (b) zoom of the local geometry of the beaks close to the adhesive, (c) stress distribution in the mid-plane of the adhesive along the overlap for tensile test and (d) stress distribution in the mid-plane of the adhesive along the overlap for shear test [CRE 15].

1.3.3. Analytical approach

This approach allows computation of stresses and strains by using the resolution of differential equations. A resolution of such equations is only possible by simplifying loads, geometry, and material. Hence, this approach is generally applied on simplified bonded assemblies. The simplest analysis considers a classic Single Lap Joint (SLJ) for which adhesive deforms only in shear and adherends are rigid. In such conditions, the shear stress distribution τ is assumed to be homogeneous in the adhesive layer (Figure 34 (a)) and is given by:

$$\tau = \frac{P}{S} \tag{1.23}$$

where *P* is the force applied and *S* the surface of the bonded area.

This analysis is too simplified and is valid only for infinitesimal deformation. In 1938, Volkersen [VOL 38] improved this analysis by introducing a differential shear stress in the adhesive as a consequence of substrate deformation. It was assumed that adhesive deforms only in shear and adherends undergo longitudinal deformation (both deform elastically). The reduction of strain along the overlap causes a non-uniform stress distribution in the adhesive as shown in Figure 34 (b).

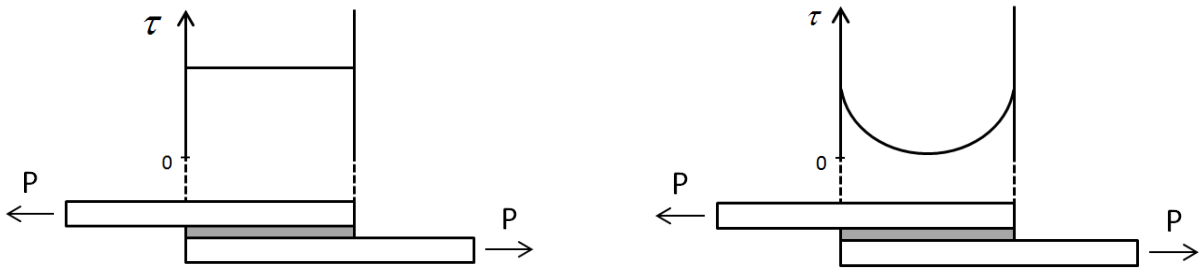

(a) (b)

Figure 34. Shear stress distribution in the adhesive for a Single-Lap Joint (SLJ) specimen: (a) linear elastic analysis and (b) Volkersen's analysis.

The real behavior of the adhesion joint is in reality more complex than those predicted by Volkersen's analysis. A particularity of the Single Lap-Joint specimen is the misalignment of adherends. It causes rotation of the sample and thus induces the adherend bending and peel stress in the adhesive layer. Goland et al. [GOL 44] provided an improvement of the Volkersen's model by considering this rotation phenomenon (Figure 35).

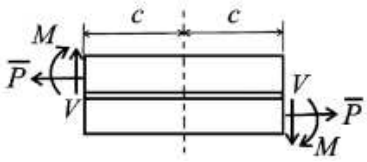

Figure 35. Goland and Reissner model [ROD 10].

Both analyses exhibit some limitations since the adhesive thickness is neglected and materials are assumed elastic. Further analyses improved these previous ones by including non-linear behavior of the adhesive [HAR 73] and incorporating steel or composite adherends [ADA 92][BIG 90][MOR 02][TSA 98]. These analytical methods are restricted to the Single Lap Shear specimen using simplified material behavior. However, the analytical analysis of adhesive joints can be highly complex and involves non-linear and non-homogeneous equations for industrial bonded structures which are generally submitted to complex loads and specific service conditions. In addition, a detailed analysis of the adhesive behavior must be investigated to strongly predict the performance of such structure. Then, numerical methods are preferred for the study of such structures.

1.3.4. Numerical approach

Numerical approach consists in computing the numerical solution of mathematical/mechanical problems which can be described by Partial Differential Equations (PDE) or integral equations. With the exponential increase of computational resources, analytical methods have become a notable tool to analyze complex mathematical/mechanical problems. The most popular methods used to solve these equations are the Finite Element Method (FEM), the Finite Difference Method (FDM) and the Boundary Element Method (BEM) (Figure 36).

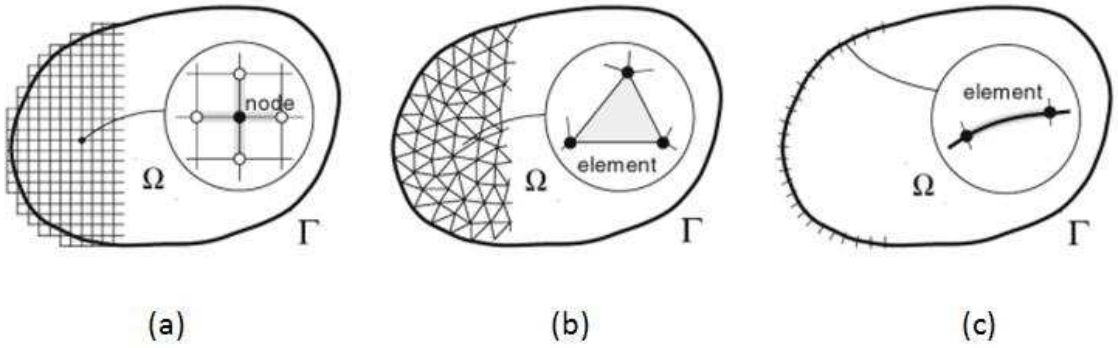

Figure 36. Computational methods: (a) Finite Difference Method, (b) Finite Element Method and (c) Boundary Element Method [SAK 14].

The Finite Difference Method is often used to solve complex governing differential equations in closed-form problems and subdivides a finite space into elements to construct the discretization of partial differential equations. This method is restricted to simple geometries due to the implementation difficulty for complex problems [OCH 11]. The Finite Element Method was primarily used to solve the problems of continuum mechanics for complex structures and uses an element grid system for a finite space to discretize domain integral equations [ADA 84]. The Boundary Element Method [VAB 08] requires only discretization at the boundary of the solution domain, thus reduces a two dimensional problem into a one dimension problem. However, this method is not effective in the case of problems with material heterogeneities and nonlinearities and thus is more relevant for solving homogeneous problems under elastic assumptions.

The Finite Element Method is commonly used since it provides solutions to complex problems (for instance in the case of complex geometries, non-linear material behavior). In addition, this method offers many approaches such as continuum mechanics and fracture mechanics to analyse a bonded joint [ASH 11].

1.3.4.1. Continuum Mechanics

This approach also called “Strength of materials approach” is based on the study of stresses and strains. Maximum values of stresses and strains predicted by Finite Element analysis are used to establish and applied a suitable based failure criterion. This was firstly proposed to predict the failure modes of brittle adhesives for single lap joint specimens [ADA 97]. This kind of criterion, in combination with elasto-plastic material models, was extensively used to predict the adhesive strength [BRO 01][HAR 74][HAR 84]. However, due to localized stress concentrations or stress singularities, this criterion was difficult to implement. In fact, a sufficiently refined mesh close to these singularities areas was necessary to predict properly the maximum stresses which are used in the failure criterion. Hence, this latter is mesh size dependent and must be used with caution. Von Mises proposed a yield criterion based on the assumption that yielding occur when the distorsion energy achieves a critical value. Such criterion was used in further studies as prediction of the strength of tubular joints [JOH 91], double lap joint [LEE 92]. This approach seems unsuitable for brittle adhesives and short overlaps since it neglects normal stresses in the adhesive layer and thus overestimates the adhesive resistance [DAS 09]. A criterion based on strains seems more appropriate for ductile adhesives. However, such criterion is difficult to implement due to stress singularities in the adhesive layer, as discussed previously for the maximum stress based failure criteria.

Crocombe et al. [CRO 89] proposed a global criterion to overcome these localized singularities in the adhesive joint and stated that the criterion can be applied at a critical distance for which a path of adhesive along region started deforming plastically. This criterion is also mesh size-dependent but considers all

strain and stress components. Hence, this strain energy based failure criteria seems more efficient than the others which are based on maximum strains/stresses.

Methods based on strength of materials approach are limited to continuous structures and requires some considerations to be used efficiently. It needs a mesh sufficiently refined particularly on areas where stress singularities occur. Furthermore, the selection of a failure criterion must consider the whole geometry of the bonded joint, notably in cases for which the failure is defined at a critical distance from the singularity.

1.3.4.2. Fracture Mechanics

Fracture mechanics is another method to predict the adhesive failure. On the contrary to the previous approach, fracture mechanics assumes the structures heterogeneities. This concept was introduced in 1920 by Griffith et al. [GRI 20]. The aim was to characterize the failure behavior of a brittle material by using assuming that the size of the plastic zone at the crack tip remains small compared to the crack length. He suggested a fracture criterion based on the critical strain energy release rate G_C. Irwin et al [IRW 57] extents this definition to the case of ductile materials and proposed a criterion based on stress, such as the stress intensity factor K. Rice et al. [RICE 68] developed the J-integral approach to determine the strain energy release rate through the use of a path independent integral contour around a crack.

The energy based fracture criteria have been widely used to predict failure in adhesives [ASH 01][ASH 04][CHA 96][CHA 98][DAG 96][IMA 03]. Some studies were conducted to evaluate the reliability of the energy criterion predicted by Griffith. The suitability of the strain energy based failure criterion was investigated by using compact tension specimens and shear tests [HAM 89]. That of stress energy based criterion was examined with butt joints [AKI 03]. The energy based failure criterion [OBR 03] [CHE 05] is generally preferred compared to stress intensity factors because these are difficult to determine when crack grows at an interface area. It is often the case for mixed mode loadings. Specific failure criteria for mixed mode fracture were developed. These are based on classical failure criteria but the fracture surface/envelope was introduced [DIL 09][KIN 87][CHA 92].

Some studies have been conducted to predict the joint performance of a cracked adhesive joint by using the J-integral with success [CHO 08] [SOR 03]. The value of the energy release rate G_C predicted with the J-integral method is geometry-dependent for ductile adhesives [KIN 81]. In fact, adherends limit the development of the yield zone that makes G_C geometry-dependent. For heterogeneous materials, the J-integral method is very difficult to perform due to its path dependence and J-integral must be extrapolated against interface to a point. For bonded joint, the adhesive thickness is thin and both interfaces adhesive/adherend may interact with each other. The integral path includes different singular sources so closely tired make numerical extrapolation difficult.

A major limitation of the fracture mechanics is the requirement of a crack tip or a known and calibrated singularity [CLA 93] to determine the energy release rate. Furthermore, such approach requires very refined mesh and thus takes high computational time.

1.3.4.3. Damage Mechanics – Cohesive Zone Modelling (CZM)

Cohesive Zone Modelling is an advanced modelling technique which overcomes to limitations associated to the strength of materials approach and fracture mechanics to model a damage evolution [CAR 07]. These models let to model one or multiple cracks in a structure without knowing the direction of crack propagation. Elices et al.[ELI 02]

Cohesive zone models consist of the establishment of a traction-separation law to model interface/region at which crack initiation, damage and failure occur. These cohesive laws are established between paired

nodes of cohesive elements and can be used to consider some boundary conditions. For instance, it allows the connection of superimposed nodes of elements representing different materials. This can be used to simulate a bonded joint or a zero thickness interface (Figure 37 (b)).

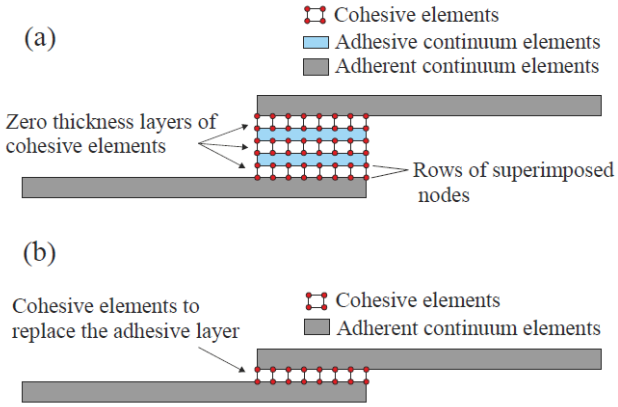

Figure 37. Cohesive elements: (a) zero thickness interface and (b) adhesive layer [KON 12].

The most commonly used traction-separation laws are triangular [AFL 01], linear-parabolic [ALL 96], exponential [CHA 02] and polynomial [CHE 02]. The kind of law is generally difficult to determine and depends on the ratio of the toughness of the interface and stiffness of the bulk material [ALF 06]. The shape of the cohesive law has an influence on the numerical performance of the solution. Alfano et. Al. [ALF 06] showed that a good compromise was brought for a bilinear law. This last one considers an elastic behavior of the cohesive zone until a critical traction. Then, damage is initiated and the stiffness of cohesive element decreases until reaching a zero value. The area under the traction-separation profile is the critical strain energy release rate G_C (Figure 38).

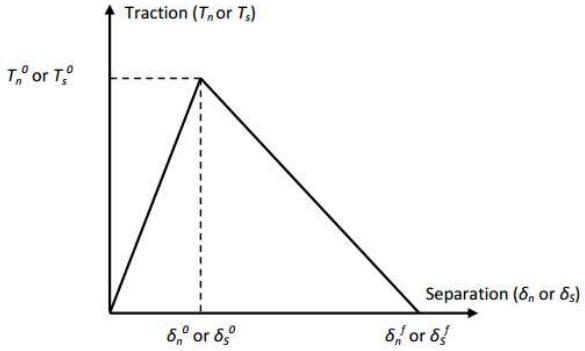

Figure 38. Typical Traction-Separation responses (bilinear law).

These models are widely used in the case of composites, adhesives or fatigue damage uptake instructures [TVE 92][TVE 93][YAN 99][YAN 00][CAM 05][CAM 07] and are implemented in most of FE codes.

1.4. Modelling adhesive behavior

This section gives an overview of the existing models for the modelling of structural adhesives on the one hand and for predicting the mechanical behavior of polymers on the other hand. As structural adhesive is a polymeric material. Both approaches must be considered.

1.4.1. Adhesive constitutive model

The present section proposes to settle the basis of rate-dependent elastic-plastic behavior of a totally cured adhesive, i.e with a maximum curing degree of *1.0*, in an assembly.

It is assumed that viscous effects are neglected. Following the framework of thermodynamics [LEM 00], the strain tensor $\underline{\underline{\varepsilon}}$ can be decomposed into one elastic part $\underline{\underline{\varepsilon}}^{e}$ and another plastic one $\underline{\underline{\varepsilon}}^{p}$ such the following equation:

$$\underline{\underline{\varepsilon}} = \underline{\underline{\varepsilon}}^{e} + \underline{\underline{\varepsilon}}^{p} \tag{1.24}$$

The limit between the elastic and the plastic domain is defined by the yield function, *f*, which depends on the stress tensor and the states variables:

$$f = f\left(\underline{\underline{\sigma}}, \underline{\underline{V_i}}\right) \tag{1.25}$$

The limit of the elastic domain (reversible transformation) is reached when the yield function goes to zero, while the plastic domain (irreversible transformations) appears under the conditions of *f=0*. The position and size of the yield function within the 3D stress domain are defined by the state variables thanks to a hardening function. For the generalized standard, the flow and hardening functions are given by:

$$d\underline{\underline{\varepsilon}}^{p} = d\lambda \frac{\partial f}{\partial \underline{\underline{\sigma}}} \qquad ; \qquad d\underline{\underline{V_i}} = -d\lambda \frac{\partial f}{\partial \underline{\underline{A_i}}} \tag{1.26}$$

A different function is used for an associated formalism:

$$d\underline{\underline{V_i}} = -d\lambda \frac{\partial F}{\partial \underline{\underline{A_i}}} \tag{1.27}$$

One limitation of the associated plasticity is for materials whose volume change over plastic shear strain. This phenomenon is called dilatancy [REY 85] and is observed for granular materials, toughened structural adhesives. For such materials, a non-associated formalism must be used.

Regarding the non-associated formalism, different functions are used for the flow and hardening functions:

$$d\underline{\underline{\varepsilon}}^{p} = d\lambda \frac{\partial g}{\partial \underline{\underline{\sigma}}} \qquad ; \qquad d\underline{\underline{V_i}} = -d\lambda \frac{\partial F}{\partial \underline{\underline{A_i}}} \tag{1.28}$$

The rate effects are described through a viscoplastic potential *Ω*, defined as follows:

$$\Omega = \phi\left(\langle f \rangle\right) \tag{1.29}$$

where *<f>=0* in the elastic domain, i.e *f<0* and *<f>=f* in the plastic domain, i.e *f≥0*.

The visco-plastic multiplier associated to that potential is written as:

$$dp = \frac{\partial \Omega}{\partial f} = \frac{\partial}{\partial f} \Phi\left(\langle f \rangle\right) \tag{1.30}$$

Those different functions must be defined using the invariants of the stress tensor $\underline{\underline{\sigma}}$ to be independent of the basis considered. This tensor is generally decomposed into a spherical $\underline{\underline{S}}$ and a hydrostatic P_h part such as:

$$\underline{\underline{\sigma}} = \underline{\underline{S}} + P_h \underline{\underline{I}} \tag{1.31}$$

The stress invariants are defined as follows:

$$P_h = \frac{1}{3}\mathrm{tr}\left(\underline{\underline{\sigma}}\right) \tag{1.32}$$

$$\sigma_{VM} = \sqrt{\frac{3}{2}\underline{\underline{S}} : \underline{\underline{S}}} \tag{1.33}$$

$$I_3 = \det\left(\underline{\underline{\sigma}}\right) \tag{1.34}$$

Once the bases of strain-rate-dependent elastic-plastic are established, the choice of an accurate model for the description of the adhesive behavior must be considered. The commonly models used for predicting the elastic-plastic behavior of structural adhesives was summarized by Maurice et al. [MAU 12], as suggested by Table 4. The terms considering the rate effects, i.e. the viscoplastic potentials, appear in Table 5.

Then, the rate-dependent elastic-plastic equations are transformed to an incremental form using an implicit backward Euler method divided in an elastic predictor phase and a plastic corrector phase [SIM 00][BRA02]. This method called radial return method is commonly used for the implementation of constitutive equations. In the Finite Element analysis, the equivalent stress, the plastic strain, the stress tensor and the elastic constitutive tensor must be known at the end of each increment.

A first, null plastic flow is assumed resulting in a trial elastic stress tensor $\underline{\underline{\sigma}}^{trial}$. It leads to the following equations at increment *n+1*:

$$f\left(\underline{\underline{\sigma}}_{n+1}, Y_{n+1}\right) = 0 \tag{1.35}$$

$$\underline{\underline{\sigma}}^{trial}_{n+1} = \underline{\underline{\sigma}}_{n+1} + \underline{\underline{\underline{\underline{C}}}}_e : \underline{\underline{\Delta\varepsilon}} \tag{1.36}$$

Where *f* is the yield criterion defined at increment *n+1*, $\underline{\underline{\underline{\underline{C}}}}_e$ the elastic constitutive matrix and $\underline{\underline{\Delta\varepsilon}}$ the strain increment tensor.

When the trial elastic stress tensor $\underline{\underline{\sigma}}^{trial}_{n+1}$ is located outside the yield surface, the plastic flow must be considered and the plastic corrector step of the algorithm is used in order to get an admissible stress state. The stress tensor at increment *n+1* goes to:

$$\underline{\underline{\sigma}}^{trial}_{n+1} = \underline{\underline{\sigma}}_{n+1} + \underline{\underline{\underline{\underline{C}}}}_e : \left(\underline{\underline{\Delta\varepsilon}} - \underline{\underline{\Delta\varepsilon}}^p\right) \tag{1.37}$$

A combination of the plastic strain tensor with the flow rule gives:

$$\underline{\underline{\sigma}}^{trial}_{n+1} = \underline{\underline{\sigma}}_{n+1} + \Delta p \underline{\underline{\underline{\underline{C}}}}_e : \left(\frac{\partial g}{\partial \underline{\underline{\sigma}}}\right)_{n+1} \tag{1.38}$$

The trial stress tensor can be decomposed into two parts, one called the stress deviator tensor and the other called the spherical $\underline{\underline{S}}^{trial}$ or the hydrostatic stress tensor $\underline{\underline{P}}^{trial}_h$:

$$\underline{\underline{\sigma}}^{trial} = \underline{\underline{S}}^{trial} + \frac{1}{3} P_h^{trial} \underline{\underline{I}} \tag{1.39}$$

In the same way, the elastic constitutive matrix $\underline{\underline{\underline{\underline{C}}}}_e$ is decomposed in its deviatoric and spheric al parts:

$$\underline{\underline{\underline{\underline{C}}}}_e = 2\mu_{rev} \underline{\underline{I}} + \lambda_{rev} \underline{\underline{I}} \otimes \underline{\underline{I}} \tag{1.40}$$

So that, the equation 1.39 is expressed in a deviatoric and a spherical part:

$$\begin{cases} \underline{\underline{S}}_{n+1} = \underline{\underline{S}}_{n+1}^{trial} - 2\mu_{rev} \Delta p \left(\dfrac{\partial g}{\partial \underline{\underline{\sigma}}} \right)_{n+1} \\ P_{h,n+1} = P_{h,n+1}^{trial} - \dfrac{1}{3} \Delta p \lambda_{rev} \left(\underline{\underline{I}} \otimes \underline{\underline{I}} \right) : \left(\dfrac{\partial g}{\partial \underline{\underline{\sigma}}} \right)_{n+1} \end{cases} \tag{1.41}$$

The determination of $\underline{\underline{\sigma}}_{n+1}$ is now linked to the unknown multiplier Δp .Hence, the determination of the stress at each increment depends on the resolution of the following final return-mapping scalar equation:

$$R_p(\Delta p) = \Delta p - \Delta t \left(\frac{\partial \Phi(\langle f \rangle)}{\partial f} \right)_{n+1} = 0 \tag{1.42}$$

The incremental multiplier Δp^{i+1} is calculated with a Newton method:

$$\Delta p^{i+1} = \Delta p^i - \frac{1}{J^i} R_p(\Delta p^i) \quad i = 1..n \text{ , where } J^i = \left. \frac{\partial R_p}{\partial \Delta p} \right|_i \tag{1.43}$$

Where *J* is calculated as follows:

$$J = 1 - \Delta t \frac{\partial}{\partial \Delta p} \left(\frac{\partial \Phi(\langle f \rangle)}{\partial f} \right)_{n+1} \tag{1.44}$$

After having determined the multiplier, the final stress tensor is obtained as:

$$\underline{\underline{\sigma}}^{trial} = \underline{\underline{S}}^{trial} + P_h^{trial} \underline{\underline{I}} \tag{1.45}$$

The algorithmic tangent modulus necessary for applying a Newton method for iterative solution of the global equilibrium problem requires the derivative of the stress tensor $\underline{\underline{\sigma}}$:

$$\underline{\underline{\underline{\underline{C}}}} = \frac{\partial \underline{\underline{\sigma}}}{\partial \underline{\underline{\varepsilon}}} \tag{1.46}$$

Straightforward differentiation renders the following result:

$$\underline{\underline{\underline{\underline{C}}}} = \frac{\partial}{\partial \underline{\underline{\varepsilon}}} \left(\underline{\underline{S}} + \frac{1}{3} P_h \underline{\underline{I}} \right) \tag{1.47}$$

$$\underline{\underline{\underline{\underline{C}}}} = \frac{\partial}{\partial \underline{\underline{\varepsilon}}}\left(\underline{\underline{S}}_{n+1}^{trial} - 2\mu_{rev}\Delta p\left(\frac{\partial g}{\partial \underline{\underline{\sigma}}}\right)_{n+1} + \frac{1}{3}\left(P_{h,n+1}^{trial} - \frac{1}{3}\Delta p\lambda_{rev}\left(\underline{\underline{I}}\otimes\underline{\underline{I}}\right):\left(\frac{\partial g}{\partial \underline{\underline{\sigma}}}\right)_{n+1}\right)\underline{\underline{I}}\right) \quad (1.48)$$

Some studies [MAH 05][JOU 08][JOU 10] showed that classical constitutive models based on the Von Mises or Exponent Drucker Prager functions were not efficient to represent accurate plastic evolutions of structural adhesives. In fact, those models do not describe the yield stress dependency on hydrostatic pressure and the strength dependency on multi-axial state. This is particularly the case for compression-shear loadings, as suggested in Figure 39. The flow direction is oriented towards the positive hydrostatic pressure which corresponds to a dilatation when plasticity occurs.

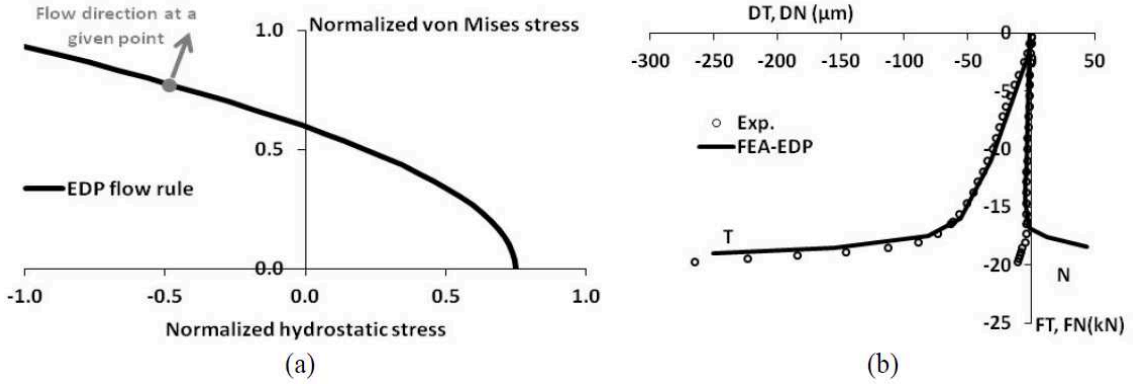

Figure 39. (a) Definition and flow function in the compression-shear domain and (b) limitation of the Exponent Drucker-Prager model. [MAU 12]

Mahnken et al. [MAH 05] and Jousset et al. [JOU 10] provide a suitable model, namely the Mahnken-Schlimmer model. A first, this model has the possibility to use non-associated formalism which is generally observed for toughened structural adhesive. In addition, this defines flow function in the compression shear domain and uses a quadratic form for the yield and flow function. Maurice et al. [MAU 14] added a dissymmetry parameter to this model of Mahnken-Schlimmer to accurately predict the behavior under tension-shear and compressive-shear loadings.

Model name	Ref.	Initial Yield Function (f=0)	Initial Flow Function (g=0)	Parameters	
				Nb	Definition
Modified Von Mises	[WAN 00] [DUN 03]	$f = \sigma_{VM} - \sigma_0 - \mu_{VM}\, p$	-	2^1	σ_0 : Initial yield stress in shear μ_{VM} : Sensitivity to hydrostatic stress
Modified Tresca	[WAN 00]	$f = \tau_{max} - \tau_0 - \mu_t\, p$ $\tau_{max} = \max_{i \neq j} \lvert \sigma_i - \sigma_j \rvert$	[A1] -	2^1	τ_0 : Initial yield stress in shear μ_t : Sensitivity to hydrostatic stress
Linear Drucker-Prager (LDP)	[WAN 00] [DEA 04]	$f = t - d - p \tan\beta$ $t = \frac{\sigma_{VM}}{2}\left[1 + \frac{1}{K} - \left(1 - \frac{1}{K}\right)\left(\frac{r}{\sigma_{VM}}\right)^3\right]$	[ACL-1] $G = t - p \tan\psi$	4	*d*: Depends on hardening β: Angle in the meridional plane K: Third invariant sensitivity ψ : Angle in the deviatoric plane $r^3 = \frac{27}{2} J_3$
				+ 1 experimental curve for hardening	
Exponent Drucker-Prager (EDP)	[WAN 00] [DEA 04] [JOU 08] [MAL 09] [COG 10a]	$f = a\,\sigma_{VM}^b + p - p_{t0}$	$G = \sqrt{(e\tilde{\sigma}\lvert_0 \tan\psi)^2 + \sigma_{VM}^2} + p \tan\psi$	6	*a:* Material parameter *b:* Material parameter p_{t0} : Pure tension hydrostatic yield stress e : Material parameter $\tilde{\sigma}\lvert_0$: Initial equivalent yield stress ψ : Dilatation angle
				+ 1 experimental curve for hardening	
Cap plasticity model	[WAN 00]	*LDP intersected with:* $f = \sqrt{(p - p_a)^2 + \left[\frac{Rt}{1 + \alpha - \alpha/\cos\beta}\right]^2} - R(d + p_a \tan\beta)$	NA	6^1	LDP parameters and: *R*: Shape of the "cap" curve α : Transition coefficient p_a : Hydrostatic compression yield stress
Cavitation model	[IMA 02] [DUN 03] [DEA 04]	$f = \left(\frac{\sigma_{VM}}{\sigma_M}\right)^2 - (q_1 s)^2 + 2q_1 s \cosh\left(\frac{3p}{2\sigma_M}\right) - \left(1 - \mu\frac{p}{\sigma_M}\right)^2$	$G = \left(\frac{\sigma_{VM}}{\sigma_M}\right)^2 - (q_1 s)^2 + 2q_1 s \cosh\left(\frac{3p}{2\sigma_M}\right) - \left(1 - \mu'\frac{p}{\sigma_M}\right)^2$	8^*	q_1 : Effect of void interactions μ : Sensitivity to hydrostatic stress (yield) μ' : Sensitivity to hydrostatic stress (flow rule) *s:* Effective volume fraction σ_M : Yield stress

				+ 1 experimental curve for hardening	
Rolfes	[ROL 08]	$f = \sigma_{VM}^2 - a_1 p - a_0$	$G = \sqrt{\sigma_{VM}^2 + \alpha p^2}$	3	a_1 : Yield parameter a_0 : Yield parameter α : Flow rule parameter
				+2 experimental curves for hardening	
Mahnken-Schlimmer (MS)	[MAH 05] [JOU 08]	$f = \sigma_{VM}^2 - \frac{1}{3}\left[Y_0^2 - a_1 Y_0 p - a_2 p^2\right]$	$G = \sigma_{VM}^2 - \frac{1}{3}\left[Y_0^2 - a_1^* Y_0 p - a_2^* p^2\right]$	8*	a_1 : Yield parameter a_2 : Yield parameter Y_0 : Shear yield stress a_1^* : Flow rule parameter a_2^* : Flow rule parameter
Modified Mahnken-Schlimmer (MS)	[MAU 13]	$f = \sigma_{VM}^2 - \frac{1}{3}\left[Y_0^2 - a_1 Y_0 p - a_2 p^2\right]$	$G = \sigma_{VM}^2 - \frac{1}{3}\left[Y_0^2 - a_1^* Y_0 p - a_2^* p^2\right]$ si $p>0$ $G = \sigma_{VM}^2 - \frac{1}{3}\left[Y_0^2 - a_1^* Y_0 p - a_3^* p^2\right]$ si $p<0$	8*	a_1 : Yield parameter a_2 : Yield parameter Y_0 : Shear yield stress a_1^* : Flow rule parameter a_2^* : Flow rule parameter a_3^* : Flow rule parameter

Table 4. Summary of the 3D pressure dependent elastic-plastic models for the modelling of structural adhesives [MAU 12] [ARN 14]

*: Including the parameters of the hardening functions

[1]: For the initial yield function only

[2]: Developed for epoxy matrix in textile composite

Model name	Ref.	Viscoplastic potential	Parameters	
			Nb	Definition
Odqvist law	[ODQ 74]	$\Phi(\langle f \rangle) = \frac{K}{n+1}\left\langle \frac{f}{K} \right\rangle^{n+1}$	2	K : Initial factor for the normalization of the yield surface n : Viscoplastic yield surface exponent
Nouailhas law	[NOU 89] [CRE 08]	$\Phi(\langle f \rangle) = \frac{K}{\alpha(n+1)} e^{\left\langle \alpha\left(\frac{f}{K}\right)\right\rangle^{n+1}}$	3	K : Initial factor for the normalization of the yield surface n : Viscoplastic yield surface exponent α : Viscosity parameter

Table 5. Summary of the commonly used viscoplastic potentials

1.4.2. Polymer constitutive models

During curing, a low-molecular weight liquid is transformed into a cross-linked solid polymer though a series of chemical reactions. This behavior, which ranges between liquid and solid, is generally associated to viscoelastic behavior. A typical stress-strain response of a polymer under compression test is depicted in Figure 40.

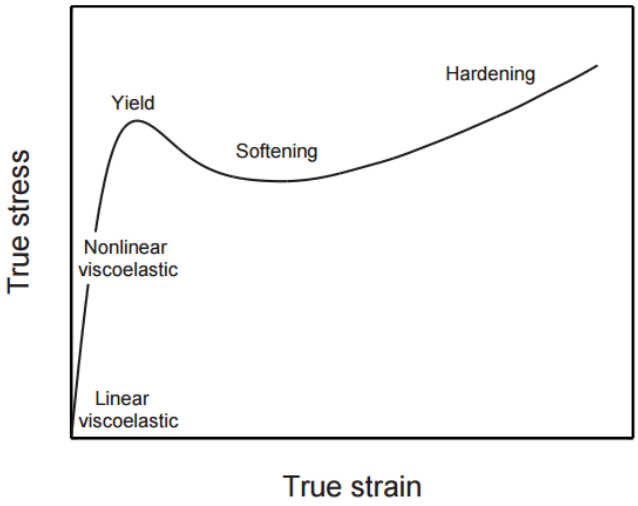

Figure 40. Schematic representation of the behavior of a polymer material.

At first, a visco-elastic time-dependent response is observed. This process is considered as fully reversible. For small deformations, the material is assumed to be linear visco-elastic. At the yield point, a change in the slope is observed. From this point, the stress-induced plastic flow leads to a structural evolution which reduces the material resistance to plastic flow. This irreversible phenomenon is the strain softening. Along with the strains increase, molecules become oriented which induces an increase of stress at large deformation. It is the strain hardening. Most constitutive equations were developed to describe the linear and non-linear visco-elastic behaviors of a polymer. Linear visco-elastic models are based on linear response theory. The Commonly non-linear constitutive models used are either generalizations or the linear Boltzmann integral or a combination of the aforementioned approaches [FIN 76][SCH 69][WAR 83]. Due to its strong temperature and strain-rate dependency, a classical yield stress criterion is not efficient to describe the yield stress of polymers. Some theories such as the Eyring theory [EYR 63] or Argon theory [ARG 73] accurately predict the influence of strain-rate and temperature but do not describe the strain softening and strain hardening domains. In recent studies, Haward et al. [HAW 68] capture the large strain

response by adding in parallel a finite extendable rubber spring to an Eyring dashpot. Several autors extended this approach to finite strain 3D constitutive equations [BOY 88][GOV 00]

At a given temperature, it has been shown that visco-elastic properties of polymer change significantly with increasing curing degree [ADO 90][KIM 96][WHI 97][KIM 97][SIM 00]. In addition, the mechanical properties of a polymer are temperature- and time- dependent. Consequently, the time, temperature and curing degree were gradually introduced in constitutive equations to describe the development of mechanical properties of a polymer during cure [OBR 01].

1.4.2.1. Cure dependent material parameters

Some material parameters are cure-dependent and must be detailed to better understand the polymer behavior during curing and to be introduced in the constitutive models.

Elastic modulus

Some studies [BOG 92] [HUA 00][JOH 01][RUI 05] used cure-dependent elastic models to compute elastic modulus of a polymer during entire cure. A linear relationship between the elastic modulus and the curing degree was reported in [BOG 92][GOL 97][HUA 00] such as:

$$\mathrm{E} = (1-\alpha)\mathrm{E}_0 + \alpha\mathrm{E}_\mathrm{r} \tag{1.49}$$

where α is the curing degree, E_0 and E_r are the uncured and fully cured modulus of the polymer respectively.

Johnston et al. [JOH 01] provided another definition of the polymer elastic modulus to capture more accurately the rubbery-glass transition occurring during the curing process. Besides being dependent on the curing state, the elastic modulus defined considers the curing temperature and the instantaneous glass transition temperature, as follows:

$$\begin{cases} \mathrm{E} = \mathrm{E}_0 & \mathrm{T}^* < \mathrm{T}_1 \\ \mathrm{E} = \mathrm{E}_0 + \left(\dfrac{\mathrm{T}^* - \mathrm{T}_1}{\mathrm{T}_2 - \mathrm{T}_1}\right)(\mathrm{E}_\infty - \mathrm{E}_0) \quad \text{for} & \mathrm{T}_1 < \mathrm{T}^* < \mathrm{T}_2 \\ \mathrm{E} = \mathrm{E}_\infty & \mathrm{T}^* > \mathrm{T}_2 \end{cases} \tag{1.50}$$

where α is the curing degree, E_0 and E_r are the uncured and fully cured modulus of the polymer respectively. T_1 and T_2 are the onset and completion of the glass transition, respectively. The variable T^* is expressed such as:

$$\mathrm{T}^* = \mathrm{T}_\mathrm{g} - \mathrm{T} = (\mathrm{T}_{\mathrm{g}0} + \mathrm{C}) - \mathrm{T} \tag{1.51}$$

where α is the curing degree, T_{g0} is the glass transition of the uncured polymer and C is a constant.

Ruiz et al. [RUI 05] proposed a linear logarithmic relationship between normalized elastic modulus and normalized degree of cure:

$$\frac{\log(\mathrm{E})}{\log(\alpha)} = \mathrm{CM} \tag{1.52}$$

This relationship is only valid for the elastic modulus evolution of pure polymer.

Shear modulus

The cure dependent shear modulus of a polymer can be investigated during the entire curing process [OBR 01] and can be written as:

$$\mu(\alpha) = \frac{E(\alpha)}{2(1+\nu(\alpha))} \tag{1.53}$$

where $\mu(\alpha)$, $E(\alpha)$ and $\nu(\alpha)$ are the cure-dependent shear modulus, the cure-dependent elastic modulus and the cure-dependent Poisson's ratio, respectively. Adolf et al. [AD0 97] proposed a time-dependent definition of the shear modulus:

$$\mu(t) = \mu_{\infty}^{f}\left(\frac{b - b_{gel}}{1 - b_{gel}}\right)^{\frac{8}{3}} \tag{1.54}$$

where μ_{∞}^{f} is the final equilibrium modulus of the fully cured polymer (α=1.0) and b, b_{gel} are the current bond probability and bond probability at the gel point of the polymer, respectively.

Poisson's Ratio

Two approaches were discussed in the literature [RUI 05]. On the one hand, plain strain bulk modulus is assumed constant during the curing process, thus the elastic modulus and the Poisson's ratio vary. On the other hand, it is assumed that the variation of the Poisson's ratio has no influence on the curing process of polymers [BOG 92][RUI 05].

Viscosity

Two main phenomena influenced the viscosity of a polymer during the liquid stage of curing process: the increase in molecular size and the effect of the temperature on molecules. The first one induces a decrease of chain mobility and thus an increase of the viscosity. Among different approaches in the literature [DUS 87][LEE 82][SEI 05], Adolf et al. [ADO 97] suggested a time-dependent expression:

$$\eta(t) = \eta_{\infty} e^{(\kappa\alpha(t))} e^{\left(\frac{U}{RT}\right)} \tag{1.55}$$

where η_{∞} is the viscosity of the totally cured polymer (α=1.0) and κ, U and R are polymer constants.

Relaxation time

During curing, stress relaxation time and glass transition temperature are both influenced by the restriction on molecular motions [KIM 96]. In such case, different relaxation time must be defined to represent the polymer [HOJ 04]. Kim et al. [KIM 96] used a second order polynomial to show the relationship between the cuing degree and the relaxation time:

$$\frac{\log(\tau(\alpha)) - \log(\tau_0)}{\log(\tau_{\infty}) - \log(\tau_0)} = \frac{\lambda\alpha}{1-(1-\lambda)\alpha} \tag{1.56}$$

where τ_0 and τ_{∞} are the relaxation times for the uncured and totally cured polymer, respectively. λ is a material parameter.

Glass transition temperature

As highlighted in section 1.2.1, the glass transition temperature is also a cure-dependent parameter.

Volume shrinkage

During the curing process, the volume shrinkage is made of chemical and thermal shrinkage [HAH 03][JEN 04]. The volume shrinkage leads to the build-up of residual stresses, strains which may modify the fracture strength of the polymer or may induce premature failure.

The chemical shrinkage can be expressed as [HIL 95][HUA 96]:

$$\left(\frac{1}{V_0}\frac{dV}{dt}\right) = -B\frac{d\alpha}{dt} \tag{1.57}$$

where V_0, B are polymer volume at uncured and a cure constant, respectively. $\frac{d\alpha}{dt}$ is the curing rate.

The thermal shrinkage is defined as follows:

$$\left(\frac{1}{V_0}\frac{dV}{dt}\right) = \left(\beta_m(1-\alpha) + \beta_p\alpha\right)\frac{dT}{dt} \tag{1.58}$$

where β_m, β_p are thermal expansion parameters and $\frac{dT}{dt}$ the rate of temperature.

For all of these cure-dependent parameters, the curing degree α is determined by solving such models detailed in Table 2.

1.4.2.2. Cure dependent constitutive models

The curing process of a polymer is complex modelling process. It consists in a time-, temperature- and cure-dependent stress analysis. A simple analogy of the mechanical behavior of a polymer is indicated in Figure 41. A polymer is primarly a visco-elastic material. However, some additional phenomenons such as volume shrinkage occur during the curing process.

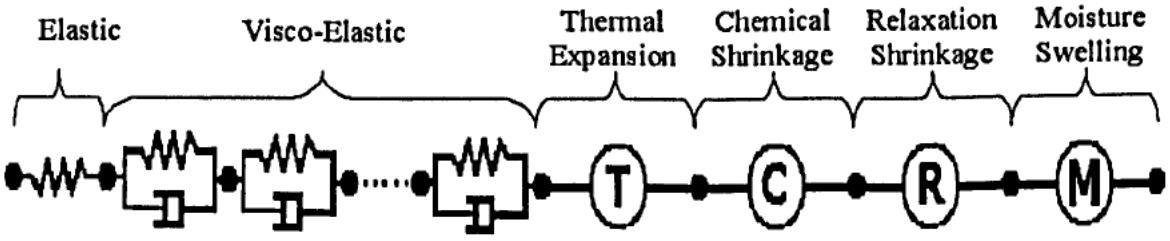

Figure 41. Mechanical analogy model [ZAR 03].

Recent modelling approaches proposed the few steps to develop general purpose continuum approaches for modelling the stress evolution and other mechanical changes during the curing processes of polymers. Some experimental and theoretical methods to describe the curing process were developed by Adolf et al. [ADO 90][AD0 96]. They proposed a modelling approach based firstly on reaction kinetics to describe a temperature history-dependent curing process and secondly to linear visco-elasticity to model the stress distribution in the polymer as a function of the deformation history. Then, they expanded that model to non-linear visco-elastic behavior [ADO 07]. Hossain et al. [HOS 10] proposed curing models for small strains and finite strains for large deformations. Other authors proposed constitutive models for curing polymers, especially adhesives, with viscoelastic properties [YAG 11].

One model particularly interesting is that proposed by Liebl et al. [LIE 11]. This model is based on continuum mechanics and formulated for three dimensional problems with small strains. The main characteristic of this model is the combination of well established material models for the visco-elastic curing of adhesives with a model for plastic deformation of cured adhesives (Figure 42).

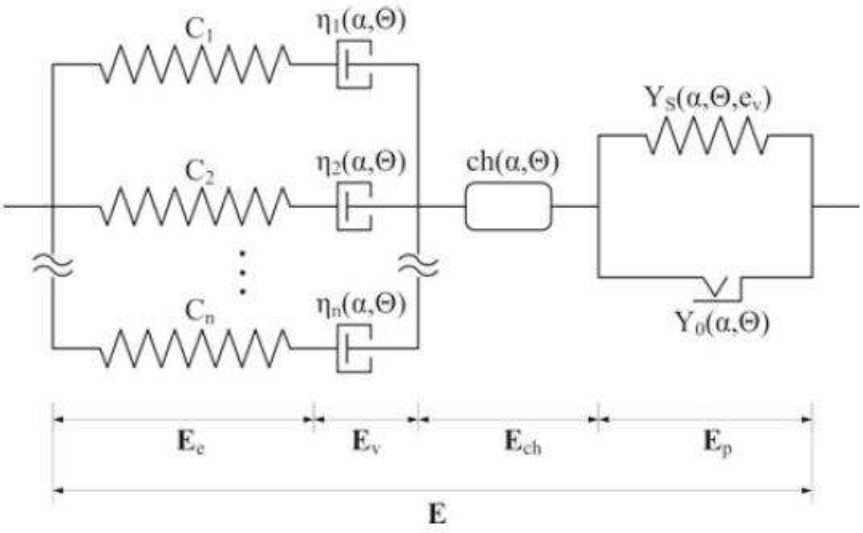

Figure 42. Combination of known rheological models for viscoelasticity and plasticity with a thermo-chemical element [LIE 12].

Regarding visco-elastic properties, the approach was similar to that of Yagimli et al. [YAG 11] by choosing the viscosities $\eta_i(\alpha,\Theta)$ of the Maxwell-element's dashpots, and thus the relaxation times τ_i , as a function of curing degree α and temperature Θ such as:

$$\tau_i(\alpha,\Theta) = \frac{\eta_i(\alpha,\Theta)}{C_i} = \tau_{i0} \cdot 10^{g(\alpha-1)-h(\Theta-\Theta_0)} \tag{1.59}$$

where τ_{i0}, g and h are material parameters and Θ_0 is the reference temperature.

The global rheological model shown in Figure 42 cannot use only one Maxwell-element since it represents a fluid and therefore the uncured adhesive. Therefore, the viscosity of at least one Maxwell-element must be increased to an infinity number in order to represent the cured adhesive. So, this element changes to equivalent of a spring parallel to the other Maxwell-elements and thus, the adhesive behavior changes from a liquid to a solid.

The volume shrinkage due to thermal gradients and chemical shrinkage are written such as:

$$\underline{\underline{\varepsilon}}_{ch} = \left[(\kappa_F + \Delta\kappa\alpha)(\Theta - \Theta_0) + \beta\alpha\right]\underline{\underline{I}} \tag{1.60}$$

where κ_F is the thermal expansion coefficient of the uncured adhesive and $\kappa_F+\Delta\kappa$ is the thermal expansion coefficient of the totally cured adhesive [31]. β is the material parameter for shrinkage.

The plastic part of the model allows describing plastic effects observed in adhesive, such as pressure dependent yield function, isotropic hardening and strength gradient effects. The yield function is those developed by Schlimmer [MAH 05], as detailed in section 1.4.2.1:

$$\Phi = \sigma_{VM}^2 - \frac{1}{3}\left[Y_S{}^2 - a_1 Y_0 p - a_2 p^2\right] \tag{1.61}$$

The yield stress is formulated in dependence of curing degree α and temperature Θ:

$$\begin{aligned} Y_S(\alpha,\Theta,e_v) &= Y_0(\alpha,\Theta) + q(\alpha,\Theta)\left[1 - e^{-be_v}\right] + He \\ Y_0(\alpha,\Theta) &= Y_{0b} + \left[l_\alpha - l_\Theta(\Theta - \Theta_0)\right]\alpha \\ q(\alpha,\Theta) &= \left[v_\alpha - v_\Theta(\Theta - \Theta_0)\right]\alpha \end{aligned} \tag{1.62}$$

The unassociated flow rule is expressed as:

$$\Phi^* = \sigma_{VM}^2 - \frac{1}{3}\left[Y_S{}^2 - a_1^* Y_0\, p - a_2^* p^2\right] \tag{1.63}$$

A viscoplastic potential is used as:

$$\underline{\underline{\dot{\varepsilon}}}_p = \frac{1}{\eta_p}\left\langle \frac{1}{r}\Theta^* \right\rangle^k \underline{\underline{n}} \tag{1.64}$$

$$\underline{\underline{n}} = \frac{\dfrac{\partial \Theta^*}{\partial \underline{\underline{\sigma}}}}{\left\| \dfrac{\partial \Theta^*}{\partial \underline{\underline{\sigma}}} \right\|} \tag{1.65}$$

$$\dot{e}_v = \frac{1}{Y_0(\alpha,\Theta)}\underline{\underline{\sigma}} \cdot \underline{\underline{\dot{\varepsilon}}}_p \tag{1.66}$$

where η_p is the plastic viscosity, r is a factor correcting the unit of the plastic potential and k is a material parameter.

Liebl et al. [LIE 12] implemented these constitutive equations and demonstrated through calculations and simulations that this model is numerically suitable to represent processes relevant in an industrial context for production issues.

A main drawback of this model, as the commonly model presented in this section is that it only represents the mechanical behavior of a polymer, an adhesive in such case, during the curing process and not following it. Hence, this model is restricted to the calculation of residual stresses and strains occurring during the curing process. This view is widely spread in advanced composite materials, surface coatings or some applications that generate residual stresses. For product designers, it is important to have an overview of the development of stresses and strains during the curing process. On the one hand, it allows them to adapt either the curing process or the product geometry to avoid the problems related to the residual stresses. Then, the Finite Element modelling of the curing process is an efficient industrial tool to study the efficiency of design choices such as geometry or curing parameters.

Moussa et al. [MOU 11], Lapique et al. [LAP 02] investigated the influence of the curing history on the mechanical behavior of a polymer, i.e. the prediction of mechanical properties following the curing process, but no efficient model was assumed.

1.5. Characterization methods

In an industrial context, the accurate prediction of a bonded assembly resistance is essential to use structural bonding as an assembly process and to design bonded assemblies using FE simulation. Adhesive

performance characterization is based on a wide variety of tests which can be divided into two main categories: bulk specimens and “in situ” specimens.

- Bulk specimens are used to investigate the mechanical behavior of the adhesive, independently of any adherend. Therefore, the characterization is reduced to a “cohesion” analysis
- Tests conducted on “in situ” joints consider the adhesive as a thin layer confined between two adherends and thus consider “adhesion” issues such as the role of interface and surfaces.

This section proposes some specimens to characterize an adhesive with a Strength of Materials approach, as previously detailed on section 1.3.4.1.

1.5.1. Bulk specimens

Bulk specimens are the most commonly used tests to determine the elastic and strength properties of adhesives. For each type of load, specific geometries of bulk specimens are proposed. In tensile configuration, “dog-bone” specimens are widely used, as suggested by classical standards [ASTM D638] (Figure 43 (a)). In compression tests, the specimens may be cylindrical, parallelepiped or tubular [ASTM D695] (Figure 43 (b)) and provide stress-strain curves and therefore compression Young’s modulus, elastic limit and failure characteristics. Shear properties can be obtained with solid or tubular bars in torsion (Figure 43 (c)). Therefore, pure shear state is observed for solid bars only if the stress distribution within the adhesive is linear along the radial direction. These kinds of tests are difficult to manufacture and dimensions are arbitrarily take since no standard exists [DEB 51][NAD 31][CHE 11].

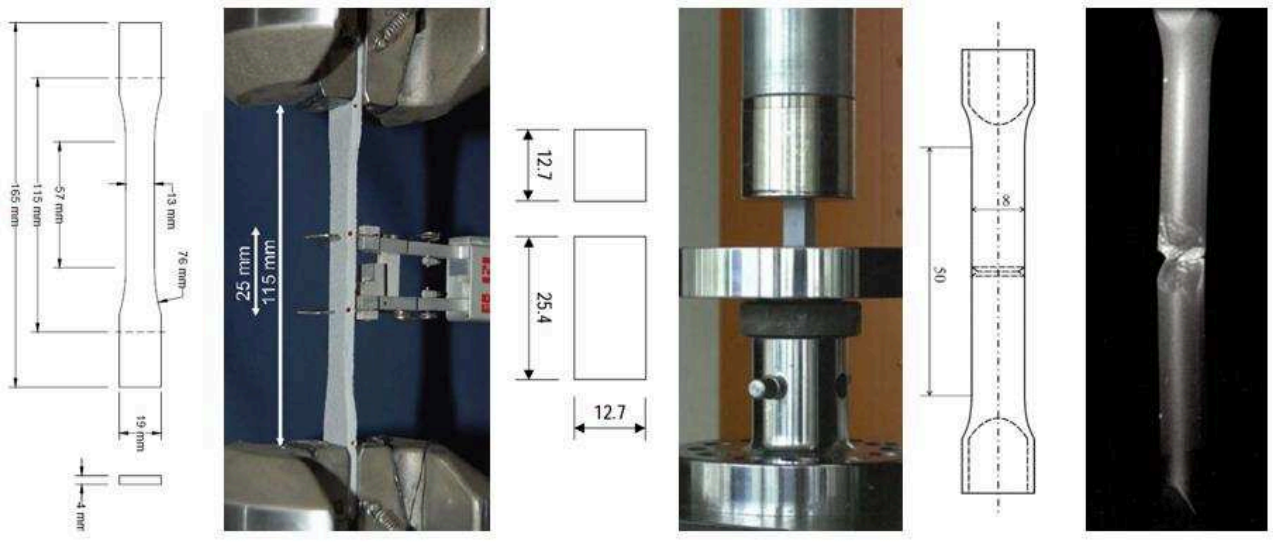

(a) (b) (c)

Figure 43. (a) Tensile load: "dog-bone" specimen according to ASTM D638 and experimental set-up [MOU 11], (b) compressive load: parallelepiped specimen according to ASTM D695 and experimental set-up [CAS 05], (c) shear load: solid bar torsion specimen [CHE 11].

The standardized Iosipescu shear test [ASTM D5379] or Arcan test [ARC 87] are one alternative to the massive torsion shear tests. The Iosipescu shear test uses a double notched specimen under an asymmetric four point bending loading mode (Figure 44 (a)) to create a uniform stress distribution within the notched region of the specimens [DOL 82]. Considering the original Arcan test, it also allows to access to shear properties of a bulk adhesive. In addition, this specimen includes a diametrically loaded circular disc containing asymmetric cut-outs with the mid-section to establish a state of uniform stress (Figure 44 (b)). Thus, various additional stress states can be produced depending on the loading angle. The main

disadvantage of these specimens is the stress concentrations/singularities near the tips of the notched which may cause premature failures, especially for brittle adhesives [DEA 96].

(a) (b)

Figure 44. (a) Iosipescu shear test [INSTRON] and (b) Arcan specimen [ARC 87] (reproduced from [ARN 14a]).

A difficulty of such tests is the manufacturing of bulk specimens, particularly for bi-component adhesives. Da Silva et al. [DAS 12] listed some methods to prepare quality bulk samples. The mixing of a two part adhesive involves generally voids which have significant effect on failure properties such as a premature crack. Some techniques such as vacuum release technique [DAS 04] were developed to provide void-free specimens but with a limited success. Another drawback of bulk specimen is the thickness of these bulk specimens. The thickness must be representative of the thin adhesive layer of the studied bonded assembly. Nevertheless, it is difficult to reach bondlines thicker than 1 mm [GRO 07].

Bulk specimens provide an idea of the mechanical properties of an adhesive. It is generally the case for an elementary investigation of the influence of the curing state (i.e, curing degree) of an adhesive on its mechanical properties. In Figure 45, Moussa et al. [MOU 11] shows the evolution of the stiffness and strength for several curing temperatures (i.e curing degrees) thanks to tensile “dog-bones”.

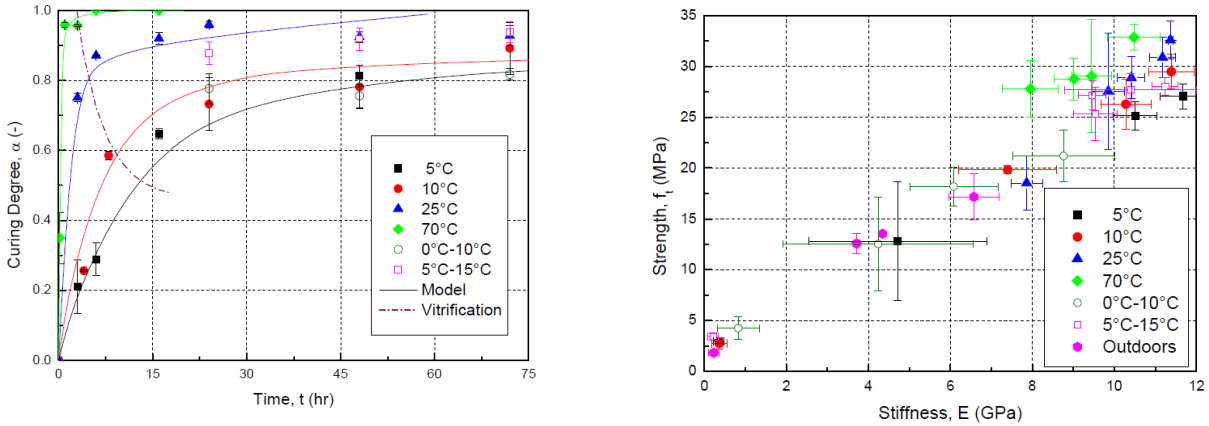

(a) (b)

Figure 45. (a) Curing degree vs. time of cured samples at different isothermal and cyclic temperatures, (b) Strength vs. stiffness relationship. [MOU 11]

However, the mechanical properties predicted by bulk tests differ from those of the real bonded assembly due to the thickness difference and the disregard of “adhesion” issues. So bulk tests must be completed by in-situ tests to properly describe the mechanical behavior of an adhesive in an assembly. Further, by considering the curing state of the adhesive, more important polymerization gradients should be observed

for bulk specimens than for in-situ specimens due to a higher thickness. Hence, the mechanical properties predicted by massive specimens will be different from those of a thin adhesive layer.

1.5.2. Bonded specimens

As shown in section 1.3.1, an adhesively bonded joint can be submitted to several modes of loading. Various tests are associated with each mode in order to characterize a bonded assembly.

1.5.2.1. Characterization in shear loading

Single Lap Joint (SLJ) Test

The Single Lap Joint specimen is the most widely test used to characterize an adhesively bonded joint in shear. This test is the bonding of two thin adherends with a defined overlap length, as recommended by standard [ASTM D1002](Figure 46 (a)). This test is extensively used in aerospace and automotive industries to quickly determine the bonded joint performance when it is submitted to aggressive environmental conditions in service, such as moisture, temperature gradients. Grant et al. [GRA 09] investigated experimentally the influence of temperature on the joint strength with single lap joint specimens for an epoxy adhesive thickness varying from 0.1 to 3.0 mm, as suggested in Figure 46 (b). For thin adhesive layers, the cold tests are stronger than the room temperature and hot tests. For thick joints, strength remains the same regardless of temperature. This comes from the complex stress distribution in Single Lap Joint specimen highlighted by Volkersen [VOL 38], as explained earlier in section 1.3.3. A large bending moment occurs at the edge of the joint and induces crack initiation. Hence, the failure comes from this moment which is high for thick adhesives, and not from the loading applied across the joint. As a result, the influence of temperature must be considered only for thin adhesive layers in that case.

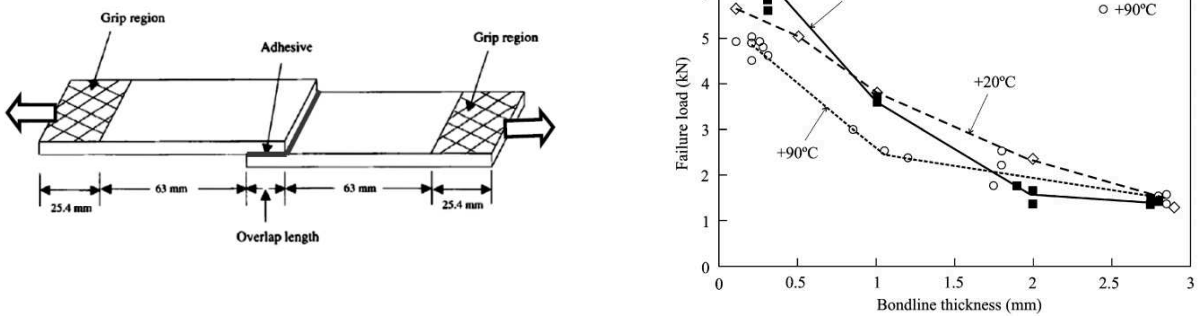

(a) (b)

Figure 46. (a) Single Lap Joint specimen [ASTM D1002] and (b) Single Lap joint of an epoxy adhesive tested in tension at different temperatures [GRA 09].

Results predicted by the Single Lap Joint specimen must be carefully considered due to its particular stress distribution in the adhesive layer.

Double Lap Joint (SLJ) Test

The Double Lap Joint test [ASTM D3528] is one alternative to the Single Lap Joint specimen. Based on the same principle, this configuration reduces the bending moment. Indeed, the load is applied through the adhesive to the adherends away from their neutral axis [KIN 83].

KANG et al. [KAN] studied the influence of the temperature, and consequently the curing state, on double-lap joint strength for three adhesive including one epoxy adhesive (Hysol EA9696), as shown in Figure 47.

As for Single Lap Joint test, Strong strengths are observed at cold temperatures. Cold temperatures reduces chain mobility within the adhesive, hence a higher strength is required to reach failure.

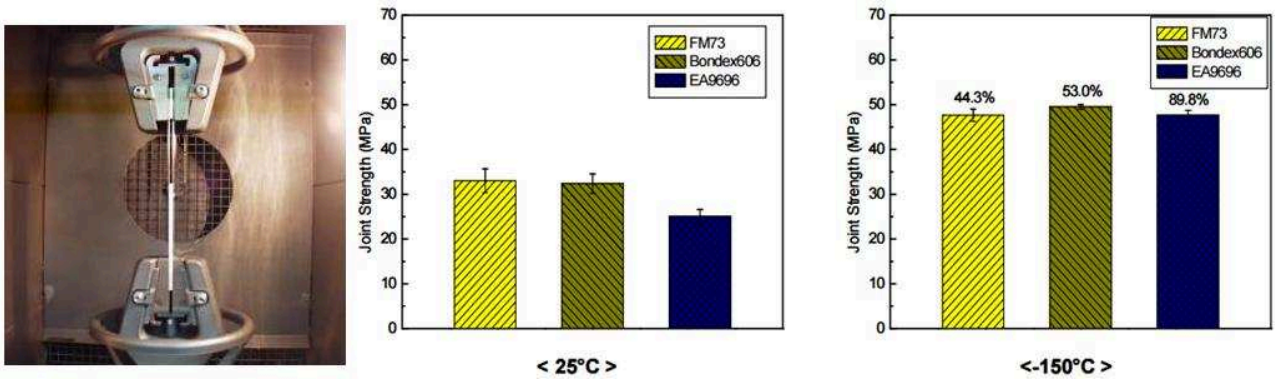

(a) (b) (c)

Figure 47. (a) Tensile test of a double-lap joint specimen in environmental chamber, Experimental results of double-lap joint specimens at: (b) room temperature and (c) cryogenic temperature. [KAN]

Thick Adherend Shear Test (TAST)

The Thick Adherens Shear Test or TAST is a Single Lap Joint test with thick adherends, as proposed by [ISO 11003-2] and represented in Figure 48 (a). The high thickness of the adherends stiffens them and reduces the deformation gradient along the joint in the overlap region. However, stress concentrations at the end of the joint and non uniform stress-distribution in the adhesive layer remain [CRE 08].

Da Silva et al. [DAS 05] used this specimen to investigate the influence of thermal loadings on several adhesives resistance in shear (Figure 48 (b)). Two of the adhesives studied are epoxies: Hysol ®EA9359.3 and Supreme® 10HT. The shear strengths decrease with the increase of temperature. As explained for the Double Lap Joint specimen, chain mobility is reduced at cold temperatures and a higher strength is necessary to cause the adhesive failure.

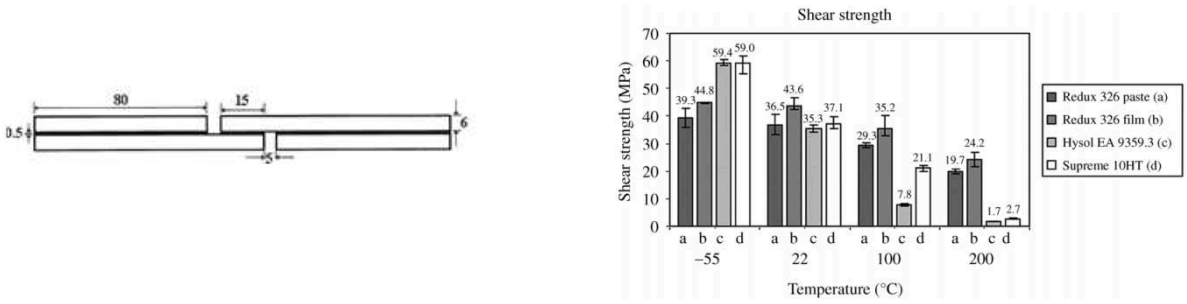

(a) (b)

Figure 48. Thick Adherend Shear Test: (a) specimen geometry [ISO 11003-2] and (b) Adhesive shear strengths [DAS 05].

1.5.2.2. Characterization in tensile/compressive/torsion loading

Butt Joint

The butt joint allows studying the mechanical behavior of an adhesive under tensile/compressive loading or shear loading.

The butt joint in uniaxial tension (compression) [ASTM D897][ASTM D2095] appears to ensure a uniform stress of stress in the adhesive layer. However, Adams et al. [ADA 77][ADA 79] and Jeandrau et al. [JEA 85] highlighted a non uniform stress distribution in the adhesive layer due to the constraint applied to the adhesive by the adherends, circumferential tensile stresses in the adhesive layer and the possible misalignement of both adherends.

The butt joint loaded in torsion induces a pure shear stress in the adhesive layer for none misalignment. This test is called “napkin-ring” and is described by the standards [ASTM E229-92]. One drawback is its complexity since bondline thickness needs to be accurately controlled and a perfectly adherends alignment is required to provide quality shear properties.

Kim et al. [KIM 13] used the butt joint under tensile loading to compare the influence of two curing cycles on the tensile strength as shown in Figure 49. Results are presented for adhesive thicknesses of 0.4 and 1.0 mm. Conventional cure refers to a curing cycle of 1h30 at 80°C and smart cure refers to a curing cycle of 48h at 20°C. For both thicknesses, a “smart cure” improves the adhesive bonded joint strength. The curing state of the epoxy adhesive remains different for each curing cycle which affects its resistance.

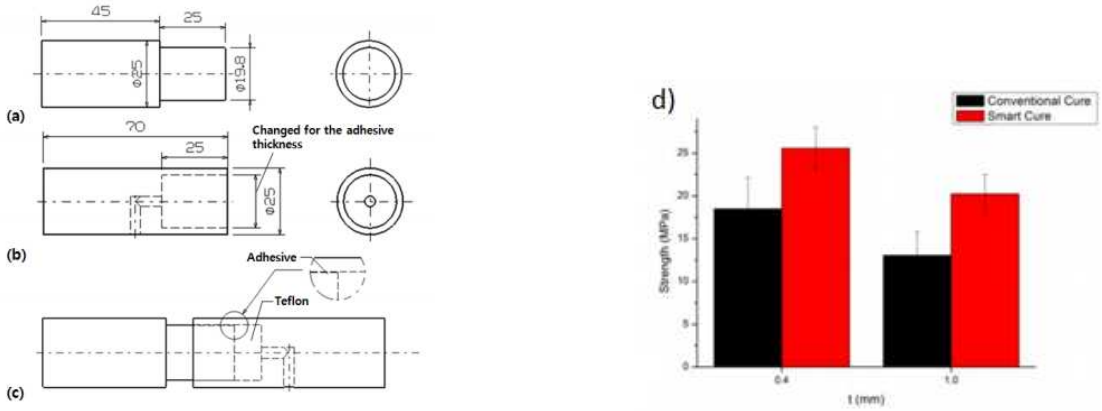

Figure 49. Butt joint specimen: (a) inner adherend, (b) outer adherend, (c) shape of the joint and (d) Tensile epoxy adhesive bonded joint by conventional and smart cycle. [KIM 13]

Guess et al. [GUE 95] used the butt joint under compressive loading to study the influence of the temperature on stress relaxation of an epoxy adhesive (Figure 50 (a)). In addition, he investigated the influence of strain rates on the stress relaxation data for the same epoxy adhesive cured at a cold-curing cycle of 18 hours at 35°C (Figure 50 (b)). Regarding the influence of temperature, the same trend as that seen for previous specimens is observed, namely a increase of compressive stress with a decrease of temperature due to a chains mobility restriction. On Figure 50 (b), a major increase in yield strength is observed with increasing strain rate. This may be due to the fact that this adhesive is cured at a cold-curing temperature and has not yet achieved its totally curing state. Thus, it is quite viscous and very sensitive to strain rate loadings.

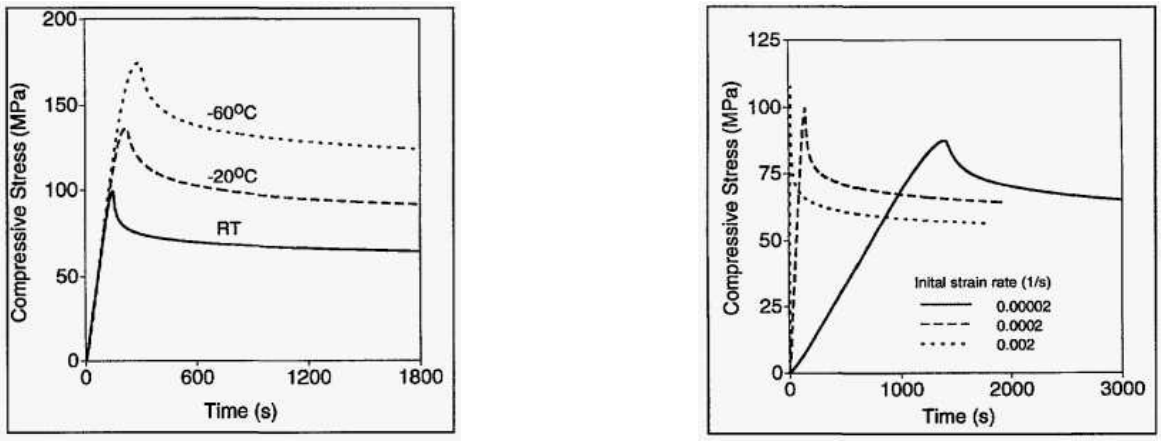

(a) (b)

Figure 50. Stress relaxation data for an epoxy adhesive cured 18 hours at 35°C: (a) tested at three temperatures and loaded to a strain rate of about 0.0002/s, (b) loaded at different strain rates. [GUE 95]

"Napkin-ring" specimen can also be used to explore the influence of temperature on shear properties of an epoxy adhesive, as suggested by Chai et al. [CHAI 04] in Figure 51. The shear stress increases with decreasing temperature loadings.

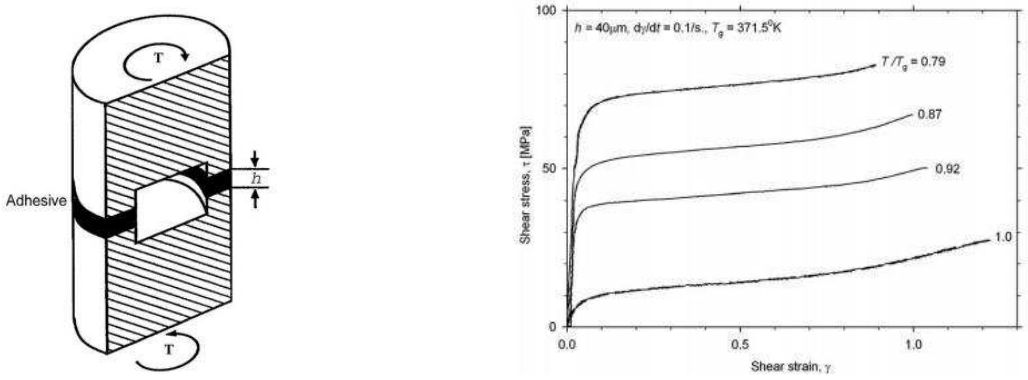

(a) (b)

Figure 51. Napkin-Ring test: (a) Sectional view of the specimen and (b) The effect of temperature (in Kelvin degrees) on the stress-strain response in shear. [CHAI 04]

1.5.2.3. Characterization in multi-axial loading

In the previous tests presented the adhesive layer was loaded under one pure mode of loading (or quasi-pure loading for the Single Lap Joint specimen). However, the mechanical behavior of an adhesive is loading-dependent [MAH 05] [CRE 08]. The non-linear behavior of an adhesive requires specific load-path to be entirely determined such as a combination of compression and shear loading [ARN 14]. Particular devices such as Arcan tests and Traction-Torsion tests have been developed for that purpose.

Traction-Torsion tests

Traction-Torsion tests were widely used by Mahnken et al. [MAH 05], Vernet et al. [VER 05], Jousset et al. [JOU 10] to characterize and valid properly material constitutive model of adhesives. These tests allowed combining simultaneously longitudinal and radial loadings with different ratio that is of great interest for characterization since it allows proportional and non proportional loadings. Nevertheless, the manufacturing process of tubular joints remains delicate and requires a perfect alignment of the adherends

and an accurate load application. Arnaud et al. [ARN 14b] developed a tension/compression-torsion test (Figure 52) to overcome to these manufacturing issues.

Arcan tests

Arcan and Iosipescu tests are another solution to produce multi-axial stress state in the adhesive layer. Such tests were originally developed for bulk specimens [ASTM D5379] under tension-shear loadings. Based on previous works [ARC 87][GIN 93], Cognard et al. [COG 05] modified the initial fixture in order to predict the behavior of an adhesive in a bonded assembly. This consists firstly in modifying the device geometry to extend the loading area to compression-shear which is rarely investigated. Hence, the modified Arcan specimen can be loaded under various mode ratios by rotating the fixture of a specific angle as shown in Figure 53 (a). Second, a clamping system was realized to fix the bonded specimen to the Arcan fixture (Figure 53 (b)) without generating preloads in the adhesive. Third, beaks were added to adherends to strongly limit the edge effects (Figure 53 (c)). From an industrial point of view, the modified Arcan specimen is difficult to use for the characterization of several adhesives in large quantities. Hence, Créac'hcadec et al. [CRE 15] developed an experimental device, called Arcan TCS (Tensile/Compression-Shear) (Figure 54) which is able to characterize an adhesive in an assembly at an industrial frequency. Such specimen retains the main improvements made by Cognard that is the control of the adhesive thickness, none preloads in the adhesive layer, a wide range of loadings, the reduction of edges effects due to the particular geometry close to the adhesive (Figure 54 (b) and (c)).

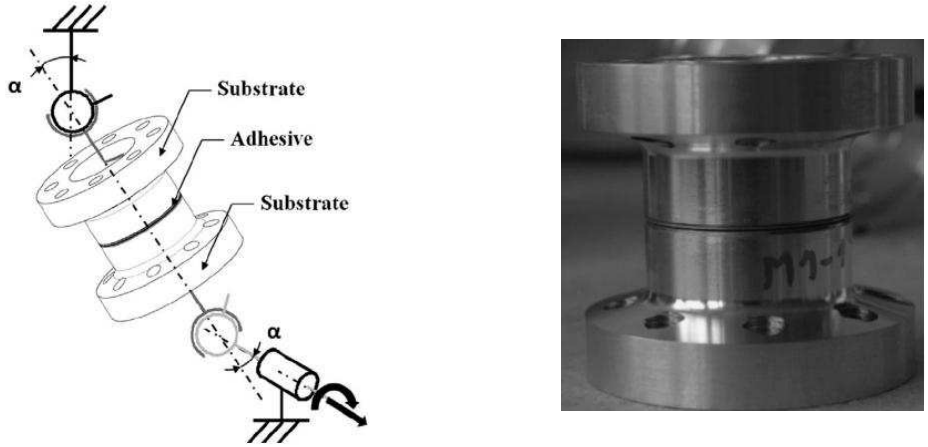

(a) (b)

Figure 52. Tension/compression-torsion test: (a) boundary conditions during the test and (b) specimen bonded and cured [ARN14b].

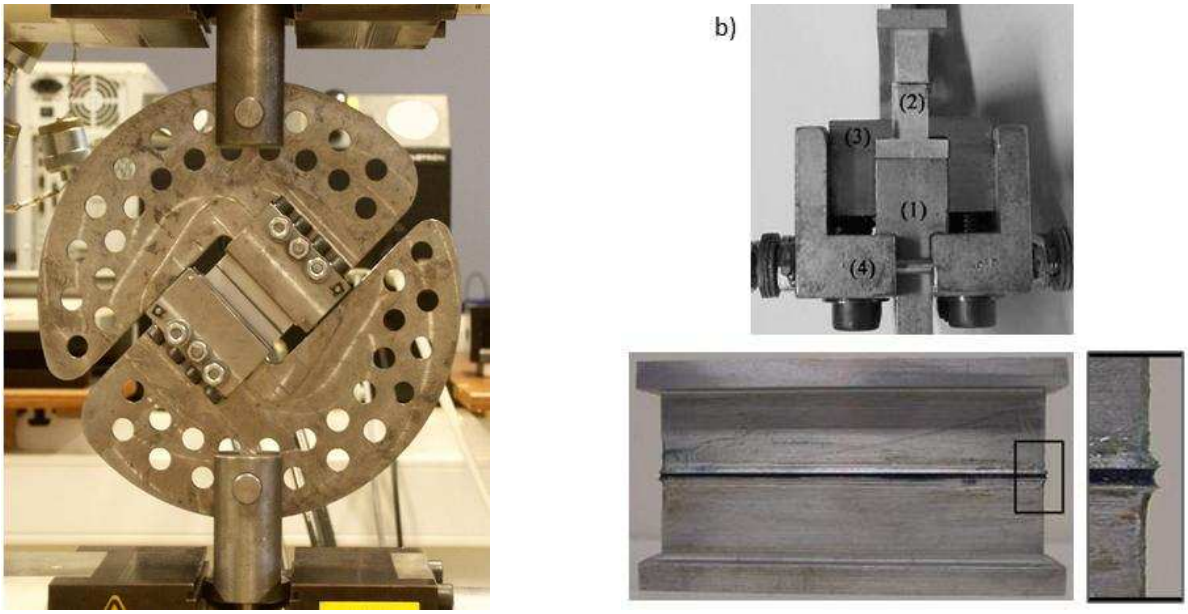

(a) (c)

Figure 53. Modified Arcan test: (a) experimental set-up, (b) focus on the clamping system, (c) bonded specimen and focus on the beaks geometry. [CRE 08]

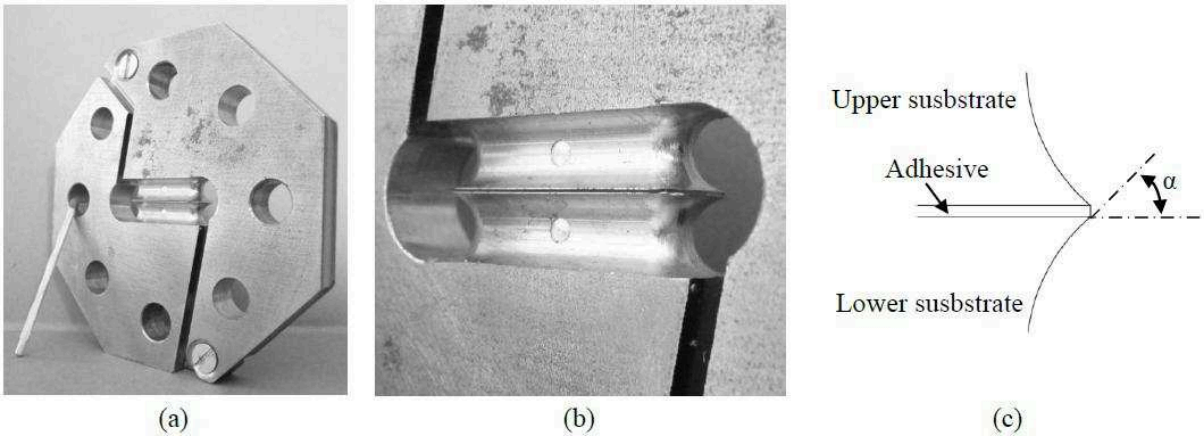

Figure 54. Tensile/compression-shear Arcan Test: (a) a general view of the test specimens, (b) focus on the local geometry of the beaks close to the adhesive and (c) definition of the angle α for the beaks. [CRE 15].

The modified Arcan specimen was widely used to identify the mechanical behavior of an adhesive in specific service conditions such as hygrothermal ageing [BER 11], humid ageing [ARN 14]. Maurice et al. [MAU 13] investigated the influence of the curing process on the mechanical response of an epoxy adhesive. Figure 55 (a) shows a dependency of the non-linear behavior to the curing state of the adhesive. He restricts the non-behavior domain to tangential forces ranging up to -15 kN. However, Arnaud et al. [ARN 14] and Thévenet et al. [THE 13] showed experimentally that the remaining section curve must be taken into account in the non-linear behavior of the adhesive since it is an adhesive contribution and does not totally come from the interfaces. Figure 55 (b) shows the behavior of the epoxy adhesive Araldite® 420 A/B under monotonic and cyclic loadings with modified Arcan test in compression-shear. Some studies [COG 06] had shown the influence of the loading rate on the behavior of this adhesive. Hence, both monotonic and cyclic tests were conducted under load control using the same and constant loading. Under monotonic loading and for the applied load rate, a non-linear behavior was observed for shear loads higher than 12 kN and maximum relative displacement was at 288 µm. Regarding cycling loading, the cumulative displacement DT at failure in the bonded joint was measured for similar magnitudes. These experimental

analyses under various types of compression-shear loadings underline that failure was reached for similar maximum relative displacement, maximum cumulative displacement. This result does not depend on loading amplitude or mean load and seems to constitute a suitable criterion under compression-shear loadings. This was not observed for monotonic and cycling tensile loading. Further, cohesive failure and adhesive failure had been observed under tensile and compression-shear loadings, respectively. Therefore, bonding mechanisms involved are load-dependent. It can be assumed that interfaces are less stressed under compression-shear loading than for others loadings and provide almost no contribution to the mechanical behavior of the adhesive. Thus, the curves predicted in Figure 55 (a) showed the non-linear behavior of the adhesive over its entire section. Curing history of the bonded joint has great influence on the non-linear section curve.

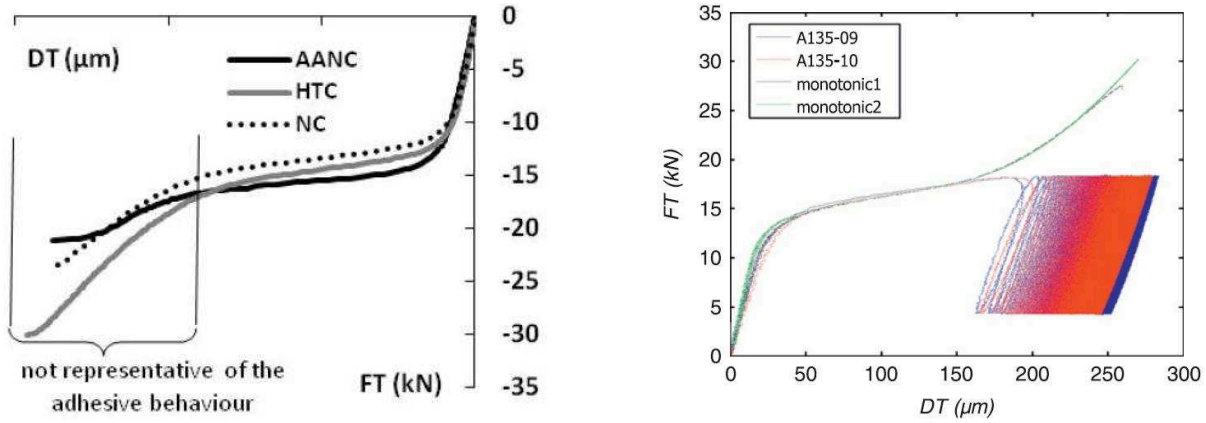

(a) (b)

Figure 55. Modified Arcan test: (a) Influence of three curing conditions on mechanical behavior of the epoxy adhesive Araldite® 420 A/B in compression-shear in the tangential direction [MAU 13] and (b) Influence of load amplitude on the cyclic behavior of the epoxy adhesive Araldite® 420 A/B in the tangential direction in compression-shear [THE 13].

The tests presented in this section allow an accurate characterization of an adhesive in an assembly thanks to a wide range of loadings. However, such tests are not standardized and it restricts considerably their use in industrial applications.

1.6. Difficulties encountered in adhesive characterization

The characterization of an adhesive is made of successive stages of identification. It requires:

- A relevant material constitutive model representative of the mechanical behavior of the adhesive studied
- Specific experimental tests to accurately predict the mechanical behavior of the adhesive
- A strong identification method to determine relevant mechanical parameters for Finite Element simulation of industrial bonded assemblies

These steps go with some difficulties. Generally, a 3D non-uniform stress state exists within the adhesive layer. However, Material and failure conditions for multi-axial loaded adhesive layers can only be determined by testing bonded specimen under homogeneous stress conditions. This means a great deal of experimental and simulation efforts.

As explained in section 1.3.2, most of adhesively bonded joints suffer from edge effects. The commonly solution proposed consist in modifying the geometry in the vicinity of the adhesive layer to reduce stress concentrations/singularities. Cognard et al. [COG 05] modified the Arcan test and the TAST test [CRE 08] by machining beaks on the adherends all around the bonded surface. Créac'hcadec et al. [CRE 15] introduced beaks technology on other multi-axial fixtures such as Arcan TCS test. Beaks geometry evolved over the use of different fixtures thanks to numerical Finite Element studies on the sensitivity if edges effects to the very local geometry. Thus, the reduction of edge effects must be considered with great interest in the characterization of an adhesively bonded joint.

Specimen bonded with thin substrates such as the Single Lap Joint test highlight deformation gradients in the adherends induce stress concentrations in the adhesive layer. The influence of substrate deformation on the assembly must be considered to be directly usable for identification purpose.

Direct identification of material parameters involved in material constitutive laws required homogeneous stress and strain states in the adhesive layer. However, the mechanical tests used for adhesives characterization include a non-homogeneous multi-axial stress distribution in the adhesive. This cannot be directly deduced from experimental curves force-displacement and as a consequence, requires an inverse identification method. Gegner et al. [GEG 04] proposed an identification method of elastic parameters constants using Finite Element modelling. This consists in finding a suitable set of parameters such that the numerical response calculated with the constitutive model matches the corresponding experimentally measured response. This method proposed was then commonly employed in multi-axial tests such as tension-torsion [JOU 10][ARN 14] or Arcan test [CRE 08][JOU 10][MAU 12][ARN 14] for the characterization of elastic-plastic behaviors. Bidaud et al. [BID 14] extended it for the identification of constitutive parameters of a visco-elastic-visco-plastic adhesive. The use of inverse identification overcomes the problem of deformation gradients in the adherends. However, it requires some cautions since it is carried out by combining Finite Element analysis and optimization techniques. Regarding Finite Element analysis, the numerical model must be representative of experiment. In addition, an optimal element size must be determined to provide short computation time and accurate results. This aspect is particularly important for the identification step where the iterative optimization process requires several repetitions of a Finite Element simulation. Regarding the optimization process, an efficient algorithm must be used to minimize the error function to ensure the convergence to the global minimum. The error function and initial set of parameters must be beforehand correctly chosen.

Some aspects concerning the application of adhesives must be regarded:

- Adhesive preparation: pot-life, mixing, heating
- Dispensing techniques: tools, applicators, appropriate quantity of adhesive dispensed evenly on the bonded surface
- Repeatability and maintenance of the dispensing equipment

Those processing parameters may weaken the adhesively bonded joint performance, as suggested by Pujol et al. [PUJ 07]

1.7. Conclusions and presentation of the approach adopted

The present section makes a state of the art about structural adhesives, characterization and modelling methods and their limitations. Structural adhesive bonding is a "multiscale" system of three interdependent variables: the polymer science, the physical chemistry of surfaces and interfaces and the mechanics (Figure 56).

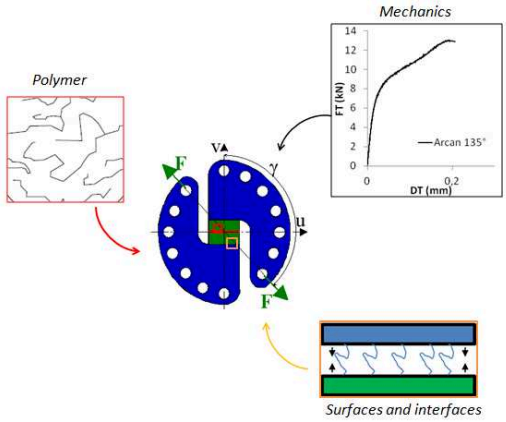

Figure 56. Adhesive bonding: a multiscale problem.

A typical application is the use of cold-curing adhesives for aerospace bonded structures. During its service life, this assembly is subjected to particular environmental conditions and loads. In fact, for both loadings (thermal and mechanical), extremes cases are observed since thermal and mechanical gradients are almost negligible in the storage step whereas they are significant in the launch phase. It has been showed previously that this kind of adhesive remains an unstable curing state and then the resulting mechanical behavior may be different according to its in-service conditions.

The effects of curing state on the mechanical behavior were observed through classical specimens. Two perspectives were identified. The first one was during the curing process and result in residual stresses. The second one was following the curing process. This amounts in assessing the adhesive resistance during its polymerization process. This latter may be affected by external loads such as temperature or mechanical loads.

The second instance must be considered for this study. The aim is to propose a numerical tool for predicting the mechanical behavior of an adhesive in a spatial bonded assembly during its life path. The achievement of this objective involves in a series of steps:

- *Chapter 2:* An extensive determination of the curing behavior of a cold-curing adhesive was realized. It was firstly experimentally investigated with Differential Scanning Calorimeter (DSC) measurements. Then, cure kinetics were applied for modelling the curing behavior of the adhesive. Finally, a Finite Element model was proposed to simulate the process of adhesive curing in a bonded assembly.

- *Chapter 3:* An extensive experimental investigation of the mechanical properties of the adhesive at different curing states was presented. To that end, several curing temperatures were applied. Then, the adhesive was testing with the Arcan Evolution fixture under monotonic loads (0°, 90°, 45°, 135°) and for strain rates to underline viscous effects.

- *Chapter 4:* A constitutive model was developed to predict the mechanical behavior of an adhesive according to its curing state. A model based on that of Mahnken-Schlimmer with some

modifications and a dependence of parameters to the curing degree was proposed. These last one were identified with a strong inverse identification method with experimental results of chapter 4.

- *Chapter 5:* The potential of the constitutive model developed to accurately and efficiently model the behavior of a bonded assembly was reviewed. For this purpose, a test representative of the adhesive behavior in the adhesive was provided in order to compare experimental and numerical responses of conical bonded assembly and to validate constitutive equations developed.

1.8. References

[ADA 77] Adams R.D., Coppendale J., The Elastic Moduli of Structural Adhesives, Adhesion, Allen K.W. ed., Applied Science Publishers, London, United Kingdom, pp 1-17, 1977.

[ADA 79] Adams R.D., Coppendale J., The Stress-Strain Behavior of Axial Loaded Butt Joints, Journal Adhesion, Vol. 10, No. 1, pp 49-62, 1979.

[ADA 84] Adams R.D., Harris J.A., Strength Prediction of Bonded Single Lap Joints by Nonlinear Finite Element Methods, International Journal of Adhesion and Adhesives, Vol. 4, pp. 65-78, 1984.

[ADA 92] Adams R. D., Malluck V., A method for the stress analysis of lap joints, J. Adhesion, Vol. 38, pp. 199-217, 1992.

[ADA 04] Adams R. D. What controls the strength of adhesive lap joints when exposed to aggressive environments. Proc. 7th European Adhesion Conference, Freiburg, Germany, 2004.

[ADA 05] Adams R.D., Adhesive bonding: Science, Technology and Applications. Woodhead Publishing Ltd, 2005.

[ADO 90] Adolf D. B. and J.E. Martin, Time-Cure Superposition During Cross-Linking, Macromolecules, Vol. 23, pp.3700-3704, 1990.

[ADO 96] Adolf D. B., Martin J.E., Calculating of stresses in crosslinking polymers. J Compos Mater 30(1), pp. 13–34, 1996.

[ADO 97] Adolf D. B., Chambers R. S., Verification of the capability for quantitative stress prediction during epoxy cure. *Polymer 38*, Vol. 21, 5481–5490, 1997.

[ADO 07] Adolf D.B., Chambers R.S., A thermodynamically consistent, nonlinear viscoelastic approach for modelling thermosets during cure. J Rheol, Vol. 51, pp.23–50, 2007.

[AKI 03] Akisanya, A.R. and C.S. Meng, Initiation of fracture at the interface corner of bi-material joints. Journal of the Mechanics and Physics of Solids, Vol. 51, pp. 27-46, 2003.

[ALF 01] Alfano, G., Crisfield, M.A., Finite element interface models for the delamination analysis of laminated composites: mechanical and computational issues. International Journal of Numerical Methods in Engineering, Vol. 50, pp. 1701-1736, 2001.

[ALF 06] Alfano, G., On the influence of the shape of the interface law on the application of cohesive-zone models. Composites Science and Technology, Vol. 66, pp. 723-730, 2006.

[ALL 96] Allix, O., Corigliano, A., Modeling and simulation of crack propagation in mixed modes interlaminar fracture specimens. International Journal of Fracture, Vol. 77, pp. 111-140, 1996.

[ASH 01] Ashcroft, I.A., D.J. Hughes, and S.J. Shaw, Mode I fracture of epoxy bonded composite joints: 1. Quasi-static loading. Int. J. Adhesion and Adhesives, Vol. 21,

pp. 87-99, 2001.

[ASH 04] Ashcroft, I.A., A simple model to predict crack growth in bonded joints and laminates under variable-amplitude fatigue. J. Strain Analysis, 39(6), pp.707-716, 2004.

[ASH 11] Ashcroft I., Fatigue Load Conditions, in Handbook of Adhesion Technology, Ed. By L.F.M. da Silva, Ochsner A., Adams R.D., 2011.

[ARC 87] Arcan L., Arcan M., Daniel L., SEM fractography of pure and mixed mode inter-laminar fracture in graphite/epoxy composites. ASTM Technical Publications, Vol. 948, pp. 41-67, 1987.

[ARC 73] Argon, A.S., A theory for the low-temperature plastic deformation of glassy polymers. Phil. Mag., 28, 839–865, 1973.

[ARN 14a] Arnaud N., PhD Thesis : Analyse de l'effet du vieillissement en milieu humide sur le comportement mécanique d'adhésifs en assemblages sous sollicitations multiaxiales, 2014.

[ARN 14b] Arnaud N., Créac'hcadec R., Cognard J.Y., A tension/compression–torsion test suited to analyze the mechanical behavior of adhesives under non-proportional loadings. International Journal of Adhesion and Adhesives, 53: 3-14, 2014.

[AST 90] ASTM D4473-90, American Society for Testing and Materials, Philadelphia, 1990.

[AST 90a] ASTM D4092-90, American Society for Testing and Materials, Philadelphia, 1990.

[AST 90] ASTM E1142-90, American Society for Testing and Materials, Philadelphia, 1990.

[AST 94] ASTM D1640-94, American Society for Testing and Materials, Philadelphia, 1994.

[ASTM D638] Standard Test Method for Tensile Properties of Plastics, ASTM D638-14, 2014.

[ASTM D695] Standard Test Method for Compressive Properties of Rigid Plastics, ASTM D695-96, 1996.

[ASTM D897] Standard test method for Tensile Properties of Adhesive Bonds, ASTM D897-08, 2008.

[ASTM D1002] Standard test method for apparent shear strength of single-lap-joint adhesively bonded metal specimens by tension loading (Metal-to-Metal), ASTM D1002-06, 2006.

[ASTM D2095] Standard Test Method for Tensile Strength of Adhesives by Means of Bar and Rod Specimens, ASTL D2095-96, 2008.

[ASTM D3528] Standard Test Method for Strength Properties of Double Lap Shear Adhesive Joint by Tension Loading, ASTM D3528-96, 2008.

[ASTM D5379] Standard Test Method for Shear Properties of Composite Materials by the V-Notched Beam Method, ASTM D5379-12, 2012.

[ASTM E229] Standard Test Method for Shear Strength and Shear Modulus of Structural Adhesives, ASTM E229-97, 2003.

[BAD 12] C. Badulescu, J.Y. Cognard, R. Créac'hcadec, P. Vedrine. Analysis of the low temperature-dependent behavior of a ductile adhesive under monotonic tensile/compression–shear loads. International Journal of Adhesion and Adhesives, 36: 56-64, 2012.

[BAK 93] De Bakker C.J., St John N.A., George G.A., Simultaneous Differential Scanning Calorimetry and Near-infra-red Analysis of the Curing of Tetreaglycidyldiaminodiphenylmethane with Diaminodiphenylsulphone, Polymer, Vol. 34, 716, 1993.

[BAN 86] Bandara U., A systematic solution to the problem of sample background correction in DSC curves, Journal of Thermal Analysis, Vol. 31, pp. 1063-1071, 1986.

[BAR 93] Bartenev G.M., Shut N.I., Danilenko G.D., Askadskii A.A., Pastukhov V.V., Polym Sci., Vol. 35, 1248, 1993.

[BAS 03] BASF HandBook on Basic of Coatings Technology, 2003.

[BID 14] Bidaud P., PhD Thesis: Analysis of the cyclic behavior of an adhesive in an assembly for offshore windmills applications, 2014.

[BIG 90] Bigwood D.A., Crocombe A.D., Non linear adhesive bonded joint design analysis, Int. J. Adhes. Adhes., Vol. 10, pp. 31-41, 1990.

[BIK 61] Bikerman J.J, The science of adhesive joints, Academic Press, New York, 1961.

[BIL 98] B. Bilyeu, W. Brostow, and K. Menard, Proceedings of the 6th International Conference on Polymer Characterization, Denton, TX, 67, 1998.

[BIL 99] B. Bilyeu, W. Brostow, and K. Menard, Epoxy thermosets and their applications. I: Chemical Structures and Applications, Journal of Materials Education, Vol. 21, 1999.

[BIL 00] Bilyeu B., Brostow W., Menard K.P., Epoxy thermosets and their applications. II: Thermal analysis, Journal of Materials Education, Vol. 22, pp. 107-129, 2000.

[BIS 89] Bishopp J.A., Sim E.K., Thompson G.E., Wood G.C., in Adhesion, Ed. K. W. Allen, Elsevier Applied Science, 1989.

[BOG 92] Bogetti, T.A. and J.W. Gillespie, Jr., Process-Induced Stress and Deformation in Thick-Section Thermoset Composite Laminates. Journal of Composite Materials, 26(5): p. 626-660, 1992.

[BOY 88] Boyce, M.C., Parks, D.M., Argon, A.S., Large inelastic deformation of glassy polymers. Part I: Rate dependent constitutive model. Mech. Mat., 7, 15– 33, 1988.

[BOW 84] Bowditch M., Stannard K., Effect of water absorption on the properties of a filled elastomer, International conference on Polymers in a marine environments, Vol. 97, pp. 117-119, 1984.

[BRO 86] Brochard F., De Gennes P.G., Polymer-Polymer Interdiffusion, Europhysics Letters, Vol. 1, pp. 221-224, 1986.

[BRO 01] Broughton, W.R., L.E. Crocker, and J.M. Urquhart, Strength of adhesive joints: A parametric study. National Physical Laboratory (NPL), 2001.

[BUD 10] Budzik M.K., PhD Thesis, Fracture in asymmetric bonded joints, 2010.

[CAM 05] Campilho, R.D.S.G., de Moura, M.F.S.F., Domingues, J.J.M.S., Modelling single and double-lap repairs on composite materials. Composites Science and Technology, Vol. 65, pp. 1948- 1958, 2005.

[CAM 07] Campilho, R.D.S.G., de Moura, M.F.S.F., Domingues, J.J.M.S., Stress and failure analyses of scarf repaired CFRP laminates using a cohesive damage model. Journal of Adhesion Science and Technology, Vol. 21, pp. 855- 970, 2007.

[CAR 07] Carlberger, T. and U. Stigh, An explicit FE model of impact fracture in an adhesive joint. Engineering Fracture Mechanics, Vol. 74, pp. 2247-2262, 2007.

[CAS 05] de Castro San Roman Julia, PhD Thesis: Experiments on Epoxy, Polyurethane and ADP Adhesives, 2005.

[CHA 92] Charalambides, M., Kinloch, A.I., Wang, Y., Williams, J.G., On the analysis of mixed mode failure, International Journal of Fracture, Vol. 54, pp. 269- 291, 1992.

[CHA 96] Chai, H. and M.Y.M. Chiang, A crack propagation criterion based on local shear strain in adhesive bonds subjected to shear. Journal of the Mechanics and Physics of Solids, 44(10), pp. 1669-1689, 1996.

[CHA 98] Chai, H. and M.Y.M. Chiang, Finite element analysis of interfacial crack propagation based on local shear, part II--Fracture. International Journal of Solids and Structures, 35(9-10), pp. 815-819, 1998.

[CHA 02] Chandra, N., Li, H., Shet, C., Ghonem, R., Some issues in the application of cohesive zone models for metal-ceramic interfaces. International Journal of Solids and Structures, Vol. 39, pp. 2827-2855, 2002.

[CHA 04] Chai Herzl, The effects of bon thickness, rate and temperature on the deformation and fracture of structural adhesives under shear loading, International Journal of Fracture, Vol. 130, pp. 497-515, 2004.

[CHA 14] Chapman Gilbert B., Nondestructive Evaluation of Adhesive Bonds Using 20 MHz and 25 Khz Ultrasonic Frequencies on Metal and Polymer Assemblies, 2014.

[CHE 87] Chern C.S., Phoehlein G.W., A kinetic model for curing reactions of epoxides with amines. Polymer Engineering and Science, Vol. 27, pp. 788-95, 1987.

[CHE 02] Chen, J., Predicting progressive delamination of stiffened fibre-composite panel and by decohesion models. Journal of Thermoplastic Composite Materials, Vol. 15, pp. 429-441, 2002.

[CHE 05] Cheuk, P.T., Tong, L., Rider, A.N., Wang, J., Analysis of energy release rate for fatigue cracked metal-to-metal double-lap shear joints. International Journal of Adhesion and Adhesives, Vol. 25, pp. 181- 191, 2005.

[CHE 11] Chen Z., Adams R.D., Lucas F.M. da Silva, Fracture toughness of bulk adhesives in

mode I and mode III and curing effect, Int. J. Fract., Vol. 167, pp. 221-234, 2011.

[CHI 92] Chiou P.L., Letton A., Polymer, Vol. 33, 3925, 1992.

[CH0 08] Choupani, N., Interfacial mixed-mode fracture characterization of adhesively bonded Joints, International Journal of Adhesion and Adhesives, Vol. 28, pp. 267-282, 2008.

[CLA 93] Clarke J.D., Mcgregor I.J., Ultimate tensile stress over a zone: a new failure criterion for adhesive joints, Journal of Adhesion, Vol. 42, pp. 227- 245, 1993.

[COG 00] Cognard J., Sciences et Technologie du collage, Presses polytechniques et universitaires romande, 2000.

[COG 05] Cognard J.Y., Davies P., Gineste B. and Sohier L., Development of an improved adhesive test method for composite assembly design. Composite Science and Technology, 65: 359-68, 2005.

[COG 06] Cognard J.Y., Davies P., Sohier L., Créac'hcadec R., A study of the non-linear behavior of adhesively-bonded composite assemblies. Composite Structures, Vol. 76, pp. 34–46, 2006.

[COG 08] Cognard J.Y., Numerical analysis of edge effects in adhesively-bonded assemblies application to the determination of the adhesive behavior. Computers & Structures, 86: 1704-1717, 2008.

[COG 10] Cognard J.Y., Créac'hcadec R., Sohier L., Leguillon D., Influence of the thickness on the behavior of bonded assemblies under shear loadings using a modified TAST fixture, International Journal of Adhesion and Adhesives, Issue 30, pp. 257-266.

[COL 91] Cole K.C., Hechler J.J., Noel D., Macromolecules, Vol. 24, 3098, 1991.

[COM] Comyn J., Adams R.D., What are adhesives and sealant and how do they work?, Adhesive Bonding-Science Technology and applications, Woodhead Publishing Limited.

[CRE 08a] Créac'hcadec R., PhD Thesis: Analyse et modélisation du comportement non-linéaire d'assemblages collés pour application marine, Laboratoire Brestois de Mécanique et des Systèmes, Université de Bretagne Occidentale, 2008.

[CRE 08b] R. Créac'hcadec, J. Y. Cognard, Th. Heuzé. On Modelling the Non-linear Behavior of Thin Adhesive Films in Bonded Assemblies With Interface Elements. Journal of Adhesion Science and Technology 22: 1541–1563, 2008.

[CRE 15] Créac'hcadec R., Sohier L., Cellard C., Gineste B., An Arcan Tensile Compression Shear Test reducing the edge effects suited for the determination of the Load-Displacement Behavior of Adhesives in Bonded Assemblies, submitted to International Journal of Adhesion and Adhesives.

[CRO 89] Crocombe, A.D., Global yielding as a failure criteria for bonded joints. International Journal of Adhesion and Adhesives 9: 145- 153, 1989.

[CRO 97] Crocombe A.D., Durability modelling concepts and tools for the cohesive environmental degraation of bonded structure, Int. J. Adhesion and Adhesives,

Vol. 17, pp. 229-238, 1997.

[DAG 96] Daghyani, H.R., L. Ye, and Y.W. Mai, Effect of thermal residual stress on the crack path in adhesively bonded joints. J. Mat. Sci., 31(10), pp. 2523-2529, 1996.

[DAR 02] Darque-Ceretti E., Felder E., Adhésion et Adhérence, Sciences et techniques de l'ingénieur, CNRS Editions, 2002.

[DAS 01] Da Silva, F. M. Lucas, Adams, R. D. The Strength of Adhesively Bonded T-Joints. Proc. 6th Int. Conference on Structural Adhesives in Engineering, Bristol, UK, 2001.

[DAS 04] Da Silva, F. M. Lucas, Adams, R. D., Gibbs L., Int. J. Adhes. Adhes., Vol. 24, pp. 69-83, 2004.

[DAS 05] Da Silva, F. M. Lucas, Adams, R. D., Measurement of the mechanical properties of structural adhesives in tension and shear over a wide range of temperatures, J. Adhesion Sci. Technol., Vol. 19, No. 2, pp. 109-141, 2005.

[DAS 09] da Silva, L.F.M., Carbas, R.I.C., Critchlow, G.W., Figueiredo, M.A.V., Brown, K., Effect of material, geometry, surface treatment and environment on the shear strength of single lap joints. International Journal of Adhesion and Adhesives, pp. 29- 32, 2009.

[DAS 12] Lucas F. M. da Silva, David A. Dillard, Bamber Blackman, Robert D. Adams, Testing Adhesive Joints, Best Practises, Wiley, 2012.

[DAV 89] Davies R. J., Kinloch A. J., in Adhesion ed. K. W. Allen, Elsevier Applied Science, 1989.

[DEA 78] Dearlove T.J., Ulicny J.C., Diluted epoxy adhesives ii: Relationship of shrinkage during cure to lap shear strengths, J. Appl. Poly. Sci., Vol. 22, pp. 2523-2532, 1978.

[DEA 96] Dean G.D, Duncan B.C., Adams R.D., Thomas R., Vaughn L., Comparison of bulk and joint specimen tests for determining the shear properties of adhesives, NPL Report CMMT(B)51, National Physical Laboratory, Teddington, 1996.

[DEB 51] De Bruyne A., Adhesion and Adhesives, De Bruyne N.A. and Houwink R. ed., Elsevier, Amsterdam, The Netherlands, pp. 92, 1951.

[DER 48] Deryagin B.V., Krotova N.A., Doklady, Vol. 61, p. 849, 1948

[DIB 87] Dibenedetto A. T., Prediction of the glass transition temperature of polymers: A model based on the principal of corresponding states, J. Polym. Sci. Part: B Polym. Phys., 1987.

[DIL 09] Dillard, D.A., Singh, H.K., Pohlit, D.J., Observations of decreased fracture toughness for mixed mode fracture testing of adhesively bonded joints. Journal of Adhesion Science and Technology, Vol. 23, pp. 515- 1530, 2009.

[DIN 91] Ding J., Chen C., Xue C., J. Appl. Polymer Sci, Vol. 42, 1459, 1991.

[DOL 82] Dolev G., Ishai O., Mechanical characterization of Adhesive Layer in-situ and as bulk material, J. Adhesion, Vol. 12, pp. 283-294, 1982.

[DUN 03] B. Duncan, G. Dean. Measurements and models for design with modern adhesives. International Journal of Adhesion & Adhesives, 23: 141-149, 2003.

[DUS 87] Dusi M. R., Lee, W. I., Ciriscioli, P. R., and Springer, G. S. Cure kinetics and viscosity of fiberite 976 resin. *J. Comp. Mater. 21*, 243–261, 1987.

[DUS 88] Dusek K., MacKnight W.J., Cross-Linked Polymers, , eds. R.A. Dickie, S.S. Labana, R.S. Bauer, Chapter 1, American Chemical Society, Washington D.C., p.2, 1988.

[EDW 73] Edwards S.F., Grant J.W.V., The Effect of Etanglements on the Viscosity of a Polymer Melt, Journal of Physics A-Mathematical & General, Vol. 6, pp. 1186-1195, 1973.

[ELI 02] Elices, M., G.V. Guinea, J. Gomez, and J. Planas, The cohesive zone model: advantages, limitations and challanges. Engineering Fracture Mechanics, Vol. 69, pp. 137-163, 2002.

[END 95] Endlich W., Fertigungstechnik mit Kleb- und Dichtstoffen: Praxishandbuch der Kleb- und Dichtstoffverarbeitung, Braunschweig: Vieweg, 1995.

[ENN 83] Enns J.B., Gillham J.K., Effect of the Extent of Cure on the Modulus, Glass Transition, Water Absorption; Density of an Amine-Cure Epoxy, Journal of Applied Polymer Science, Vol. 28, p. 2831, 1983.

[EYR 83] Eyring, H. Viscosity, plasticity, and diffusion as examples of absolute reaction rates. J. Chem. Phys., 4, 283–295, 1963.

[FIN 76] Findley, W.N., Lai, J.S., Onaran, K. (1976). Creep and Relaxation of Nonlinear Viscoelastic Materials: With an Introduction to Linear Viscoelasticity. In Kanninen, M.F., editor, Applied Mathematics and Mechanics, volume 18. North-Holland, Amsterdam.

[GIN 93] B. Gineste, PhD Thesis: Assemblages de structures en matériaux composites par stratification d'un élément de liaison caractérisation de l'endommagement, Nantes, 1993.

[GIL 74] Gillham J.K., Benci J.A., Isothermal Transitions of a Thermosetting System, Journal of Applied Polymer Science, Vol. 18, 1974.

[GOL 44] Goland M., Reissner E., The stresses in Cemented Joints, Journal of Applied Mechanics, Vol. 11, pp. A17-A27, 1944.

[GOL 97] Golestanian, H. and A. Sherif El-Gizawy, Cure dependent lamina stiffness matrices of resin transfer molded composite parts with woven fiber mats. Journal of Composite Materials, 31(23): p. 2402, 1997.

[GOV 00] Govaert, L.E., de Vries, P.J., Fennis, P.J., Nijenhuis, W.F., Keustermans, J.P., Influence of strain rate, temperature and humidity on the tensile yield behavior of aliphatic polyketone. Polymer, 41, 1959–1962, 2000.

[GRA 09] Grant L.D.R., Adams R.D., Lucas F.M. da Silva, Effect of the temperature on the strength of adhesively bonded single lap and T joints for the automotive industry, Int. J. Adhes. Adhes., Vol. 29, pp. 535-542, 2009.

[GRI 20] Griffith A.A., The phenomenon of rupture and flow in solids, Philosophical transactions of the Royal Society, Vol. A221, pp. 163-98, 1920.

[GR0 07] Grohs J.W., PhD Thesis: Comparing in situ and bulk constitutive properties of a structural adhesive, 2007.

[GUE 95] Guess T.R., Reedy E.D. Jr, Yield strength and stress relaxation data for an adhesive used in butt joint tests, proceedings of the 27th International SAMPE Technical Conference October 9-12, Albuquerque, 1995.

[HAH 03] Hahn O., Jendrny J., Evaluation of simulation models for the estimation of deformation of adhesively bonded steel sheets during curing. Weld World 47(7–8):31–38, 2003.

[HAI 88] Haight R., White R.C., Silverman B.D., Ho P.S., Complex Formation and Growth at the Cr- and Cu-Polyimide Interface, Journal of Vacuum Science & Technology, Vol. 6, pp. 2188-2199, 1988.

[HAM 89] Hamoush, S.A. and S.H. Ahmad, Fracture energy release rate of adhesive joints. Int. J. Adhesion and Adhesives, 9(3), pp. 171-178, 1989.

[HAR 73] Hart-Smith L.J., Adhesive-bonded double-lap joints, NASA CR-112235, National Aeronautics and Space Administration, 1973.

[HAR 74] Hart-Smith, L.J., *Analysis and design of advanced composite bonded joints*. 1974, NASA.

[HAR 84] Harris, J.A. and R.D. Adams, Strength prediction of bonded single lap joints by non-linear finite element methods. Int. J. Adhesion and Adhesives, Vol. 4 pp. 65-78, 1984.

[HAW 68] Haward, R. Thackray, G. The use of a mathematical model to describe isothermal stress-strain curves in glassy thermoplastics. Proc. Roy. Soc. A, 302, 453–472, 1968.

[HER 10] Ehrhart B., Valeske B., Muller C.E., Bockenheimer C., Methods for the Quality Assessment of Adhesively Bonded CFRP Structures – A Resumé, 2nd International Symposium on NDT in Aerospace 2010 – We.5.B.2, 2010.

[HIL 94] Hildebrand M., The strength of adhesive bonded joints between fibre-reinforced plastics and metals. Espoo, Technical Research Center of Finland, 1994.

[HIL 95] Hill R. R., Mazumdar J. S. V., Lee L. J., Analysis of volumetric changes of unsaturated polyester resins during curing. *Polym. Engr. Sci. 35*, Vol. 10, 852–859, 1995.

[HO 85] Ho P.S., Hahn P.O., Bartha J.W., Rubloff G.W., LeGoues F.K., Silverman B.D., Chemical Bonding and Reaction at Metal/Polymer Interfaces, Journal of Vacuum Science & Technology, Vol. 3, pp. 739-745, 1985.

[HOJ 04] Hojjati M., Johnston A., Hoa S. V., and Denault J., Viscoelastic behavior of cytec, fm73 adhesive during cure. *J. Appl. Poly. Sci. 91*, 2548–2557, 2004.

[HOR 70] Horie K., Hiura H., Sawada M., Mita I., Kambe H., Calorimetric investigation of

polymerization reactions. III. Curing reaction of epoxides with amines, Journal of Polymer Science: part A-1, Vol. 8, pp. 1357-1372, 1970.

[HOR 90] Horn R.G., Smith D.T., Measuring surface forces to explore surface chemistry: Mica, sapphire and silica, Journal of Non-Crystalline Solids, Vol. 120, pp. 72-81, 1990.

[HOR 92] Horn R.G., Smith D.T., Contact Electrification and Adhesion Between Dissimilar Materials, Science, Vol. 256, pp. 362-364, 1992.

[HOS 10] Hossain M., PhD Thesis: Modelling and Computation of Polymer Curing, 2010.

[HUA 96] Huang Y. J., Liang C. M., Volume shrinkage characteristics in the cure of low-shrink unsaturated polyster resins. *Polymer 37*, Vol. 3, pp. 401–412, 1996.

[HUA 00] Huang, X., J.W. Gillespie, Jr., and T. Bogetti, Process induced stress for woven fabric thick section composite structures. Composite Structures, 49(3): p. 303, 2000.

[HUR 83] Hurwitz F.I., Polymer Compos., Vol. 4, 89, 1983.

[IMA 03] Imanaka, M., Y. Nakamura, A. Nishimura, and T. Iida, Fracture toughness of rubber modified epoxy adhesives: effect of plastic deformability of the matrix phase. Composites Science and Technology, Vol. 63, pp. 41-51, 2003.

[INSTRON] www.instron.com, POD_V-NotchSeries_rev1_0513.

[IRW 57] Irwin G.R., Analysis of stresses an strains near the end of a crack traversing a plate, J. Appl. Mech., Vol. 24, pp. 361-364, 1957.

[ISO 05] ISO 9000-2005 : Quality management systems – Fundamentals and vocabulary, 2005.

[ISO 09] ISO 9004-2009: Quality management systems – Managing for the sustained success of an organization, 2009.

[ISO 11003-2] ISO 11003-2: 1993 (E), Adhesives – Determination of shear behavior of structural bonds, Part 2: Thick-adherend tensile-test method, 1993.

[JAR 06] Jarry E., Shenoi R.A., Performance of butt strap joints for marine applicatios, Int. J. Adhesion and Adhesives, Vol. 26, pp. 162-176, 2006.

[JEA 85] Jeandreau J.P., Grolade D., Méthodes de calculs des assemblages collés, Colloquium on Tendances actuelles en calcul des structures, DRET à Bastia 6-7 novembre, France, pp 873-890, 1985.

[JEA 06] Jeandreau J.P., Guide du collage, CETIM, France, 2006.

[JEN 04] Jendrny J., Entwicklung von Berechnungsmodellen zur Abschätzung der Verformung geklebter dünnwandiger Stahlbauteile in Leichtbaukonstruktionen während der Warmaushärtung, 2004.

[JOA 07] Joannes S., PhD Thesis: Caractérisation numérique et outil d'aide au dimensionnement des collages structuraux, Centre des Matériaux, 2007.

[JOH 91] John, S.J., Kinloch, A.I., Matthews, F.L., Measuring and predicting the durability of bonded fibre/ epoxy composite joints. Composites, Vol. 22, pp. 121-127, 1991.

[JOH 92] St John N.A., George G.A., Cure Kinetics and Mechanisms of a Tetraglycidyl – 4,4' – diamindiphenylmethane / diaminodiphenylsulphone Epoxy Resin Using Near I.R. Spectroscopy, Polymer, Vol. 33, 2679, 1992.

[JOH 01] Johnston, A., R. Vaziri, and A. Poursartip, A plane strain model for process-induced deformation of laminated composite structures. Journal of Composite Materials, 35(16): p. 1435, 2001.

[JOU 08] Jousset, P., Rachik, M., and Koch, S., "Konstitutive Modelle beschreibend die Plastizität", Adhäsion, 03.2008.

[JOU 10] Jousset P., Rachik M., Pressure-Dependent Plasticity for Structural Adhesive. Journal of Adhesion Science and Technology, Vol. 24, pp. 1995-2010, 2010.

[KAM 73] Kamal M.R., Sourour S., Kinetics and thermal characterization of thermoset cure, Polymer Engineering and Science, Vol. 13, pp. 59-64, No. 1, 1973.

[KAM 76] Kamal M.R., Sourour S., Differential scanning calorimetry of epoxy cure: isothermal cure kinetics, Thermochim. Acta, Vol. 14, pp. 41-59, 1976.

[KAN] KANG S.G., KIM M.G., KIM C.G., P66 Evaluation of cryogenic performance of adhesive using composite-aluminium double lap joints, Korea Advanced Institute of Science and Technology.

[KAW 08] L.F. Kawashita, A.J. Kinloch, D.R. Moore, J.G. Williams. The influence of bond line thickness and peel arm thickness on adhesive fracture toughness of rubber toughened epoxy–aluminium alloy laminates. International Journal of Adhesion and Adhesives, 28: 199-210, 2008.

[KIM 96] Kim Y.K. and S.R. White, "Stress Relaxation Behavior of 3501-6 Epoxy Resin During Cure" Polymer Engineering and Science, Vol. 36, No. 23, pp. 2852-2862, 1996
.

[KIM 97] Kim Y.K. and S.R. White, "Process-Induced Stress Relaxation Analysis of AS4/3501-6 Laminate" Journal of Reinforced Plastics and Composites, Vol. 16, No.1, pp. 2-16, 1997.

[KIM 98] Kim S., Lu M., Shim M., Polymer Journal, Vol. 30, No. 2, pp. 90-94, 1998.

[KIN 81] Kinloch A.J., Smart N.R., J. Adhes., Vol. 12, pp. 23-35, 1981.

[KIN 83] Kinloch A.J., Young R.J., Fracture Behavior of Polymer, Applied Science Publishers, London, New York, 1983.

[KIN 87] Kinloch A.J., Adhesion and Adhesives-Science and Technology, Chapman and Hall, 1987.

[KIN 97] Kinloch A.J., Adhesives in engineering, Proceedings of the Institution of Mechanical Engineers – Part G, Journal of Aerospace Engineering, Vol. 211, pp. 307-335, 1997.

[KIN 04] Kinloch A. J., Korenberg C. F., Tan K. T. The durability of structural adhesive joints. Proc. 7th European Adhesion Conference, Freiburg,, Germany, 2004.

[KLE 79] Klein J., The Self-diffusion of Polymers, Contemporary Physics, Vol. 20, pp. 611-629, 1979.

[KNA 91] Knauder E., Kubla C., Poll D., Kunstoffe German Plastics, Vol. 81, 39, 1991.

[KNI 97] Knipe R., Advanced Materials and Processes, 1997.

[KON 12] Kontantinos Anyfantis, PhD thesis: Analysis and Design of Composite-to Metal Adhesively Bonded Joints, 2012.

[LAN 87] Lane J.W., Khattacj R.K., in SPE ANTEC Technical Papers, Vol. 33, 982, 1987.

[LAS 10] La Saponara V., Sugita Y., Winkelmann C., Environmental and chemical degradation of carbon/epoxy lap joints for aerospace applications, and effects on their mechanical performance, Composites Science and Technology, Vol. 70, pp. 829-839, 2010.

[LEE 82] Lee W.I., Springer G.S., Heat of reaction, degree of cure, and viscosity of hercules 3501-5 resin. *J. Comp. Mater. 16*, 510–520, 1982.

[LEE 92] Lee, S.J., Lee, D.G., 1992. Development of a failure model for the adhesively bonded tubular, single lap joint. Journal of Adhesion, Vol. 40, pp 1-14.

[LEE 00] Lee J.Y., Choi H.K., Shim M.J., Kim S.W., Kinetics studies of an epoxy cure reaction by isothermal DSC analysis, Thermochim Acta, 343 (1-2), pp. 111-117, 2000.

[LEM 00] J. Lemaître, J.L. Chaboche. Mechanics of Solid Materials. Cambridge University Press, 2000.

[LEV 77] Levi D.W., J. Appl. Polym. Sci., Vol. 32, pp. 189-199, 1977.

[LIE 11] Liebl C., Johlitz M., Yagimli B., Lion A., Simulation of curing- induced viscoplastic deformation: a new approach considering chemo-thermomechanical coupling. Arch Appl Mech, 2011.

[LIE 12] Liebl C., Johlitz M., Yagimli B., Lion A., Three-dimensional chemo-thermomechanically coupled simulation of curing adhesives including viscoplasticity and chemical shrinkage, Comput. Mech., Vol. 49, pp. 603-615, 2012.

[LIL 05] Liljedahl C. D. M., Crocombe A. D., Abdel Wahab M. M., Ashcroft I. A., The effect of residual strains on the progressive damage modelling of environmentally degraded adhesive joints, J. Adhesion Sci. Technol., Vol. 19, No. 7, pp. 525–547, 2005.

[LOC 95] Loctite. Worldwide Design Handbook. 2nd edition, Erasmusdruck Gmbh, Germany, 1995.

[MAC 25] Mac Bain J.W., Hopkins D.G., J. Phys. Chem., pp. 29-188, 1925.

[MAC 70] MacCallum J.R., Tanner J., in Nature, Vol. 225, 1127, 1970.

[MAH 05] Mahnken R., Schlimmer M., Simulation of strength difference in elasto-plasticity for adhesive materials. Int. J. Numer. Meth. Eng, 63:1461–1477, 2005.

[MAL 09] I. Malvade, A. Deb, P. Biswas, A. Kumar. Numerical prediction of load-

displacement behaviors of adhesively bonded joints at different extension rates and temperatures. Computational Materials Science, 44: 1208-1217, 2009.

[MAL 89] Malkin A. Ya, Kulichikin S.G., in Advanced Polymer Science, Vol. 101, 218, 1989.

[MAR 10] Martin P.M., Handbook of Deposition Technologies for Films and Coatings: Science, Applications and Technology, Third Edition, Elsevier, 2010.

[MAU 12] Maurice J., PhD Thesis: Characterization and modeling of the 3D elastic-plastic behavior of structural adhesive films for aeronautical applications, 2012.

[MAU 13] J. Maurice, J.Y Cognard, R. Creac'hcadec, P. Davies, L. Sohier, S. Mahdi. Characterization and modelling of the 3D elastic-plastic behavior of an adhesively bonded joint under monotonic tension/compression-shear loads: influence of three cure cycles. J Adhes Sci Technol., 27:1-25, 2013.

[MEN 99] Menard K.P., Dynamic Mechanical Analysis, CRC Press, Boca Raton, 1999.

[MES 04] Messler R.W. Jr., Joining of Materials and Structures: From Pragmatic Process to Enabling Technology, Elsevier/Butterworth-Heinemann, 2004.

[MIC 87] Michalske T., Bunker B., Steric Effects in Stress Corrosion Fracture of Glass, Journal of the American Ceramic Society, Vol. 70, pp. 780-784, 1987.

[MIC 93] Michalske T.A., Bunker B.C., A Molecular Mechanism for Stress Corrosion in Vitreous Silica, Journal of the American Ceramic Society, Vol. 66, pp.284-288, 1993.

[MIC 05] PhD-Thesis: Michaloudaki M., An approach to Quality Assurance of Structural Adhesive Joints, 2005.

[MOR 02] Mortensen F., Thomsen O.T., Analysis of adhesive bonded joints: a unified approach, Compos. Sci. Technol., Vol. 62, pp. 1011-1031, 2002.

[MOU 11] Moussa O., PhD Thesis: Thermophysical and Thermomechanical Behavior of Cold-Curing Structural Adhesives in Bridge Contruction, 2011.

[NAD 31] Nadai A., Plasticity: a mechanics of the plastic state of matter, New York: McGraw-Hill, 1931.

[NOU 89] Nouaihlas D., Unified modelling of cyclic viscoplasticity: application to austenitic stainless steels, International Journal of Plasticity 1989 ; 5 : 501-520.

[OBR 01] O'Brien E.P., Mather P.T., White S.R., Viscoelastic properties of an epoxy resin during cure, J. Composites Materials 35, Vol. 10, pp. 883-903, 2001.

[OBR 03] O'Brien, E.P., Ward, T.E., Guo, S., Dillard, D.A., 2003. Strain energy release rates of a pressure sensitive adhesive measured by the shaft-loaded blister test. Journal of Adhesion, Vol. 79, pp. 69-97, 2003.

[OCH 11] Öchsner A., Special Numerical Techniques in Handbook of Adhesion Technology, Ed. By L.F.M. da Silva, Öchsner A., Adams R.D., 2011.

[ODQ 74] Odqvist F.K.G., Mathematical theory of creep and creep rupture, The ClarendonPress, Oxford, 1974.

[PAC 83] Packham D.E., Adhesion Aspects of Polymeric Coatings, Ed. K. L. Mittal, 1983.

[PAC 05] Packham D.E., Handbook of adhesion, Second. Edition. Hoboken N.J.: John Wiley, 2005.

[PAS 90] Pascault J.P., Williams R.J.J., Relationships between glass transition temperature and conversion – analyses of limiting cases, Polym. Bull., Vol. 24, pp. 115-121, 1990.

[PET 00] Petrie E., Handbook of adhesives and sealants, Second. Edition. New York: McGraw-Hill, 2000.

[PET 07] Petrie E., Handbook of adhesives and sealants, Second. Edition. New York: McGraw-Hill, 2007.

[PIZ 03] Pizzi A., Handbook of adhesive technology, Second. Edition. New York: M. Dekker, 2003.

[PLE 90] Plepys A.R., Farris R.J., Evolution of residual stresses in three-dimensionally constrained epoxy resins, Polymer, Vol. 31, pp. 1932-1936, 1990.

[PLU 91] Plueddemann E.P., Adhesion through Silane Coupling Agents, Fundamentals of Adhesion, Plenum Press, New York, Vol. 2, pp. 79-151, 1991.

[POL 90] Politi R.E., Structural Adhesives in the Aerospace Industry, Handbook of Adhesives, pp. 713-728, 1990.

[POS 88] Possart W., Experimental and Theoretical Description of the Electrostatic Component of Adhesion and Adhesives, Vol. 8, pp. 77-83, 1988.

[PRA 04] Pradyot P., Deans' analytical chemical handbook: Thermal Analysis, chapter 15. USA: New York, The McGraw-Hill Companing, 2004.

[PUJ 07] Pujol S., Johnson M.S., Warrior N.A., Kendall K.N., Hill D.J., The effects of processing parameters on reactive epoxy adhesives, 16^{TH} international conference on composite materials, 2007.

[RAB 37] Rabinowitch E., Luget A., Wilson R., Thermochim. Acta 238, 295, 1937.

[REY 85] Reynolds O., On the dilatancy of media composed of rigid particles in contact, Phil. Mag., 5(20):469, 1885.

[RIC 68] Rice, J.R., Rosengren, G.F., 1968. Plane strain deformation near a crack tip in a powerlaw hardening material. Journal of the Mechanics and Physics of Solids, Vol. 16, pp. 1-12, 1968.

[RIC 84] Riccardi C.C., Adabbo H.E., Williams R.L.L., in Journal of Applied Polymer Science, Vol. 29, 2481, 1984.

[RIT 98] Ritter J.E., Fox J.R., Hutko D.I., Larner T.J., Moisture Assisted Crack Grow at Epoxy-Glass Interfaces, Journal of Materials Science, Vol. 33, pp. 4581-4588, 1998.

[ROB 77a] Roberts A.D., J. Phys., 10:1801, 1977.

[ROB 77b] Roberts A.D., Adhesion, 1:207, London, 1977.

[ROC 02] Roche A.A., Collage des matériaux, in Formation INSA CAST, p. 2., 2002.

[ROD 10] Rodriguez René Q., Paiva William P., Sollero Paulo, Albuquerque Eder L., Rodrigues Marcelo B., Analytical and numerical tools for bonded joint analysis, Mecanica Computacional Vol XXIX, pp. 7557-7569, 2010.

[ROL 08] R. Rolfes, M.volger, G. Ernst, C. Hühne. Strength of Textile Composites in Multiscale Simulation, in Trends. In Computational Structures Technology, Saxe-Coburg Publications, Stirlingshire, Scotland, chap. 7, pp. 151-171, 2008.

[RUI 05] Ruiz E., Trochu F., Thermomechanical properties during cure of glass-polyester rtm composites: Elastic and viscoelastic modeling. *J. Compos. Mater. 39*, Vol. 10, 2005.

[RYA 73] Ryan M.E., M. Eng. Thesis, McGill University, Montreal Canada, 1973.

[RYA 84] Ryan M.E., Polymer Engineering and Science, Vol. 24, No. 9, pp. 698-704, 1984.

[SAK 14] Sakuma T., Sakamoto S., Otsuru T., Computational Simulation in Architectural and Environmental Acoustics, 2014.

[SEI 05] Seifi R., and Hojjati, M., Heat of reaction, cure kinetics, and viscosity of araldite ly-556 resin, *J. Comp. Mater. 39*, Vol. 11, 1027–1039, 2005.

[SCH 69] K. A. SCHAPERY On the characterization of nonlinear viscoelastic materials. Pol. Eng. Sci., 9, 295–310, 1969.

[SCH 90] Schmueser D.W., J. Eng. Mater. Technol., Vol. 112, p. 321, 1990

[SHA 64] Sharpe L.H., Schonhorn H., Surface energetics and adhesive joints, in Fowkes F.M. (ed.), Contact Angle, Wettability and Adhesion, Washington, American Chemical Society, 189, Advances in Chemistry Series, p. 43, 1964.

[SHU 85] Shulka R.K., Mencinger N.P., Solid State Technology, pp. 67-74, 1985.

[SKE 90] Skeist I., Handbook of Adhesives, Third Edition, Elsevier, 1990.

[SIM 93] Simon S.L., Gillham J.K., in Journal of Applied Polymer Science, Vol. 47, 461, 1993.

[SIM 00] Simon S.L., G.B. McKenna, and O. Sindt, “Modeling the Evolution of the Dynamic Mechanical Properties of a Commercial Epoxy During Cure after Gelation” Journal of Applied Polymer Science, Vol. 76, pp. 495-508, 2000.

[SIN 06] Sina Ebnesajjad, Cyrus F. Ebnesajjd, Surface Treatments of Materials for Adhesion. William Andrew Publishing, Vol. 0, Issue 8155, 2006.

[SIC] Sichina W.J., Characterization of Epoxy Resins Using DSC, Perkin Elmer Instruments.

[SIR 96] Sircar A.K., Galaska M.L., Rodrigues S., Chartoff R.P., Proc. Amer. Chem. Soc., Rubb. Div. Conf., Vol. 150, 11, 1996.

[SNO 02] Snodgrass J.M., Pantelidis D., Jenkis M.L., Bravman J.C., Dauskardt R.H., Subcritical

Debonding of Polymer/Silica Interfaces Under Monotonic and Cyclic Loading, Acta Materiala, Vol. 50, pp. 2395-2411, 2002.

[SOR 03] Sorensen, B.F., Jacobsen, T.K., Determination of cohesive laws by the J integral approach, Engineering Fracture Mechanics, Vol. 70, pp. 1841- 1858, 2003.

[SUN 02] Sun L., Pang S., Sterling A., Negulescu I., Stubblefield M., Thermal analysis of curing process of Epoxy Prepreg, J Appl Polym Sci, Vol. 83, No. 5, pp. 1074-1083, 2002.

[TAS 09] Surface Treatment, The Adhesive and Sealant Council, 2009.

[THE 13] Thevenet D., Créac'hcadec R., Sohier L., Cognard J.Y., Experimental analysis of the behavior of adhesively bonded joints under tensile/compression-shear cyclic loadings, Int. J. Adhes. Adhes., Vol. 44, pp. 15-25, 2013.

[TSA 98] Tsai M.Y., Oplinger D.W., Morton J., An improved theoretical solutions for adhesive lap joints, International Journal of Solids and Structures, Vol. 35, pp. 1163-1185.

[TVE 92] Tvergaard, V., Hutchinson, J.W., The relation between crack growth resistance and fracture process parameters in elastic-plastic solids. Journal of the Mechanics and Physics of Solids, Vol. 40, pp. 1377- 1397, 1992.

[TVE 93] Tvergaard, V., Hutchinson, J.W., The influence of plasticity on the mixed-mode interface toughness. Journal of the Mechanics and Physics of Solids, Vol. 41, pp. 1119- 1135, 1993.

[VAB 08] Vable M., Stress Analysis of Bonded Joints by Boundary Element Method, Modeling of Adhesively Bonded Joints, Ed. By L.F.M. da Silva, Ochsner A., 2008.

[VAL 05] Valery L., Zvetkov, Thermochim. Acta 435, pp. 71, 2005.

[VEN 97] Venditti R.A., Gillham J.K., A relationship between the glass transition temperature and fractional conversion in thermosetting systems, J. App. Polym. Sci., Vol. 64, pp. 3-14, 1997.

[VOL 38] Volkersen O., Die Niektraftverteiling in Zugbeanspruchten mit Konstanten Laschrnquerschritten, Luftfahrtforschung 15, pp. 41-47, 1938.

[VOY 63] Voyutskii S.S., Adhesion of High Polymers, Autohesion and Adhesion of High Polymers, Interscience, Vol. 5, pp. 140-149, New York, 1963.

[WAG 11] Wagner W., High-Strength Glass Bonding – a New Era in Façade Design, Glass Performance Days Finland, 2011.

[WAN 93a] Wang X., Gillham J.K., Physical Aging in the Glassy State of a Thermosetting System vs. Extent of Cure, Journal of Applied Polymer Science, Vol. 47, p. 447, 1993.

[WAN 93b] Wang X., Gillham J.K., Tg-Temperature Property (TgTP) Diagram for Thermosetting Systems: Anormalous Behavior of Physical Properties vs. Extent of Cure, Journal of Applied Polymer Science, Vol. 47, p. 425, 1993.

[WAN 00] C.H. Wang, P. Chalkley. Plastic yielding of a film adhesive under multiaxial stresses. International Journal of Adhesion & Adhesives, 20: 155-164, 2000.

[WAR 83] Ward, I.M., Mechanical Properties of Solid Polymers. John Wiley & Sons, Chichester, 1983.

[WEI 79] Weitsman Y., Residual thermal stresses dur to cool-down of epoxy resin composites, J. Appl. Mech., Vol. 46, pp. 563-567, 1979.

[WHI 97] White S.R. and A.B. Hartman, "Effect of Cure State on Stress Relaxation in 3501-6 Epoxy Resin" Journal of Engineering Materials and Technology, Vol. 119, pp. 262-265, 1997.

[WHI 02] White S.R., Mather P.T., Smith M.J., Polymer Engineering and Science, Vol. 42, No. 1, pp. 51-67, 2002.

[WIL 55] Williams M.L., Landel R.F., Ferry J.D., The Temperature Dependence of Relaxation Mechanisms in Amorphous Polymers and Other Glass-Forming Liquids, J. Am. Chem. Soc., Vol. 77, 3701, 1955.

[WIS 90] Wisanrakki G., Gillham J.K., Enns J.B., The Glass Transition Temperature (Tg) as a Parameter for Monitoring the Cure of an Amine/Epoxy System at Constant Heating Rates, Journal of Applied Polymer Science, Vol. 41, p. 1895, 1990.

[WIS 97] Wise C.W., Cook W.D., Goodwin A.A., in Polymer, Vol. 38, 3251, 1997.

[YAG 11] Yagimli B., Lion A., Experimental investigations and material modelling of curing processes under small deformations, ZAMM 91:342–359, 2011.

[YAN 91] Yang Y.S., Suspene L., in Polymer Engineering and Science, Vol. 31, 321, 1991.

[YAN 99] Yang, Q.D., Thouless, M.D., Ward, S.M., Numerical simulations of adhesively bonded beams failing with extensive plastic deformation. Journal of the Mechanics and Physics of Solids, Vol. 47, pp. 1337- 1353, 1999.

[YAN 00] Yang, Q.D., Thouless, M.D., Ward, S.M., Analysis of the symmetrical 90° peel test with extensive plastic deformation. Journal of Adhesion, Vol. 72, pp. 115- 132, 2000.

[YOU 97] Yousefi A., Lafleur PG., Gauvin R., Kinetic studies of thermoset cure reactions: a review. Polym Composite, Vol. 18, No. 2, pp. 157-168, 1997.

[YU 13] Yu H., Adams R.D., Lucas F.M. da Silva, Development of a dilatometer and measurement of the shrinkage behviour of adhesives during cure, International Journal of Adhesion and Adhesives, Vol. 47, pp. 26-34, 2013.

[ZAR 03] Zarrelli M., PhD Thesis: Cured Induced Property Changes and Warpage in Thermoset Resins and Composites, 2003.

CHAPTER 2:

EXPERIMENTAL INVESTIGATION AND FINITE ELEMENT MODELLING OF THE CURING BEHAVIOR OF THE ADHESIVE HYSOL EA-9321

Résumé

Ce chapitre a pour objet de caractériser le comportement physico-chimique d'un adhésif dans un assemblage au cours du procédé de cuisson. Dans un premier temps, la cinétique de la réaction réticulation de l'adhésif époxy Hysol EA-9321, utilisé sur la structure SYLDA, a été étudiée expérimentalement par analyse calorimétrique (DSC – Differential Scanning Calorimetry). L'étude de cette cinétique de réaction a eu pour finalité l'établissement d'un modèle cinétique permettant de prédire l'évolution du couple taux de polymérisation, température (α, T) quelque soit l'histoire thermique ou le chargement thermique appliqué. Un soin particulier a été apporté à la prise en compte des phénomènes diffusifs, responsables du ralentissement de la conversion d'origine chimique, dans l'établissement du modèle cinétique. Une deuxième étape a été consacrée au couplage de ce modèle cinétique avec l'équation de la chaleur afin de prédire l'évolution du taux de polymérisation et de la température de l'adhésif lors du procédé de cuisson. Ce couplage a été numériquement implémenté dans le code de calcul industriel Abaqus® par l'intermédiaire de subroutines et complété par une validation avec comparaison de mesures expérimentales.

Les travaux développés, ici, permettent d'aboutir à un outil numérique pour la modélisation du comportement thermochimique d'un adhésif dans un assemblage lors du procédé de cuisson.

Summary

This chapter is dedicated to the prediction of the curing behavior of an adhesive in a bonded assembly during curing process. At first, curing kinetics of the adhesive were experimentally investigated with DSC (Differential Scanning Calorimetry) analyses and the model associated to this reaction was developed. A special attention was given to the introduction of the diffusion effects in the kinetic model to take into account the lower reactivity of the system. Then, a finite element model in the software Abaqus® was developed to simulate the process of adhesive curing by taking into account a thermo-kinetic coupling. The applicability of the model was verified by comparing the predicted temperature profiles and curing profiles inside a cylindrical block of adhesive with experimental data. It has been shown that the predicted results were in good agreement with experimental data.

This work leads to the development of a numerical tool to predict the thermo-physical behavior of an adhesive in a bonded assembly during curing.

Contents

2.1. Introduction

Thermosetting resins, such as the adhesive used in this study, are well-founded in the aerospace, automotive and aircraft industries. In addition, composite materials are of great and still increasing industrial importance that makes the structural bonding, an assembly technique increasingly used.

Despite the advantages named for structural adhesives in the previous chapter, there is one major disadvantage in using them, particularly during the manufacturing process. During curing, the initially liquid adhesive is gradually transformed into a cross-linked polymer and builds up its final mechanical properties. Hence, the adhesive mechanical properties of the adhesive changes according to its curing state (i.e., its curing degree reached after the curing process) and are time- and temperature-dependent. Thus, thermo-physical aspects of the adhesive must be regarded to accurately predict the mechanical properties of the adhesive.

This chapter was dedicated to better understanding the effect of curing process on the physical state of the cold-curing epoxy adhesive used in this study (Hysol EA-9321 [HEN]).

On a first part, the variation of the physical properties of the adhesive was investigated by a DSC (Differential Scanning Calorimetry) analysis. This analysis gives an access to changes of curing degree with temperature and time for a wide-range of thermal loads applied. These ones are taken in accordance with the storage and operating conditions of the bonded structure studied in this study. Then, curing models were applied to describe properly the curing behavior of the adhesive.

A second part was dedicated to the introduction of the curing model in a Finite Element code to predict the curing behavior of an adhesive in a bonded assembly. An experimental set-up was realized.A comparison between experimental results and numerical data to verify the applicability of the model was carried on.

2.2. Material: Adhesive Hysol EA-9321

Hysol EA-9321 [HEN] is the cold-curing structural adhesive considered in this thesis. It is a thixotropic, bi-component adhesive from Henkel®. The base resin is a bisphenol-A-based epoxy (DGEBA) (Figure 57) with a DETA (diethylene triamine) hardener (Figure 58).

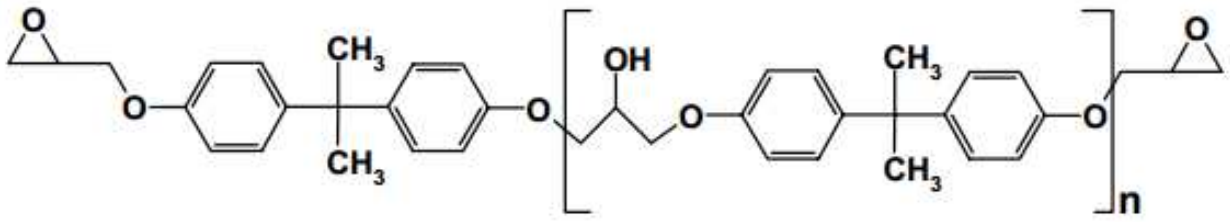

Figure 57. Chemical structure: DGEBA resin [JOA 07].

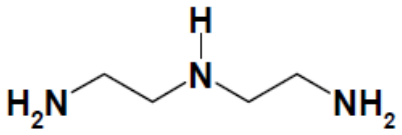

Figure 58. Chemical structure: DETA hardener [MAR 07].

The adhesive is prepared using a mixing ratio of 100:50 by weight of the respective constituents (resin and hardener). There are several ways to realize the adhesive preparation. The two components can be hand

mixed until a homogeneous blend. However, lot of heterogeneities [DAV 09] such as the presence of air bubbles [DAS 12] in the resulting compound are generated by this manual procedure. One alternative consists in speed mixing each constituent of the adhesive. For this purpose, the weighted components, i.e. resin and hardener, are placed in a container. Then, this last one is closed and mixed 3 minutes à 1600 rpm in a centrifugal mixer Speedmixer™ from FlackTeck Inc. (Landrum, SC) [SPE](Figure 59) .

Figure 59. Mixing of epoxy resin and hardener process [SPE].

The manufacturer recommends two curing cycles: 1 hour at 82°C and 5-7 days at 25°C. The first one is defined as the cycle for which the adhesive is fully cured. The second one is the thermal history corresponding to an achievement of normal performance for the adhesive. Table 6 lists the main mechanical/physical properties of the adhesive Hysol EA-9321 given by Henkel®.

Bulk Resin Properties – *tested using 3.18 mm castings per ASTM D-638*

Tensile Strength @ 25°C	49.00 MPa
Tensile Modulus @ 25°C	2.90 MPa
Elongation at Break @ 25°C	6 %
Shore D Hardness @ 25°C	84
Shear Modulus @ 25°C	1.55 GPa
Glass Transition Temperature	88°C

Bulk Resin Properties – *tested using 12.7 mm castings per ASTM D-695*

Compressive Strength@ 25°C - Yield	64.00 MPa
Compressive Strength@ 25°C - Ultimate	116.42 MPa

Bonded Strength Performance – *tested per ASTM D-1002*

Tensile Lap Shear Strength – Cured 7 days @ 25°C	27.60 MPa
Tensile Lap Shear Strength – Cured 1 hour @ 82°C	27.60 MPa

Table 6. Mechanical/Physical characteristics –Hysol EA-9321.

2.3. Experimental investigation of the curing kinetics

2.3.1. Differential Scanning Calorimetry (DSC) measurements

Curing kinetics analysis of the adhesive Hysol EA-9321 was realized with a heat-flux differential scanning calorimeter (DSC Perkin Elmer) connected to a thermal analyzer (Figure 60). This calorimeter is made of two steel pans. One of these is empty and is used as a reference for all scans. The other one contains sample. After mixing the hardener and resin in the same manner as explained previously, uncured adhesive samples weighting from 5 to 10 mg were placed in a hermetic pan. This one was enclosed with a lid and sealed with a manual press.

Figure 60. DSC Calorimeter Perkin Elmer DSC-7.

In Differential Scanning Calorimetry (DSC) analysis, there are two sign conventions: “exo-up” and “endo-up”. Depending on the sign convention, the exothermic or endothermic transitions are either positive or negative peaks in the thermogram. “Endo-up” corresponds to a positive exothermic transition whereas it is negative for “exo-up”. In this chapter, results are presented in convention “exo-up” for dynamic scans, respectively in convention “endo-up” for isothermal scans.

The conventional method [IVA 03][AZI 96]consists in studying the whole polymerization reaction. To that end, a first DSC investigation was performed on the uncured adhesive resulting from mixing, as described previously. Two subsequent dynamic scans at a heating rate of 20°C/min from 25°C to 250°C were realized on the prepared sample. The thermogram monitored by the DSC machine appears in Figure 61.

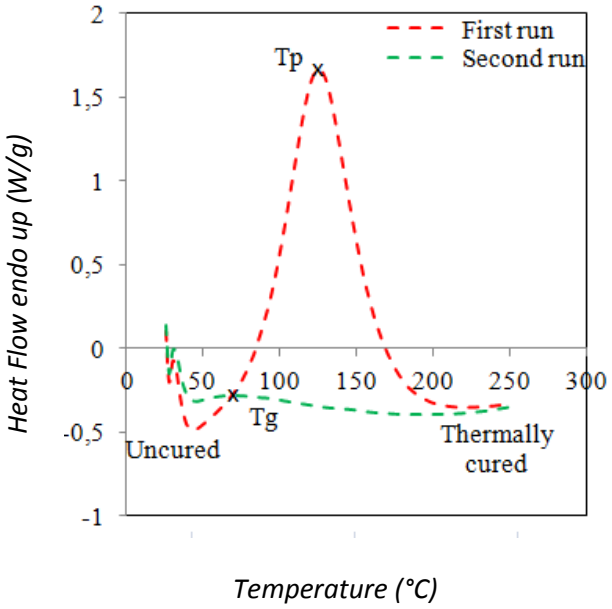

Figure 61. Subsequent dynamic DSC scans of the adhesive Hysol EA-9321.

The first dynamic scan shows a change of the heat flow monitored by the DSC machine in the early stage of the heating ramp (around 45°C). This emphasizes the onset of the polymerization reaction. Then, a large

exothermic peak, corresponding to the adhesive curing reaction, is observed. The maximum rate of cure is reached at the exothermic peak temperature T_p of 125°C. The reaction is generally considered as complete when the heat flow returns to a quasi-linear response. A quasi-static heat flow is observed at temperatures ranging from 60 to 250°C. In addition, the lack of residual peak on the second DSC confirms the completion of the curing reaction. The integration of the area under the exothermic gives a heat of curing reaction ΔH_T of about 354 J/g. The glass transition step is observed at T_g=62°C as an endothermic gradual increase in the heat flow monitored.

The curing of a thermoset such as the adhesive Hysol EA-9321 generates change in the heat of cure measured by DSC. These variations can be used to quantify the degree of cure of the adhesive. Hence, from the previous study, it is possible to determine the degree of cure of the adhesive for dynamic curing conditions. Nevertheless, in our context, it seems more interesting to get the curing degree for an imposed curing cycle. Considering the thermal loads imposed, this cycle will be made of temperature ramps and isotherms. Consequently, more investigations need to be conducted to study the curing behavior of the adhesive for thermal loads corresponding to our study.

Another way to monitor the curing of the adhesive with a DSC machine is an isothermal test (heating at constant temperature) where the cumulative heat of reaction can be calculated by recording the maximum heat flow generated by the curing reaction.

2.3.2. Experimental kinetic analysis

As shown previously, DSC experiments can be conducted in dynamic or in isothermal conditions.

The dynamic mode one was used to determine the total heat released during a complete curing process, i.e. for a fully cured adhesive at the end of this process. The second one let the measurement of the maximum heat of reaction reached at different isothermal temperatures, i.e. for an intermediate degree of cure.

Dynamic runs in the temperature range of 25 to 250°C were conducted at constant heating rates of 5, 10, 15 and 20°C/min.

Isothermal scans were run at temperatures ranging from 35 to 82°C. Equilibrium at the target isothermal temperature was reached in the sample holder with a heating rate of 20°C/min. This ramp was chosen sufficiently high to prevent the adhesive from curing and thereby measuring the heat flow released only for isothermal curing.

For each scan, a second heating run on the same sample under the same conditions was carried. This second run provides information on the curing of the adhesive. Indeed, a horizontal second run indicates that the cure reaction is almost complete. This run can also be used to define a baseline which will be used to calculate the total heat of reaction released.

Parameter	dT/dt *(°C/min)*			
	5	10	15	20
ΔH_T *(J/g)*	334.1	351.03	326.66	353.1
T_{onset} *(°C)*	36.25	46	45.25	55.33
T_{peak} *(°C)*	94.75	106.67	115	125.33
α_{peak} *(-)*	0.48	0.50	0.51	0.52

Table 7. Dynamic scanning results.

Figure 62 shows a typical DSC curve of a dynamic scan for the adhesive Hysol EA-9321 at a heating rate of 20°C/min. The total heat of reaction released during a dynamic scan ΔH_T is determined by integrating heat flow vs. time under the exotherm along the baseline generated by a second heating run.

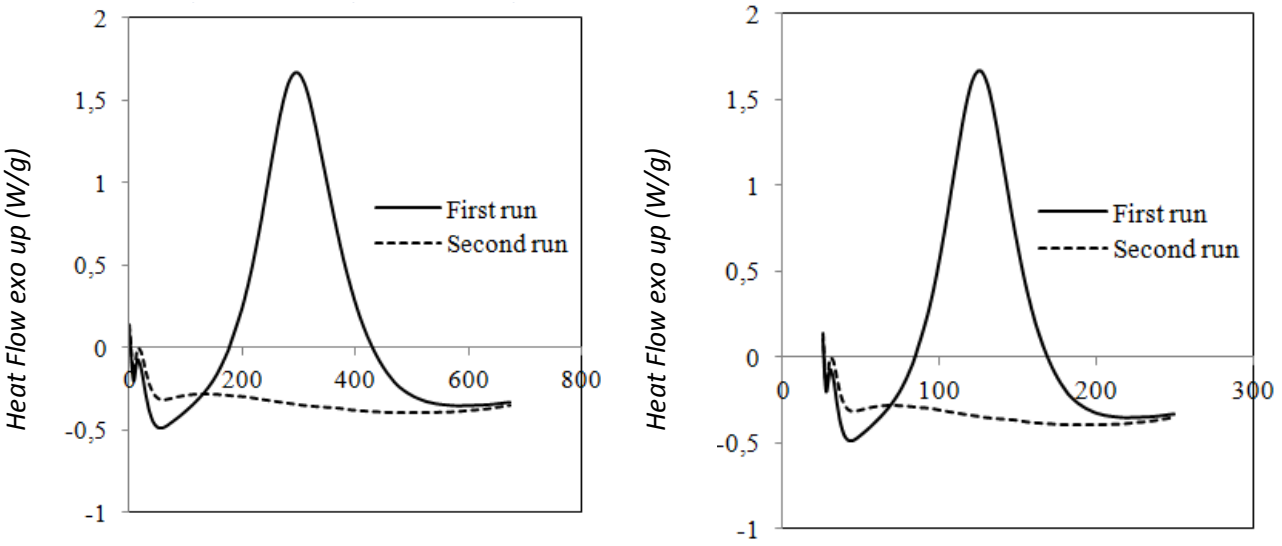

(a) (b)

Figure 62. Typical DSC dynamic scan at a 20°C/min: (a) Heat flow vs. time and (b) Heat flow vs. Temperature.

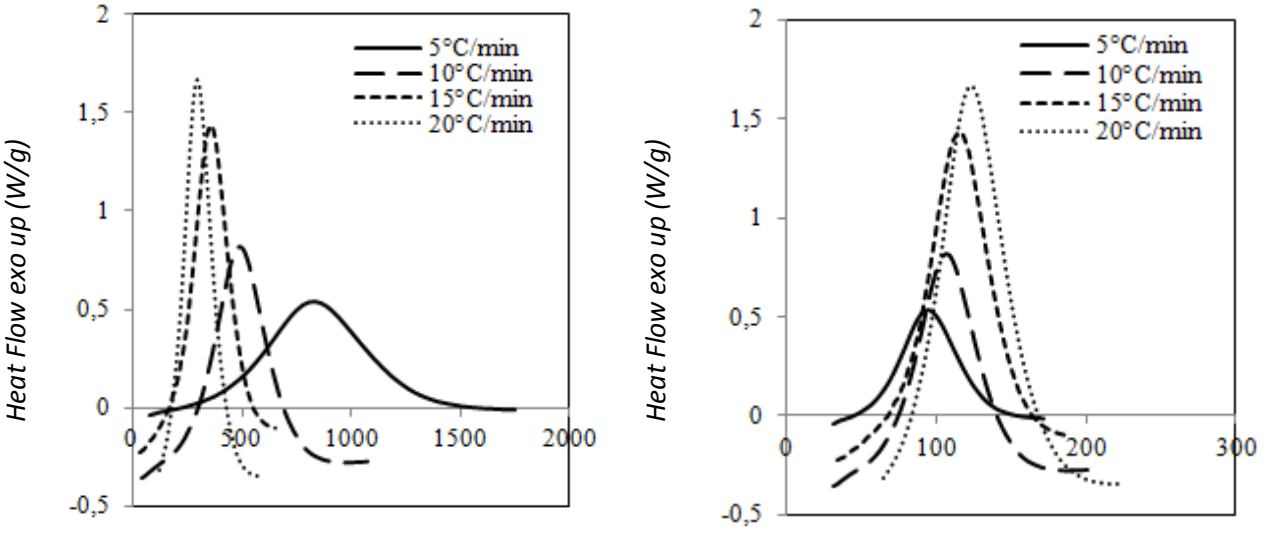

(a) (b)

Figure 63. Dynamic scanning: Heat flow at different heating rates as function of (a) time and (b) temperature.

The dynamic DSC curves are shown in Figure 63. It appears that the shape of the exotherm was heating dependent. The heat of reaction ΔH_T, was independent of the heating rate (Table 7). Other results, such as the onset of cure reaction temperature T_{onset}, the peak temperature T_{peak} depend on the heating rate

Figure 64 shows a typical DSC isothermal curve. In the same way as for dynamic analysis, the second run defined the baseline along which the curve heat flow vs. time is integrated. The resulting data is the maximum heat flow released ΔH_{ISO}.

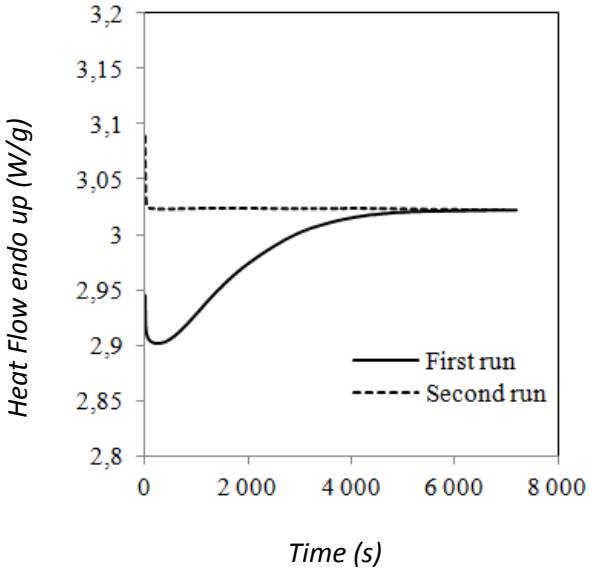

Figure 64. Typical isothermal DSC scan of the adhesive Hysol EA-9321 at 60°C.

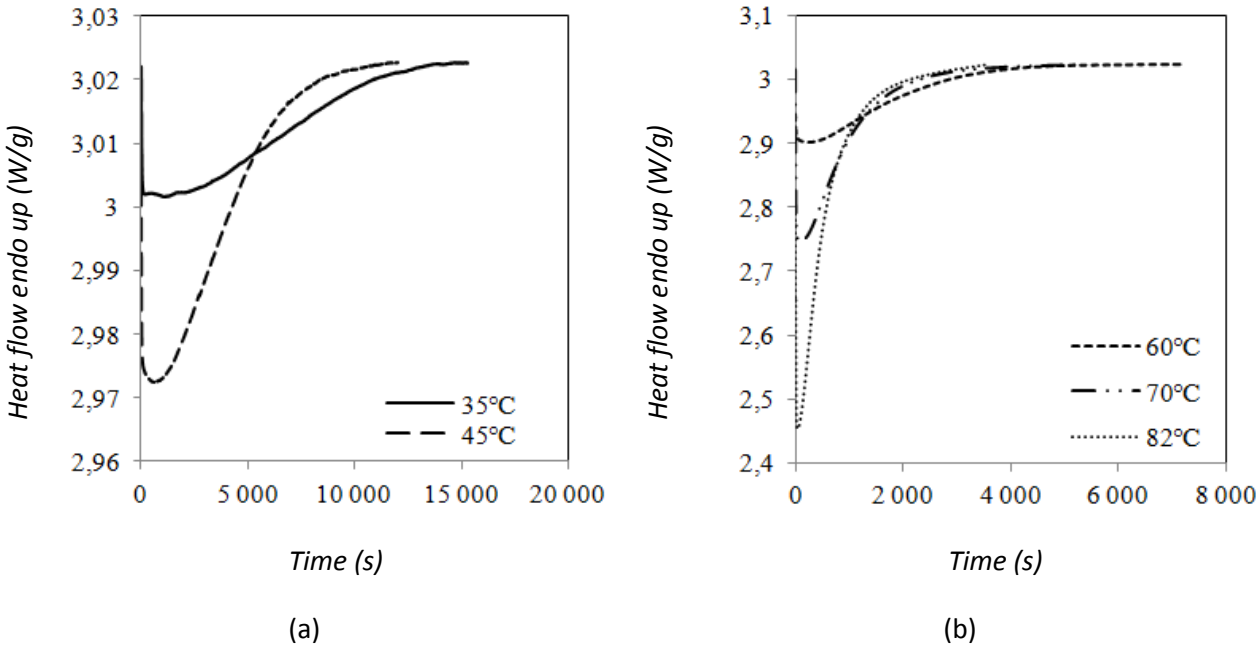

Figure 65. Heat flow at different isothermal temperatures: (a) low-curing temperatures and (b) high-curing temperatures.

Parameter	T_{cure} *(°C)*				
	35	45	60	70	82
ΔH_{ISO} *(J/g)*	130.73	202.07	240.03	310.03	341.18
α *(-)*	0.38	0.59	0.70	0.91	1.0
t	4h25	3h33	2h40	1h30	46min

Table 8. Isothermal scanning results.

Based on dynamic and isothermal results, the curing degree α can be determined according to the following equations:

The heat flux measured by the DSC-system can be written in term of enthalpy as:

$$\Phi = \left(\frac{dH}{dt}\right)_t \quad (2.1)$$

From the equation 2.1, it comes:

$$\frac{d\alpha}{dt} = \frac{1}{\Delta H_T}\left(\frac{dH}{dt}\right)_t \quad (2.2)$$

where ΔH_T is the total heat of reaction calculated during dynamic scans and $\left(\frac{dH}{dt}\right)_t$, the heat flow at time t (for an intermediate state of cure of the adhesive) measured by isothermal or dynamic scans. Hence, the curing degree α can be written as follows:

$$\alpha = \frac{\Delta H_t}{\Delta H_T} \text{ , with } \Delta H_t = \int_0^t \left(\frac{dH}{dt}\right)_t \quad (2.3)$$

where ΔHt is the heat of reaction released during isothermal or dynamic scan at an intermediate curing state of the adhesive at time t.

In this way, intermediate curing rate of reaction and curing states of the adhesive are plotted in Figure 66 and Figure 68.

As shown in Figure 66 and in Table 7, the onset of reaction is shifted according to the applied heating rates. For instance, the curing reaction initiates at 36.35°C for a ramp of 5°C/min against 55.33°C for a heating rate of 20°C/min. For a fixed temperature, the curing degree is higher at low heating rates: at 95°C, a curing degree of 0.49 is reached for a heating rate of 5°C/min against a value of 0.11 for a ramp of 20°C/min. In one hand, this can be due to heat transfer limitations of the DSC calorimeter. Indeed, it might have a gap between the theoretical temperature and the material temperature. At low heating rates, the sample reaches almost instantaneously the temperature equilibrium and consequently the polymerization reaction starts at lower temperatures than for high heating rates. On the other hand, this phenomenon is the result of higher heat flow evolution for higher heating rates. A significant energy is supplied to the adhesive resulting in a large evolution of the heat flow released by the curing reaction.

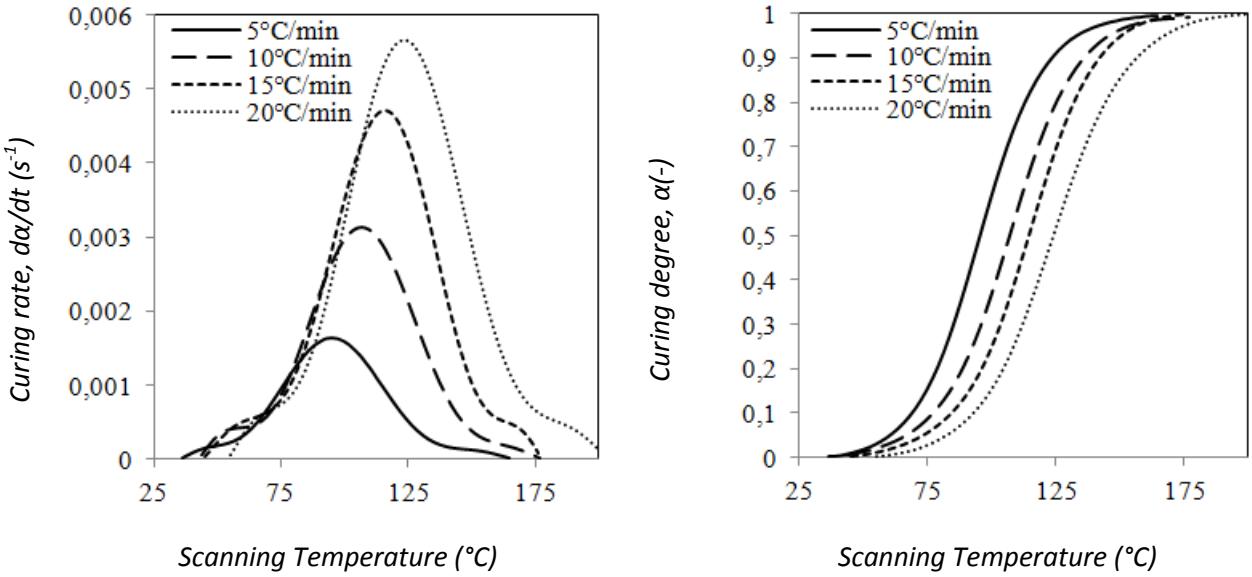

(a) (b)

Figure 66. Dynamic DSC scans: (a) curing rate vs. temperature and (b) curing degree vs. temperature.

Figure 67. (a) shows the reaction rate as a function of the curing degree. For a fixed state of cure, the reaction rate increases with the heating rate and reaches a maximum value. Thus, the polymerization reaction is the same for all heating rates. Figure 67. (b) shows reaction rate, normalized by its maximum value at the corresponding heating rate, versus curing degree. The overlapping curves validate a same curing mechanism for all heating rates.

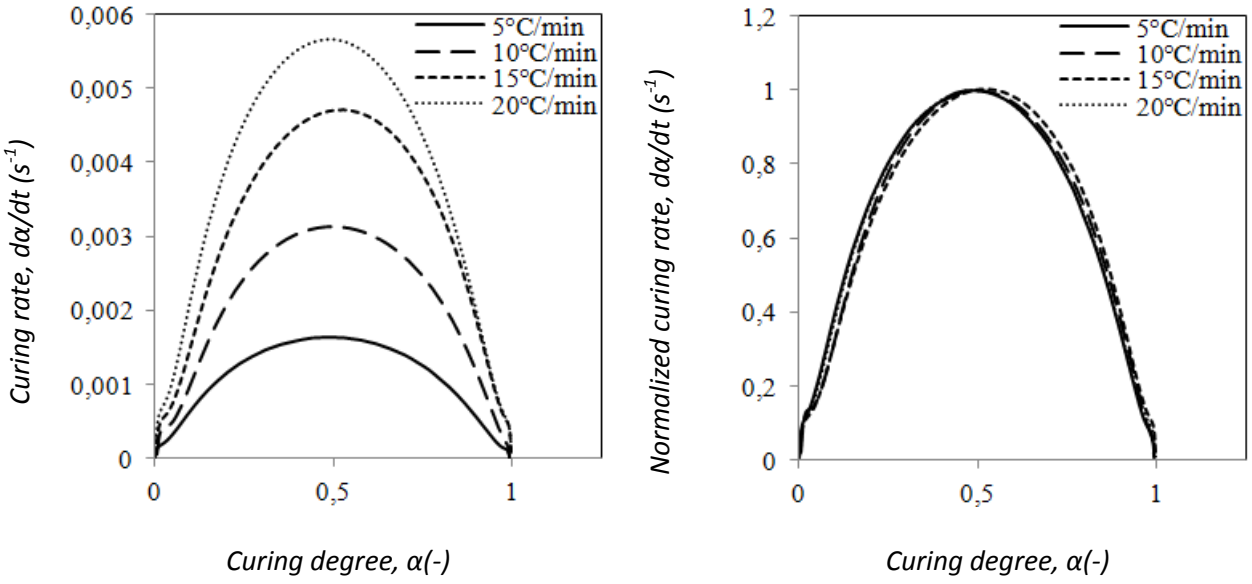

(a) (b)

Figure 67. DSC dynamic scans: (a) curing rate vs. curing degree and (b) normalized curing rate vs. curing degree.

Figure 68 shows the evolution of the curing rate and the curing degree for some isothermal temperatures. For each temperature, the curing degree increases until a plateau. At high temperatures, the plateau is reached after few minutes: 100% of curing requires 46 minutes at 82°C. At low temperatures curing, this

one is delayed: 38% is attained after 4 hours and 25 minutes at 35°C. Higher temperatures accelerate the reaction between resin and hardener. Hence, the plateau is quickly reached for high-curing temperatures.

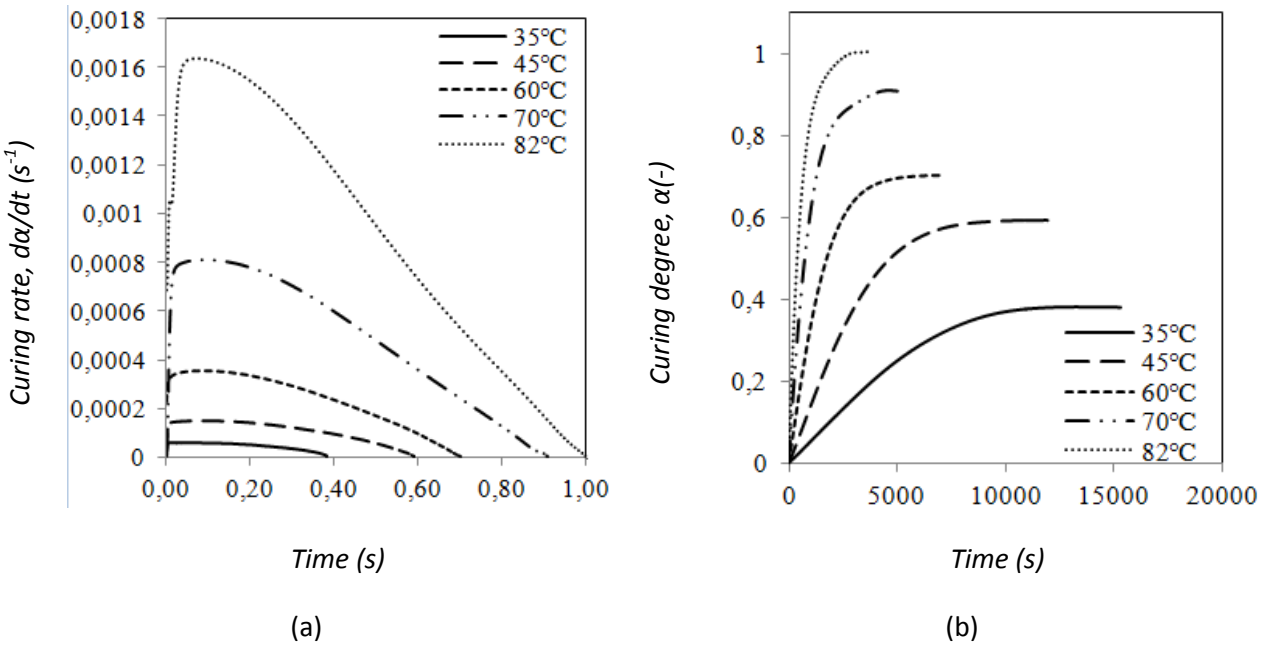

Figure 68. Isothermal DSC scans: (a) curing rate vs. time and (b) curing degree vs. time.

Further investigation of DSC scans can be made to better understand the curing process of the adhesive Hysol EA-9321. During the curing process of the adhesive, two phenomena such as gelation and vitrification occur. Gelation appears at a curing degree for which the adhesive changes from a liquid to a rubber. Vitrification occurs close to the glass transition temperature T_g. This temperature evolves with the cure temperature and its relationship gives some informations on the physical state of the adhesive and on the reaction rate during the curing process. At low curing temperature (below the glass transition), the development of the glass transition temperature is slowed and achieved a low value: this reaction is diffusion controlled. However, at curing temperatures above the glass transition, the reaction proceeds rapidly and is controlled by kinetics. The phase transitions caused by gelation and vitrification are generally described in a Time-Temperature-Transformation (TTT-diagram) isothermal cure diagram (Figure 69 (a)) [Gil 83]. The physical states of the adhesive during curing process are represented by different regions.

The required time to reach the same curing degree changes with the different isothermal temperatures applied: it needs almost 10000 s to reach a curing degree of 0.37 for an isothermal temperature of 35°C whereas it takes 255s to achieve the same curing state at 82°C. The iso-conversional plots of isothermal temperatures versus log time appear in Figure 69 (b). A quasi-linear relationship between the logarithmic cure time and cure temperature is observed for curves with curing degrees ranging from 0.1 to 0.3 over a curing temperature going until 50°C. This observation is representative of a controlled reaction by the curing kinetics. On the contrary, a non-linear relationship is observed from curing states ranging from 0.4 to 0.9 for isothermal temperatures going from 60°C to 82°C. Therefore, the reaction is diffusion-controlled for these ranges of temperatures and curing degrees. It is generally suggested that this diffusion area is the onset of vitrification on the TTT cure diagram (Figure 69) [Dus 85].

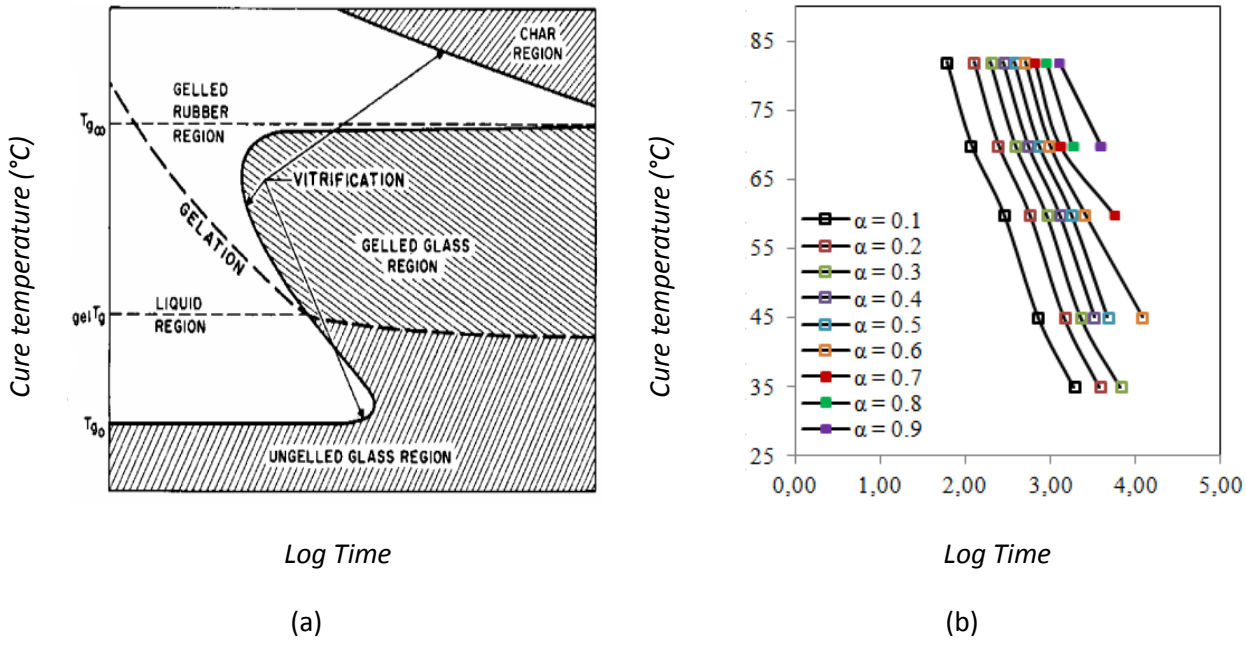

Figure 69. (a) Generalized isothermal cure diagram of Time-Temperature-Transformation and (b) Iso-conversional plots of Cure Temperature vs. Logarithmic time for the adhesive Hysol EA-9321.

Considering the previous isothermal DSC scans (Figure 68), a maximum curing degree corresponds to each isothermal curing temperature. Figure 70 shows the maximum curing degree reached for various isothermal curves. The dependence of the maximum curing degree α_{max} on the cure temperature can be plotted with a linear relationship. The same trend was observed by Ivankovic et al. [IVA 03] whereas an interpolating polynomial of degree 2 was used by Ruiz et al. [RUI 08]. In our case, the use of such polynomial does not conduct to a better interpolation. Observations theoretically predicted are retrieved experimentally: at lower curing temperatures, the reaction is diffusion-controlled, thus the curing rates decrease rapidly and lower curing states are achieved. At higher curing temperatures, the reaction proceeds rapidly by kinetic control and reaches higher degrees of cure.

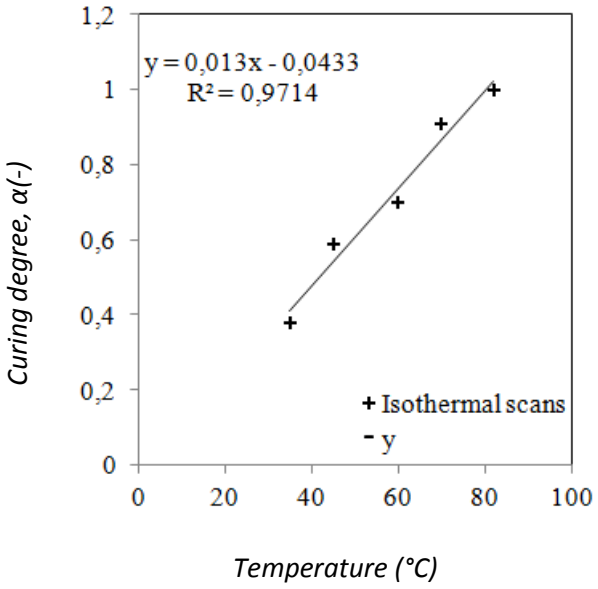

Figure 70. Maximum curing degree vs. isothermal temperature.

Another important phenomenon of the isothermal curing process is the time, called half life, for which the sample reaches half of its maximum curing state. Figure 71 gives the evolution of the life time and the half life time of the adhesive as a function of isothermal cure temperature. For a fixed isothermal temperature, the time necessary to reach the half time curing is smaller than that required to achieve a maximum cured adhesive. For instance, for an isothermal curing degree, the maximum curing state of the adhesive (α_{max}=0.7) is reached after 120 minutes, whereas a half life curing degree (α_{half_life}=0.35) is achieved in 15 minutes. It is not surprising since the curing rate at the onset of the curing reaction is higher than that in the late cure stage. As a result, it takes more time in the later stage of curing process to get the same increase of curing degree than in the onset of reaction. On Figure 71 (a), it appears that the maximum cure time and the half life cure time decrease exponentially with the isothermal curing temperatures. In addition, the half-life temperature after 60 minutes of curing, i.e. the temperature for which the adhesive reaches a curing state of 0.5 in 60 minutes was evaluated at 60°C.

This half-life temperature was very important to verify the validity of DSC results. To that end, a dynamic scan from 25 to 250°C at a heating rate of 20°C/min was investigated on an uncured sample and on a sample aged at 60°C for 60 minutes (partially cured specimen). The heat flows generated by those dynamic scans are shown in Figure 71 (b). It appears that the heat flow measured for the partially cured specimen is almost half that the uncured specimen. The integration of the area under the exotherm peak gives a heat of reaction of 353.1 J/g for the uncured specimen and 168.2 J/g for the partially cured specimen. The ratio between these two values is 0.48, close to 0.5. Hence, the predicted half-life temperature in Figure 71 (a) is in good agreement with experimental results obtained in Figure 71 (b).

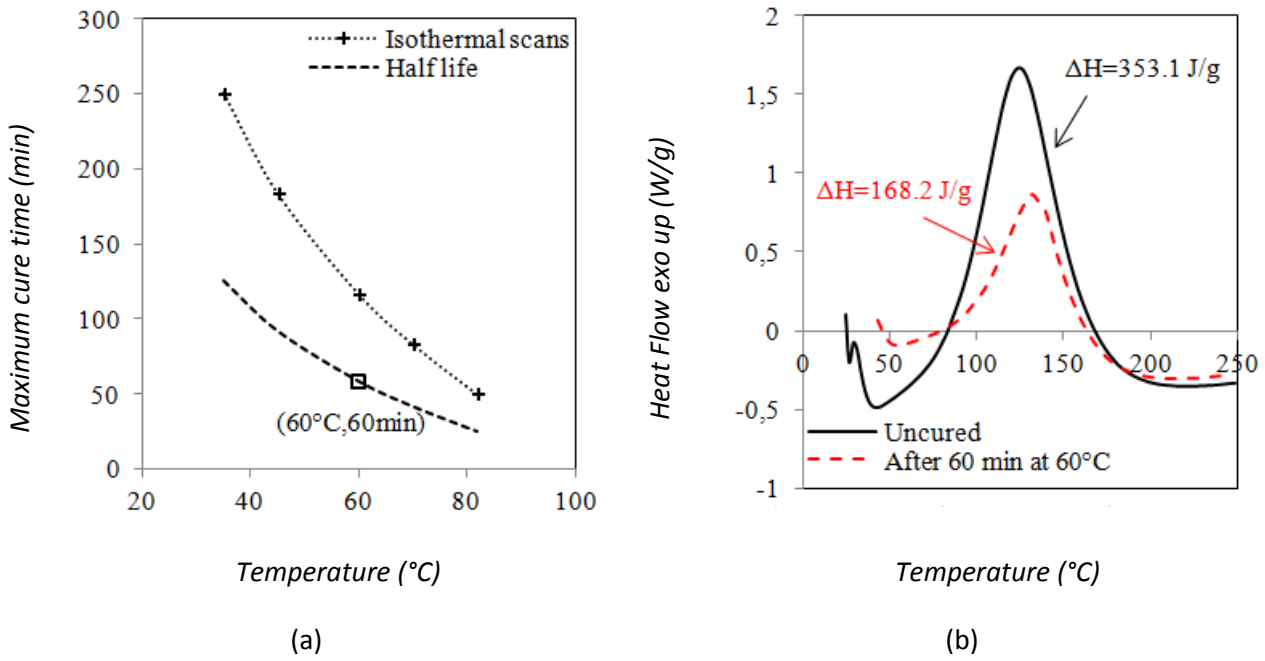

Figure 71. (a) Maximum cure time vs. isothermal temperature and (b) comparison of dynamic scans for uncured and partially cured adhesive (after a curing cycle of 1 hour at 60°C) at a heating rate of 20°C/min.

2.4. Cure kinetics modeling

The previous experimental responses of the adhesive Hysol EA-9321 can be described numerically with kinetics models.

The curing kinetics could be approached in two ways: either phenomenological [LIL 05] [HOJ 04] [KAR 96] [LIO 07] [SAJ 96] [SIM 00] or mechanistic models [VAL 05] [LEE 00] [YOU 97]. Phenomenological models were based on an empirical relation between reaction kinetics. The mechanistic approach was made from the balance of reactive species involved in the chemical reaction. Since the chemical composition of the adhesive constituents is unknown, phenomenological models were preferred to study the cure kinetics of the adhesive. These models are based on dynamic and isothermal approaches. The first one describes the curing for non-zero curing rate whereas the other one is used for isothermal loadings. Hence, both issues needs to be investigated to predict properly any curing cycle which is a combination of dynamic and isothermal scans.

2.4.1. Dynamic modelling

An empirical model relating the curing rate, $d\alpha/dt$, to a function of the curing degree, α, for epoxies has the following expression:

$$\frac{\mathrm{d}\alpha}{\mathrm{dt}} = \mathrm{k}\mathrm{f}(\alpha) \tag{2.4}$$

where k is the time-dependent reaction rate, following the Arrhenius law [ARR 89]:

$$\mathrm{k} = \mathrm{A}\mathrm{e}^{-\frac{\mathrm{E_a}}{\mathrm{RT}}} \tag{2.5}$$

where A (s^{-1}) is the pre-exponential factor, E_a (J/mol) is the activation energy, R (8.314 J/mol-K) is the universal gas constant and T (K) the temperature.

According to the previous curves, an autocatalytic model was suggested [SUN 02a]:

$$\mathrm{f}(\alpha) = \alpha^{\mathrm{m}}(1-\alpha)^{\mathrm{n}} \tag{2.6}$$

where n and m are the reaction orders.

The kinetic parameters E_a, A, m and n were determined by fitting the experimental results to the autocatalytic model with the Kissinger [SUN 02b] and Ozawa [KISS 57] methods.

A similar definition of the curing rate was obtained by defining a modified pre-exponential factor as:

$$\mathrm{A_f} = \mathrm{C_f}.\mathrm{A} = \mathrm{C_f}.\frac{\mathrm{e}^{\mathrm{K}}\left(\frac{\mathrm{d}\alpha}{\mathrm{dT}}\right)_{\mathrm{p}}}{{\alpha_{\mathrm{p}}}^{\mathrm{m}}\left(1-\alpha_{\mathrm{p}}\right)^{\mathrm{n}}} \tag{2.7}$$

where C_f is the correction factor of A, K a parameter coming from the Kissinger method [YOU 97]. The terms $(d\alpha/dT)_p$ and α_p are the derivative of degree of cure to temperature and curing degree at the exothermic peak, respectively. Substituting k in Eq.(2.4) by Eq.(2.5-2.6) and A_f in Eq.(2.5) by Eq.(2.7) results in the rate equation:

$$\frac{\mathrm{d}\alpha}{\mathrm{dt}} = \mathrm{C_f}.\frac{\mathrm{e}^{\mathrm{K}}\left(\frac{\mathrm{d}\alpha}{\mathrm{dT}}\right)_{\mathrm{p}}}{{\alpha_{\mathrm{p}}}^{\mathrm{m}}\left(1-\alpha_{\mathrm{p}}\right)^{\mathrm{n}}}.\mathrm{e}^{-\frac{\mathrm{E_a}}{\mathrm{RT}}}.\alpha^{\mathrm{m}}(1-\alpha)^{\mathrm{n}} \tag{2.8}$$

For both models, a non-linear least-square regression based on the Levenberg-Marquardt algorithm [MOR 77] was used to determine the parameters *m*, *n* and C_f. Table 4 shows its estimation. Then, equation 2.8 is numerically solved by using the fourth-order Runge-Kutta method [CAR 92]. A time-step size of 1s was used to reach numerical convergence.

Figure 72 shows the results for the different heating rates for both models. The curves predicted by both models correlate as well the experimental results. However, on Figure 72 (a), curves predicted by the modified autocatalytic model in the peak area are closed to experimental results. Hence, the modified autocatalytic model is preferred to model dynamic scans because of its reliability and its accuracy compared to the empirical model.

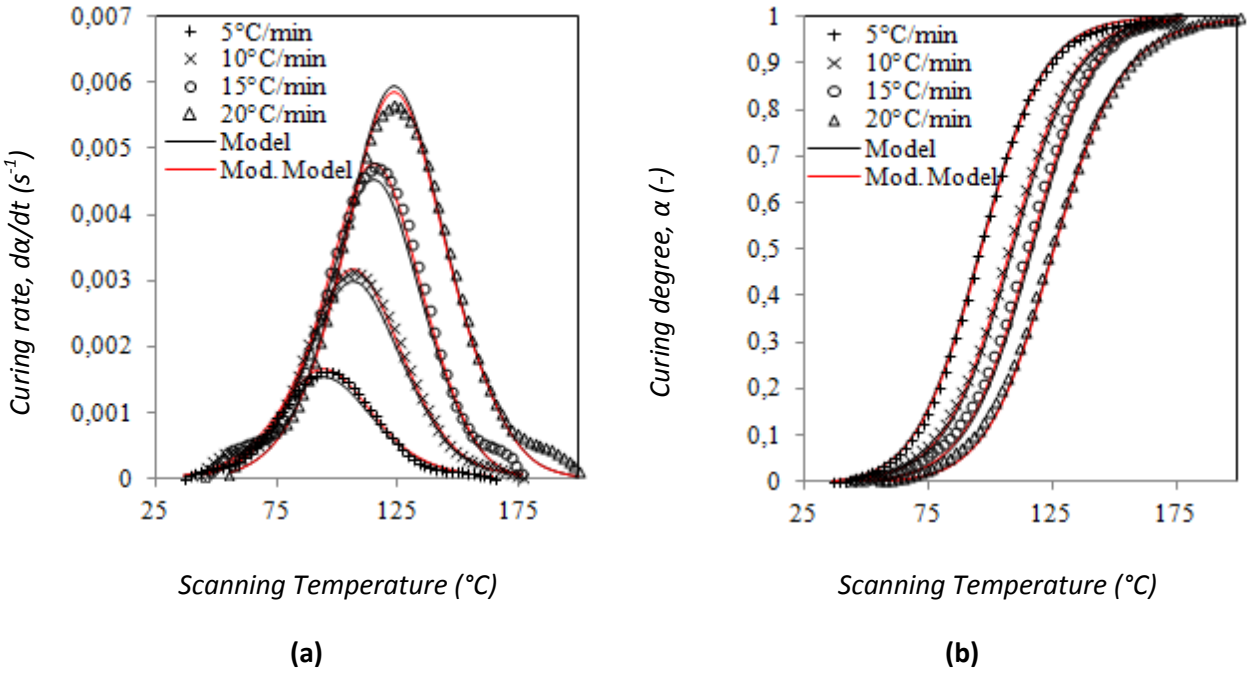

Figure 72. Comparison of experimental autocatalytic models results: (a) curing rate vs. temperature and (b) curing degree vs. temperature.

Model	Parameter	dT/dt (°C/min)			
		5	10	15	20
Kissinger & Ozawa	Ea (kJ/mol)	60.03	60.03	60.03	60.03
	A (s^{-1})	$1.77x10^6$	$1.77x10^6$	$1.77x10^6$	$1.77x10^6$
	m	0.16	0.21	0.23	0.29
	n	1.54	1.51	1.41	1.63
Modified Model	C_f	0.97	1.06	1.05	0.98

Table 9. Kinetic parameters from dynamic model.

2.4.2. Isothermal modelling

The isothermal curing behavior of an adhesive is written as a function of its curing degree:

$$\frac{d\alpha}{dt} = g(\alpha) \tag{2.9}$$

Some models were used to describe this process. The simplest model corresponds to an n-th order kinetic expression as follows:

$$g(\alpha) = k(1-\alpha)^n \tag{2.10}$$

where *n* is the reaction order and *k,* the rate constant given by the Arrhenius law defined previously in equation 2.5. Table 10 shows the kinetic parameters identified for the n-th order model with the non-linear least square regression analysis. The parameter *k* decreases with the increase of temperature, as suggested by equation 2.5. On the contrary, the parameter *n* increases with the increase of temperature. Figure 73 shows a comparison between experimental results and those predicted by the n-th order model. The modeling curve curing degree vs. time correlates well with the experimental data until a critical curing degree value for each isothermal temperature (Figure 73 (b)). Regarding Figure 73 (a), the polymerization rate predicted by the model is not in good agreement with experimental results, particularly at the onset of the curing reaction (for a curing degree α=0 to α=0.2). For a fixed isothermal temperature, the curing rate predicted by the n-th order model decreased linearly with the curing degree. In addition, the curing rate is maximum for a zero curing degree. An autocatalytic system, such as DGEBA (resin)/DETA (hardener) system does not exhibit this kind of behavior. Thus, the n-th order model is not appropriate to describe the curing behavior of the adhesive Hysol EA-9321 in isothermal conditions.

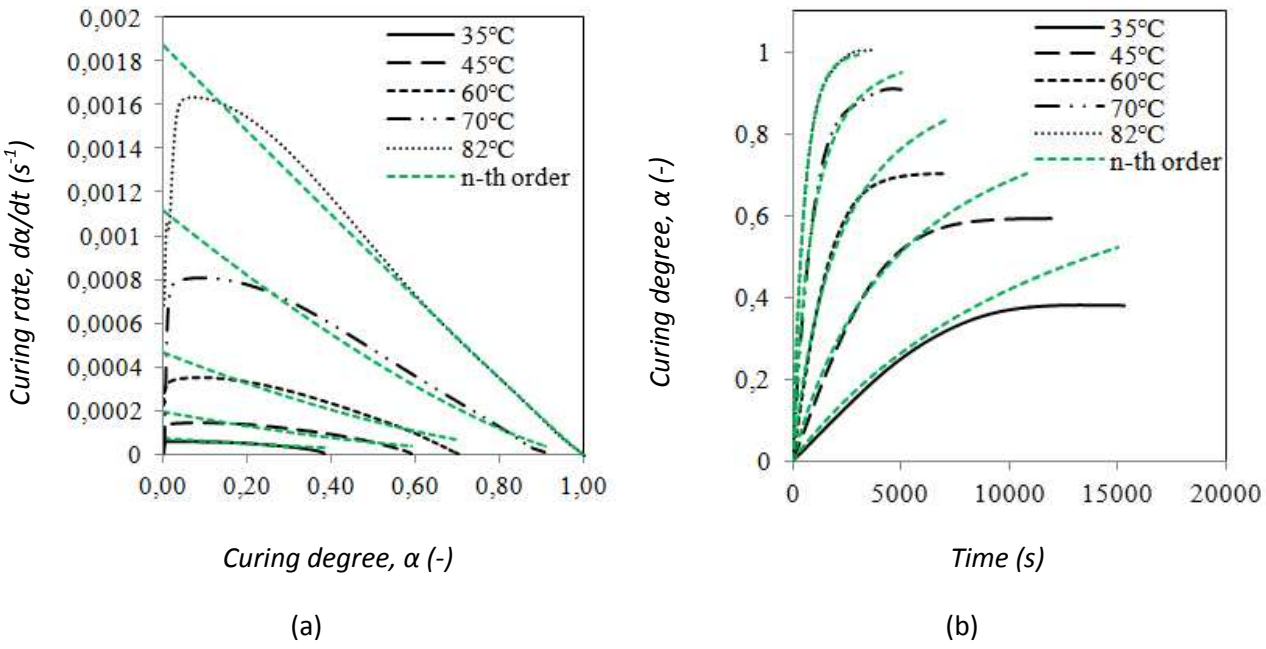

(a) (b)

Figure 73. Comparison of experiment and the isothermal n-th order model: (a) curing rate vs. curing degree and (b) curing degree vs. time.

Model	Parameter	T (°C)				
		35	45	60	70	82
n-th order	n	1.92	1.84	1.63	1.38	1.04
	k (s^{-1})	$7.10x10^{-5}$	$1.96x10^{-4}$	$4.69x10^{-4}$	$1.12x10^{-3}$	$1.87x10^{-3}$

Table 10. Kinetic parameters of n-th order model.

Another kinetic expression was proposed by Horie [HOR 70] as following equation:

$$g(\alpha) = (k_1 + k_2\alpha)(1-\alpha)^2 \tag{2.11}$$

where k_1 and k_2 are the kinetic rate constants, described by an Arrhenius law [ARR 89]:

$$k_i = A_i e^{-\frac{E_{a_i}}{RT}} \qquad i=1, 2 \tag{2.12}$$

where A_i (s^{-1}) is the pre-exponential factor, E_{ai} (J/mol) is the activation energy, R (8.314 J/mol-K) is the universal gas constant and T (K) the temperature.

Contrary to the n-th order model, this one takes into account the autocatalytic cure behavior of the adhesive. In the same way as previously, the results predicted by the model and the experiments are in good agreement until a critical curing degree for each isothermal temperature (Figure 74 (b)). On Figure 74 (a), a difference is observed between experimental and numerical curves. It seems that a total reaction order of 3 does not correspond to the adhesive.

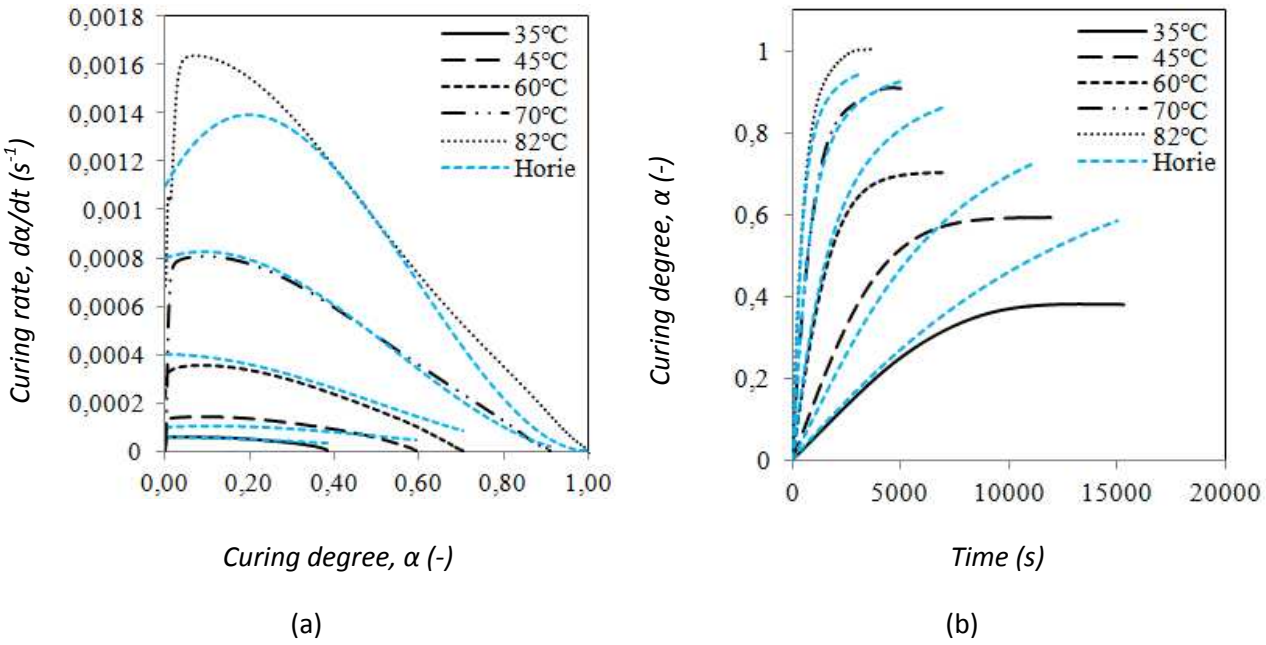

Figure 74. Comparison of experiment and the isothermal model of Horie: (a) curing rate vs. curing degree and (b) curing degree vs. time.

The identified kinetic parameters appear in Table 11. It is important to note that values of k_2 are much higher than those of k_1. For instance, at isothermal temperatures of 35, 45, 60 and 70°C, the value of k_2 is

almost two or three times higher than k_1. However, as defined previously, k_1 is the curing rate constant at the onset of reaction and k_2 the curing rate constant in the late cure stage. Such a difference between these parameters indicates the important catalytic activity of the cure reaction.

Model	Parameter	T (°C)				
		35	45	60	70	82
Horie	k_1 (s^{-1})	$6.00x10^{-5}$	$1.00x10^{-4}$	$4.00x10^{-4}$	$8.00x10^{-4}$	$1.10x10^{-3}$
	K_2 (s^{-1})	$1.00x10^{-4}$	$3.00x10^{-4}$	$8.00x10^{-4}$	$2.20x10^{-3}$	$5.40x10^{-3}$

Table 11. Kinetic parameters of Horie model

Kamal & Sourour [KAM 73][KAM 76] extended the previous model using two additional empirical power law exponents *m* and *n* in addition to the constants k_1 and k_2. These exponents are the orders of reaction. In the context of this model, it is assumed that the curing process is based on autocatalytic reactions. Equation 2.11 becomes:

$$g(\alpha) = (k_1 + k_2 \alpha^m)(1-\alpha)^n \tag{2.13}$$

Table 12 lists the values of identified parameters for this model. Ryan et al. [RYA 79] showed that the overall reaction order *m+n* was assumed to be constant (*m+n=2)* whereas the identified value decreased with increasing temperature.

Model	Parameter	T (°C)				
		35	45	60	70	82
Kamal&Sourour	k1 (s^{-1})	$1.52\ x10^{-6}$	$7.48\ x10^{-6}$	$2.26\ x10^{-4}$	$2.38x10^{-5}$	$6.84x10^{-4}$
	k2 (s^{-1})	$8.80x10^{-5}$	$2.18x10^{-4}$	$4.14x10^{-3}$	$1.21x10^{-3}$	$1.60x10^{-3}$
	m	0.0905	0.12	0.311	0.13	0.15
	n	1.92	1.8363	1.63	1.38	1.04
	m+n	2.01	1.96	1.94	1.51	1.20

Table 12. Kinetic parameters from isothermal model of Kamal & Sourour.

Figure 75 shows a comparison between experiment and numerical predictions of the model of Kamal & Sourour. The numerical prediction of the curing rate as a function of the curing degree correlates as well with experimental results until a critical curing degree value (Figure 75 (a)). The same phenomenon can be observed on the curing degree response in Figure 75 (b). Without taking account the curves after the critical curing degree value for which experimental and numerical results differ, it appears that the model of Kamal & Sourour seems relevant to describe the first part of the curing behavior of the adhesive Hysol 9321.

On Figure 75 (b), it appeared a critical value of the curing degree for which experiment and Kamal & Sourour model no longer correlate. For low curing temperature, this degree of cure is reached at 23% for 35°C and around 50% for 45°C. Regarding high curing temperature, the value is 62% for 60°C, 82% for 70°C. This phenomenon is not observable for an isothermal temperature of 82°C. Regarding the polymerization rate, Figure 75 (a) was enlarged close to this critical curing degree (Figure 76). In For each isothermal curing, experimental curves show a kinetic slowdown at critical curing degrees identified on Figure 75 (b). This highlights the diffusion phenomenon.

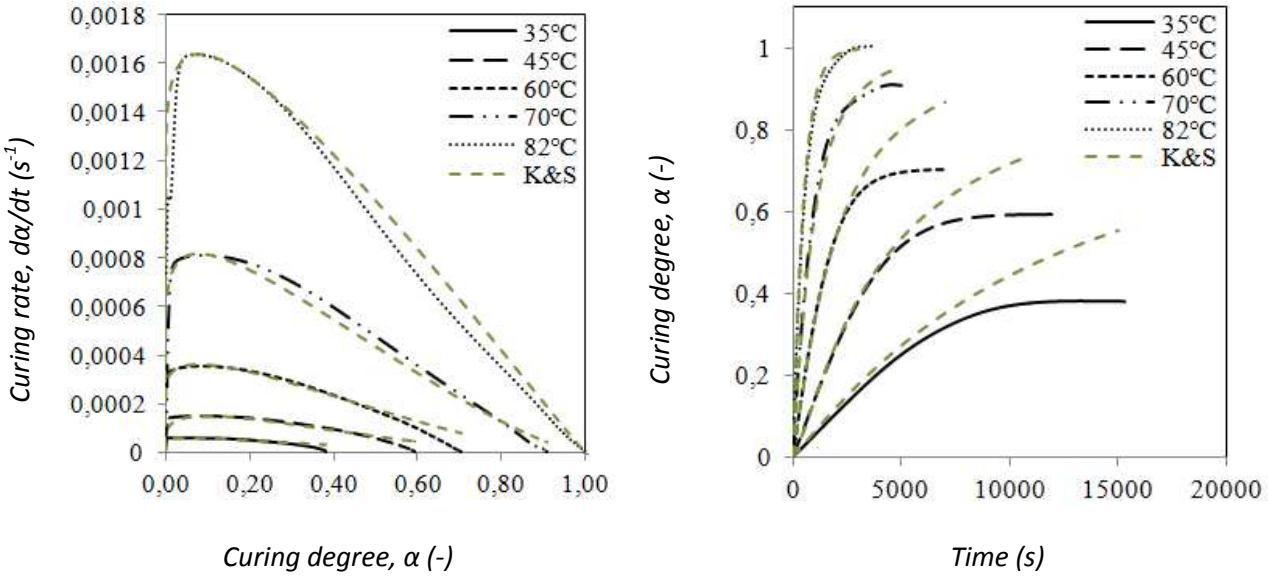

(a) (b)

Figure 75. Comparison of experiment and isothermal model of Kamal & Sourour: (a) curing rate vs. curing degree and (b) curing degree vs. time.

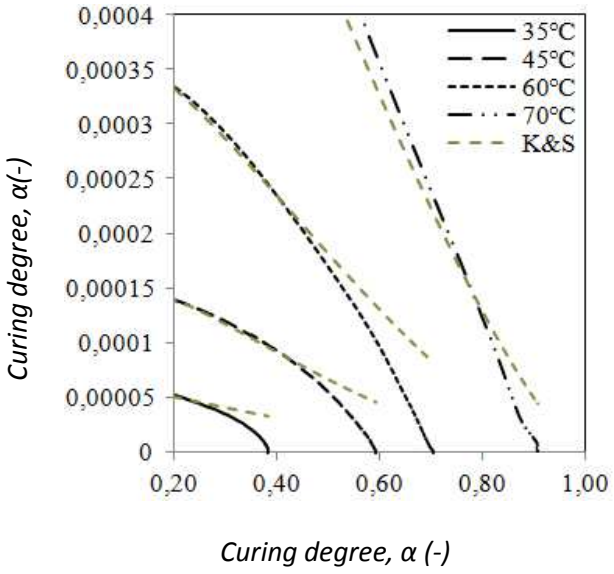

Figure 76. Diffusion phenomena with the model of Kamal & Sourour.

Approaching the glass transition temperature, the formed chains induced decreasing of the movement of the reactive species. In such case, the reaction rate was decelerated and the further reaction became diffusion controlled. To take into account this phenomenon, Chern et al. [CHE 87] proposed another definition of the reaction rate by adding a diffusion factor to the kinetic model *g(α)*:

$$\left[\frac{d\alpha}{dt}\right]_{diffusion} = g(\alpha).\frac{1}{1+e^{C(\alpha-\alpha_c)}} \qquad (2.14)$$

where $\frac{1}{1+e^{C(\alpha-\alpha_c)}}$ is the diffusion control factor, *C* is an empirical constant which is temperature dependent and α_c is the critical curing degree at which diffusion initiates. *g(α)* is the kinetic expression of the previous models.

Hence, the model of Kamal & Sourour with the diffusion term was written as follows:

$$\left[\frac{d\alpha}{dt}\right]_{\substack{K\&S\\Diffusion}} = \left(k_1 + k_2\alpha^m\right)(1-\alpha)^n . \frac{1}{1+e^{C(\alpha-\alpha_c)}} \qquad (2.15)$$

In order to evaluate the kinetic parameters appearing in each equation, the following procedure was followed. At first, the diffusion-controlled phenomena was ignored in order to determine which kinetic model best described the cure process of the adhesive. The parameters were determined using a non-linear least square regression analysis [MOR 77] and each curing rate equation was solved with the fourth-order Runge-Kutta method [CAR 92]. Then, kinetic parameters of the Kamal & Sourour model were determined by taking account of diffusion. In one hand, the initial parameters and the diffusion parameters were defined separately by using two non-linear least square regressions. In other hand, these ones are determined with only one regression. The first method was preferred because of the accuracy of the results. For all simulations, the time step was taken sufficiently small (time step of 1s) to reach the Runge Kutta-method convergence.

Figure 77 shows the correlation between experimental results and numerical predictions of Kamal & Sourour models with and without diffusion. The difference between these models is primarily seen on the curves curing degree vs. time (Figure 77(a)). In the late stage of cure reaction, the effect of diffusion on the cure rate is apparent, especially at low isothermal cure temperatures. The isothermal maximum degree of cure goes from 0.55 to 0.38 for a curing temperature of 35°C and from 0.7 to 0.6 for a curing temperature of 45°C. It stands from 0.86 to 0.70 for an isothermal temperature of 60°C, from 0.95 to 0.92 for an isothermal temperature of 70°C. (Figure 77(b)). Experimental results were accurately simulated by the Kamal & Sourour model with diffusion.

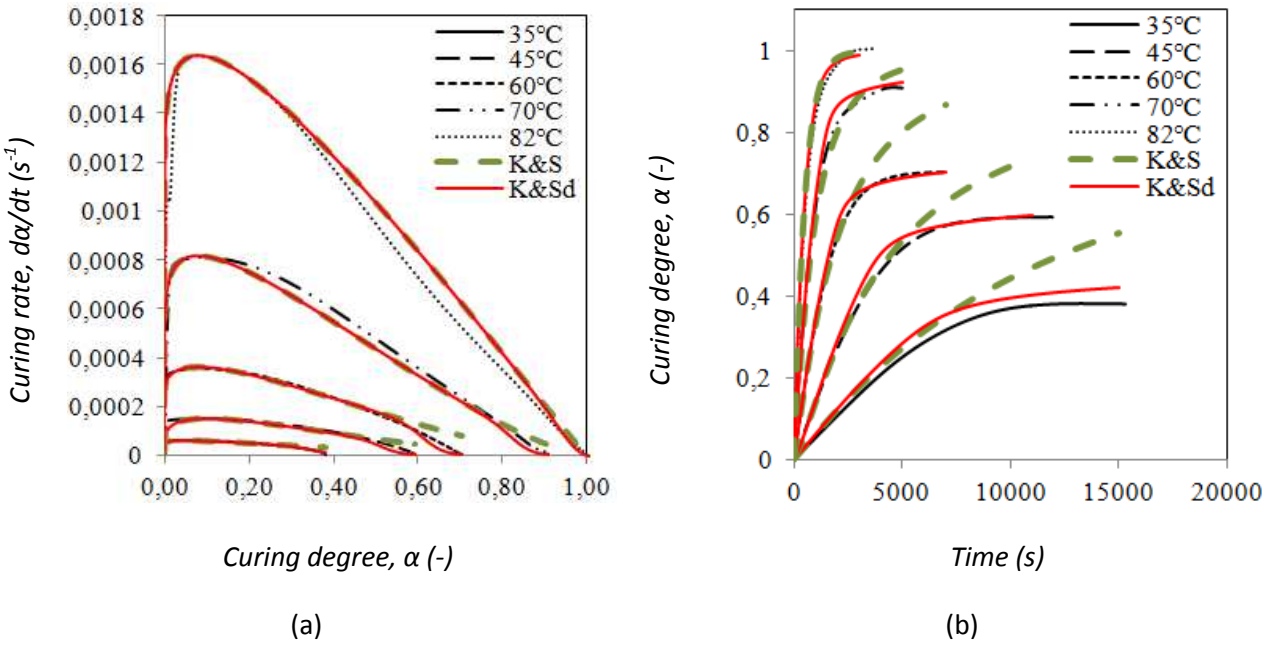

(a) (b)

Figure 77. Comparison of experiment and isothermal models of Kamal & Sourour with and without diffusion: (a) curing rate vs. curing degree and (b) curing degree vs. time.

The curing behavior of the adhesive Hysol EA-9321 for the studied isothermal temperatures is summarized in Figure 78.

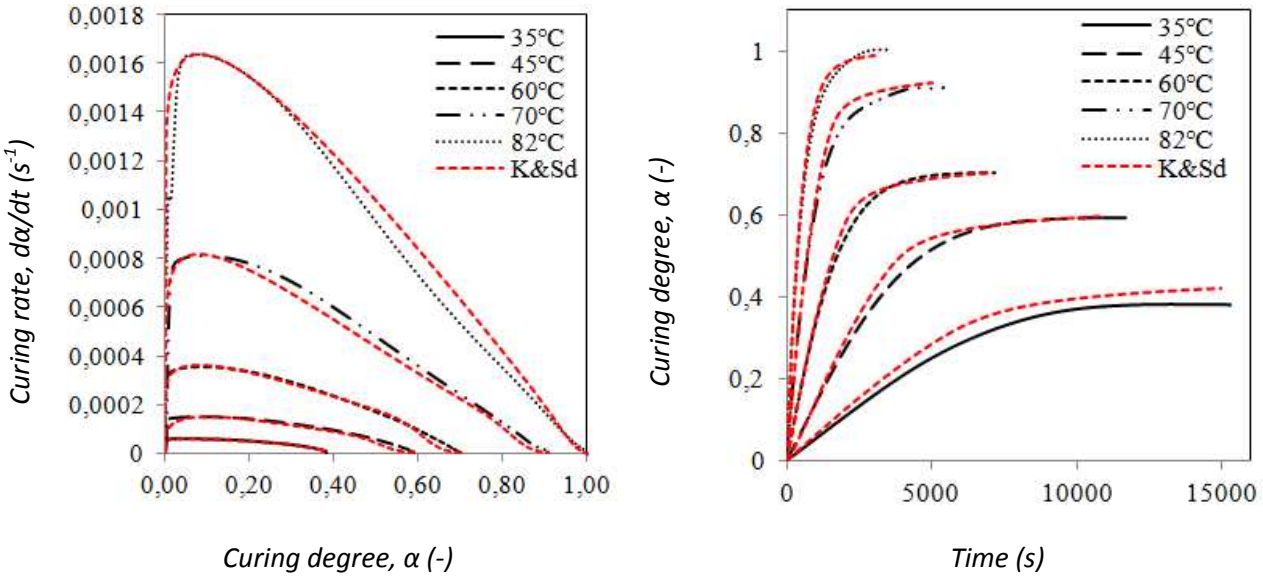

(a) (b)

Figure 78. Comparison of experimental and isothermal models results with diffusion for high-curing temperature: (a) curing rate vs. curing degree and (b) curing degree vs. time.

Model	Parameter	T (°C)				
		35	45	60	70	82
Kamal&Sourour	k1 (s^{-1})	1.52 x10^{-6}	7.48 x10^{-6}	2.26 x10^{-4}	2.38x10^{-5}	6.84x10^{-4}
	k2 (s^{-1})	8.80x10^{-5}	2.18x10^{-4}	4.14x10^{-3}	1.21x10^{-3}	1.60x10^{-3}
	m	0.0905	0.12	0.311	0.13	0.15
	n	1.92	1.8363	1.63	1.38	1.04
Kamal&Sourour diffusion	C	38	38	38	38	38
	α_c	0.36	0.52	0.64	0.84	0.98

Table 13. Kinetic parameters from isothermal model Kamal & Sourour with diffusion.

Table 13 shows the kinetic parameters identified with the non-linear least square regression analysis. The values of several parameters can be related to the temperature. The rate constants k_1 and k_2 increases with the curing temperature. These quantities are related to the temperature with the Arrhenius law (equation 2.12). The reaction order *n* decreased with increased temperature. The critical curing degree increased with isothermal temperature. Thus, the curing behavior of the adhesive Hysol EA-9321 depends only on the temperature.

2.4.3. Discussion

As previously studied, the curing behavior of the adhesive Hysol EA-9321 can be described through dynamic and isothermal approaches. Regarding the isothermal model, the curing behavior is temperature dependent. Hence, this previous one is known for a wide range of temperatures. Dynamic scans can be considered as a series of isothermal heating with a period of one second. Thus, we can assume that the isothermal model can be used to model dynamic heating.

In order to validate this assumption, experimental dynamic results were simulated with the isothermal model described previously. This model was modified to take into account the global behavior of the adhesive Hysol EA-9321, i.e on a series of isothermal temperatures. Table 14 shows the kinetic parameters used to model the dynamic scans. The parameters m and n were approximated by an average value independent of the temperature. The critical curing degree evolved linearly with temperature until the glass transition temperature.

Parameters							
m	n	A_1 (s^{-1})	A_2 (s^{-1})	E_1 (J/mol)	E_2 (J/mol)	C	α_c
0.16	1.56	6.6e-5	4.6e5	2000	6.0e4	38	0.013T-0.09 $T \leq T_g$ 0.97 $T > T_g$

Table 14. Cure kinetic coefficients of the Hysol EA-9321 for the Kamal & Sourour model with diffusion.

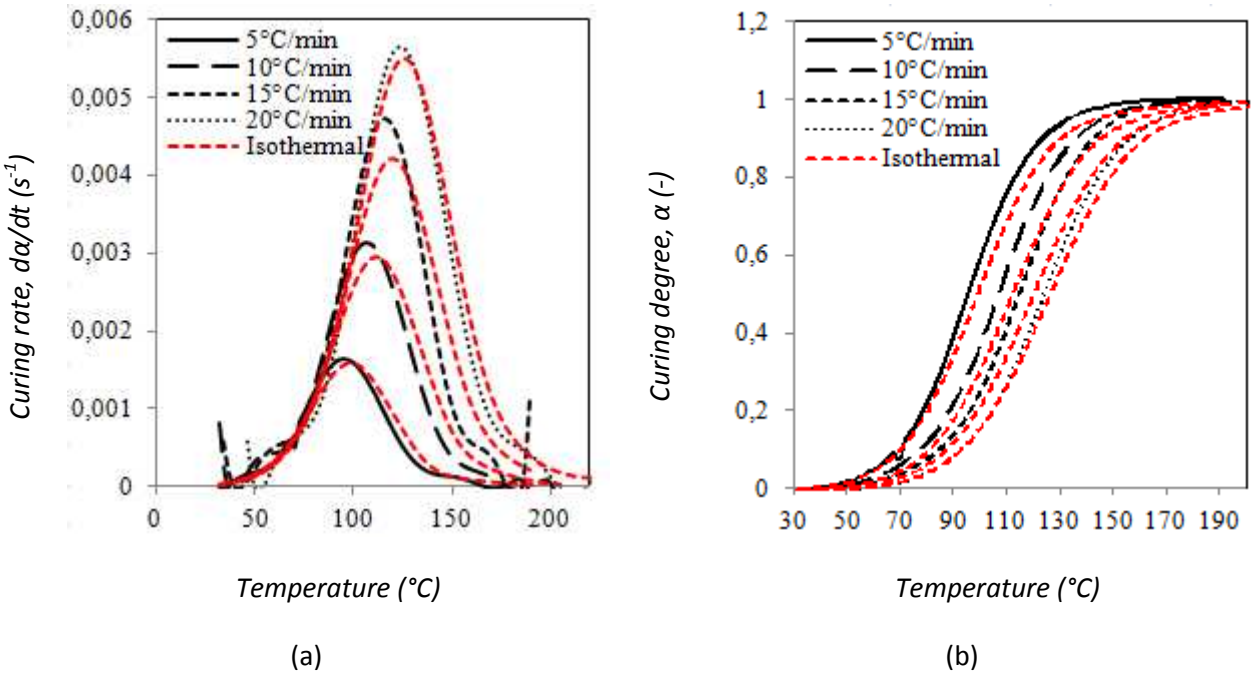

Figure 79. Isothermal modeling of dynamic experimental data: (a) curing rate vs. temperature and (b) curing degree vs. temperature.

Figure 79 shows that the curves predicted by the isothermal model correlate well with those of experimental dynamic scans. The slight delay caused by the isothermal model (Figure 79.b) seems acceptable regarding the fast heating rates. The kinetic parameters identified and the consideration of dynamic scans as a series of isothermal temperatures is validated.

2.5. Finite element modeling of curing of epoxy adhesive Hysol EA-9321

In this section, a model for the simulation of the curing process of an adhesive, particularly the adhesive Hysol EA-9321, in a bonded assembly was developed. This model was based on the three dimensional nonlinear heat transient conduction equation in association with a curing kinetics model, as found in the previous section, in order to evaluate the curing state of the adhesive during curing of the assembly. Then, the curing process of a cylindrical block of adhesive was experimentally set up. The validity of the suggested model was demonstrated by comparing the simulated results and measured data.

2.5.1. Problem statement

Considering the kinetic analysis, the cure modeling of the adhesive Hysol EA-9321 may be considered as a transient heat-transfer analysis by taking into account the effect of the adhesive polymerization reaction. This section is dedicated to the modeling of the curing behavior of the adhesive Hysol EA-9321 in a bonded assembly.

The curing process of a cold-curing adhesive such as the Hysol EA-9321 is analyzed by solving the energy equation [HUA 94]:

$$\rho C_p \frac{\partial T}{\partial t} = \nabla(\lambda \nabla T) + \phi_r + \phi_s \quad \text{, with} \quad \begin{cases} \phi_r = \rho \Delta H_r \dfrac{\partial \alpha}{\partial t} \\ \phi_s = T\{(3\lambda + 2\mu)\beta\}\dot{\varepsilon}^e \end{cases} \tag{2.16}$$

where ρ is the density of the adhesive, C_p the specific heat, λ the conductivity of the adhesive, T the temperature, H_r the total heat of the polymerization reaction and α is the degree of cure. Φ_r is the heat flux produced by the polymerization reaction. The kinetic term $\frac{\partial \alpha}{\partial t}$ was calculated thanks to the model of Kamal & Sourour with diffusion, as defined in section 2.4.2. Φ_s is the heat flux generated by the internal stresses. These last ones refer to the thermal dilatation and the chemical shrinkage during process. Throughout the study, we made the assumption that residual stresses (chemical shrinkage and thermal dilatation) are negligible for such adhesives as suggested by YU et al. [YU 13]. Thus, the energy equation becomes:

$$\rho C_p \frac{\partial T}{\partial t} = \nabla(\lambda \nabla T) + \phi_r \quad \text{, with} \quad \phi_r = \rho \Delta H_r \frac{\partial \alpha}{\partial t} \tag{2.17}$$

There are several models to describe the change of thermal properties over the curing. Regarding the specific heat capacity, an approach comes from Balvers et al. [BAL 08], who defined the specific heat capacity by a hyperbolic function depending on the temperature and on the glass transition temperature. A second approach was found by Johnston et al. [JOH 97] and defined that in the solid phase the heat capacity is only dependent on temperature. In the rubbery phase, the behavior is also depending on the curing degree. A third approach used a rule of mixture definition [GUS 91][GUS 94][VAN 99]. In the same way, there are several approaches to predict thermal conductivity. Skordos et al. [SKO 99] defined it as a polynomial function of temperature and curing degree. Chern et al. [CHE 02] defined the thermal conductivity by a temperature dependent fourth order polynomial. Another approach consists in using a simply rule of mixture [BAI 96][MIJ 88]. In this paper, the modification of the specific heat and thermal conductivity during curing was described by considering the chemical blend as perfect mixture of resin and hardener weighted by the curing state α [BAI 96][MIJ 88], i.e according to a simple rule of mixtures, as

shown in equation 2.18 and 2.19 [GUS 91][GUS 94][VAN 99]. The validity of this assumption will be discussed later. There are some ways to quantify these material properties. The specific heat capacity can be experimentally determined, with a Differential Scanning Calorimetry (DSC) analysis, by comparing the heat flow released by the sample to those of a calibration standard of known specific heat [MIJ 88]. The thermal conductivity is investigated through the Transient Plane Source method (TPS) [GU 91][GUS 94][MIJ 88][MOI 06].

$$C_p(\alpha, T) = (1-\alpha)C_p(0, T) + \alpha C_p(\alpha_{max}, T) \quad (2.18)$$

$$\lambda(\alpha, T) = (1-\alpha)\lambda(0, T) + \alpha\lambda(\alpha_{max}, T) \quad (2.19)$$

By considering the energy equation, it appears that the curing degree is a key parameter for the curing process study.

As shown in the previous section, the curing of an adhesive consists of a series of chemical reactions in which the system goes from a liquid to a solid state. Hence, this phenomena is set by the degree of cure α which is governed by an equation of time and temperature, such as kinetic equation of Kamal & Sourour with diffusion [KAM 73][KAM 76][CHE 87]. Therefore, the knowledge of the couple (α,T) at any time of the curing process let to determinate the cure dependent and mechanical properties of the adhesive. Considering the modeling of the thermal behavior of a bonded assembly, it consists in solving the thermo-kinetic coupling problem summarized in the equation 2.17.

2.5.2. Cure-dependent material properties: specific heat and thermal conductivity

As shown in equations 2.18 and 2.19, the specific heat and the thermal conductivity of the adhesive vary significantly during the curing process. These changes have an important effect on heat transfers generated within the adhesive during the heating process and therefore on transformation kinetics of the adhesive. As a result, the variation of these thermal properties must be introduced into the finite element model developed in order to give accurate predictions of temperature and curing degree of the adhesive. These data were experimentally determined in uncured and fully cured state according to the following methods described.

2.5.2.1. Measurement of specific heat

Determination of specific heat was accomplished by using a Differential Scanning Calorimetry (DSC). These DSC experiments were carried out on a Perkin-Elmer DSC-7 (Figure 60). The DSC heat flow signal from the adhesive Hysol EA-9321 was compared to the DSC signal of a calibration standard of known specific heat. Both curves are corrected by a baseline correction. This one was achieved by measuring heat flow released by an empty sample. Isothermally, the baseline indicated the differential losses of the two sample holders at the initial temperature. Determination of C_p according to ASTM E1269 [AST 05] was determined by using a three steps technique. Experiment was conducted with an empty sample crucible for baseline determination. Then, a measurement with a sample crucible of sapphire was made for calibration standard. At last, heat flow was measured for a sample crucible of cured and uncured adhesive Hysol EA-9321. The same procedure was used for the four experiments: an isothermal scan was made 10 minutes at 25°C, a dynamic scan from 25°C to 150°C at heating rate of 10°C/min and an isothermal measurement 10 minutes at 150°C was performed.

To determine the specific heat capacity of the uncured adhesive, the previous procedure was applied directly on the resulting mixture of the resin and hardener. Concerning the heat capacity of the cured adhesive, a heating from 25°C to 150°C was performed before applying the previous procedure.
Figure 80 shows results obtained after testing. Regarding the uncured adhesive, a change of the slope is observed. It corresponds to the glass transition temperature. The specific heat capacity of the uncured adhesive was the value calculated before this point.

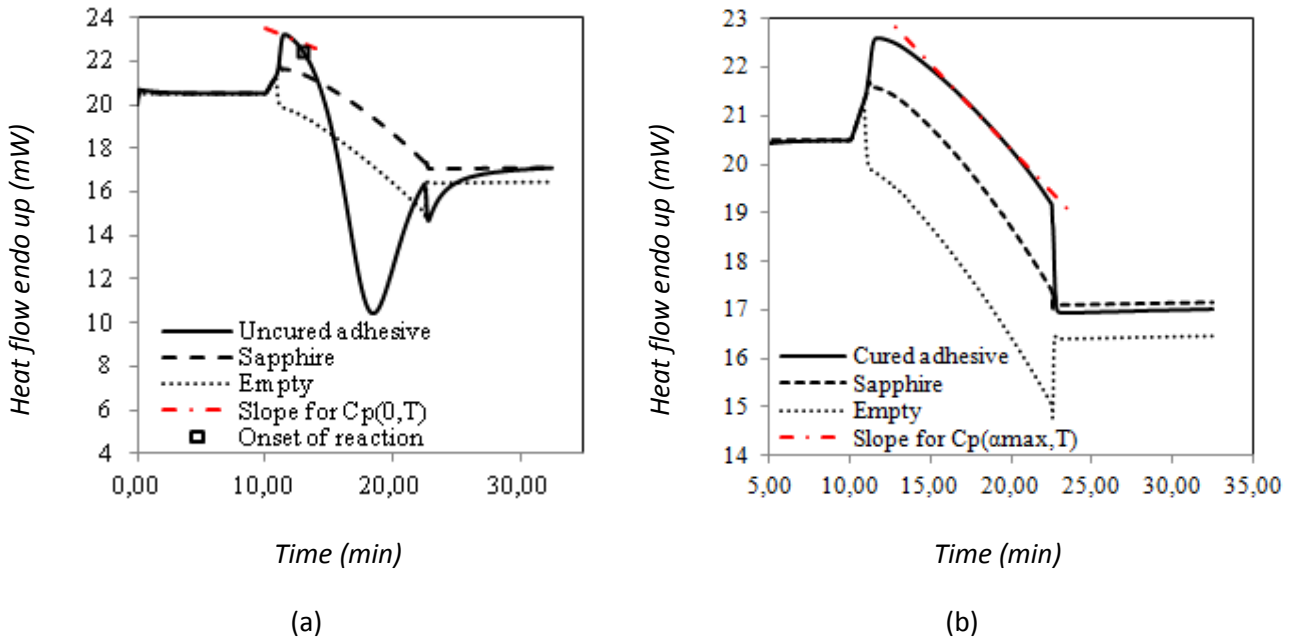

Figure 80. Heat flow endo up vs. time: (a) uncured adhesive sample and (b) cured adhesive sample.

Specific heats of cured and uncured adhesive were calculated as follows:

In a DSC cell, in the previous conditions, the heat flow measured on the sample side is expressed by the following heat transfer equation:

$$\left(\frac{dH(T)}{dt}\right)_{sample} - \left(\frac{dH(T)}{dt}\right)_{baseline} = m_{sample} C_{p,sample} \frac{dT_{sample}}{dt} \quad (2.20)$$

where $dH/dt(T)_{sample}$, $dH/dt(T)_{baseline}$ are the heat flow rates of sample (adhesive Hysol EA-9321), baseline. m_{sample} is the mass of the sample and T_{sample} the temperature of the sample.
In the same way, for the experiment with the standard, it can be written:

$$\left(\frac{dH(T)}{dt}\right)_{standard} - \left(\frac{dH(T)}{dt}\right)_{baseline} = m_{standard} C_{p,standard} \frac{dT_{standard}}{dt} \quad (2.21)$$

where $dH/dt(T)_{standard}$, $dH/dt(T)_{baseline}$ are the heat flow rates of reference (sapphire), baseline. $m_{standard}$ is the mass of the reference and $T_{standard}$ the temperature of the reference.
In the previous procedure, the sample and reference are submitted to the same temperature, hence the same heating rate. It comes:

$$C_{p,sample} = \frac{m_{standard}}{m_{sample}} \frac{\left(\frac{dH(T)}{dt}\right)_{sample} - \left(\frac{dH(T)}{dt}\right)_{baseline}}{\left(\frac{dH(T)}{dt}\right)_{standard} - \left(\frac{dH(T)}{dt}\right)_{baseline}} . C_{p,standard} \quad (2.22)$$

$\left(\frac{dH(T)}{dt}\right)_{sample}$ for the uncured and fully cured adhesive was chosen as detailed in Figure 80 (a) and Figure 80 (b). For the uncured adhesive, it is necessary to consider temperatures below the onset of the polymerization reaction (in our case, for temperatures under 45°C) to avoid the adhesive curing. The previous kinetic analysis (section 2.4) shows a value of curing degree below to 0.1. It is not surprising since, in this area, the temperature goes from 25 to 40°C at a heating rate of 10°C/min. This rate is sufficiently high to prevent the adhesive curing.

By applying equation 2.20 to results given by Figure 80, the specific heats of uncured and cured adhesive Hysol EA-9321 were related to the temperature as follows:

$$\begin{aligned} C_p(0,T) &= 1.50 + 0.002T \quad \left(J.g^{-1}°C^{-1}\right) \\ C_p(\alpha_{max},T) &= 0.91 + 0.004T \quad \left(J.g^{-1}°C^{-1}\right) \end{aligned} \quad (2.23)$$

The orders of magnitude of specific heat capacity of uncured and cured adhesive are not surprising since more the adhesive is cross-linked, the easier it is to heat. Therefore, the specific heat decreases.

2.5.2.2. Measurement of thermal conductivity

Thermal conductivities of uncured and cured adhesive can be determined with the Transient Plane Source (TPS) Method. This one used a circular double nickel spiral (10 µm thick), sandwiched between two layers of Kapton (polyamide film) (25 µm thick) in contact with the material sample. The spiral serves of heat source and resistance thermometer. When measuring, the sensor (Figure 81) is clamped between two identical samples of the material. Then, a constant electric power is conducted through the spiral to introduce an increase of temperature. As a consequence of this temperature increase, the resistance of the sensor changes. The thermal conductivity of the material can be calculated with the variation of the voltage, temperature and heat flow during experiment. Gustafsson et al. [GUS 91] described how the thermal conductivity is calculated using the TPS data.

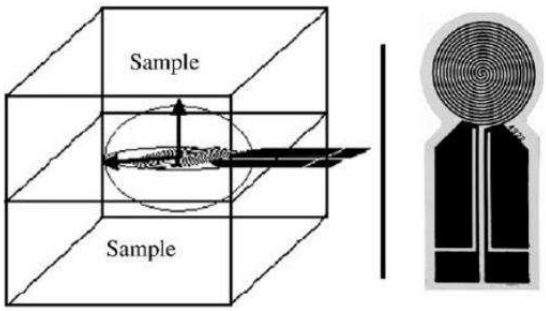

Figure 81. Experimental set-up and TPS method sensor.

In our case, for lack of experimental set-up, no experiment was investigated to determine the thermal conductivities of fully cured and uncured adhesive. However, these quantities have already been determined in a previous study conducted by CNES, as follows:

$$\lambda(0,T) = 0.19 \quad (W.m^{-1}K^{-1})$$
$$\lambda(\alpha_{max},T) = -2.73.10^{-4}T + 4.00.10^{-1} \quad (W.m^{-1}K^{-1}) \qquad (2.24)$$

The magnitude of these thermal conductivities are not surprising since more the adhesive is cross-linked, the easier it is to heat. The heat transfer is more important, thus, the thermal conductivity increases.

2.5.3. Solution procedure

The problem can be classified into two categories. In one hand, it consists in a transient thermal analysis by solving the energy equation. In other hand, an evolution law for the curing degree must be provided.
A procedure is proposed in which a general-purpose FE package is employed to perform transient heat-transfer analysis and programs are developed to simulate the cure reaction of the adhesive Hysol EA-9321. Figure 82 provides the flow chart of the procedure.

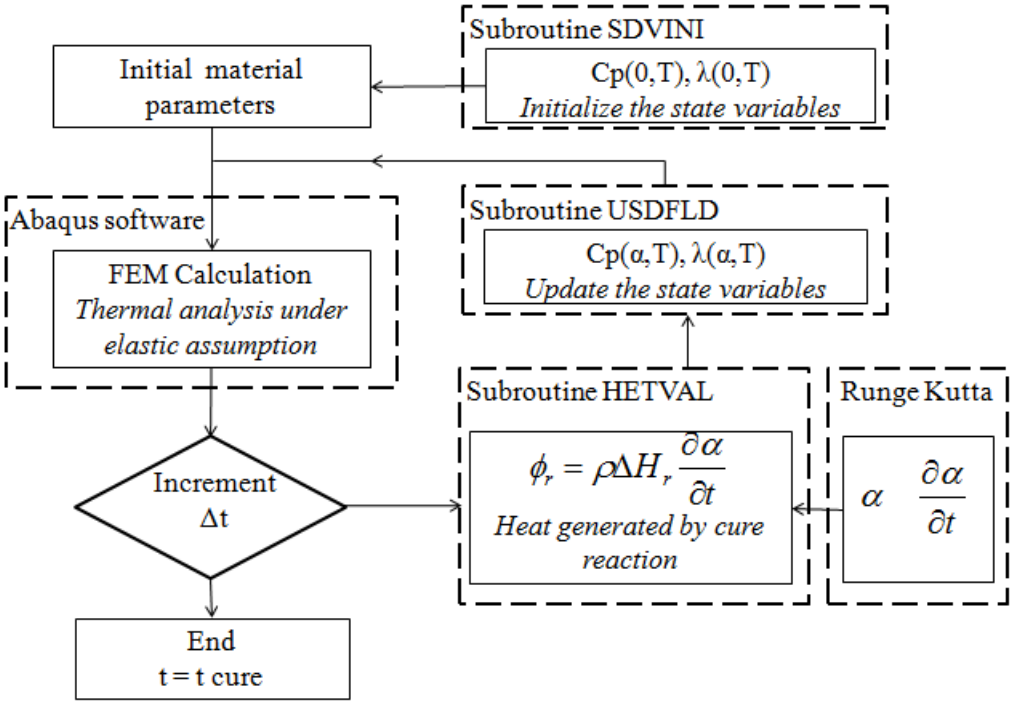

Figure 82. Flow chart for FE procedure of curing process.

The available pre-processor to the FE package is used to create model and to generate the initial input data file for the analysis. Three user subroutines were developed to take into account problems generated by the adhesive curing. The subroutine SDVINI was used to define the initial values of specific heat $C_p(0,T)$ and conductivity $\lambda(0,T)$. These quantities were experimentally determined according to the procedure detailed in the previous section. The subroutine HETVAL consisted in determining, at each Gauss point, the heat produced by the reaction of polymerization and the curing degree by solving the cure kinetic equation of Kamal & Sourour with diffusion (equation 2.15) with parameters validated in section 2.4. As defined previously, specific heat and conductivity are related to temperature and curing degree. Hence, the subroutine USFLD enabled to update these material parameters at each increment.

2.5.4. FE Model and Validation

In order to validate the previous procedure and to test its reliability, the curing of an adhesive block was considered. Other experiments were performed simultaneously in order to determine values of specific heat and conductivity for uncured and totally cured adhesive.

2.5.4.1. Experiment: curing of a cylindrical block of adhesive

To determine curing degree evolutions of the adhesive Hysol EA-9321 under various curing time and temperature conditions, an experimental procedure was developed. The uncured adhesive was introduced in a steel tube (h2=43mm, e=1.2mm and r=11.3mm). This one was placed vertically on a steel plate (h1=3mm) to avoid the adhesive from flowing out (Figure 83).The whole was then kept in the oven at several curing cycles (1h at 100°C, 3h at 60°C). In order to verify the numerical modeling, temperature profiles inside the adhesive block were recorded through the experiment and compared with the numerical results. Figure 83 (b) illustrates the schematic diagram of the experimental set-up used to measure the temperature evolution during the curing process. The thermocouples were placed at different locations inside the adhesive, points A, B and C in the Figure 83 (b) and connected to a data acquisition system to monitor the temperature versus time.

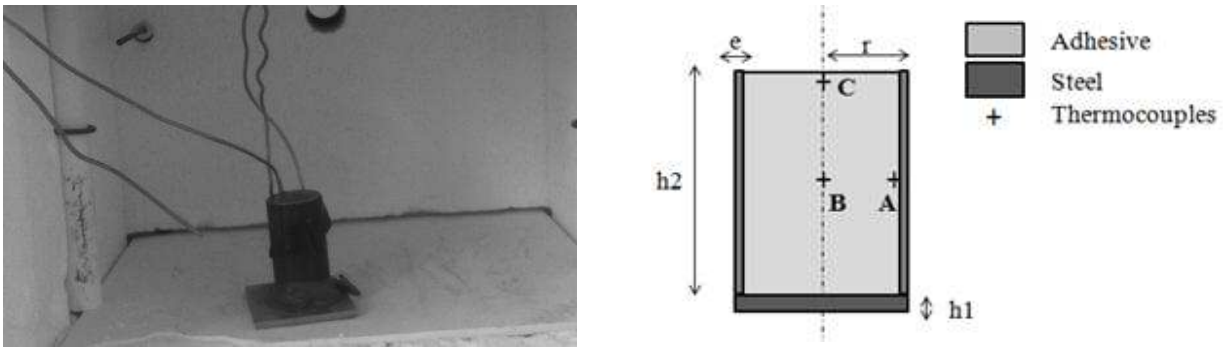

(a) (b)

Figure 83. (a) Experiment and (b) schematic diagram of the experimental set-up.

2.5.4.2. Finite Element model

In order to understand the curing behavior of the previous experiment, a two-dimensional FE analysis on an axisymmetric slice was performed (Figure 84) by using adequate boundary conditions. Due to the axial symmetry, the mesh was performed with 8-node axisymmetric thermally coupled quadrilateral, biquadratic in displacement and bilinear in temperature (CAX8T elements of the Abaqus element library). A mesh with 6 elements in the x-direction and 40 elements in the y-direction was used for adhesive. A step-time size of 1s was used to predict accurate results. In this model, a film convection on the faces of the assembly exposed to the oven environment modeled the thermal loading, using a heat transfer coefficient characteristic of forced convective heating. Results are presented for steel plate and an elastic behavior was assumed for the adhesive Hysol EA-9321. Table 15 shows material parameters used.

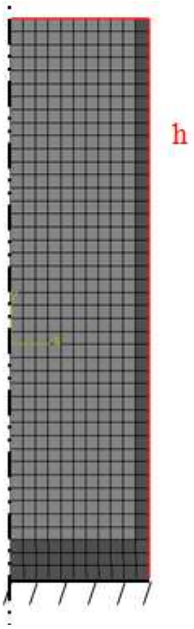

Figure 84. Mesh and boundary conditions.

Material	Steel	Hysol EA-9321
Young Modulus E [MPa]	210 000	3480
Poisson ν	0.3	0.369
Density ρ [$kg.m^{-3}$]	7800	1250
Specific Heat Cp [$J.kg^{-1}.K^{-1}$]	0.5	$Cp(0,T)=1.50+0.002T$ $Cp(\alpha_{max},T)=0.91+0.004T$
Conductivity λ [$W.m^{-1}.K^{-1}$]	25	$\lambda(0,T)=0.19$ $\lambda(\alpha_{max},T)=-2.73^{e-4}T+4.0^{e-1}$

Table 15. Material properties.

The FE procedure of curing process was firstly applied to one element (a 4-node plane strain thermally coupled quadrilateral, bilinear in displacement and temperature). A ramp from 25°C to 200°C at a heating rate of 10°C/min was applied. Then, the curves curing-rate vs. temperature and curing degree vs. temperature were compared with those predicted by the model of Kamal & Sourour with diffusion (Figure 79). It appears that the curves predicted by the FE model correlates well with the curves of the model. This intermediate step was a way to validate the FE procedure.

Then, the temperature and the degree of cure of the adhesive during the curing were simulated by using the finite element model described previously. Then, these last one were compared with experimental data. The simulated temperature and degree of cure were taken at the location of the thermocouple probes used in the experimental procedure. It was assumed that no thermal perturbation was generated by the thermocouple.

2.5.4.3. Results and discussion

Figure 85 shows the temperature and curing degree profiles for different curing cycles obtained by simulation and experiment in B location (Figure 83 (b)). The evolution of the curing degree for experiment was obtained as follows:
Figure 85 shows the temperature and curing degree profiles for different curing cycles obtained by simulation and experiment in B location (Figure 83 (b)). The evolution of the curing degree for numerical and experiment results were obtained from the evolution of the temperature inside the adhesive, as follows:

As shown previously in section 2.3, a modified model of Kamal & Sourour with a dependence of some parameters to the temperature was proposed. Hence, the parameters of this model were known for the temperature measured during experiment and the one that was predicted by the FEM model on Figure 85. Then, the equation 2.18 was solved using a fourth-order Runge-Kutta method. Thus, it came the evolution of the curing degree versus time corresponding to the experimental and numerical temperatures of Figure 85 (b).

The predicted temperature and curing degree for each curing cycles were in good agreement with the experimental results. Thus, the validity of the model was confirmed, as well as the values determined for kinetic and thermal parameters. Similar results are observed for locations in A and C (Figure 83 (a)).

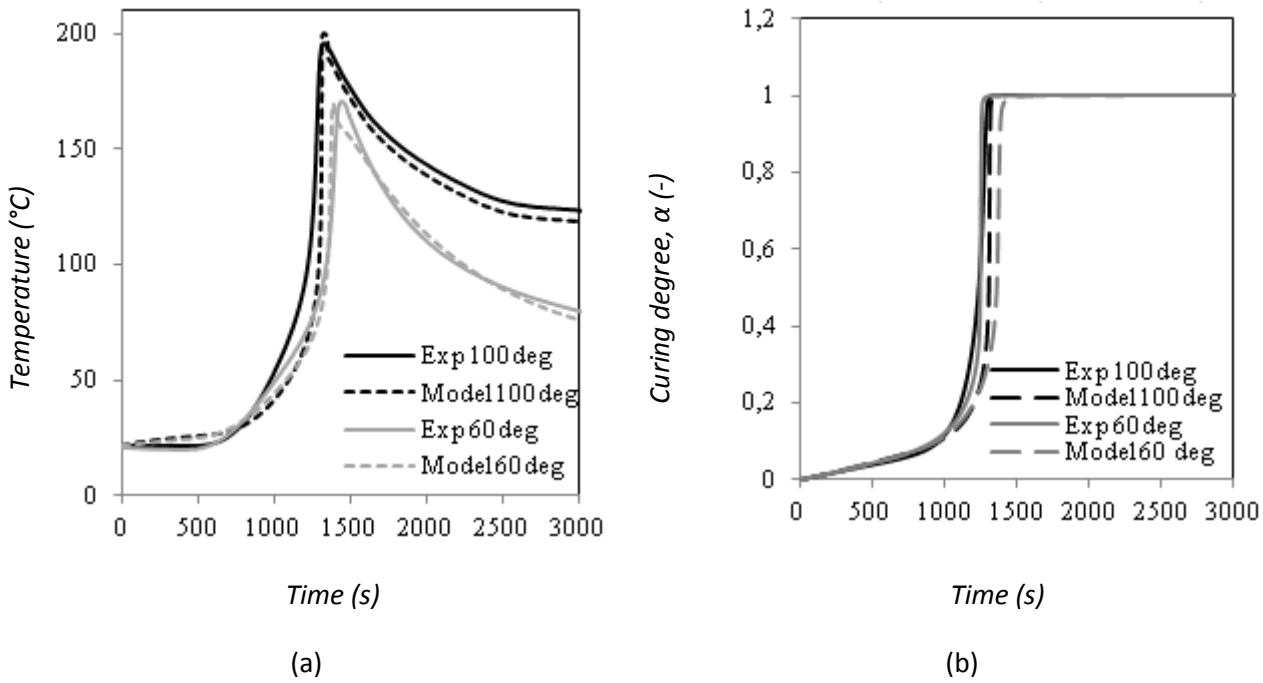

Figure 85. Comparison of experimental and predicted results: (a) Temperature-time history and (b) Curing degree-time history.

The predicted temperature and curing degree profiles (Figure 85) are in good agreement with the experimental results. There are few temperature and curing degree discrepancies between experimental and simulation results. These differences can firstly come from kinetic and thermal parameters. Secondly, it can be explained by the assumptions considered for the modeling. Furthermore, the adhesive thickness was supposed to be constant whereas in reality a shrinkage behavior due to the cure reaction and thermal expansion can be generated [YU 13]. In addition, the thermocouples could be displaced from their initial position during the experiment.
A sensitivity analysis on thermocouple position, kinetic, thermal parameters and the adhesive thickness was performed to better understand the differences between experiment and simulation results.

2.5.4.4. Influence of the thermocouple location

The temperature in the adhesive was experimentally measured thanks to thermocouples. These last ones were placed in the adhesive cylinder before the curing process. During the curing process, the adhesive passed from the raw (uncured liquid) to the cured rubbery and ultimately, to the cured glassy state. At the beginning of curing, the adhesive was an uncured liquid. Hence, the thermocouples positions may be affected by the adhesive state during curing.

The experiment was the same as previously but the thermocouple was located in point D (Figure 86) between points A and B (Figure 83 (a)). In order to show the influence to get closer to the side wall or to the middle of the tube, the temperature was experimentally measured and compared to results predicted by simulation. Then, the location of the thermocouple was used as a reference and the temperature and curing degree were numerically investigated around this reference.

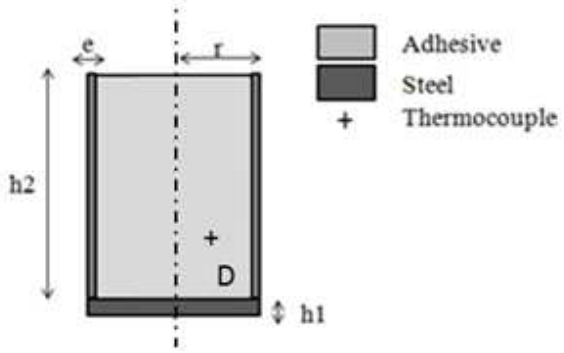

Figure 86. Location of the thermocouple used for the sensitivity analysis of the thermocouple location.

Figure 87 and Figure 88 show the effect of vertical and horizontal displacement on the temperature and the curing degree profiles for a curing at 60°C.

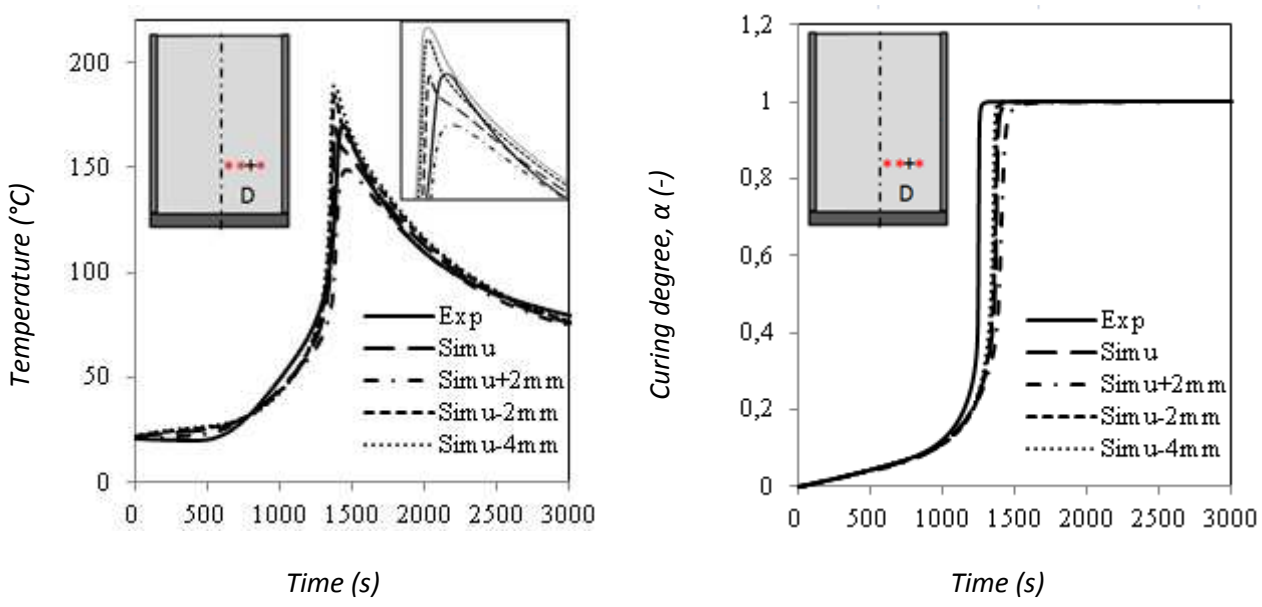

(a) (b)

Figure 87. Effect of the thermocouple location in the horizontal direction on (a) the temperature-time history and (b) the curing degree-time history at the point D(8;10) in the adhesive.

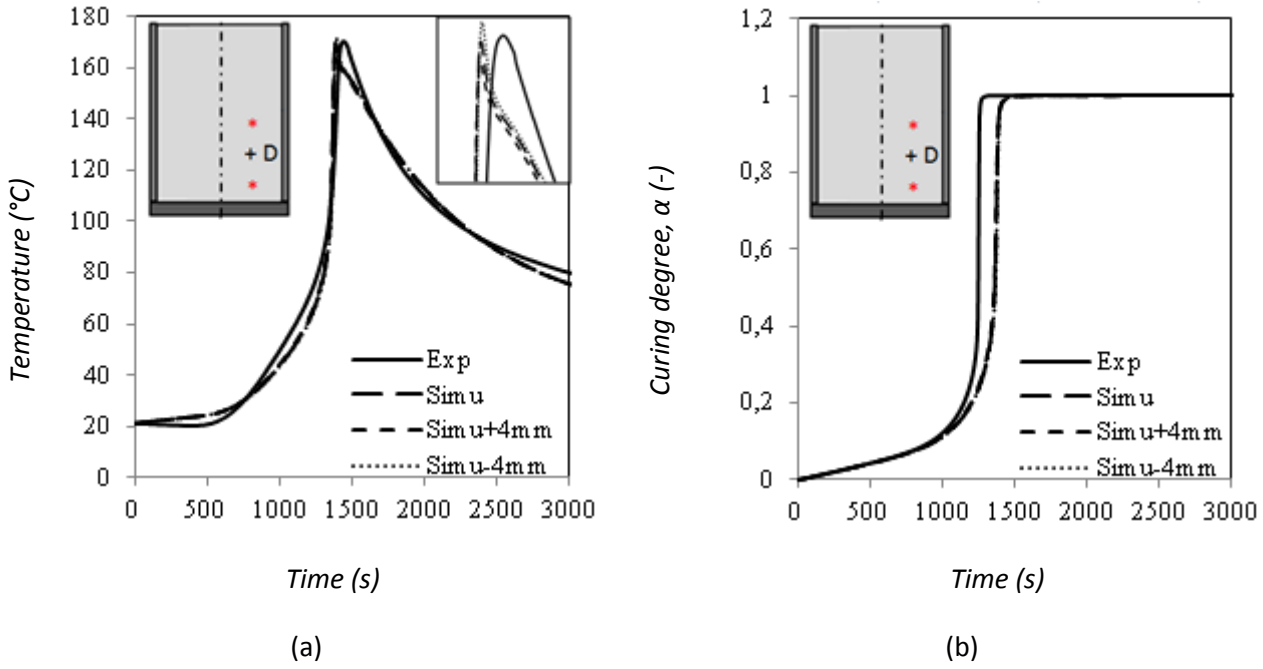

Figure 88. Effect of the thermocouple location in the vertical direction on (a) the temperature-time history and (b) the curing degree-time history at the point D(8;10) in the adhesive.

The temperature and the curing degree were not affected by a vertical displacement of the thermocouple (Figure 88). However, radial displacements were important (Figure 87). Regarding the temperature, the difference being essentially the change in the maximum value reached. For instance, a thermocouple 2 mm beside its initial position (closer to the adhesive core) was responsible of an increase of maximum temperature of 13°C. In the same way, a probe 4 mm beside the first location caused a reduction of 17°C of the peak temperature. This modification had repercussion on the curing degree (Figure 87 (b)). It is not surprising since, the thermal conductivity is lower for the steel tube than the adhesive. Thus, the difference with the temperature applied on external surfaces of the tube is more important in the adhesive core than close to the side wall. Indeed, a change in the maximum temperature delayed or accelerated the maximum value reached by the curing degree. This last one reached its maximum after 1515s for a probe 2 mm above the first position against a maximum got after 1366s for a thermocouple down from 4 mm.

2.5.4.5. Influence of kinetic parameters

The model used to describe the curing behavior of the adhesive Hysol EA-9321 (section 2.4.1) came from the assumption that dynamic scans were a series of isothermal measurements. Hence, the parameters of this model were an average of parameters of each isothermal scans. This assumption caused a modification of the physical properties of input parameters of the kinetic problem and can affect the temperature and curing degree profiles resulting from the energy equation.

A parametric study was realized on kinetic parameters such as total heat of reaction ΔH_T, reaction orders m, n, the activation energies E_1, E_2 and the rate constants k_1, k_2. For each simulation, a cure cycle of three hours at 60°C was applied. The temperature and curing degree profiles were simulated at the location of a thermocouple used during experiment.

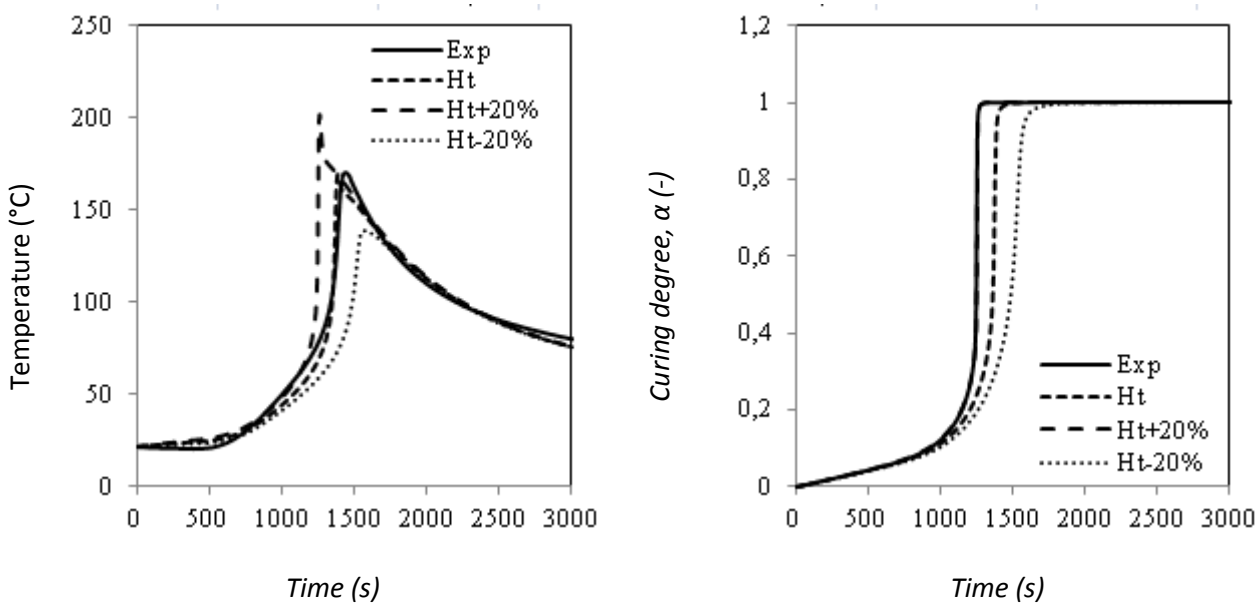

Figure 89. Effect of the total heat of reaction on (a) the temperature-time history and (b) the curing degree-time history at the point D(8;10) in the adhesive.

Figure 89 shows the effect of the total cure enthalpy on the temperature and curing degree profile during curing. This parameter had an important impact on the predicted results, not only for the peak temperature but also for the slopes of these curves. A variation of 20% of the total heat of reaction got a change of about 32°C in the peak temperature (Figure 89 (a)). Considering this, a modification of the cure enthalpy delayed or accelerated the time for which the maximum value of the curing degree is reached: delayed of 162s for a decreased of 20% of the enthalpy and accelerated of 319s for an augmentation of 20% of the total heat of reaction.

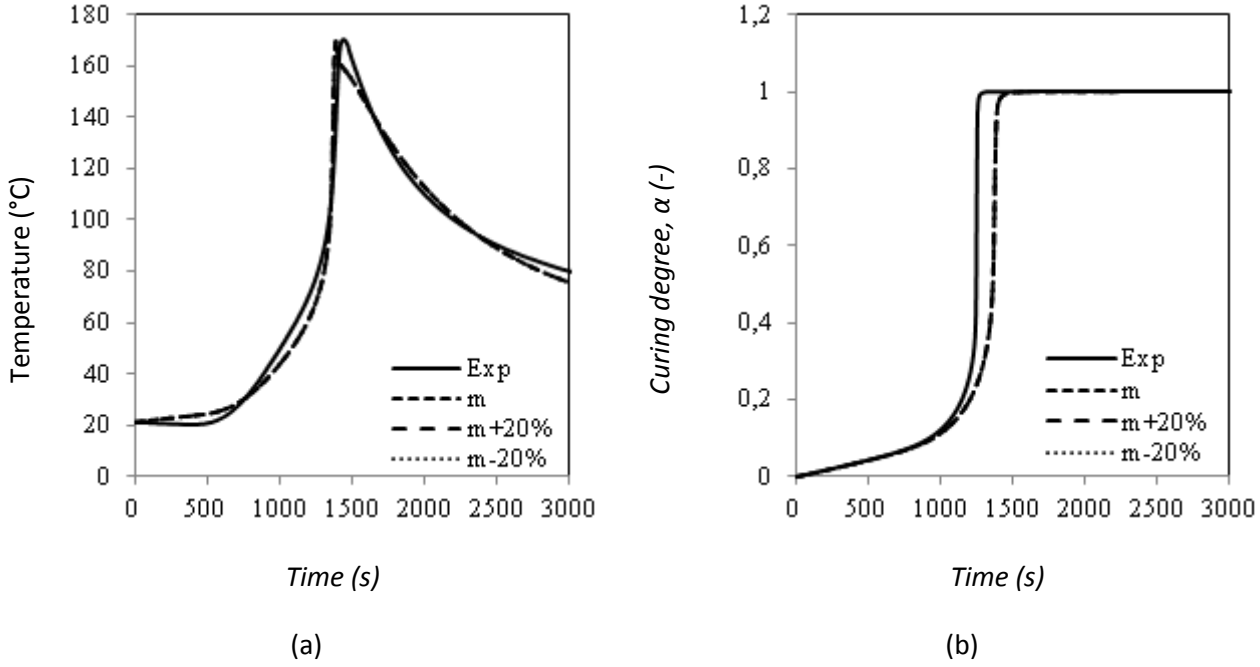

Figure 90. Effect of the reaction order m on (a) the temperature-time history and on (b) the curing degree-time history at the point D (8;10) in the adhesive.

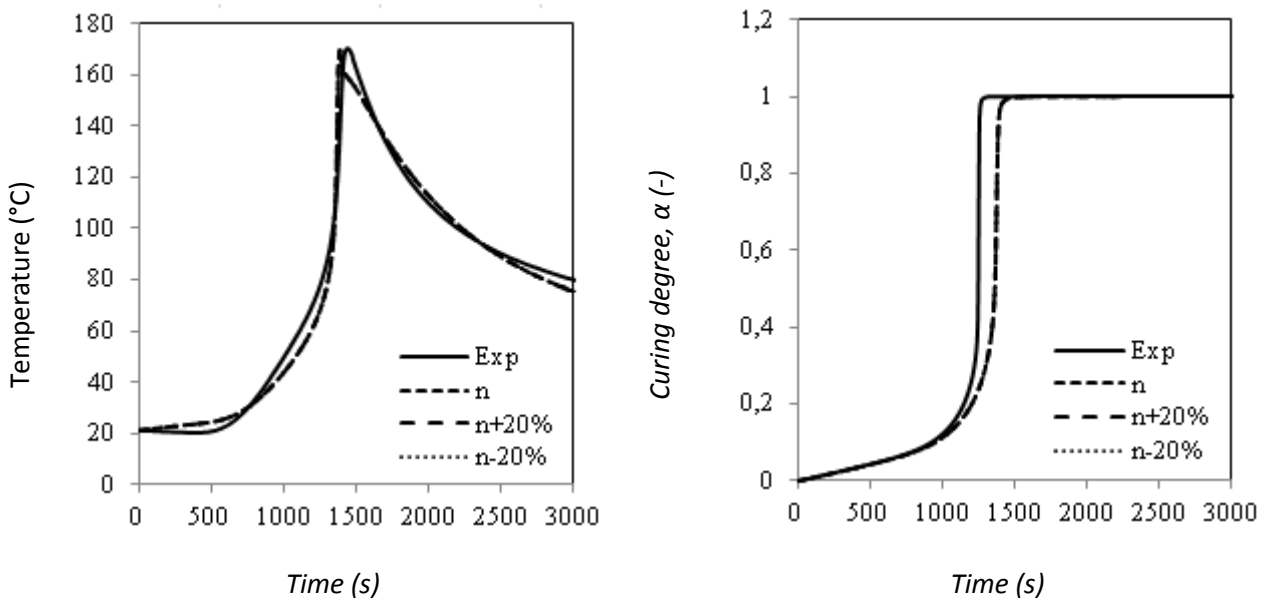

(a) (b)

Figure 91. Effect of the reaction order n on (a) the temperature-time history and on (b) the curing degree-time history at the point D (8;10) in the adhesive.

The reaction order *m* and *n* have very few effects on the temperature and curing degree profiles (Figure 90 and Figure 91). In fact, a variation of 20% of the orders had no impact on the slopes of the curves and the maximum values reached.

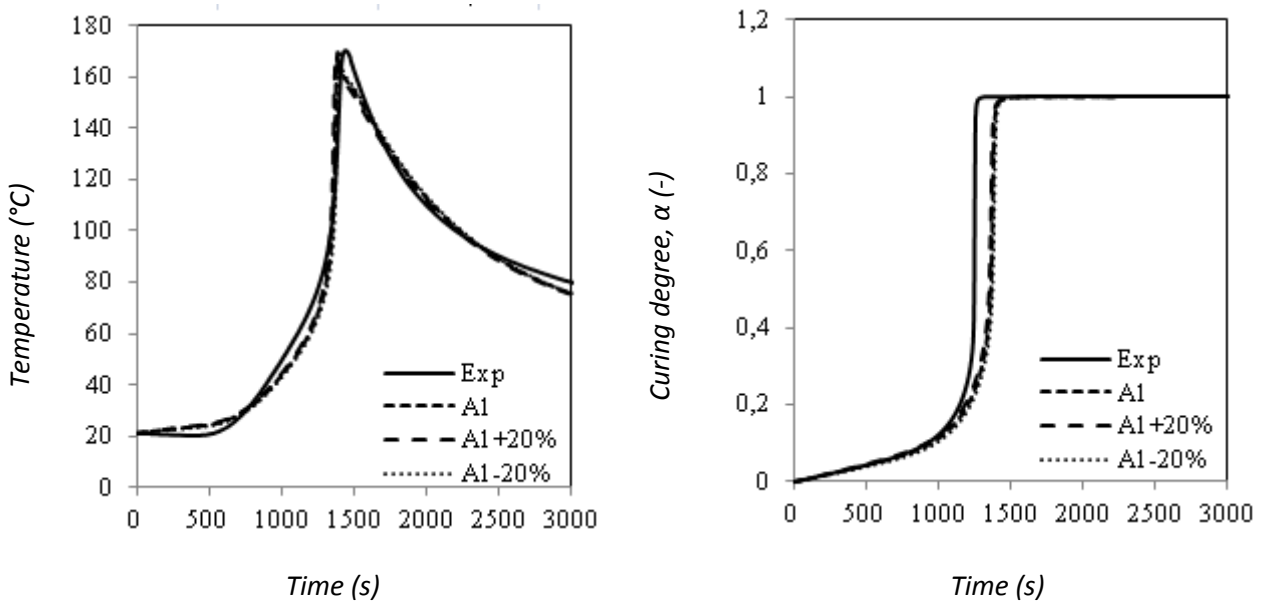

(a) (b)

Figure 92. Effect of the rate constant A_1 on (a) the temperature-time history and on (b) the curing degree-time history at the point D (8;10) in the adhesive.

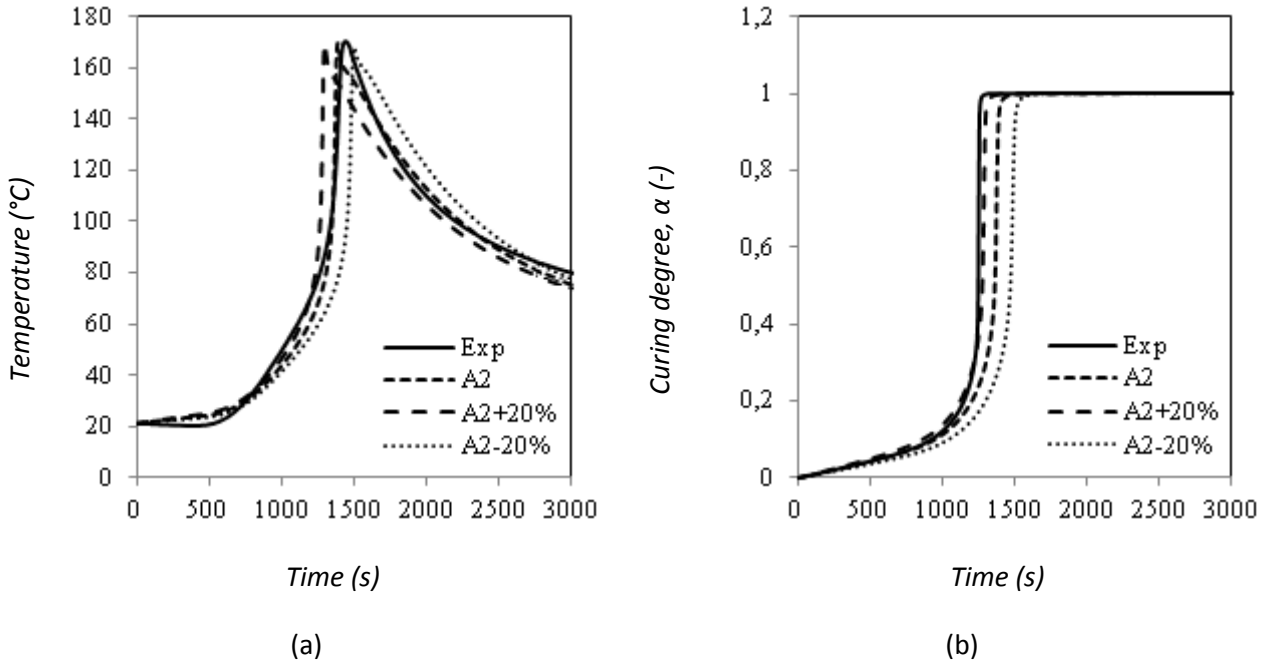

(a) (b)

Figure 93. Effect of the rate constant A_2 on (a) the temperature-time history and on (b) the curing degree-time history at the point D (8;10) in the adhesive.

Variations of the rate constants had different impact on the simulation results (Figure 92 and Figure 93). Regarding the first rate constant A_1, a modification caused no effect on the temperature and curing degree responses. It was not surprising since, in equation 2.18, the first constant rate had no effect on the curing rate. It was just used to initialize its value. Contrary to the previous constant, the secondly rate constant affected the temperature and curing degree profiles (Figure 93): the higher the rate constant, the faster the cure reaction. This was responsible for a higher slope of the temperature-time response corresponding to the highest value of the rate constant. It appeared once the reaction took place, i.e. at around 60°C. The state of cure was changed in time as shown in Figure 93 (b). About 1420 s were necessary to attain the maximum curing degree for an increase of 20% of the rate constant A_2 against 1563s for the initial reaction rate and 1589s for a decrease of 20% of the rate constant.

The effects of a variation in the activation energies E_1 and E_2 on the temperature-time and curing degree-time profiles appeared in Figure 94 and Figure 95. For the same reasons as for the rate constant A_1, Figure 94 shows that the energy activation E_1 had no effect on the temperature and curing degree responses. Regarding the secondly activation energy E_2, Figure 95 shows that this one caused a great impact on the simulation responses. The lower is the activation energy, faster is the cure. Thus, the slopes of the temperature curves (Figure 95 (a)) were lower for the higher value of activation energy. Furthermore, an increase of the energy activation value E_2 increased the time necessary to get the maximum value of the curing degree. About 936s were necessary to attain the maximum curing degree for a decrease of 5% of the activation energy E_2 against 1420s for the initial reaction rate and 2269s for an increase of 5% of the rate constant.

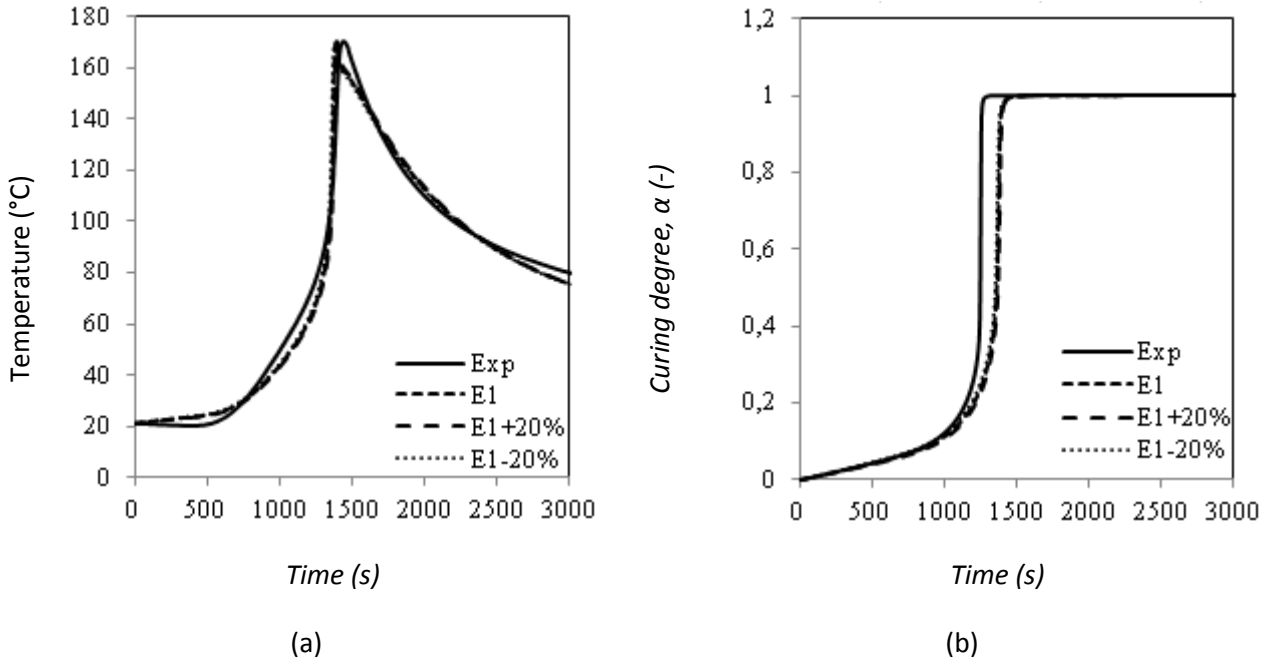

(a) (b)

Figure 94. Effect of the activation energy E_1 on (a) the temperature-time history and on (b) the curing degree-time history at the point D (8;10) in the adhesive.

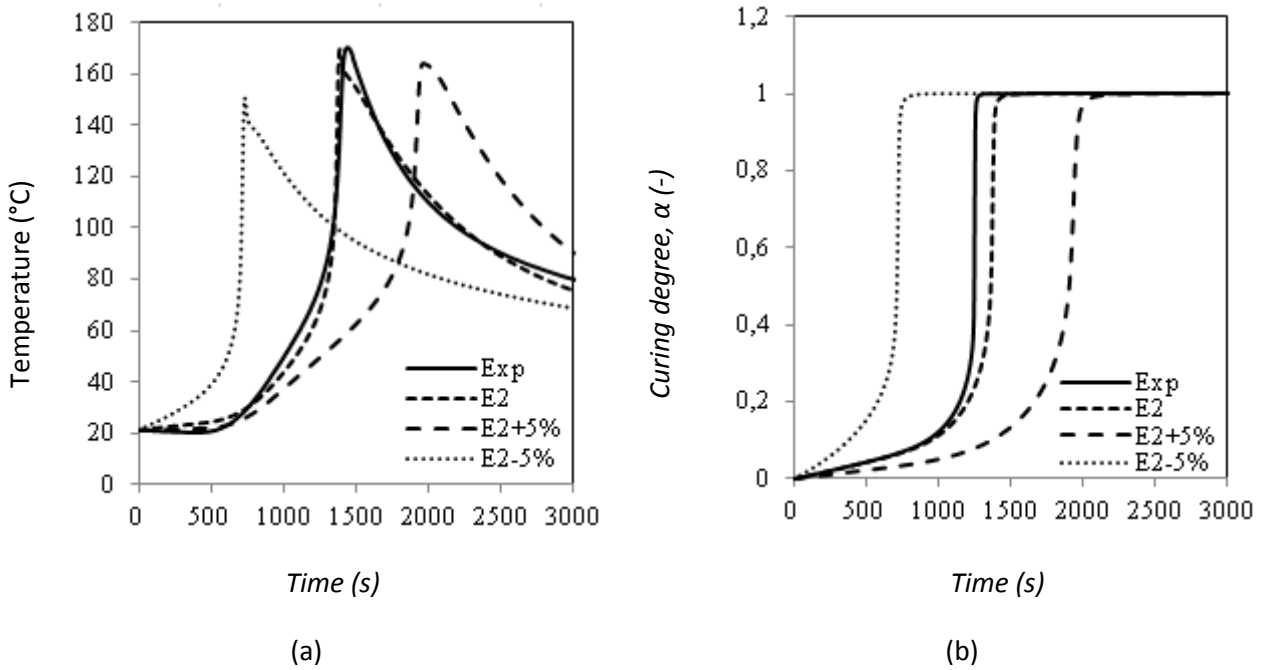

(a) (b)

Figure 95. Effect of the activation energy E_2 on (a) the temperature-time history and on (b) the curing degree-time history at the point D (8;10) in the adhesive.

2.5.4.6. Influence of thermal parameters

Thermal parameters such as heat capacity and thermal conductivity were previously related to temperature and curing degree. Hence, these previous ones were also influenced by the modification of the physical properties of the input parameters. In the same way as previously, a sensitivity study on these parameters was investigated. A curing cycle of 60°C was applied and the temperature at the place of a thermocouple was simulated.

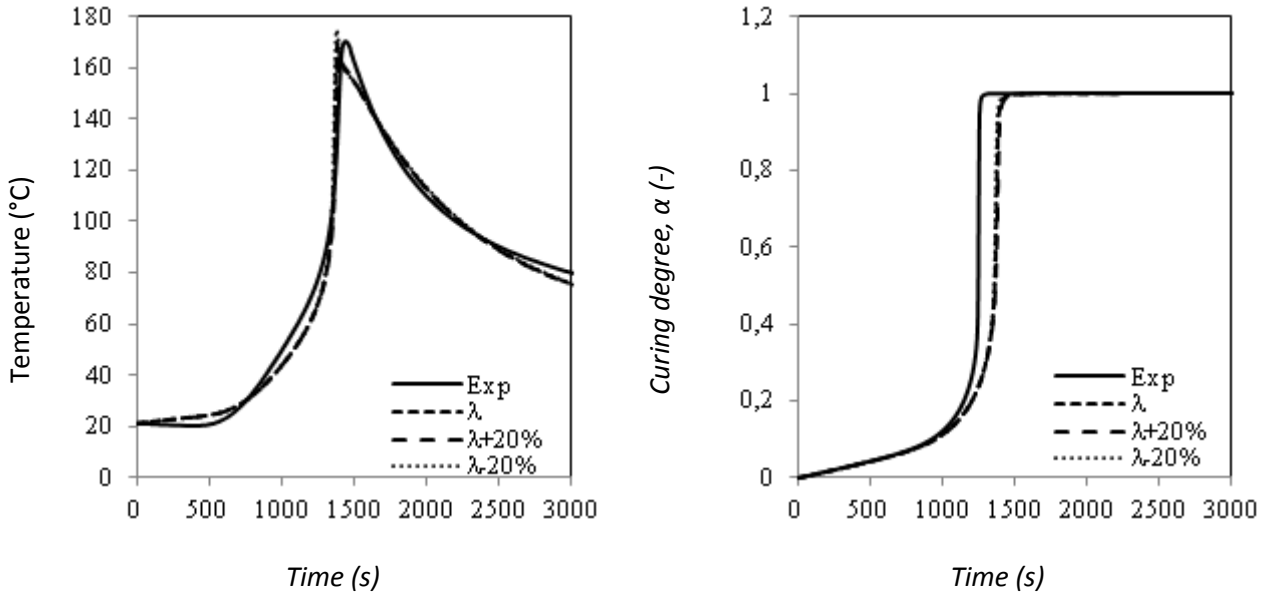

(a) (b)

Figure 96. Effect of the thermal conductivity on (a) the temperature-time history and on (b) the curing degree-time history at the point D (8;10) in the adhesive.

Figure 96 shows the influence of the thermal conductivity on the simulation responses. It appeared that this last one had negligible effects.

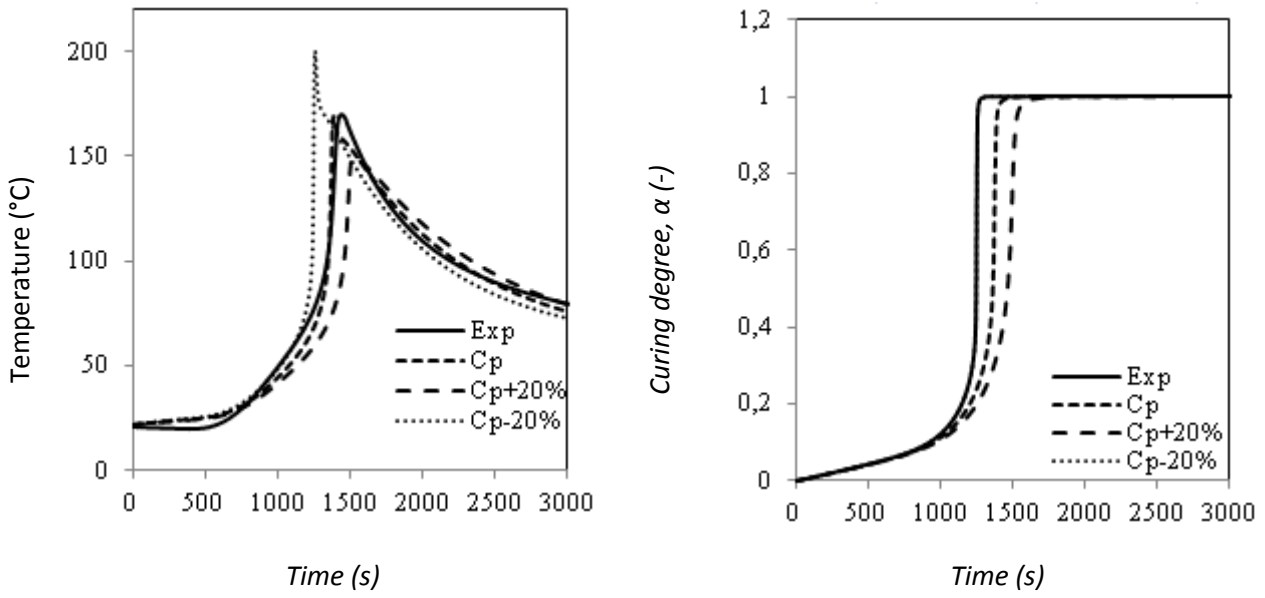

(a) (b)

Figure 97. Effect of the heat capacity on (a) the temperature-time history and on (b) the curing degree-time history at the point D (8;10) in the adhesive.

The specific heat affected the temperature-time and the curing degree-time histories (Figure 97). It can be predicted, since, according to equation 1, the specific heat was related to the conduction heat and the internal heat generated from the cure. An increase of the specific heat caused a decrease of the maximum temperature reached and, therefore, delayed the time necessary to attain the maximum value of the curing

degree: for Cp+20%, the maximum temperature was decreased of around 16°C and the maximum curing degree was attained 235s after the experiment.

As shown previously, thermal properties such as specific heat and thermal conductivity were described with a rule of mixture laws. However, these material properties, particularly the specific heat capacity, have an influence on the temperature response predicted by the FEM model (Figure 97). Figure 85 shows a good correlation between experimental and numerical results. Therefore, it seems acceptable to use such laws.

2.5.4.7. Thickness effects on cure predictions

The effect of adhesive thickness on temperature and curing degree responses was studied. The simulation was based on the same boundary conditions and the same assumptions as previously. The temperature and the curing degree were taken at the center of the adhesive to reflect the thermal gradients generated during curing for several adhesive thicknesses.

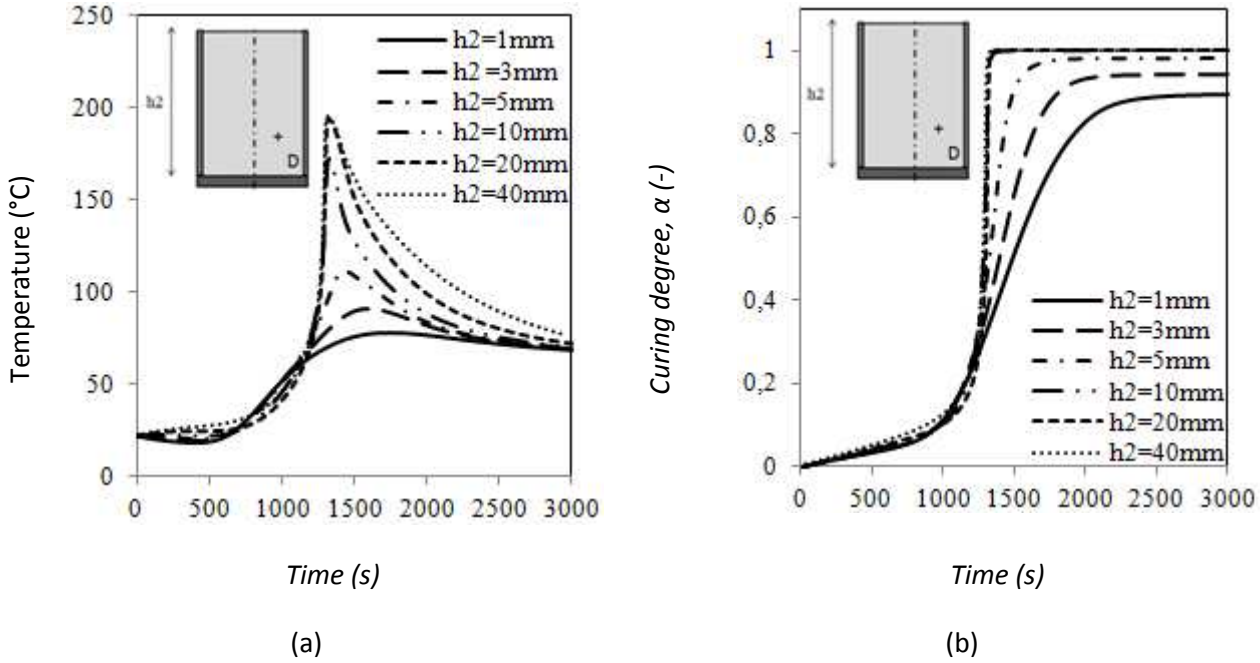

Figure 98. Effect of the adhesive thickness on (a) the temperature-time history and (b) the curing degree-time history at the center of the adhesive.

Figure 98 shows that the adhesive thickness generated thermal gradients during the cure of the adhesive. A decrease of the adhesive thickness caused a reduction of the maximum temperature reached at the center of the adhesive and, thus, a decrease of thermal gradients. The center of the adhesive was submitted to different curing cycle according to the adhesive thickness. Thus, the curing degree evolved differently as shown in Figure 98 (b). For instance, for a thickness of 1 mm, the maximum peak temperature was around 76°C whereas this peak was of 194°C for a thickness of 40 mm. It is not surprising that the maximum curing degree is lower for a thickness of 1mm than for a higher thickness considering thermal gradients generated during each curing cycles.

It appeared that parameters such as the total heat of reaction, the specific heat, the rate constant A_2 and the activation energy E_2 played an important role in the curing process. Considering the influence on these parameters and the location of the thermocouples on the temperature-time and the curing degree-time histories, it can be conclude that the thermo-chemical model proposed accurately predicts the curing behavior of the adhesive Hysol EA-9321. Indeed, the discrepancies shown in Figure 85 are negligible compared with those created by the sensitivity analysis.

2.6. Conclusions

The curing behavior of the adhesive Hysol EA-9321 was experimentally and analytically investigated. A thermo-kinetic model was used to study the temperature and curing degree distribution in an adhesive during curing process.

Regarding the curing kinetics of the adhesive, it can be concluded that:

- Autocatalytic model and isothermal Kamal & Sourour with diffusion models simulate well the curing behavior of the adhesive Hysol EA-9321 at low temperatures, i.e below the glass transition temperature. These models have to take into account a heating rate-dependent pre-exponential factor and diffusion control.
- Curing the adhesive at low temperatures of 25-45°C decelerates significantly the curing process. High curing degrees are obtained at higher temperatures of 80-100°C and more rapidly.
- Concerning the potential use of this adhesive in spatial domain, the long curing period at low temperatures provides curing degrees of around 50%. Hence, adhesive properties are subjected to change depending on the environment in which it evolves. Increasing curing temperatures or doing a post-cure are recommended in order to increase the curing state of the adhesive and thus to improve its properties.

The FE model was developed for a block of adhesive. The comparison with experimental data shows that the procedure is numerically stable and produces accurate results. This model makes the assumption that curing residual stresses (chemical shrinkage and thermal dilatation) are negligible for the adhesive studied.

The FE proposed is particularly interesting for applications for which large-scale bonded structures are used. These ones are generally erected and stored in outdoor conditions and the curing state of the bonded area is heterogeneous according to thermal loadings applied. Hence, the FE model let to know the curing degree at each location of the bonded area. Since the mechanical properties of the bonded assembly are curing degree dependent. It will be a way to predict the strength of the structure according to its curing state.

∞

In the next chapter, the determination of mechanical properties of the adhesive Hysol EA-9321 and their dependence on the curing state will be investigated. The knowledge of these properties will be a way to predict the lifetime of a bonded-structure.

2.7. References

[ARR 89] Arrhenius, Über die Dissociationswärme und den Einfluss der Temperature auf den Dissociationsgrad der Elektrolyte, Z. Physik Chem, Vol 4., pp. 96-116, 1989.

[AST 05] ASTM E 1269, Standard test method for determining specific heat capacity by differential scanning calorimetry, 2005.

[AZI 96] Azizeh Youssefi-Moshirabad. Cure analysis of promoted polyester and vinyester reinforced composites and heat transfer in RTMmolds. PhD thesis, Université de Montréal, Montréal, 1996.

[BAI 96] Bailleul J., Delaunay D., Jarny Y., Determination of temperature variable properties of composite materials: methodology and experimental results. Journal of Reinforced Plastics and Composites, Vol. 15, pp. 479-496, 1996.

[BAL 08] Balvers J., Bersee H., Beukers A., Jansen K., Determination of Cure Dependent Properties for Curing Simulation of Thick-Walled Composites. 49th AIAA/ASME/ASCE/AHS/ASC Structures, Structural Dynamics, and Materials Conference, Schaumburg, IL, USA, April 7-10, 2008.

[CAR 92] Cartwright J.H.E, Piro O., The Dynamics of Runge-Kutta Methods, Int. J. Bifurcations Chaos 2, pp. 427-449, 1992.

[CHE 87] Chern C.S., Phoehlein G.W., A kinetic model for curing reactions of epoxides with amines. Polymer Engineering ans Science, Vol. 27, pp. 788-95,1987.

[CHE 02] Chern B-C., Moon Tess J., Howell J.R. and Wiling Tan, New Experimental Data for Enthalpy of Reaction and Temperature- and Degree-of-Cure-Dependent, Journal of Composite Materials, vol. 36, no. 17, 2002.

[DAS 12] L.F.M. da Silva, D.A. Dillard, B. Blackman, R.D. Adams. Testing Adhesive Joints: Best Practices. First Edition, Wiley-VCH Verlag GmbH & Co. KGaA, 2012.

[DAV 09] Davies P., Sohier L., Cognard J.Y., Bourmaud A., Choqueuse D., Rinnert E., Créac'hcadec R., Influence of adhesive bond line thickness on joint strength, International Journal of Adhesion and Adhesives, pp. 724-36.

[DUS 85] Dusi M.R., Galeos R. M., Maximovich M.G., Physiorheological Characterization of a Carbon/Epoxy Prepreg System, Journal of Applied Polymer Science, Vol. 30, 1985.

[GIL 74] Gillham J.K., Benci J.A., Isothermal Transitions of a Thermosetting System, Journal of Applied Polymer Science, Vol. 18, 1974.

[GUS 91] Gustafsson S.E., The transient plane-source technique: for measurements of thermal conductivity and diffusivity of solid materials. Review of Scientific Intruments. Vol. 62, pp. 797-804, 1991.

[GUS 94] Gustafsson S.E., Thermal conductivity, thermal diffusivity, and specific heat of thin samples form transient measurements with hot disc sensors. Review of Scientific Intruments. Vol. 65, pp. 3856-3859, 1994.

[HOJ 04] Hojjati M., Johnston A., Hoa S. V., Denault J., Viscoelastic behavior of cytec fm73 adhesive during cure, . J. Appl. Poly. Sci., Vol. 91, pp. 2548–2557., 2004.

[HOR 70] Horie K., Hiura H., Sawada M., Mita I., Kambe H., Calorimetric investigation of polymerization reactions. III. Curing reaction of epoxides with amines, Journal of Polymer Science: part A-1, Vol. 8, pp. 1357-1372, 1970.

[HUA 94] Huang H.C., Usmani A.S., Finite Element Analysis for Heat Transfer: theory and software, Springer, pp. 13-14, London, 1994.

[HEN] Henkel Hysol EA 9321, Technical data sheet.

[IVA 03] Ivankovic M., Incarnato L., Kenny J.M., and Nicolais L., Curing kinetics and chemorheology of epoxy/anhydride system. Journal of Applied Polymer Science, Vol. 90, pp. 3012–3019, 2003.

[JOA 07] Joannès S., Caractérisation mécanique et outil d'aide au dimensionnement des collages structuraux, PhD Thesis, Mines ParisTech, 2007.

[JOH 97] Johnston A., An Integrated Model of the Development of Process-Induced Deformation in Autoclave Processing of Composite Structures, Ph.D. Thesis, The University of British Columbia, Vancouver, B.C., February 1997.

[KAM 73] Kamal M.R., Sourour S., Kinetics and thermal characterization of thermoset cure, Polymer Engineering and Science, Vol. 13, pp. 59-64, No. 1, 1973.

[KAM 76] Kamal M.R., Sourour S., Differential scanning calorimetry of epoxy cure: isothermal cure kinetics, Thermochim. Acta, Vol. 14, pp. 41-59, 1976.

[KAR 96] Karkanas P. I., Partridge I. K., Modelling the cure of a commercial epoxy resin for applications in resin transfer moulding, Polymer International, Vol. 41, pp. 181-191, 1996.

[KES 96] Keshavarz S. A. M., Nekoomanesh M., Kinetic investigation of the free-radical crosslinking copolymerization of styrene with a mixture of divinylbenzene isomers acting as the crosslinker. Polymer, Vol. 18, pp. 4141-4148, 1996.

[KIM 02] Kim J., Moon T. J., Howell J. R., Cure kinetic model, heat of reaction, and glass transition temperature of as4/3501-6 graphite-epoxy prepregs. J. Composite Materials, Vol. 36, No. 21, pp. 2479–2497, 2002.

[KIS 57] Kissinger H.E., Reaction kinetics in differential thermal analysis, Analytical Chemistry, Vol. 29, pp. 1702-1707, 1957.

[LIL 05] Liljedahl C. D. M., Crocombe A. D., Abdel Wahab M. M., Ashcroft I. A., The effect of residual strains on the progressive damage modelling of environmentally degraded adhesive joints, J. Adhesion Sci. Technol., Vol. 19, No. 7, pp. 525–547, 2005.

[LIO 00] Lion A., Hofer P., On the phenomenological representation of curing phenomena in contiuum mechanics. Arch. Mech., Vol. 59, pp. 59–89, 2007.

[LEE 00] Lee J.Y., Choi H.K., Shim M.J., Kim S.W., Kinetics studies of an epoxy cure reaction by isothermal DSC analysis, Thermochim Acta, Vol. 343, pp. 111-117, 2000.

[MAR 07] Mario O., Etude du vieillissement des assemblages structuraux acier/aluminium : Influence de l'environnement sur le dimensionnement, PhD Thesis, Mines ParisTech, 2007.

[MIJ 88] Mijovic J., Wang H.T., Modeling of processing of composites part II – Temperature distribution during cure. SAMPE Journal, pp. 42-55, 1988.

[MOR 77] Moré J.J., The Levenberg-Marquardt algorithm: Implementation and Theory, *Numerical Analysis*, ed. G.A. Watson, *Lecture Notes in Mathematics* 630, Springer Verlag, pp. 105-116, 1977.

[MOI 06] Moisala A., Li Q., Kinloch I.A., Windle A.H., Thermal and electrical conductivity of single- and multi-walled carbon nanotube-epoxy composites, Composite Science and Technology , Vol.66, pp. 1285-1288, 2006.

[RYA 79] Ryan M.E., Dutta A., Kinetics of epoxy cure : a rapid technique for kinetic parameter estimation, Polym, Vol. 20, Issue. 2, pp. 203-206, 1979.

[RUI 08] Edu Ruiz and C. Billotte. Predicting the cure of thermosetting polymers: the isoconversion map. Polymer Composites, 30 :1450–1457, 2008.

[SKO 99] Skordos A. A., Partridge K., Monitoring and Heat Transfer Modelling of the Cure of Thermoset Composites Processed by Resin Transfer Moulding, Polymer Composites'99, October 6-8, Canada, 1999.

[SIM 00] Simon S. L., Mckenna G. B., Sindt O., Modeling the evolution of the dynamic mechanical properties of a commercial epoxy resin during cure after gelation, J. Appl. Poly. Sci., Vol. 76, Issue 4, pp. 495-508, 2000.

[SPE] FlackTek Inc. (Landrum, SC), www.speedmixer.com/products1.php.

[SUN 02a] Sun L., Pang S., Sterling A., Negulescu I., Stubblefield M., Thermal analysis of curing process of Epoxy Prepreg, J Appl Polym Sci, Vol. 83, No. 5, pp. 1074-1083, 2002.

[SUN 02b] Sun L., Pang S., Sterling A., Negulescu I., Stubblefield M., Dynamic analysis of curing process of Epoxy Prepreg, J Appl Polym Sci, Vol. 86, No. 8, pp. 1911-1923, 2002.

[VAL 05] Valery L., Zvetkov, Thermochim. Acta 435, pp. 71, 2005.

[VAN 99] Van Mele B., Van Assche G., Van Hemelrijck A., Modulated Differential Scanning Calorimetry to study reacting polymer system, Journal of reinforced plastic and composites, Vol.18, No. 10, 1999.

[YOU 97] Yousefi A., Lafleur PG., Gauvin R., Kinetic studies of thermoset cure reactions: a review. Polym Composite, Vol. 18, No. 2, pp. 157-168, 1997.

[YU 13] Yu H., Adams R.D., Lucas F.M. da Silva, Development of a dilatometer and measurement of the shrinkage behavior of adhesives during cure, IJAA, vol.47, pp 26-34, 2013.

CHAPTER 3:

EXPERIMENTAL CHARACTERIZATION OF THE 3D ELASTIC-VISCO-PLASTIC BEHAVIOR OF THE 3D ELASTIC-VISCO-PLASTIC BEHAVIOR OF THE ADHESIVE HYSOL EA-9321

Résumé

Ce chapitre consiste à étudier expérimentalement l'influence du taux de polymérisation de l'adhésif Hysol EA-9321 sur ses propriétés mécaniques. Pour cela, trois procédures de cuisson ont été définies puis utilisées sur des éprouvettes Arcan. Dans un premier temps, le modèle élément fini développé dans le chapitre précédent a été appliqué à la cuisson de telles éprouvettes afin de déterminer les distributions de taux de polymérisation et de températures au sein de l'adhésif à l'issu des chargements thermiques choisis. Dans un deuxième temps, les éprouvettes ont été d'abord sollicitées en traction, cisaillement, traction-cisaillement et compression-cisaillement via l'essai Arcan Evolution à vitesse de traverse constante. Les effets de vitesse ont ensuite été étudiés en cisaillement et compression-cisaillement à différentes vitesses de chargements. Ces essais ont été réalisés pour chaque procédure de cuisson. Ces essais constituent une base de données expérimentale nécessaire à l'identification des effets de polymérisation sur les propriétés mécaniques.

Summary

This chapter focuses on studying the influence of the curing state of the adhesive Hysol EA-9321 on its mechanical properties. To this end, three curing processes were defined and applied to Arcan Evolution specimens. At first, the Finite Element strategy defined previously was conducted on such specimens for the three curing cycles to predict the temperature and curing degree distributions within the adhesive layer. Then, Arcan Evolution tests under tension, shear, tension-shear and compression-shear loadings were performed for each curing cycle identified. After, rate effects were investigated in shear and compression-shear configurations at several traverse speeds on several curing histories specimens. The aim was to provide a strong database for the identification of the 3D behavior of the adhesive including curing degree effects.

Contents

3.1. General strategy overview

3.1.1. Presentation of the Arcan Evolution test

The Arcan Evolution device used for the characterization of the adhesive is presented Figure 1. This specimen is based on the same principle as the modified Arcan device [ARC 87][COG 05][KOK 13][MAU 13]. offers the possibility to combine tension or compression with shear loadings. This device uses two perforated plates with different holes. These holes allow angling the direction of the load regarding the direction of the test specimen. On Figure 99, the orientation between the loading direction and the mean plane of the adhesive is defined by the angle γ. The fixture design allows this angle varying from 0° to 135°.

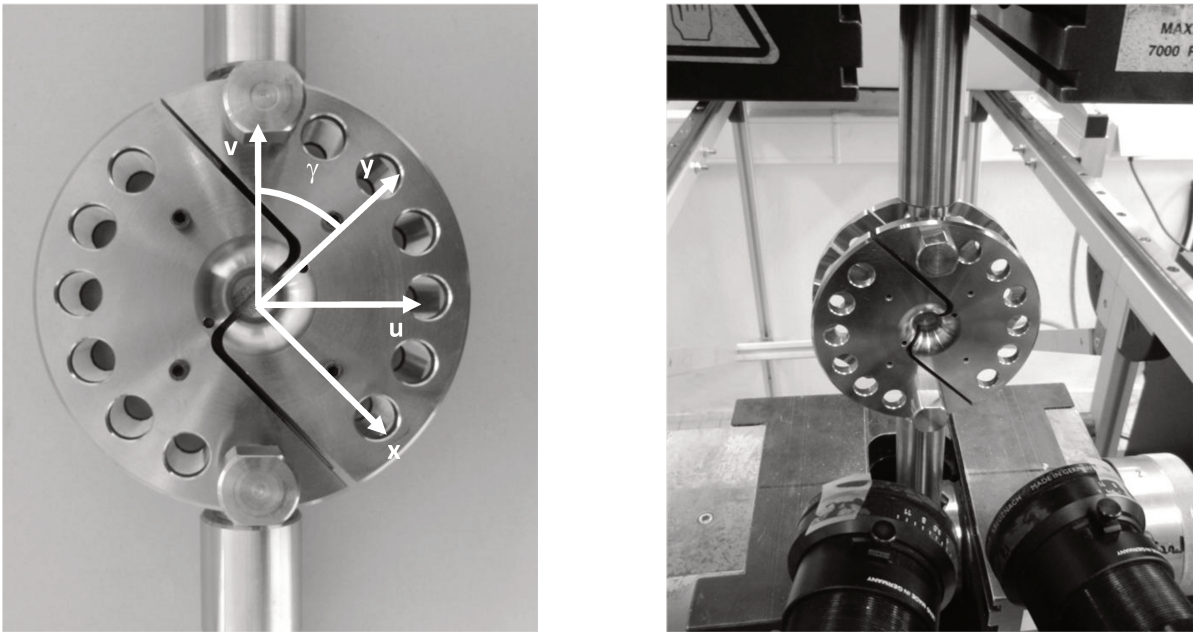

(a) (b)

Figure 99. Arcan Evolution device: (a) Test under tensile-shear loading (γ=135°), (b) Arcan Evolution device within the tension machine and 3D images acquisition system.

For tensile tests, γ is equal to 0°; for tensile-shear tests with the same load in tension and shear; γ=45°; for shear tests: γ=90° and for compression-shear tests with the same load in compression and shear γ=135°. Those different configurations are illustrated in Figure 100.

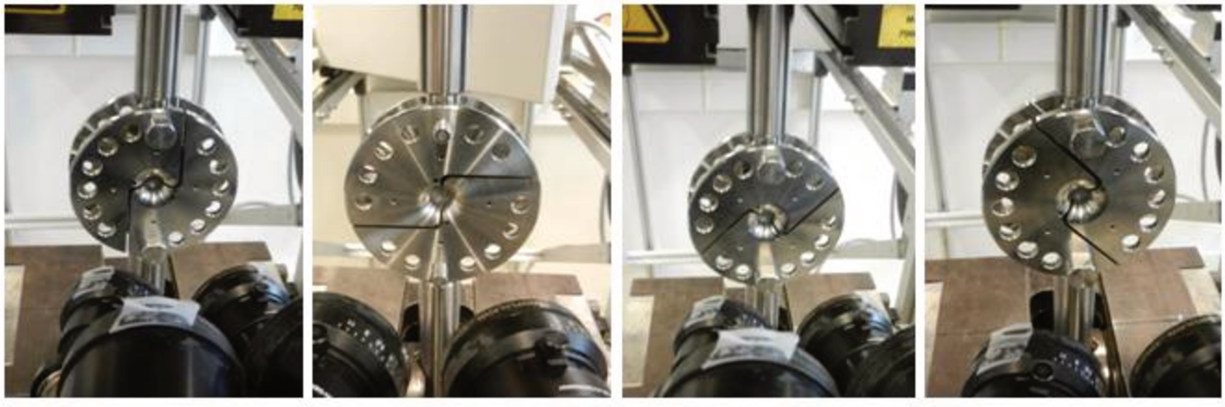

(a) (b) (c) (d)

Figure 100. Arcan Evolution fixture at: (a) γ=0°, (b) γ=90°, (c) γ=45° and (d) γ=135°.

Figure 101 and Figure 102 represent both geometry of the bonded specimens and geometry of the substrates. Spaces appearing in Figure 101 are generated during the machining process to control the

adhesive thickness thanks to screws that realize the positioning between both adherends during the curing process. Further, a screwdriver applied a torque of 2.5 mN. Both manufacturing precautions allow reducing the scatter that is well suited in the case of long curing time [COG 08][ETA 99]. Each bonded specimen is fixed to the perfored plates thanks to clamping jaws and is then put in a tensile test machine. The load transmission to the adhesive is realized with two spindles put in the different holes of the substrates. Following the curing process, the final shape of the Arcan Evolution specimen is obtained by cutting the spacers, as suggested in Figure 102 (a). This results in four specimens of by rods. Such specimens have a bonded area of 25 x 9.5 mm² and an adhesive thickness of 0.2 mm. The particular geometry of the beaks allows reducing the edge effects [CRE 15].

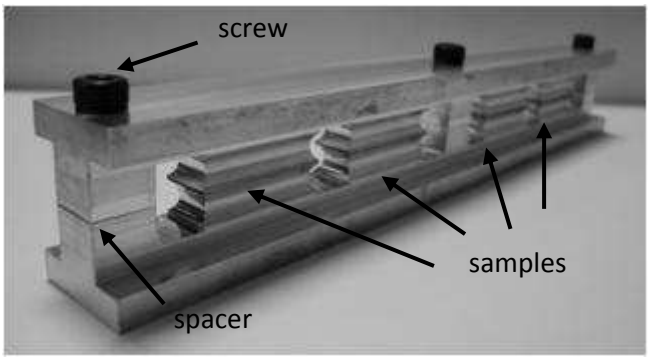

Figure 101. Presentation of the bonded specimens: bonding procedure.

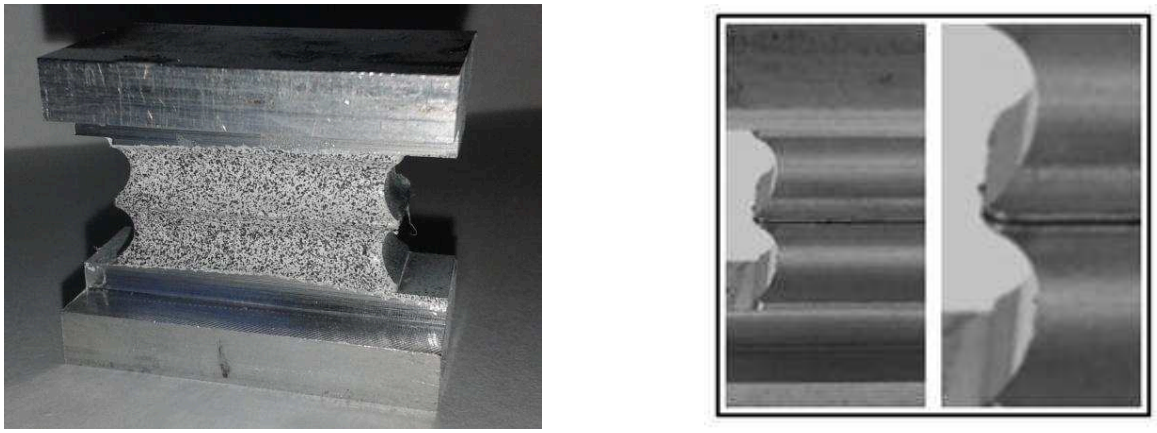

(a) (b)

Figure 102. Presentation of the bonded specimens: (a) bonded specimens and (b) geometry of the beak.

3.1.2. Numerical analysis of stress singularities under elastic assumption

As explained in chapter 1, bonded assemblies are generally affected by edges effects which contribute to crack initiation and propagation in the adhesive. This makes experimental and numerical analyses of the mechanical behavior of an adhesive particularly difficult. The stress state within the adhesive layer of an Arcan Evolution specimen was numerically analyzed through 2D finite element analysis under elastic assumptions, for aluminium 2017 substrates (Young's modulus E_S=70GPa, Poisson's ratio v_S=0.30) and epoxy adhesive Hysol EA-9321 (Young's modulus E_A=3480 MPa, Poisson's ratio v_A=0.369). Its clamping with the Arcan Evolution device was considered perfect and the boundary conditions were represented by

kinematic couplings between driving points A, B and the driven surfaces of the bonded specimen. A refined mesh at the ends of overlap (three-node linear elements) and within the adhesive layer (40 8-node bilinear elements in the adhesive thickness) was used through a thickness of 0.2 mm, as shown in Figure 103.

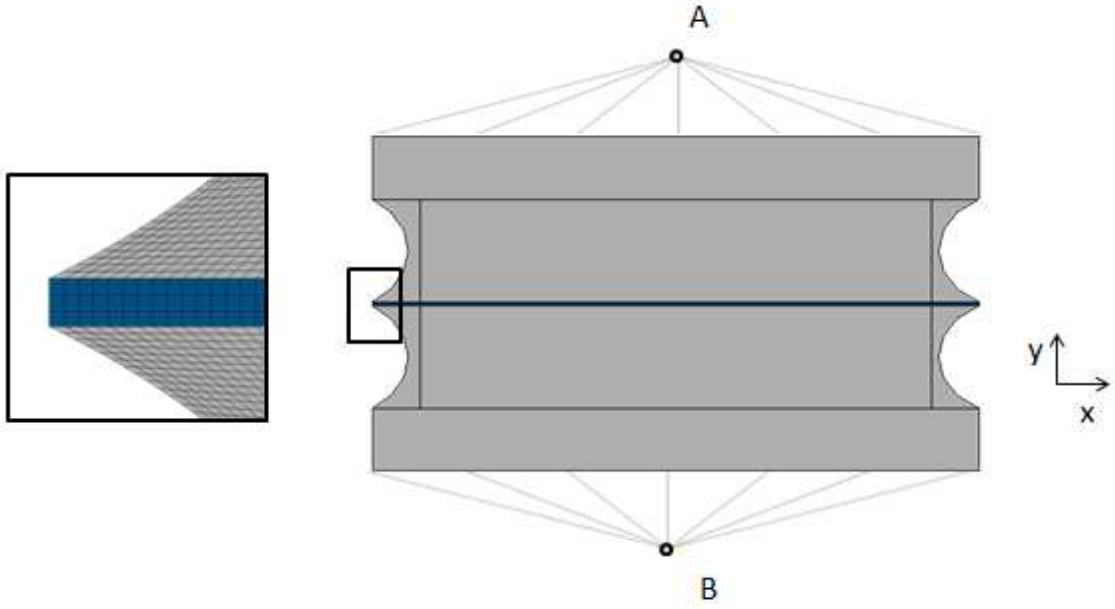

Figure 103. Finite Element model: zoom on the beak at the end of the overlap and boundary conditions.

Figure 104 represents the Von Mises stress distribution in the (0, X, Y) axis along the overlap of the joint and in the mid-plane of the adhesive layer for tension (γ=0°) and shear configurations (γ=90°). Results are normalized to make analysis of the stress distributions easier. Values are normalized to the unity at the middle of the adhesive. The geometry of beaks used in our study seems to reduce accurately stress concentrations.

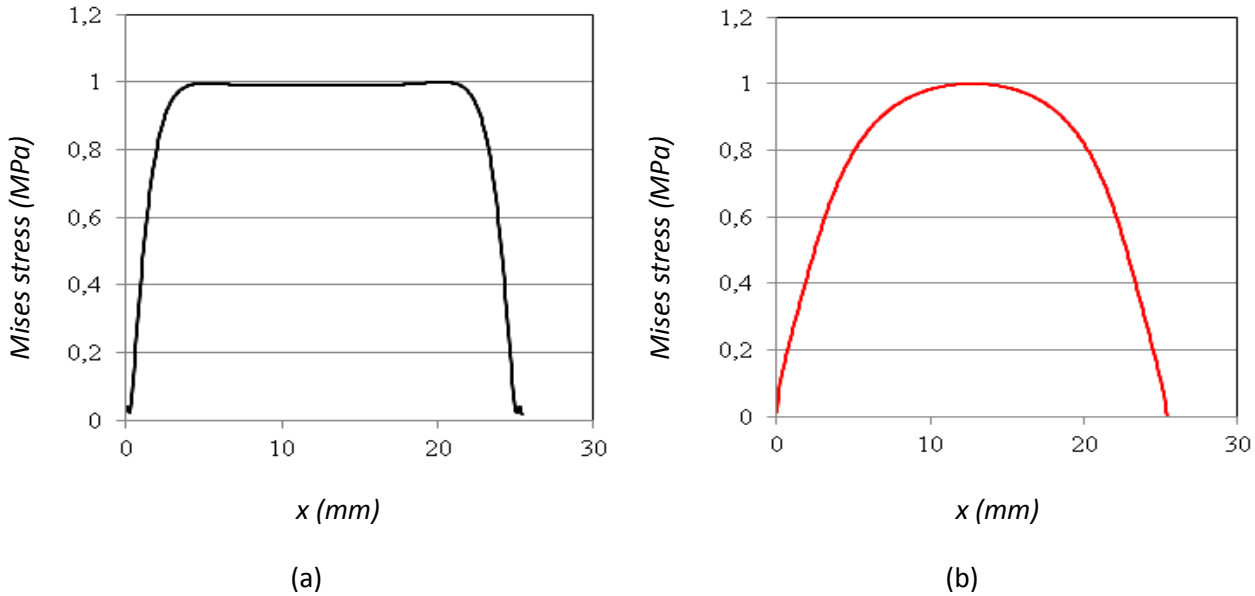

Figure 104. Von Mises stress along the overlap of the joint and in mid-plane of the adhesive for: (a) tension (γ=0°) test and (b) shear (γ=90°) test.

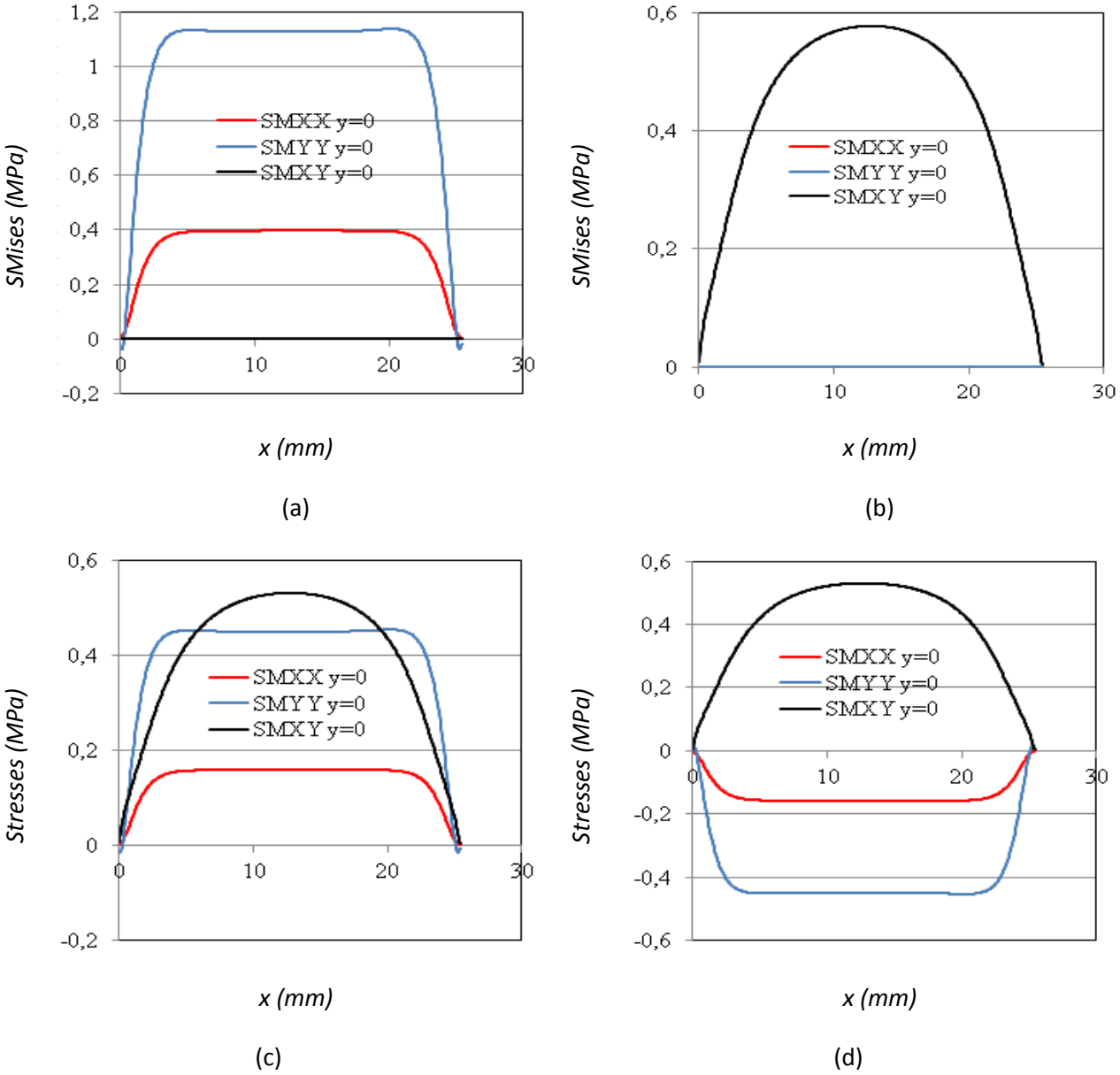

Figure 105. Stress distribution along the overlap of the joint and in the mid-plane of the adhesive for: (a) tensile (γ=0°) test, (b) shear (γ=90°) test, (c) tension-shear (γ=45°) test and (d) compression-shear (γ=135°) test.

Figure 105 shows the stress distribution in the (0, X, Y) axis along the overlap in the mid-plane of the adhesive layer for the four loadings configurations γ=0°, 90°, 45° and 135°. Three stresses are plotted: the normal stresses SMXX, SMYY and the tangential stresses SMXY. Those stresses are normalized by the maximum von Mises stress. Those results underline the non-uniform stress state in the mid-plane of the adhesive layer. For tension (Figure 105 (a)), the tangential stress SMXY is equal to zero whereas it is parabolic with a maximum stress in the middle of the overlap length for shear configuration (Figure 105 (b)). Regarding mixed mode of loading (Figure 105 (c) and (d)), parabolic normal and tangential stresses are noticed with a maximum value in the middle along the overlap length. Edges effects are strongly limited at the end of the overlap length, i.e. at the edges of the adhesive: stresses are approximately equal to zero near x= 0 and x= 25.4 mm. This highlights the importance of using beaks.

3.1.3. Stress state in the adhesive layer

The distribution of the stresses, σ_{xx}, σ_{yy}, τ_{xy}, with respect to the overlap length in the adhesive is non uniform: for σ_{xx}, σ_{yy} it is quite uniform, whereas for τ_{xy} is a parabolic distribution. Under elastic assumption, the maximum stresses components ($\sigma_{yy\ max}$, $\tau_{xy\ max}$) can be obtained from the finite element results and from

the average stresses ($\sigma_{yy\ average}$, $\tau_{xy\ average}$) obtained with the loads applied on the specimens and the section of the adhesive plane (S_c) considering the materials parameters previously described:

$$\sigma_{yy\_max} = 1.16\sigma_{yy\_average} \quad , \text{ with} \quad \sigma_{yy\_average} = \frac{FN}{S_C} \tag{1}$$

$$\tau_{xy\_max} = 1.42\tau_{xy\_average} \quad , \text{ with} \quad \tau_{xy\_average} = \frac{FT}{S_C} \tag{2}$$

3.2. Test procedure

3.2.1. Measurement set-up and Post-processing method

In this study, the local relative displacements of the two substrates, and thus the deformation of the adhesive, in the normal and tangential directions were measured by the optical 3D measuring GOM/Aramis™ system using Digital Image Correlation (DIC) [GOM].

Digital Image Correlation is a non-contacting technique that compares the similarity of speckle patterns in images acquired at distinct mechanical configurations during a test. This requires some steps. A random speckle pattern was firstly applied on the surface of the Arcan Evolution specimen to provide a distribution of grey levels sufficiently contrasted that can be monitored from image to image. Then, an image under undeformed configuration which is called “reference image” is subdivided into correlations domains, i.e. a number of pixels or subsets. The displacement and strain fields are measured in these areas. A correspondence of each subset to the respective calculated subset at the second deformed image is then established by defining the maximum value of the correlation coefficient, as suggested in Figure 106. This will determine the new position of the deformed subsets, thus, yielding the displacement vector of each subset by the difference between the reference and the deformed images. Once the displacement vectors have been determined, the strains can be computed. Further studies [FAZ 10][PAN 09] gives more information about Digital Image Correlation.

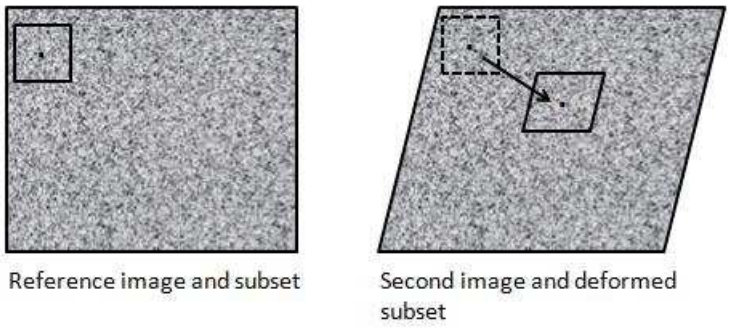

Figure 106. Digital Image Correlation principle: determination of the correlation coefficient.

3D Digital Image Correlation method requires a pair of digital cameras for image acquisition necessary to provide full-displacement and full-strain fields combined with a bundle adjustment. This is realized by using the stereo-photogrammetry principle, as represented in Figure 107. It assumes a constant relative position of both cameras defined thanks to a calibration process. Aiming a common point with both cameras, its location can be triangulated in three-dimensional space [MCG 05]. Therefore, the entire 3D shape of an Arcan Evolution specimen can be captured and displacement/strain field associated to such specimen over the entire field of view can be obtained throughout the test.

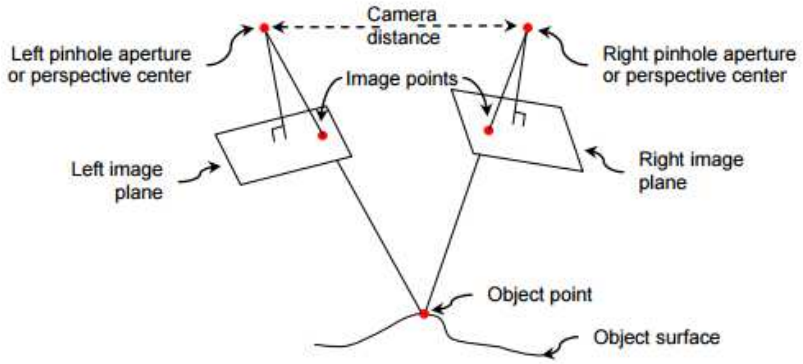

Figure 107. Stereo-photogrammetry principle [AVI 10].

In this work, the measurement system was made of a pair of digital cameras (8-bit Baumer Optronic FWX20 cameras) with a pixel resolution of 2400 by 1728 pixels coupled with Schneider-Kreuznach lenses, a laser pointer and a tripod with panoramic head. The camera support was mounted on this latter and was positioned with regard to a specimen risen into the Arcan Evolution fixture. The laser pointer was used to ensure a correct alignment. Then, camera lenses were adjusted to be in focus with respect to the specimen surface. The lights were finally adjusted to provide sufficient illumination across the entire speckled area and to avoid pixels saturation. The instrumentation used is shown in Figure 108. An acquisition bay and a computer were additionally required for recording and processing the acquired images.

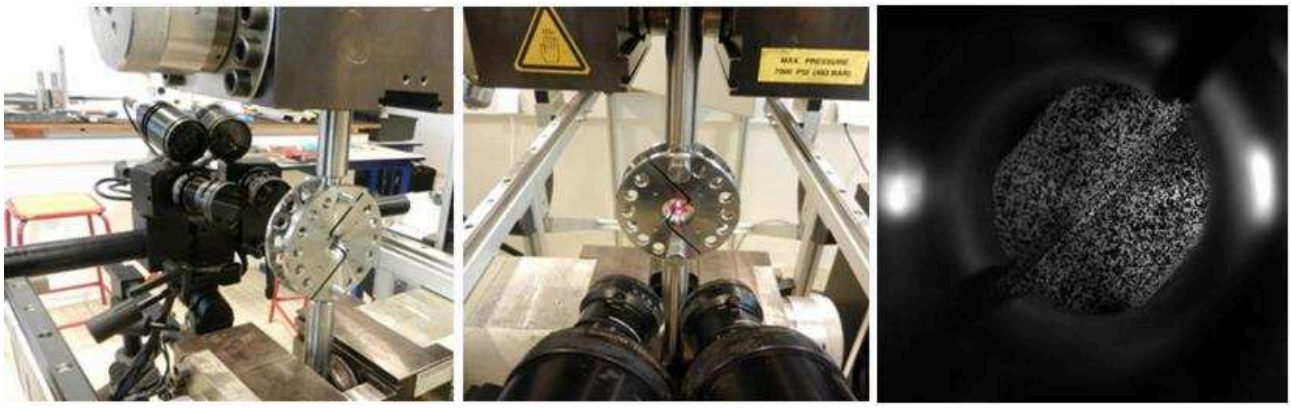

(a) (b) (c)

Figure 108. DIC/mechanical set-up for compression-shear test: (a) camera support, (b) camera positioning thanks to laser pointer and (c) example of image obtained.

After recording images, a post-processing is necessary to determine the local relative displacements of the adherends. This involves two main steps by using the GOM/Aramis software:

- The image sequence is corrected to go from cameras reference frame to specimen coordinate system defined by the tangential and normal directions (*T*; *N*) (Figure 109). To that end, two "best-fit" cylinders, each with a radius of 3 mm, are created from the curved surfaces of the substrates. Then, the intersection of the longitudinal plane of each cylinder with the vertical plane tangent the speckled curved surface of each adherend gives two points *B1* and *B2*. Considering the middle between these two points, the center of the coordinate system *C* is defined by a translation of this last one in the transverse direction from a distance of a radius, as shown in Figure 109 (c).

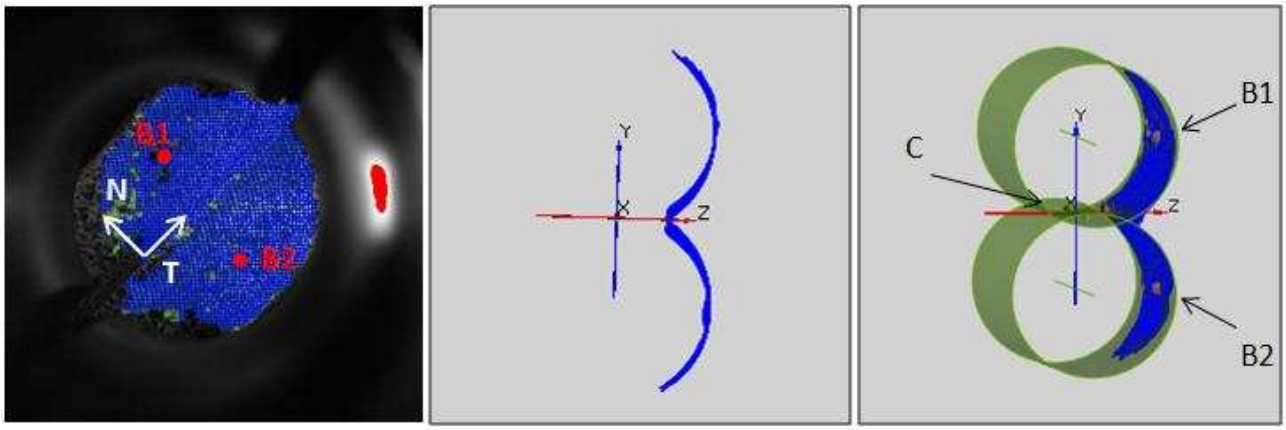

(a) (b) (c)

Figure 109. Arcan Evolution test under compression-shear loading (γ=135°): (a) correlated specimen, (b) correlated surface and (c) principle of image sequence correction.

- The relative displacements are computed in tangential and normal directions between two symmetrical areas about the mid-plane of the adhesive layer (Figure 110 (a) and (b)). These regions must be three-dimensional due to curved surfaces of adherends and are parallelepipeds of width *WW*, height *H* and depth *D* whose centers are the points *B1* and *B2* defined previously (Figure 110). The relative parallelepiped to point *B2* is on the lower substrate. In such zone, all displacements are forced to *0* and do a movement correction. Regarding, the region associated with the point *B1*, the average displacements are computed on all the points of the parallelepiped surrounding the point B1, thus allowing the computation of the relative displacements in the tangential (*T*) and normal (*N*) directions. Figure 110 (c) shows the computed displacements of the correlated area after post-processing for an Arcan Evolution specimen under compression-shear loading.

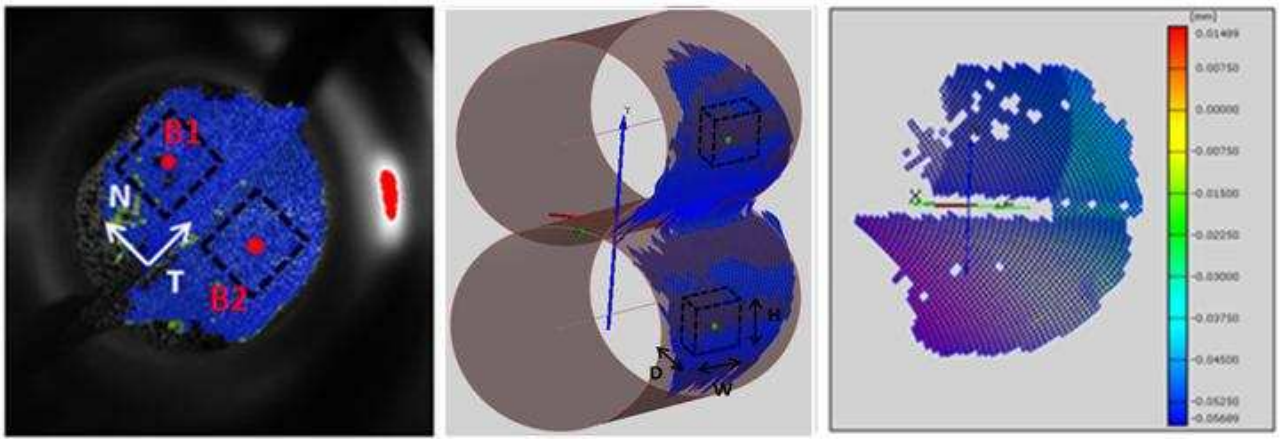

(a) (b) (c)

Figure 110. Arcan Evolution specimen under compression-shear loading (γ=135°): (a) correlated specimen, (b) definition of the symmetrical areas for displacements computation and (c) displacements after post-processing.

These two steps were automatically established through a python user-script implemented during the PhD in the GOM/Aramis™ software. This allows parameterizing the size of both areas necessary to relative displacements computations. Since such regions are defined from the known specimen geometry, their position is exactly defined and is the same from one test to another, regardless of the type of loading (γ=0°, 45°, 90° or 135°). Furthermore, as explained in chapter 1, an inverse identification is required to characterize an adhesive via Arcan Evolution fixture due to edge effects. Thus, the exact position of areas is used to compare experiments with Finite Element responses within the inverse identification process. In

chapter 4, a Finite Element sensitivity analysis to the influence of the position of such areas on the load/displacement behavior of adhesive will highlight the importance of knowing such positions. This post-processing method considers also the deformation of the adherends.

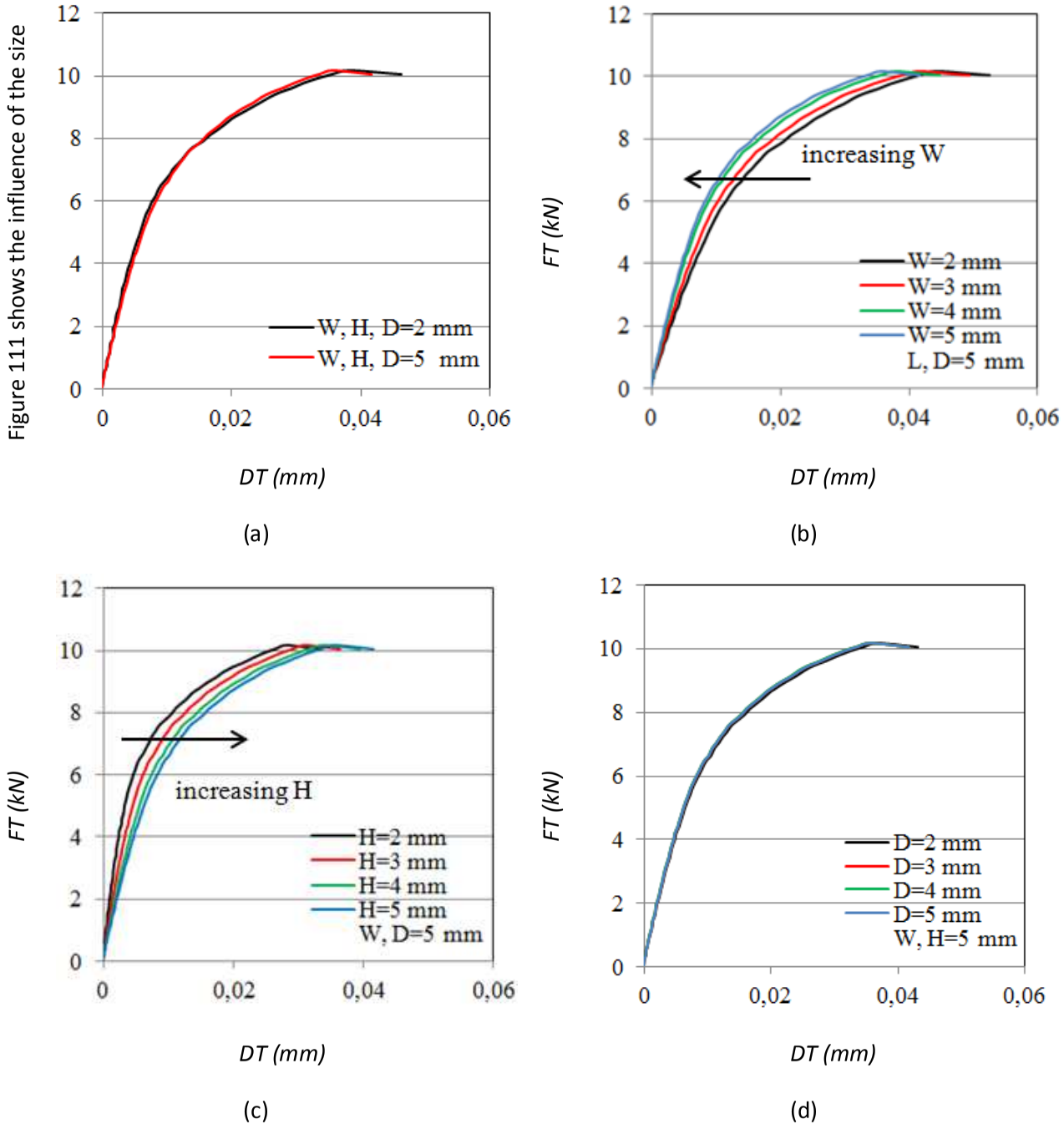

Figure 111. Arcan Evolution specimen under shear loading (γ=90°), load-displacement curves after post-processing: (a) influence of the size of post-processing regions, (b) influence of the length L, (c) influence of the height.

A major interest of the 3D- DIC is to identify the out-of-plane displacements of adhesive bonded joints (z-direction). Figure 112 shows the evolution of out-of-plane displacements and angle for an Arcan Evolution specimen under shear loading. For each case, the curves FT vs. DT and DZ vs. DT are represented. Out-of-plane displacements are considerably lower than tangential displacements. Thus, it can be assumed that no cleavage occurs during testing and misalignment may result from external facts such as defect of the adjustment of the Arcan Evolution fixture within the tension machine due to a poor positioning of spacers or defects occurring during manufacturing process of adherends or bonding.

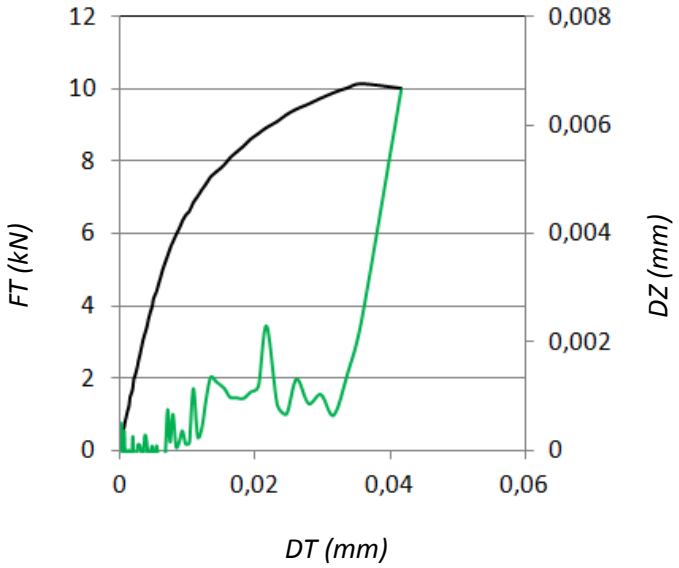

Figure 112. Arcan Evolution specimen under shear loading (γ=90°): evolution of DZ.

The system exhibits an accuracy of 1/100 of pixel. For tests presented in this study, 1 pixel represents approximately 10 µm. Thus, the accuracy measurement is of about 0.1 µm, which is quite sufficient for requirements identified previously.

3.2.2. Curing process

Arcan Evolution tests under tensile (γ=0°), shear (γ=90°), tensile-shear (γ=45°) and compression-shear (γ=135°) loadings were performed on several curing histories specimens to provide a strong database for the identification of the 3D behavior of the adhesive including polymerization effects. Thus, different curing processes were applied on Arcan specimens, namely:

- 5h30 at 35°C
- 3h30 at 60°C
- 1h at 82°C

Each curing cycle corresponds to a specific curing state of the adhesive. This was determined by applying to the Arcan Evolution sample the cure simulation model developed in chapter 2. The curing of an Arcan Evolution specimen is not a homogeneous process. Firstly, the sample was cured in a convection oven. Hence, the theoretical curing cycle predicted is not those sustained by the adhesive in the bonded assembly. Secondly, the heterogeneity was also developed by the exothermic behavior of the polymerization reaction. It was then important to have access to properties gradients that may arise in the adhesive layer to predict the true curing state of the adhesive following the curing process. The idea is to ensure a homogeneous curing state of the entire adhesive layer to ensure a suitable repeatability and to avoid premature cracks or weakening of the bonded assembly resistance during mechanical testing.

The FE procedure of curing process [DEV 15] (Figure 82 of chapter 2) was introduced in the software Abaqus® and applied to an Arcan Evolution sample in order to predict the temperature and curing degree distributions in the adhesive layer. FE studies were undertaken under elastic assumption, for aluminium 2017 substrates (Young's modulus E_S=70GPa, Poisson's ratio ν_S=0.30) and epoxy adhesive Hysol EA-9321 (Young's modulus E_A=3480 MPa, Poisson's ratio ν_A=0.369). The model used is presented in Figure 113. Only the bonded specimen was considered. Its clamping within the Arcan Evolution device was considered perfect, and the boundary conditions were represented by kinematic couplings between driving points *A*, *B* and the driven surfaces of the bonded specimen, as shown in Figure 113 (b) and (c). A film condition (Figure 113 (d)) on external surfaces exposed to the oven environment modeled the thermal loading, using a heat

transfer coefficient characteristic of forced convective heating. Thermal properties of adherends and adhesive associated with the curing process modeling are defined in Table 10 of chapter 2.

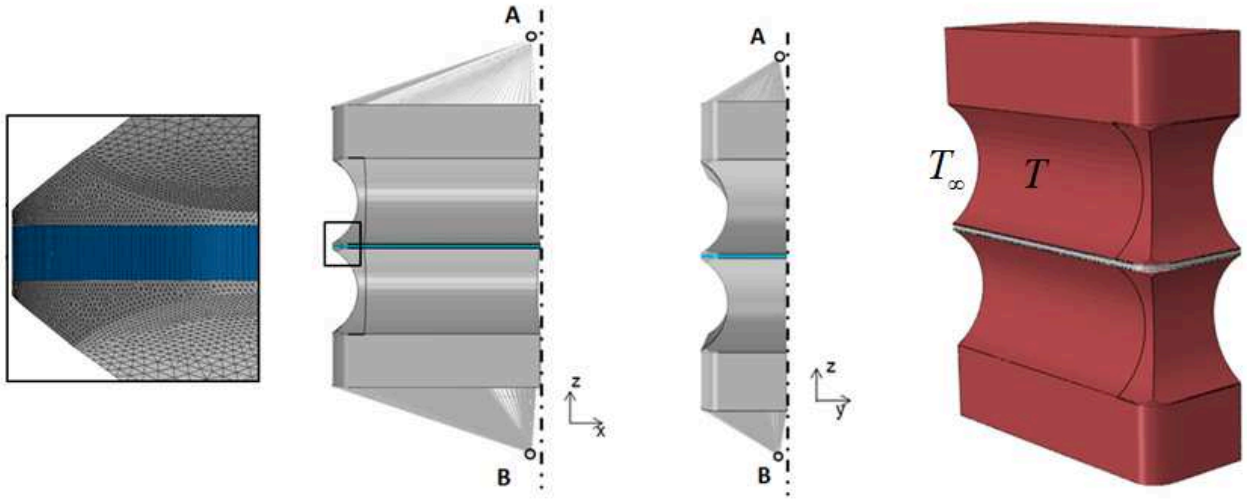

(a) (b) (c) (d)

Figure 113. FE model used for the curing process simulation: (a) zoom on the beak at the end of the overlap, (b), (c) boundary conditions overview with symmetries plane and (d) film convection on external surfaces of the bonded assembly.

Only one quarter of the specimen was represented due to the symmetries in the transverse and longitudinal directions. The reliable determination of the couple curing degree, temperature in the mean plane of the adhesive required the use of a mesh sufficiently refined. The global element size of the substrate was 0.2 mm and the global element size in the adhesive layer was 0.005 mm (40 elements in the thickness), as illustrated in Figure 113 (a). This mesh represented 989093 elements and 298800 elements in the adhesive layer. These elements were 8-node trilinear coupled temperature-displacement elements (C3D8RT) in the adhesive layer. Regarding adherends, the mesh was made of C3D8RT elements and ten-node tetrahedral coupled temperature-displacement elements (C3D10T).

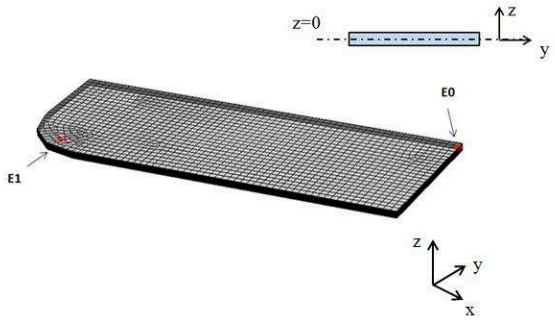

Figure 114. Locations of the points used to investigate the temperature and curing degree distributions within the adhesive layer.

The curing cycles identified were applied to an Arcan Evolution specimen. The purpose was to verify the curing heterogeneities in the adhesive layer. The evolution of temperatures and curing conversions were investigated at two locations in the mid-plane of adhesive layer, as detailed in Figure 114. The expected results should have been a lower polymerization in the center (E0) of the adhesive layer than close to the edges of the joint (E1). In fact, external surfaces of the adhesive layer were directly submitted to the oven heat flux and then reached rapidly the required temperature. Regarding the core of the adhesive layer, a

heat transfer occurred between adherends/adhesive and within the adhesive. Thus, it required more time to achieve the selected temperature.

The computed temperature profiles at locations described above for a curing cycle of 1h at 82°C are depicted in Figure 115.

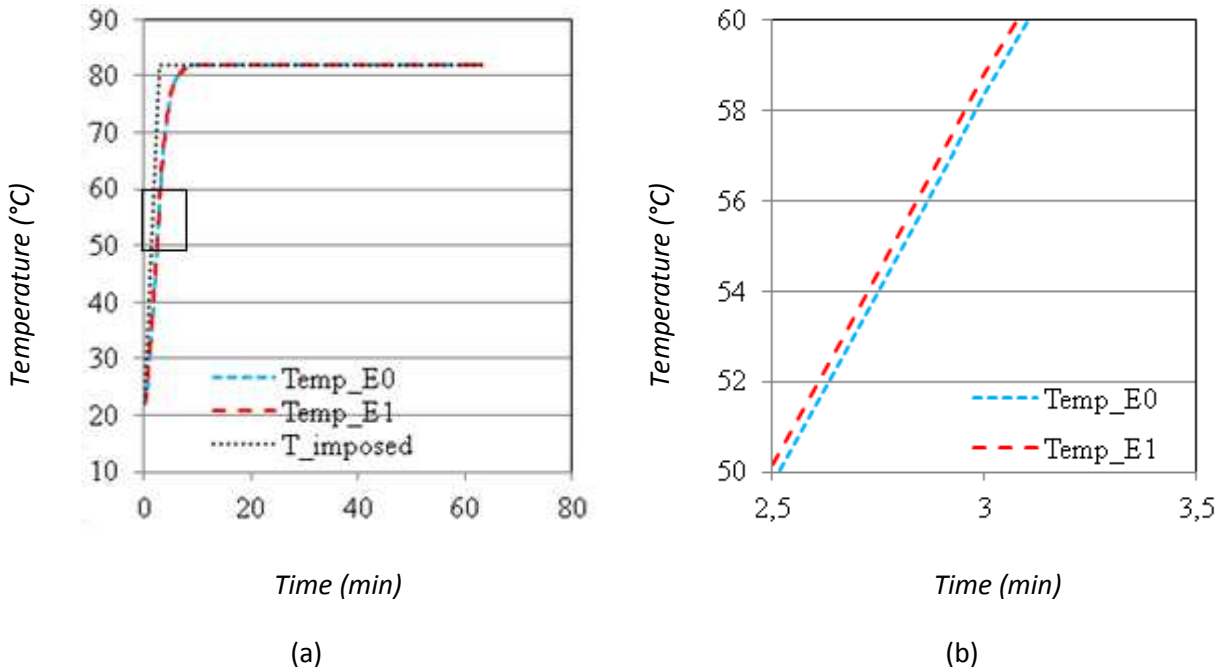

Figure 115. (a) Predicted temperatures within the adhesive layer for a curing cycle of 1h at 82°C at both locations and (b) zoom of the outlined area.

As expected, it is seen that the predicted temperatures within the adhesive layer differs from the predicted temperature due to the convection phenomena (Figure 115 (a)). Further, as shown in Figure 115 (b), there is a slight offset between the temperatures predicted in locations E0 and E1. The center of the adhesive reaches more quickly the required temperature than the external regions. An extra explanation is the heat generated by the cure kinetics of the adhesive when the curing cycles starts. This internal heat leads to an increase within the adhesive temperature, and then this additional heat is transferred back to the oven air. Once the adhesive is fully cured, there is no more internal exothermic curing reaction. The difference temperature observed between both locations is in the order of about 1%. It is mainly due to the thinness of the adhesive layer (thickness of 0.2 mm). As shown in Figure 98 of chapter 2, there is a critical adhesive thickness for which the temperature, and thus the conversion degree, remains homogeneous within the adhesive layer. This value was assessed approximately 0.5 mm in the application case described in the chapter 5. Given the small value of the adhesive line in the Arcan Evolution specimen (five times lower than that of the case study of chapter 2), there is almost no thermal gradients inside the adhesive bonded joint. This is reflected on the curing degree profiles (Figure 116 (b)). A fully curing state of the adhesive is firstly reached at the center of the adhesive layer. A difference of 2% is observed between curing state values computed at both locations E0 and E1 (Figure 116 (b)).

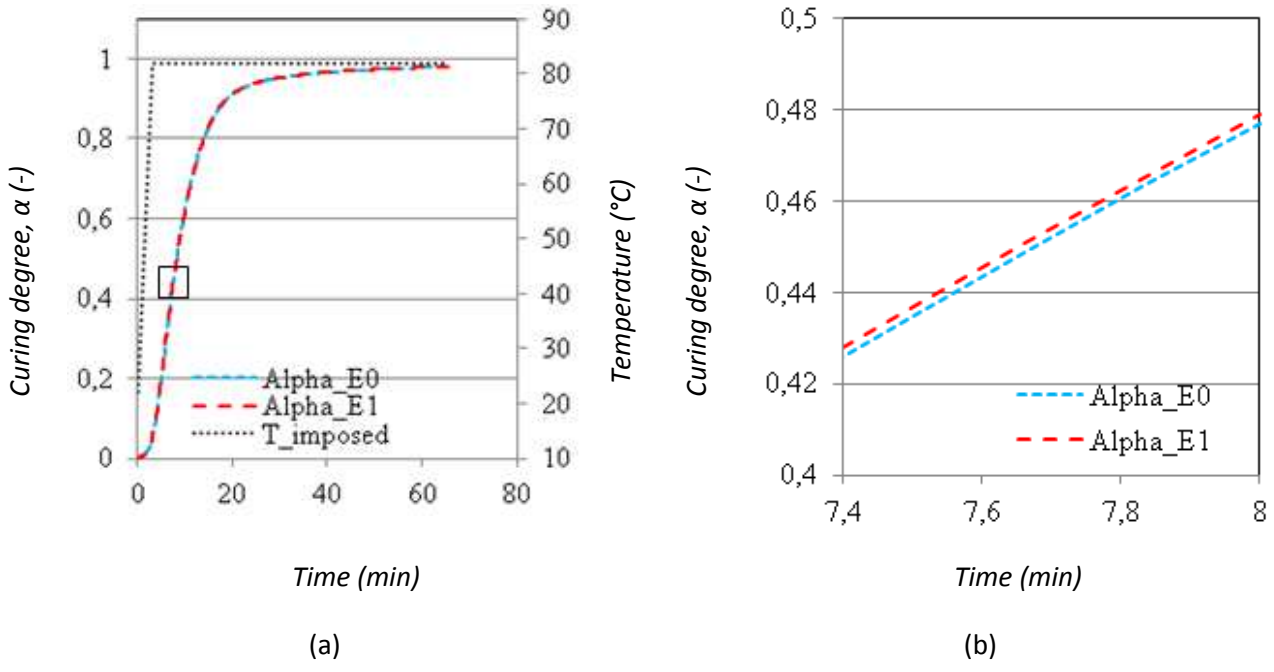

Figure 116. (a) Predicted curing degrees within the adhesive layer for a curing cycle of 1h at 82°C at both locations and (b) zoom of the outlined area.

The change in the curing degree is low during the first stage of the oven curing cycle: the conversion degree α ranges goes from 0 to 0.01 after 4 minutes of curing. This corresponds to the heating step necessary to reach the required curing temperature (in such case 82°C). A heating rate of 20°C/min was applied. This ramp was sufficiently high to prevent the exothermic curing reaction from started. In the second stage of the oven heating (from 4 to 65 minutes), the entire adhesive layer reaches the final temperature and there is enough energy to activate the polymerization reaction. Thus, the curing state of the adhesive goes from 0.01 to 1.0.

Figure 117 shows the contour plot of the temperature (Figure 117 (a)) and conversion degree (Figure 117 (b)) distribution at various times of the curing process of 1h at 82°C within the adhesive layer. As identified previously on Figure 115 and Figure 116, the temperature and cure profiles were not uniform across the adhesive and remain lower on external locations than in the inner part of the adhesive layer. The deviation between both locations is 1%, 0.3%, 0%, 0% for temperatures and 2%, 2%, 0.1%, 0% for curing degrees at t=120, 230, 550 and 3370 s respectively. Similar conclusions to those reflected in the previous paragraph may be done.

Figure 118 shows the evolution of the curing degree at both specific locations inside the adhesive layer for the three curing cycles used in this study. It can be seen that there are almost no gradients during the cure of the adhesive. It can be explained by the slight thickness of the adhesive layer. In fact, a sensitive study to the adhesive thickness during the curing process [DEV 15] showed that there is a critical thickness for which thermal gradients can be neglected. This value was evaluated at 0.5 mm. Nevertheless, the adhesive thickness on the Arcan Evolution was 0.2mm. That's why, scarcely gradients were observed during the curing process. The curing cycles used in this study are associated with the curing degrees suggested in Table 16.

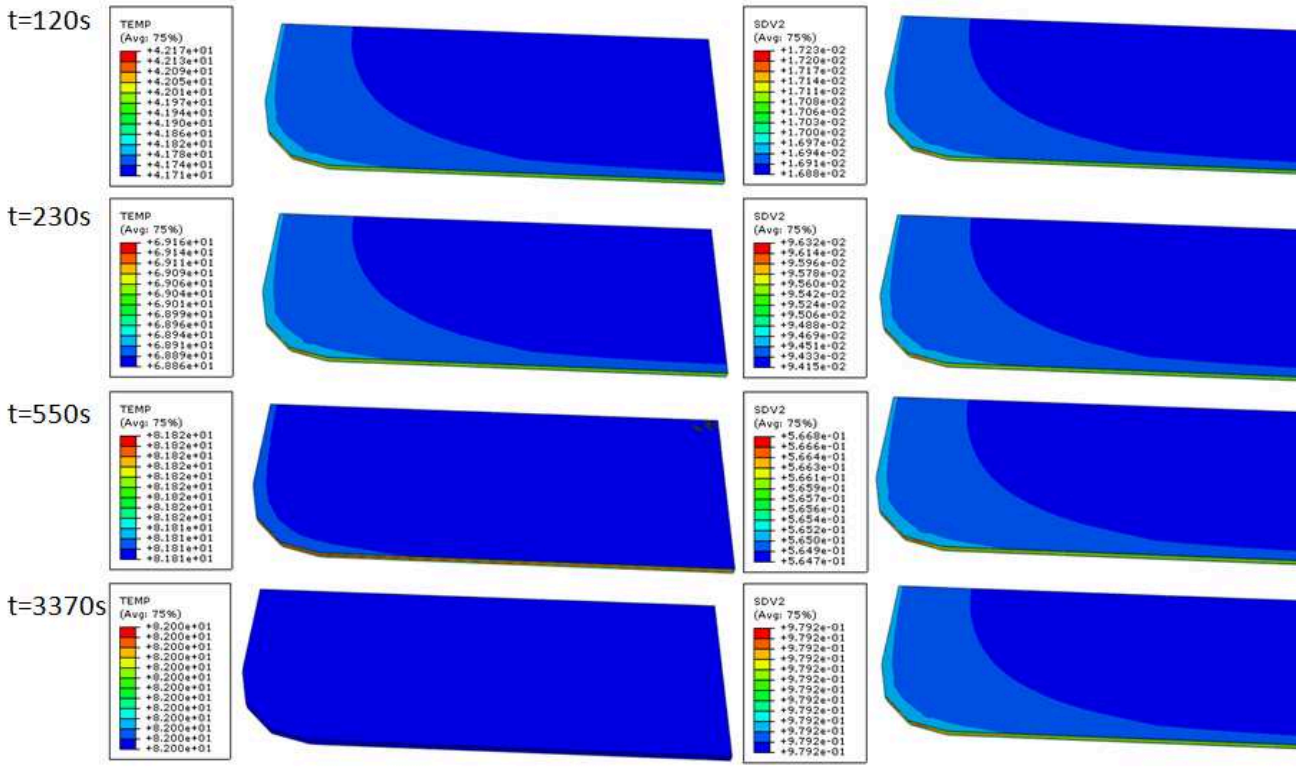

Figure 117. Predicted responses within the adhesive layer for a thermal loading of 1h at 82°C: (a) temperatures and (b) curing state.

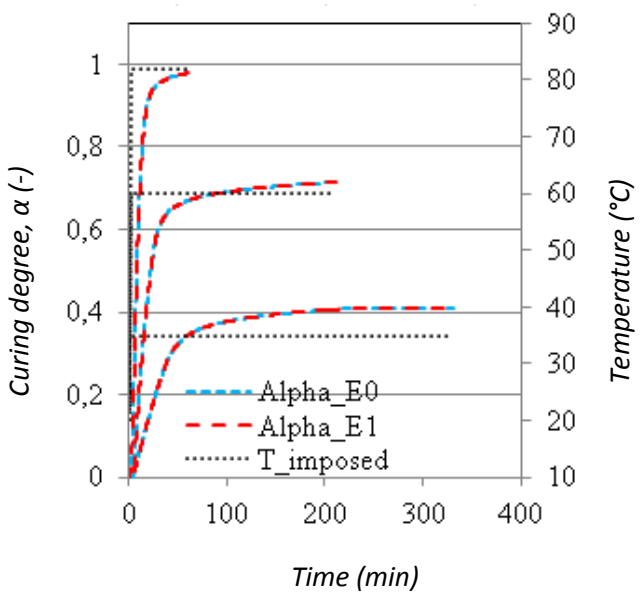

Figure 118. Predicted curing degrees vs time for the three curing cycles applied.

Curing cycle	Curing degree, α (-)
5h30 at 35°C	0.40
3h30 at 60°C	0.70
1h at 82°C	1.00

Table 16. Curing cycles and degrees of cure details.

3.2.3. Strain-rate effects

In most applications such as that in this study, the design of the bonded joint requires to known the mechanical behavior of the adhesive for slow and high strain rates [MAR 98][YU 01][IWA 10]. Some studies generally considered separately the influence of temperature and loading-rate on the adhesive behavior. Richeton et al. [RIC 06] studied the influence of temperature and strain-rate on the behavior of three amorphous polymers with uniaxial compression stress-strain tests. He established that the initial Young's modulus, the yield stress and the strain hardening rate exhibit similar dependency on temperature and loading rate: these quantities decrease with an increasing temperature and increase with an increasing strain-rate. From this statement, he proposed a yield stress model based on a strain rate/temperature superposition principle to predict the yield stress for a wide range of temperature and strain rates. In the same manner, Banea et al. [BAN 11] investigated the combined effect of temperature and strain-rate on the tensile properties of a high temperature epoxy adhesive. Similar observations to that of Richeton were found. It was observed that for temperatures far below the glass transition T_g, a reduced sensitivity of tensile strain to the loading-rate was found as compared to the effect at temperatures around T_g. For such studies, the curing process of the polymer materials remained identical, i.e. the curing state is the same for all specimens before submitting thermal/strain-rate loading. Li et al.[LI 11] considered the combined effect of conversion degree, thermal history (cooling rate), temperature and strain rate on the thermal and mechanical properties of thermoset polymers. Regarding temperature and strain rate, similar observations to those seen previously were highlighted. Further, for a given strain-rate, it was shown that the yield stress increases with an increasing conversion degree. Two effects instigated this trend. The first one is the increase in molecular weight and network cross-linking. The other one is the increase of the glass transition with curing degree.

Considering these investigations, the effect of conversion degree (i.e. the curing history) and loading-rate must be studied to better understand the mechanical properties/behavior of the cold-curing adhesive used in this study. To that purpose, four loading rates (v=0.01, 0.05, 0.5 and 10 mm.min^{-1}) were applied to Arcan Evolution samples cured under the third curing cycles defined previously. These specimens were loaded in shear (γ=90°) and compression-shear (γ=135°). Indeed, the nonlinear behavior mainly occurring for such loadings, loading-rate effects will be more noticeable.

3.3. Experimental characterization

The characterization of the adhesive Hysol EA-9321 for the three curing cycles previously defined was performed using the Arcan Evolution specimen. For each curing state of the adhesively bonded joint, monotonic loadings, i.e. tension, shear, tension-shear and compression-shear loadings were firstly considered at a crosshead speed of 0.5 mm/min. Then, rate effects were investigated on shear and compression-shear loadings at traverse speeds of 10 mm/min, 0.5 mm/min, 0.05 mm/min and 0.01 mm/min. The purpose was to analyze correctly the viscous effects. For each loading ration, only two or three specimens were tested since very low scatter was observed.

3.3.1. Curing cycle of 1h at 82°C

3.3.1.1. Monotonic loadings

Figure 119 shows the experimental results of Arcan Evolution specimens cured 1h at 82°C and tested under tension (γ=0°), shear (γ=90°), tension-shear (γ=45°) and compression-shear (γ=135°) loadings. To make reading of the curves easier, results in compression-shear were plotted in terms of absolute value. Both normal and tangential displacement contributions were considered. It can be noticed that the scatter of results is quite low, except for results at 135° in the normal direction. However, as discussed in the next chapter, this will have negligible consequences on the determination of the constitutive law of the adhesive

since it will be nearly fully identified in tangential direction. Thus, experimental results are of sufficiently high quality for the analysis stage of the mechanical behavior of the adhesive Hysol EA-9321. Normal and tangential displacements are not in the same orders of magnitude. Indeed, a ratio DN/DT ≈ 0.45 at failure is observed for tension-shear loads, and DN/DT ≈ 0.005 for compression-shear loads. Given these conflicting values, the experimental results in the normal and tangential directions are plotted in separate figures.

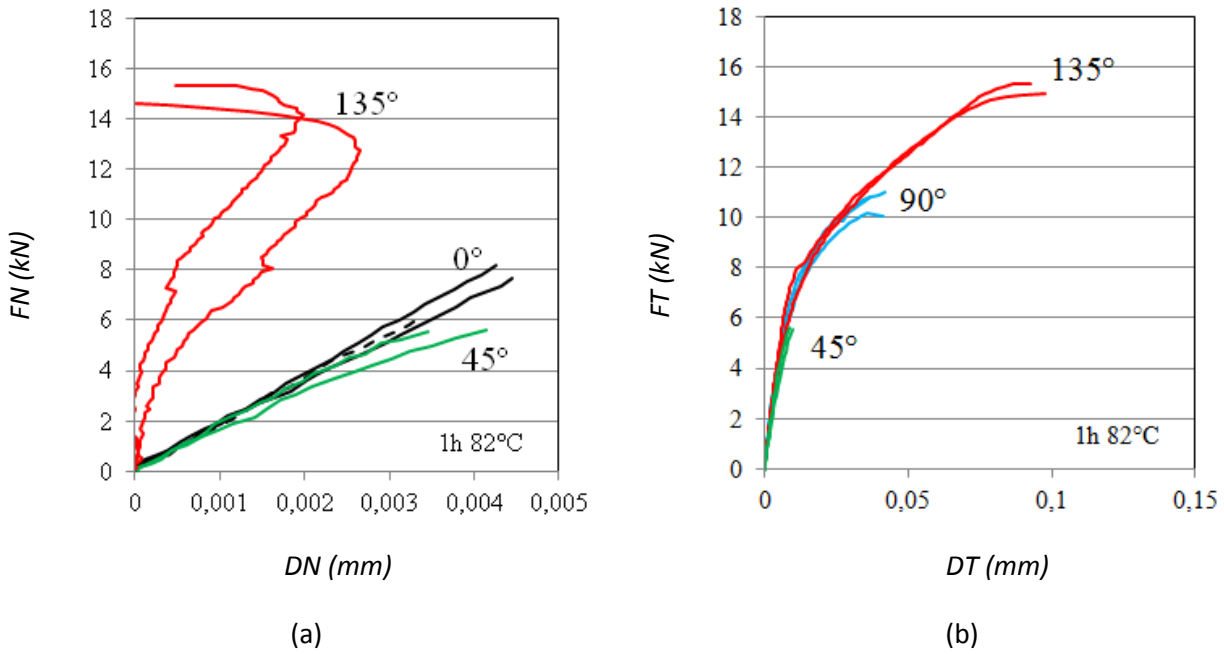

(a) (b)

Figure 119. Experimental results for the curing cycle of 1h at 82°C under tensile (γ=0°), shear (γ=90°), tensile-shear (γ=45°) and compression-shear (γ=135°): (a) in normal direction: FN vs. DN and (b) in tangential direction: FT vs. DT.

A linear behavior is observed under tensile loading (Figure 119 (a)). It is not surprising since the adhesive Hysol EA-9321 is brittleness in tension. Considering the other loadings, the responses of the bonded specimens exhibit a significant non-linear behavior. It can be noticed that stiffnesses are identical for the linear-part of the behavior in tension-shear for a given direction. Tension-shear and compression-shear responses underline an important difference. In fact, the strength at failure is more than three times higher in compression-shear than in tension-shear: (FN, FT) = 5.5, 5.7 kN for tension-shear loading and (FN, FT) = 14.90, 15.3 kN for compression-shear loading. As shown in the previous paragraph, the load ratio at failure between the normal and tangential displacement is ninety times lower in compression-shear than in tension-shear. This is mainly associated with the different behaviors of the adhesive in the normal direction. The adhesive behavior is almost linear in tension-shear whereas the ductile transition in compression-shear appears clearly and is quite short (from 0 to 5e-5 mm, as illustrated in Figure 119 (a)). As it will be detailed in the next chapter, the mechanical behavior of the adhesive was based on a 3D elastic-plastic constitutive law for which the flow function was dyssimmetric because of the non-linear behavior under tension-shear in the normal direction of the adhesives used [MAU 12][ARN 14]. However, in our study, the adhesive highlighted a linear behavior in such configurations. Thus, the flow function was not necessarily dyssimmetric.

3.3.1.2. Strain-rate effects

Figure 120, Figure 121 show the effect of traverse speed on the Arcan Evolution specimens cured 1h at 82°C and loaded in shear (γ=90°) configuration, in compression-shear (γ=135°) configuration, respectively. For each loading case, a low scatter of results is noticed, showing good reproducibility.

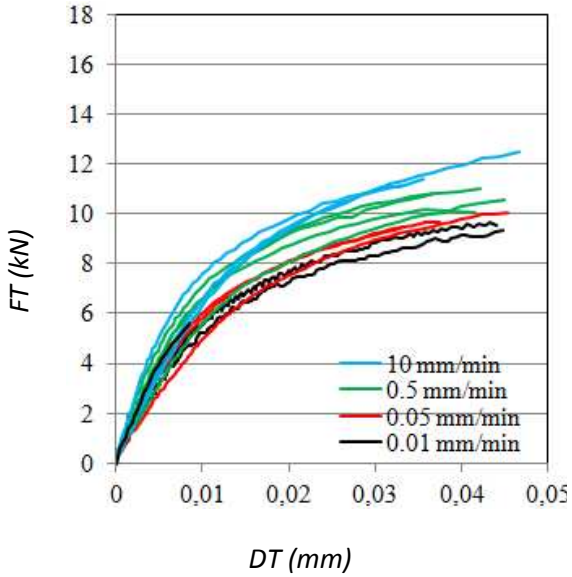

Figure 120. Strain-rate effects using the Arcan Evolution specimen under shear (γ=90°) loading for a curing cycle of 1h at 82°C.

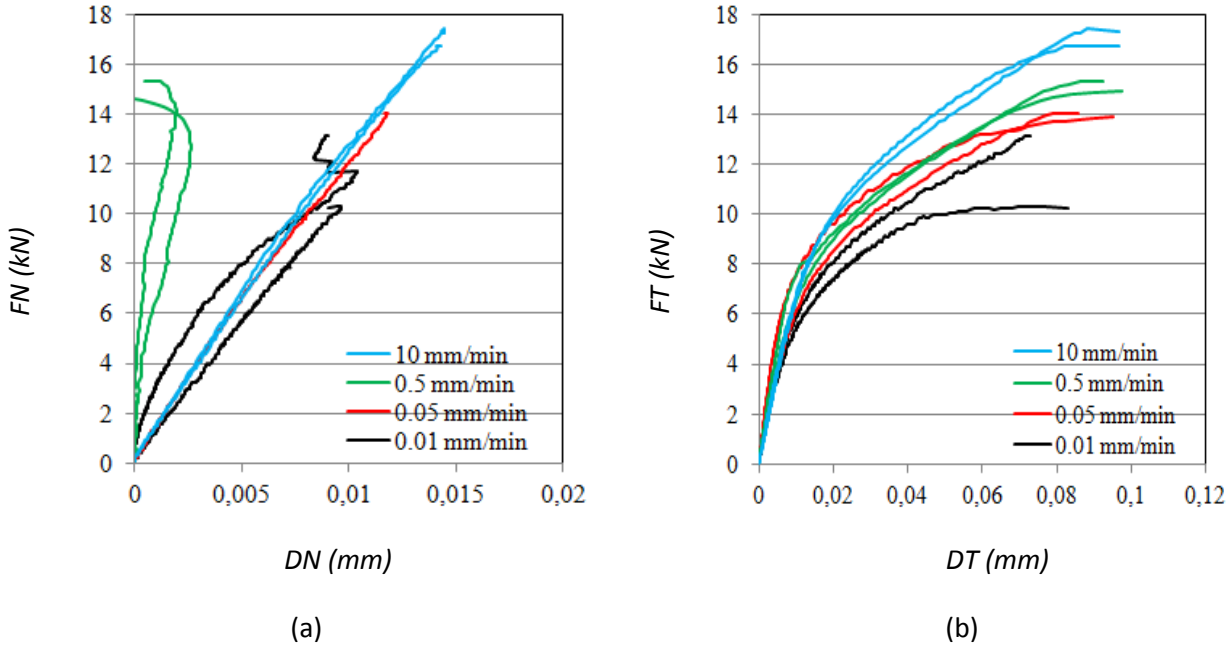

(a) (b)

Figure 121. Strain-rate effects using the Arcan Evolution specimen under compression-shear (γ=135°) loading for a curing cycle of 1h at 82°C: (a) in normal direction: FN vs. DN and (b) in tangential direction: FT vs. DT.

Both figures confirm the influence of strain-rate on this curing cycle responses. Regarding compression-shear results (Figure 121), larger effects are observed in the tangential direction. The main observation is an increase of the yield stress with strain-rate. Increasing the traverse speed gives the adhesive less time to stress relax, thus raising the yield strength. Another consideration is a low ratio DN/DT ≈ 0.1 between the normal and the tangential displacements at failure in 135° regardless of the strain-rate value.

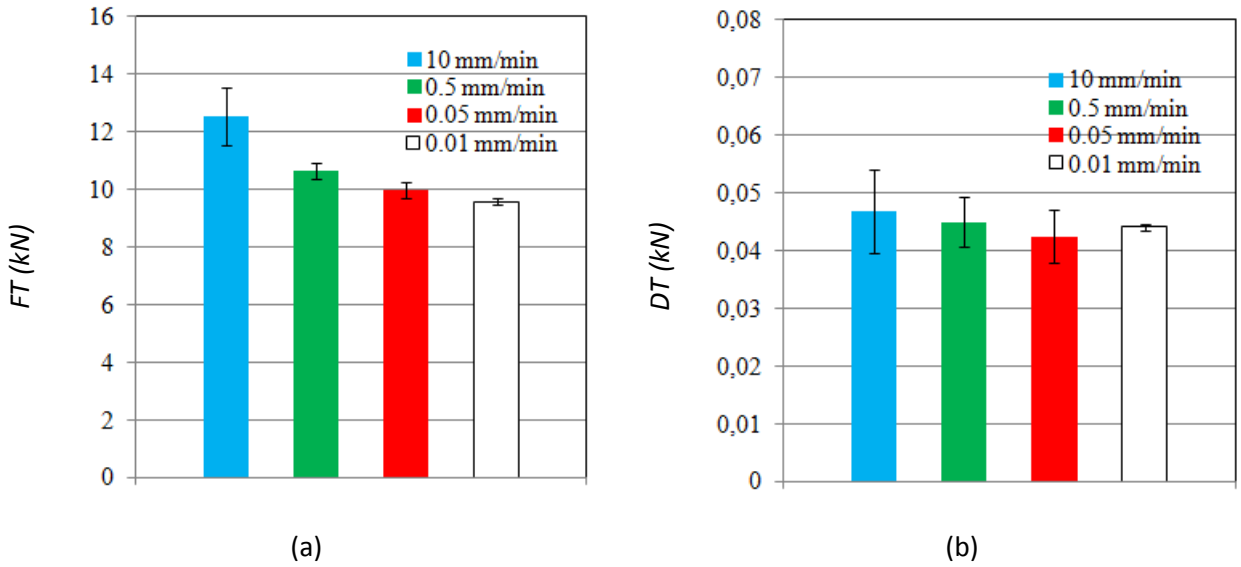

(a) (b)

Figure 122. Influence of strain-rate on the load at failure of the bonded Arcan Evolution specimens tested in shear (γ=90°) for a curing cycle of 1h at 82°C: (a) Tangential load at failure and (b) Tangential relative displacement at failure.

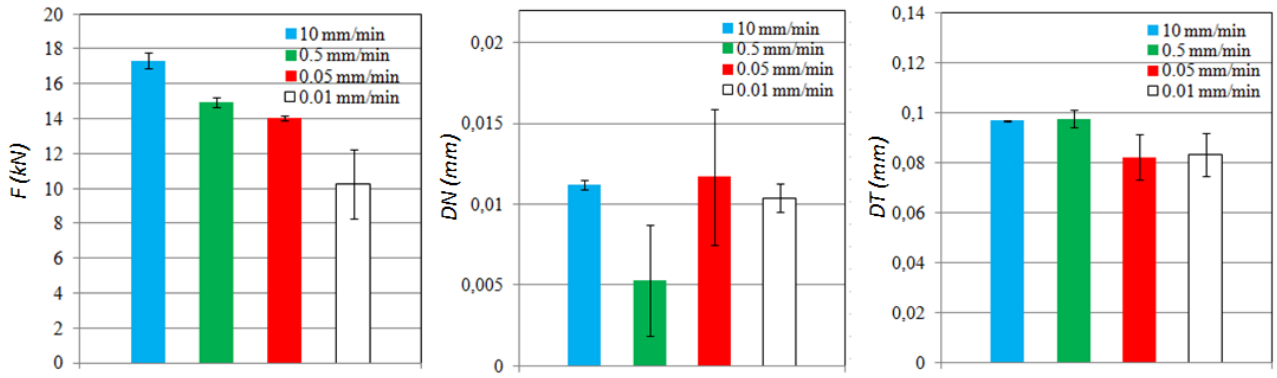

(a) (b) (c)

Figure 123. Influence of strain-rate on the behavior of the bonded Arcan Evolution specimens under compressive-shear (γ=135°) loads: (a) load at failure, (b) normal displacement DN at failure and (c) tangential displacement DT at failure.

Results obtained for the failure loads are presented in Figure 122 for shear loads and in Figure 123 for compression-shear loads. A good correlation is obtained for the mean values at failure associated with each traverse speed. Considering the normal and tangential displacements at failure at 90° and at 135, one can notice that no clear trend emerged. On the contrary, strain-rate effects are mainly observed on failure strengths for both loading which exhibit a similar pattern. The load at failure increases with an increasing strain-rate. This is related to the phenomenon of increasing yield stress with traverse speed.

3.3.2. Curing cycle of 3h30 at 60°C

3.3.2.1. Monotonic loadings

Figure 124 presents the results for Arcan Evolution specimens cured 3h30 at 60°C in both normal and tangential directions for the same loading ratios than previously. Figure 124 (a), Figure 124 (b) give the responses in normal direction, tangential direction, respectively. Compression-shear (γ=135°) results are plotted in absolute terms. Similar conclusions than those of the previous paragraph (curing cycle of 1h at 82°C) can be drawn. Resulting displacements-forces show a low scatter. The ratio DN/DT at failure reaches a value of approximately 0.4 in tension-shear (γ=45°) and DN/DT ≈ 0.1 in compression-shear (γ=135°). At

135°, this data differs widely from that obtained for a curing of 1h at 82°C. A choice was made not to consider these experimental results in the normal direction for the constitutive behavior proposed in the following chapter.

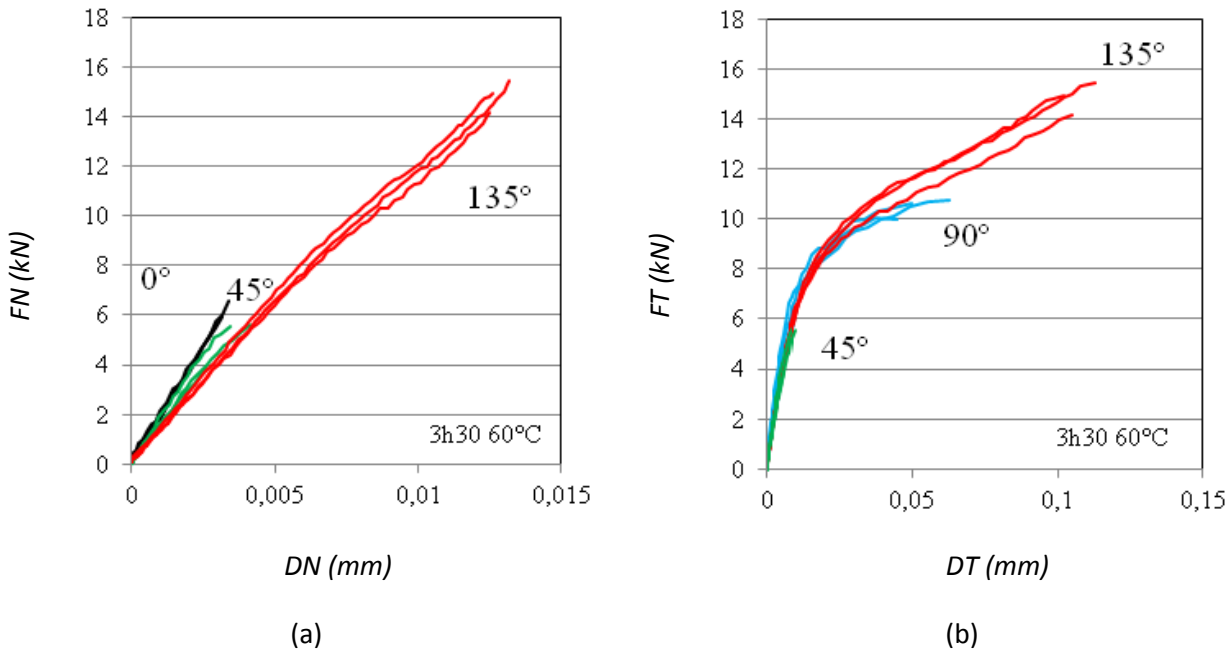

(a) (b)

Figure 124. Experimental results for the curing cycle of 3h30 at 60°C under tensile (γ=0°), shear (γ=90°), tensile-shear (γ=45°) and compression-shear (γ=135°): (a) in normal direction: FN vs. DN and (b) in tangential direction: FT vs. DT.

As noticed earlier, the adhesive Hysol EA-9321 indicates a linear behavior in tension against a non linear behavior in shear, tension-shear and compression-shear. In tangential direction, the initial stiffness is identical for the linear part of the behavior of the adhesive. As to normal direction, Figure 124 (b) shows that the initial stiffness of the elastic part of the bonded joint behavior at γ=135° is slightly weaker than those at γ=0°, 45°. In the normal direction (Figure 124 (a)), the load at failure is about twice and a half higher for compression-shear loading compared to tensile-shear configuration: (FN,FT)=14.20, 14.90, 15.50 kN at γ=135° and (FN,FT)=3.90, 5.60 kN at γ=45°. This indicates different behaviors for such loading ratios. The difference of displacements ratios in normal and in tangential directions for each loading case ensures this comment. In the same manner as before, the use of a dissymmetric flow function in the constitutive modelling was not required.

3.3.2.2. Strain-rate effects

The force-displacement responses corresponding to the testing of Arcan Evolution specimens at several strain-rates in shear (γ=90°) and in compression-shear (γ=135°) configurations are plotted in Figure 125 and Figure 126, respectively. These experimental results exhibit low discrepancy and thus good repeatability of Arcan Evolution tests. As shown for the curing cycle of 1h at 82°C (section 3.3.1.2), an increase in the strain-rate results in an increase of the yield stress of the adhesive which is independent of the loading ratio. Regarding the ratio between normal and tangential displacements at failure for compression-shear tests, DN/DT is almost equal to 0.1 regardless of the traverse speed applied.

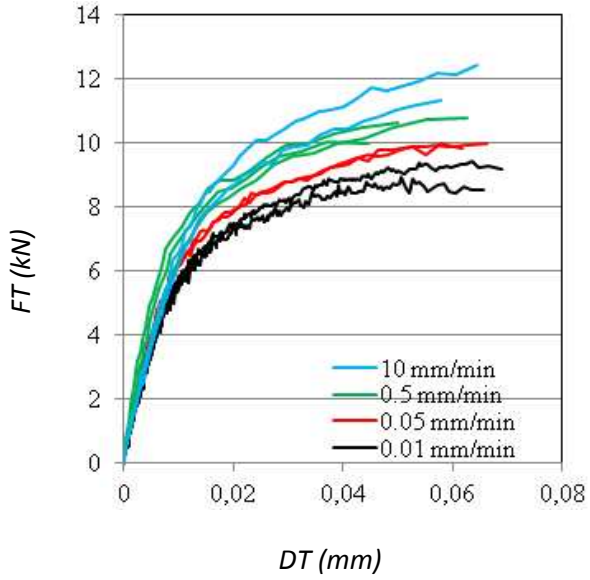

Figure 125. Strain-rate effects using the Arcan Evolution specimen under shear (γ=90°) loading for a curing cycle of 3h30 at 60°C.

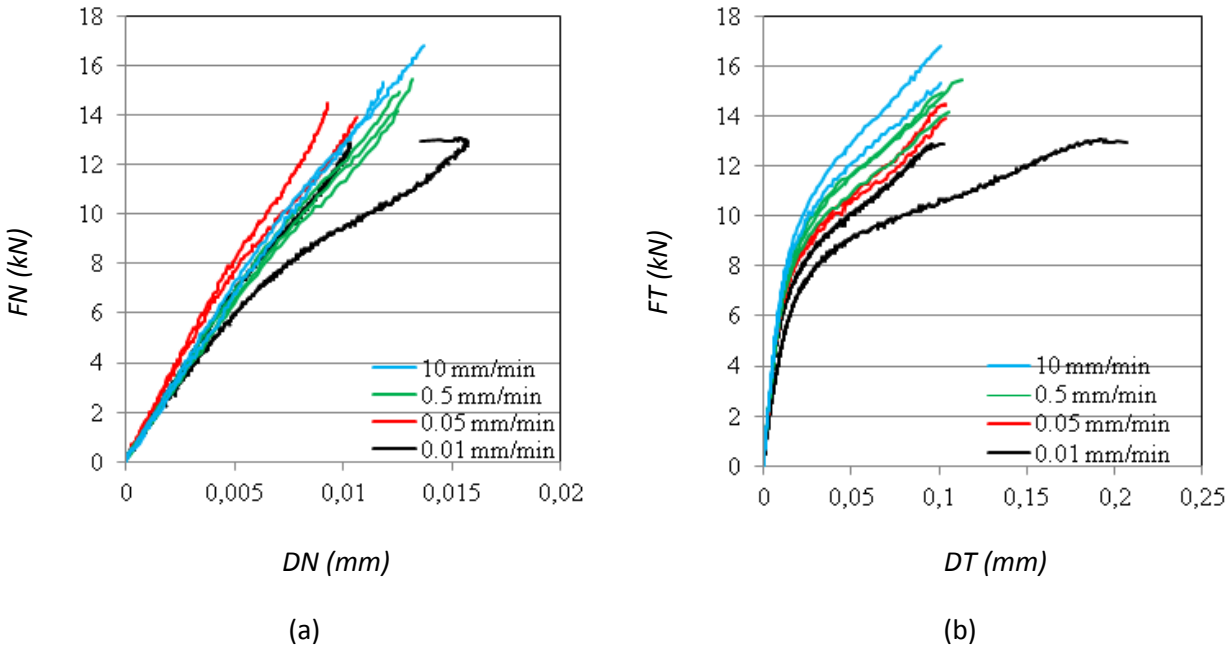

Figure 126. Strain-rate effects using the Arcan Evolution specimen under compression-shear (γ=135°) loading for a curing cycle of 3h30 at 60°C: (a) in normal direction: FN vs. DN and (b) in tangential direction: FT vs. DT.

Figure 127 and Figure 128 show the values at failure for strengths, displacements in both directions in shear and in compression-shear. A first observation is that the loads at failure (Figure 127 (a) and Figure 128 (a)) clearly decrease with the strain-rate: the failure strength range from 12.43 to 9.14 kN at strain-rates going from 10 to 0.01 mm/min in shear and vary from 16.80 to 12.90 kN for traverse-speeds ranging from 10 to 0.01 mm/min. A second one is that larger discrepancies are observed for tangential and normal displacements (Figure 127 (b) and Figure 128 (b), (c)). Thus no clear trend can be drawn.

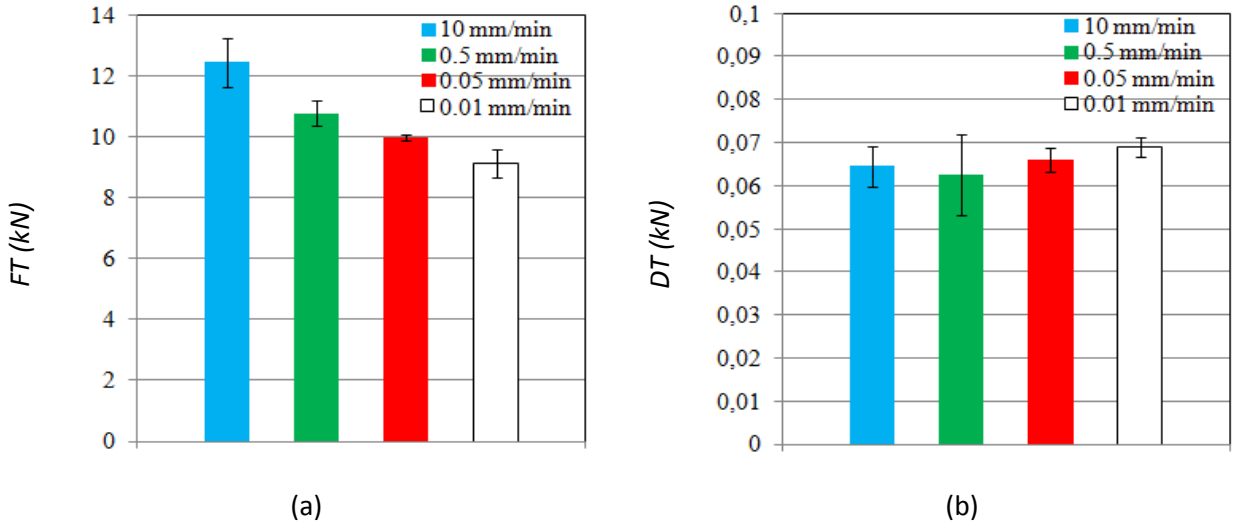

Figure 127. Influence of strain-rate on the load at failure of the bonded Arcan Evolution specimens tested in shear (γ=90°) for a curing cycle of 3h30 at 60°C: (a) Tangential load at failure and (b) Tangential relative displacement at failure.

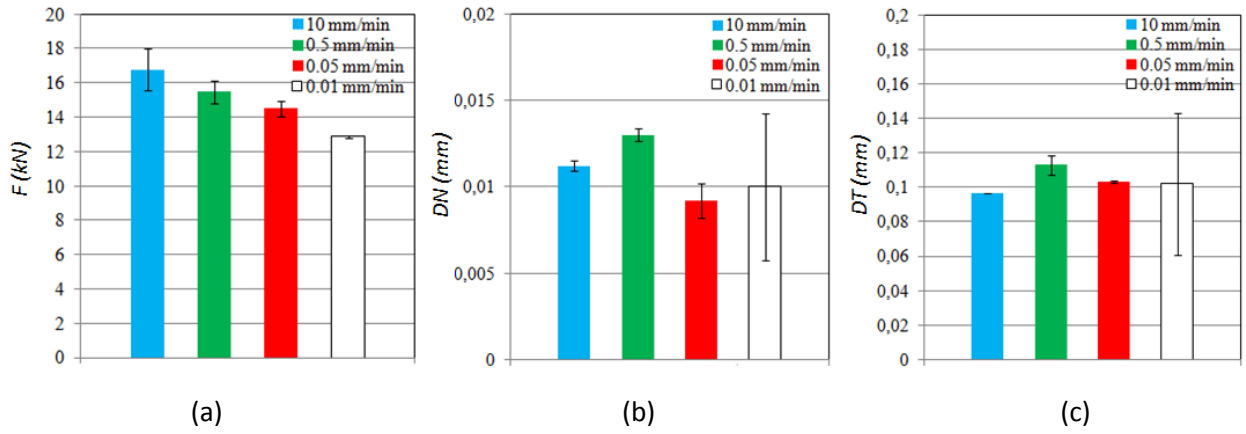

Figure 128. Influence of strain-rate on the behavior of the bonded Arcan Evolution specimens under compressive-shear (γ=135°) loads: (a) load at failure, (b) normal displacement DN at failure and (c) tangential displacement DT at failure.

3.3.3. Curing cycle of 5h30 at 35°C

3.3.3.1. Monotonic loadings

Figure 129 shows the experimental results obtained for Arcan Evolution specimens cured 5h30 at 35°C, considering a loading ratio γ=0°, 45°, 90° and 135°. Absolute values of results in compression-shear are presented to improve curves readability. As noticed for the both curing cycles 1h at 82°C and 3h30 at 60°C, force-displacements responses highlight good repeatability of the tests. A linear behavior is still observed in tension (γ=0°) that proves the ductile behavior of the adhesive Hysol EA-9321 in such configuration. Other loading directions expose a non linear behavior. As represented in Figure 129 (b), force-displacement responses show an identical initial stiffness of the elastic part of the adhesive behavior at γ=45°, 90°, 135°. The initial stiffness differs when comparing the elastic part of results at γ=0°, 45°, 135° in the normal direction, as illustrated in Figure 129 (a). The ratio between displacements in normal and tangential directions reaches values of DN/DT ≈ 0.4 in tension-shear (γ=45°) and DN/DT ≈ 0.08 in compression-shear (γ=135°). This latter value is slightly lower from that computed experiments whose the curing cycle was 3h30 at 60°C (DN/DT ≈ 0.1). As regards the loads at failure, it is approximately three times lower in tension-shear than in compression-shear: (FN, FT) = 4.34, 4.24, 4.12 kN at 45° and (FN, FT) = 11.60, 12.27, 11.09 kN at 135°. The discrepancies identified in the normal direction for such loading directions underline different

behaviors: a ductile transition is clearly apparent for tension-shear and compression-shear results whereas the behavior is linear in tension.

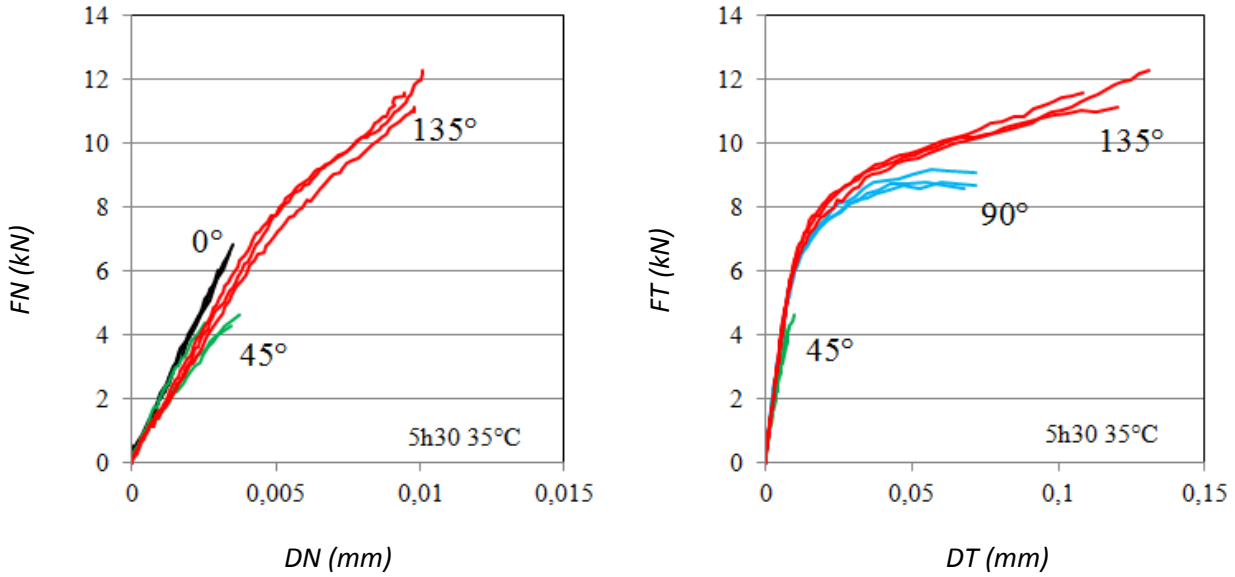

(a) (b)

Figure 129. Experimental results for the curing cycle of 5h30 at 35°C under tensile (γ=0°), shear (γ=90°), tensile-shear (γ=45°) and compression-shear (γ=135°): (a) in normal direction: FN vs. DN and (b) in tangential direction: FT vs. DT.

3.3.3.2. Strain-rate effects

Measured force-displacement responses of Arcan Evolution specimens (curing cycles of 5h30 at 35°C) under shear and compression-shear loading for several traverse speeds are plotted in Figure 130 and in Figure 131 respectively. A low scatter is noticed between responses whose the loading case is identical. As for the previous curing histories responses (sections 3.3.1.2 and 3.3.2.2), an increase of the strain-rate results in a higher yield stress of the adhesive for any loading ratio. Further, the ratio between displacements at failure in both directions reaches approximately a value of DN/DT ≈ 0.075 and is slightly below those obtained for other curing cycles.

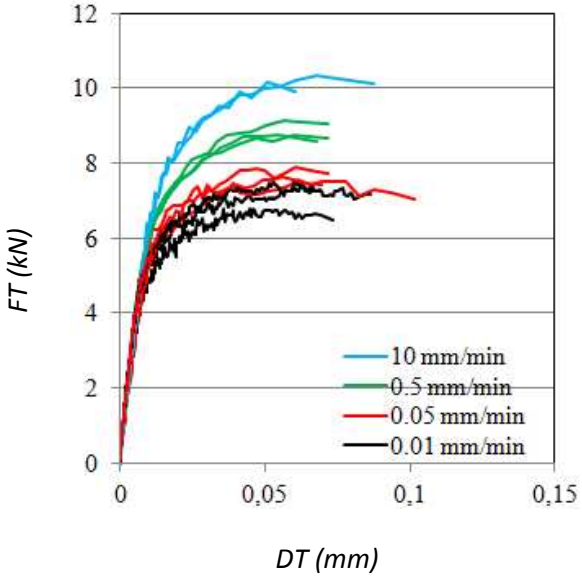

Figure 130. Strain-rate effects using the Arcan Evolution specimen under shear (γ=90°) loading for a curing cycle of 5h30 at 35°C.

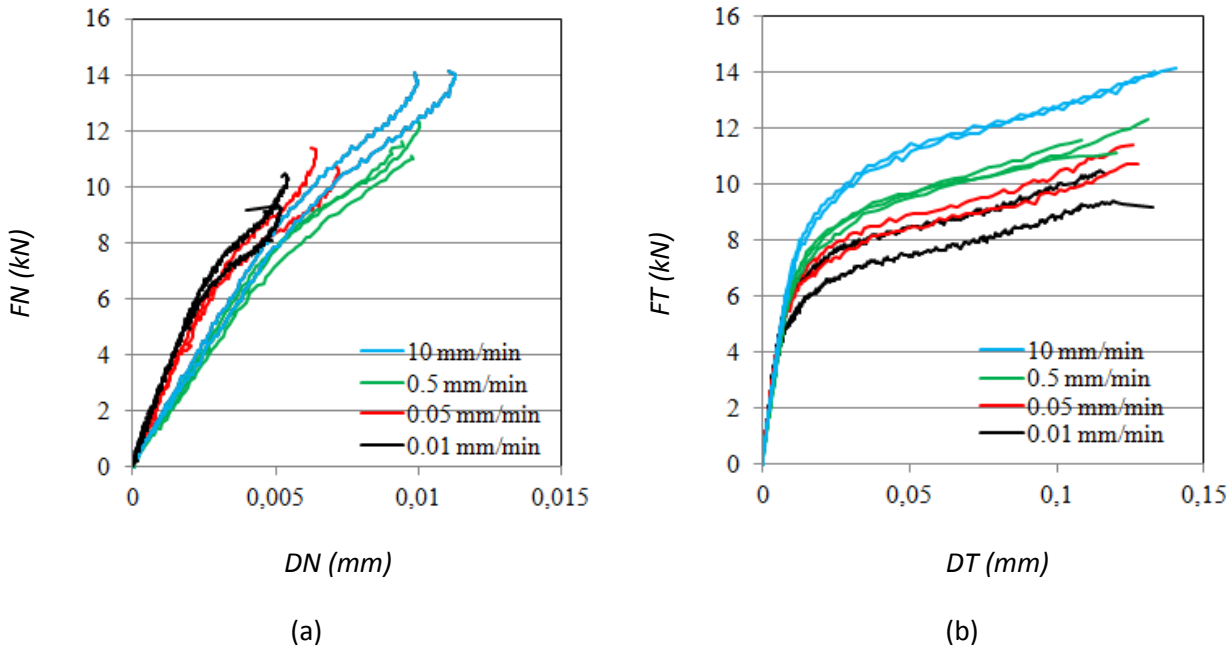

Figure 131. Strain-rate effects using the Arcan Evolution specimen under compression-shear (γ=135°) loading for a curing cycle of 5h30 at 35°C: (a) in normal direction: FN vs. DN and (b) in tangential direction: FT vs. DT.

The load and displacements at failure in normal and tangential directions under shear and compression-shear loadings are represented in Figure 132 and Figure 133. As shown in Figure 132 (a) and Figure 133 (a), the failure strengths decrease with reduction of traverse speed. This is associated with the change in yield stress when modifying strain-rate. Regarding displacements at failure, no tendency can be identified in the tangential direction, as illustrated in Figure 132 (b) and Figure 133 (c): it goes from 10 to 6.5 kN at 90° and varies from 14.04 to 10.36 kN at 135° when reducing strain-rate from 10mm/min to 0.01 mm/min. It seems that the normal displacement in compression-shear configuration decreases with the loading rate (Figure 133 (b)). However, given the differing magnitudes between displacements in both directions, this observed trendy must not be considered.

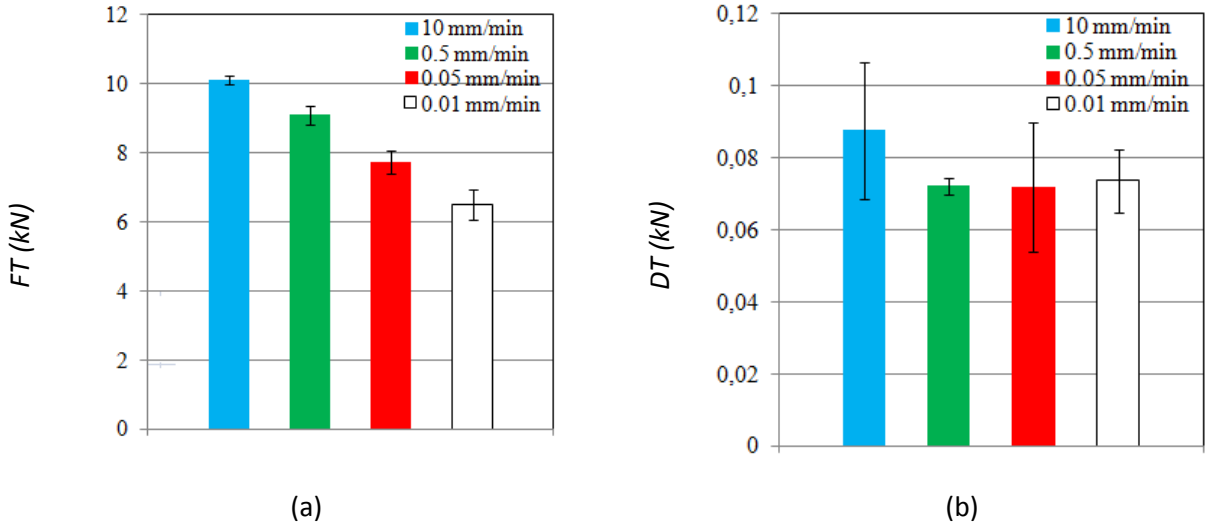

Figure 132. Influence of strain-rate on the load at failure of the bonded Arcan Evolution specimens tested in shear (γ=90°) for a curing cycle of 5h30 at 35°C: (a) Tangential load at failure and (b) Tangential relative displacement at failure.

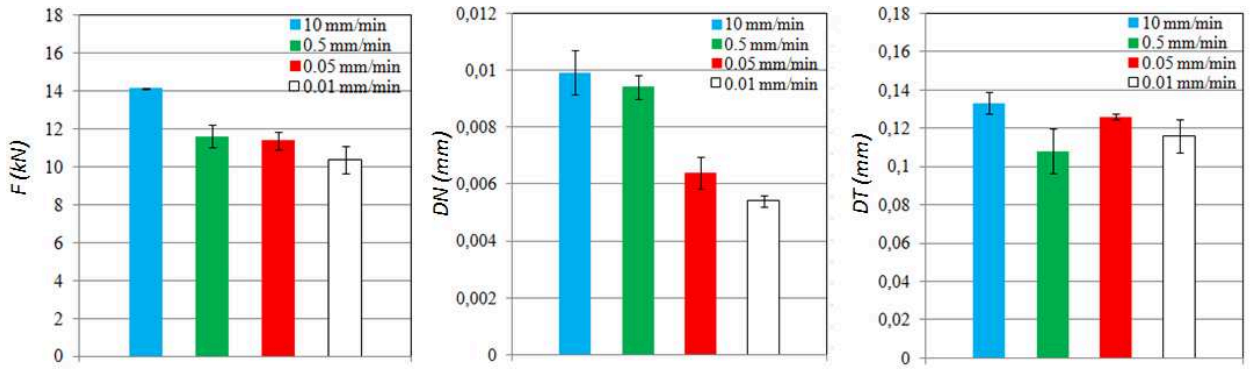

Figure 133. Influence of strain-rate on the behavior of the bonded Arcan Evolution specimens under compressive-shear (γ=135°) loads: (a) load at failure, (b) normal displacement DN at failure and (c) tangential displacement DT at failure.

3.3.4. Effect of the curing state of the adhesive Hysol EA-9321 on its mechanical properties

3.3.4.1. Monotonic loadings

Figure 134 presents the experimental results for the three curing states identified earlier in both normal and tangential directions for tensile, shear, tensile-shear and compression-shear loadings. For each loading case, only one curve was represented to ensure a clearer view of results.

For tensile loadings (γ=0°) (Figure 134 (a)), the stiffness don't almost varies almost between the different curing specimens. Regarding the failure load, the curve exhibits an increase for a curing state of α=1.0. However, no finding can be made since this adhesive is very brittle under tension loading.

For shear configuration (γ=90°) (Figure 134(b)), the three cured specimens show a similar behavior since the slopes of the non-linear part are virtually identical. The curves are shifted up with the increase of the curing degree. On the contrary, the failure load decreases and the tangential displacement at failure decreases with ageing: from 8.65, 10.8 to 10.9 kN for curing degrees of 0.4, 0.7 and 1.0, respectively. A higher difference exists for curing degrees of 0.4 and 0.7. One explanation may be that the chain mobility is more important for low curing degrees than for almost completely cured adhesives. Thus, the bonded joint is more resistant for high curing degrees and as a consequence, failure loads difference is higher between a "flexible" low cured and high cured adhesive than between high cured and completely cured adhesive.

For tension-shear configuration (γ=45°) (Figure 134 (b) and (c)), similar conclusions that for tensile loadings can be drawn. The non-linear part is almost unseen compared to that of shear and compression-shear in tangential directions (Figure 134 (b) and (f)). Further, the brittleness of the adhesive makes comparisons of the failure loads difficult. The comparison of experimental results in compression-shear is difficult in the normal direction (Figure 134 (e)) since those results are assumed to be wrong. In addition, for mixed-mode loadings, the values of the displacements in the tangential direction are ten times higher than those in the normal direction. Thus, there may be a lack of precision of the post-processing area for the derivation of the normal relative displacements. However, a non-linear behavior is seen for curing states of 0.4 and 0.7.

Considering the compression-shear configuration (γ=135°) in tangential direction (Figure 134 (f)), similar observations as shear results can be made. Indeed, the curves are moved up and the load failure is reduced with increase of curing degree (from 12.27 to 15.56 kN for curing states of 0.4 to 0.7, respectively). A slight decrease is observed between curing degrees of 0.7 and 1.0 (from 15.46 to 14.67 kN for curing states of 0.7 and 1.0, respectively). Additionally, the three specimens do not show exactly similar behaviors. Regarding

the curing state of 0.4, an inflection point followed by a slope increase is observed around a tangential displacement of 0.075 mm. This slope modification attenuates with increasing of the curing state.

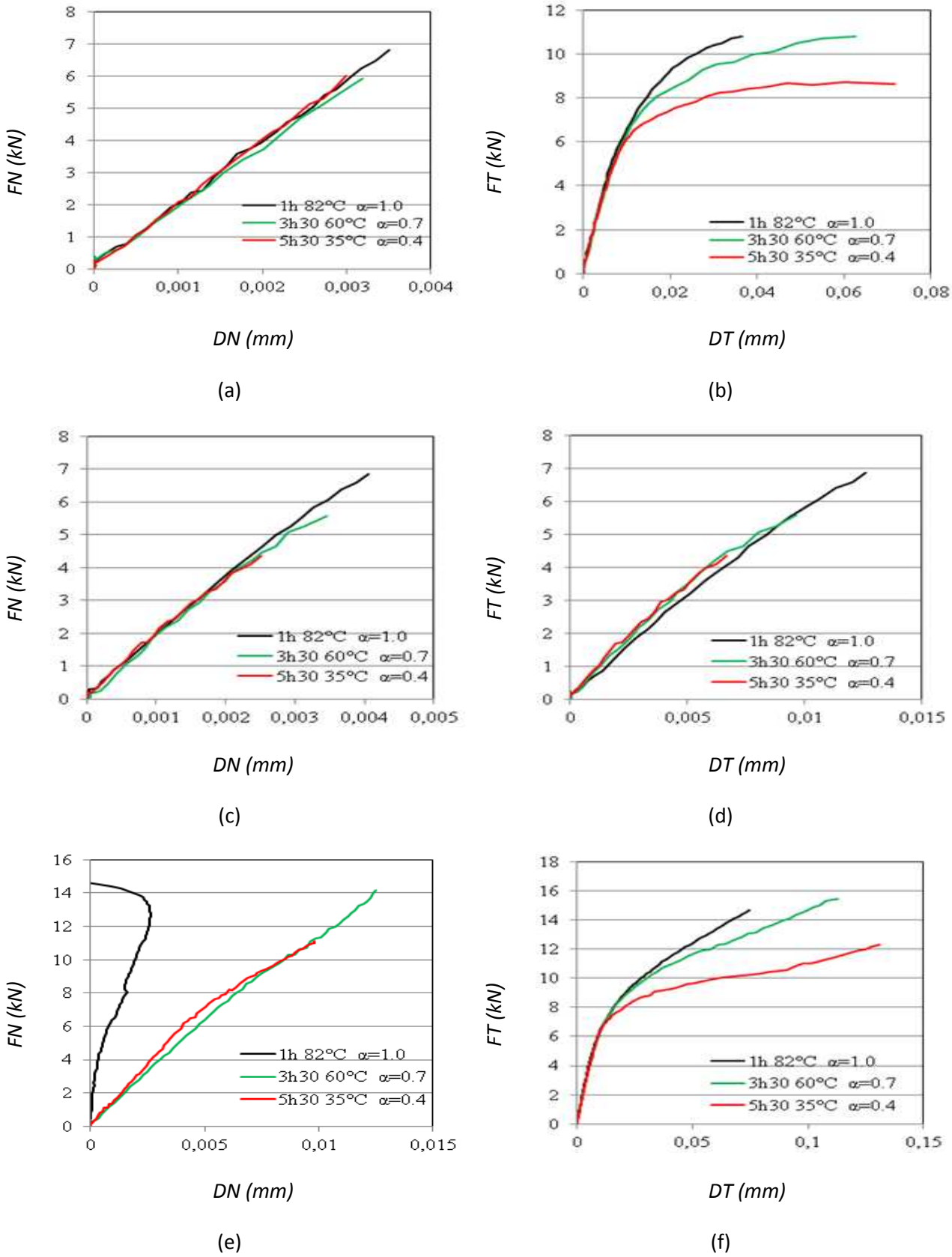

Figure 134. Comparisons of experimental results for the three curing states under different loadings: (a) tension (γ=0°), (b) shear (γ=90°), (c-d) tension-shear (γ=45°) and (e-f) compression-shear (γ=135°). Results are given as force vs. relative displacement in the normal (FN vs. DN) or tangential (FT vs. DT) directions.

From the first experimental results in sections 3.3.1, 3.3.2 and 3.3.3, the adhesive exhibits an elasto-plastic behavior. Considering the results in compression-shear, main changes with the curing state occur in the non-linear parts. Moreover, the change slope at the half of the curve leads to a modification of the hardening with the curing state of the adhesive.

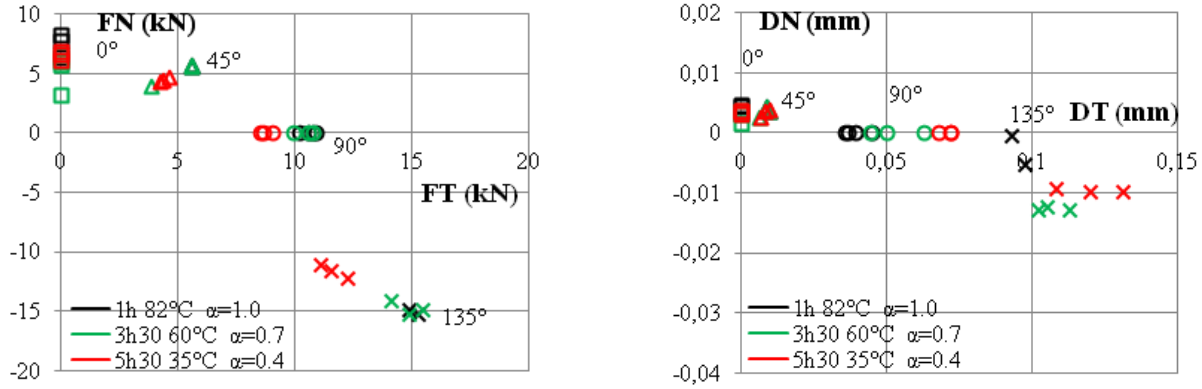

(a) (b)

Figure 135. Influence of the curing degree on the failure envelope for Arcan Evolution specimens tested in each loading direction: (a) normal-tangential load diagram and (b) normal-tangential displacement diagram.

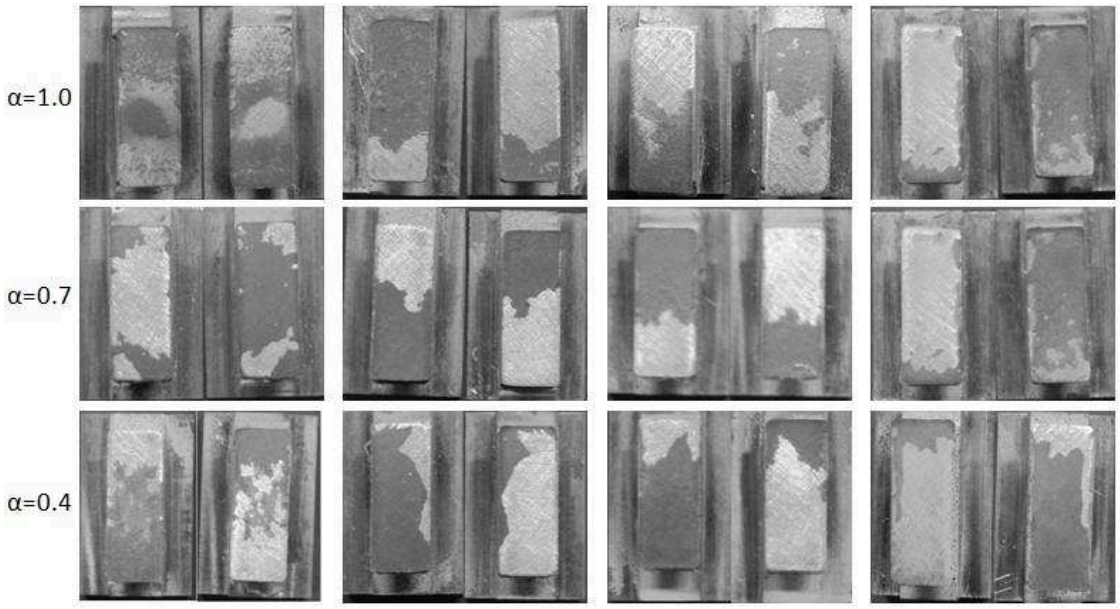

Figure 136. Fracture surfaces in tension (γ=0°), tension-shear (γ=45°), shear (γ=90°) and compression-shear (γ=135°) for the three curing degrees of the adhesive.

Figure 135 summarizes the results at failure obtained under the four different loading ratios γ = 0°, 45°, 90° and 135° for the three curing states of the adhesive α =0.4, 0.7 and 1.0. As previously observed, both normal-tangential diagrams a low scatter. Considering the displacements at failure (Figure 135 (b)), a larger difference is observed between normal and tangential data. However, it is difficult to estimate the influence of curing states with the latter. Figure 135 (a) underlines the strong influence of the tangential load component on the adhesive behavior. Further, this is widely influenced by the curing state of the adhesive. It appears that the load at failure increases with the curing state of the adhesive. Furthermore, a greater difference is noticed between low curing states than for high curing degrees: in compression-shear (γ=135°), (FN, FT) ≈ 11.6, 14.92 kN for curing degrees α = 0.4, 0.7 and (FN, FT) ≈ 14.92, 15.31 kN for curing

degrees α = 0.7, 1.0 respectively. This is mainly due to a low cross-linking and large chain mobility at low curing states. Thus, a lower strength is required to cause failure than for high polymerized adhesive. The adhesive is clearly brittle in tension and no trend is observed with the change of the adhesive polymerization.

The examination of fracture surfaces illustrated in Figure 136 shows a mixed adhesive failure, which is an adhesive failure with adhesive remaining on both substrates, for each loading ratio regardless of the curing state of the adhesive. Thus, the curing state of the adhesive does not affect the type of failure. Some comparable studies [MAU 13] found similar results.

3.3.4.2. Strain-rate effects

Figure 137 and Figure 138 represents the influence of the curing state of the adhesive Hysol EA-9321 on the strain-rate responses under shear (γ=90°) and compression-shear (γ=135°) configurations, respectively. Four traverse speeds were applied: 10 mm/min, 0.5 mm/min, 0.05 mm/min and 0.01 mm/min. One force-displacement response was plotted for each loading case. Further, only results in the tangential direction were considered in compression-shear. In fact, it was previously noticed that normal displacements were significantly lower than those in tangential direction and were not affected by curing state of the adhesive.

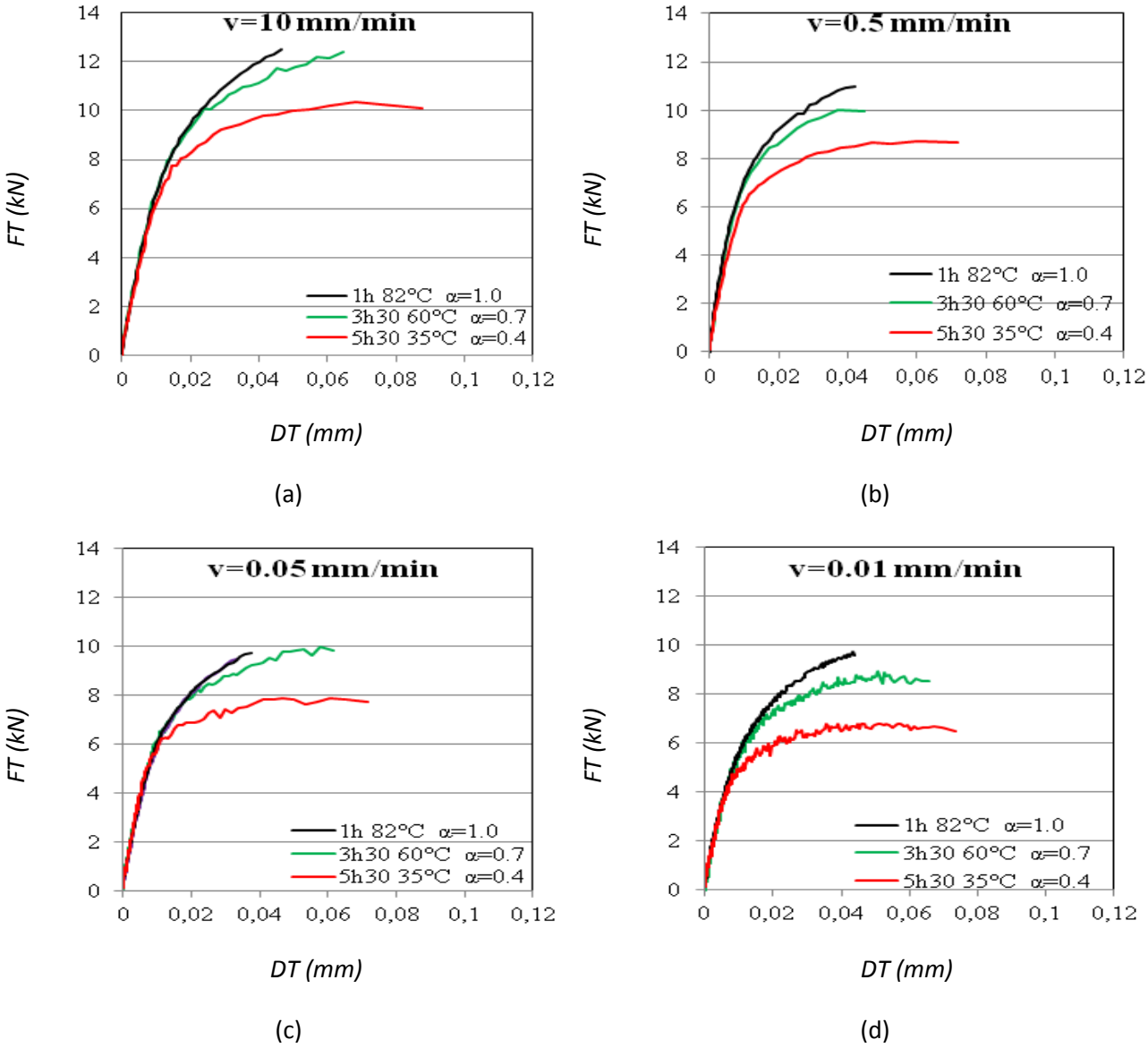

Figure 137. Influence of the curing degree on the strain-rate responses for Arcan Evolution specimens tested in shear (γ=90°): (a) v=10 mm/min, (b) v=0.5 mm/min, (c) v=0.05 mm/min and (d) v=0.01 mm/min

Regarding responses in shear (Figure 137), similar behaviors are observed for each strain-rate loading. The curves are moved up with an increasing curing degree. Conversely, the strengths and displacements at failure decrease when reducing curing conversion. A main explanation is that the cross-linking density and the chain mobility are higher for low curing degrees than for almost completely cured adhesives. Thus, the adhesive is more flexible at low curing degrees that at high curing conversions. As a consequence, the bonded assembly is less resistant and the loads at failure are weak for low curing degrees. In the same manner, the adhesive deforms more easily and the strains at failure increase for low polymerization.

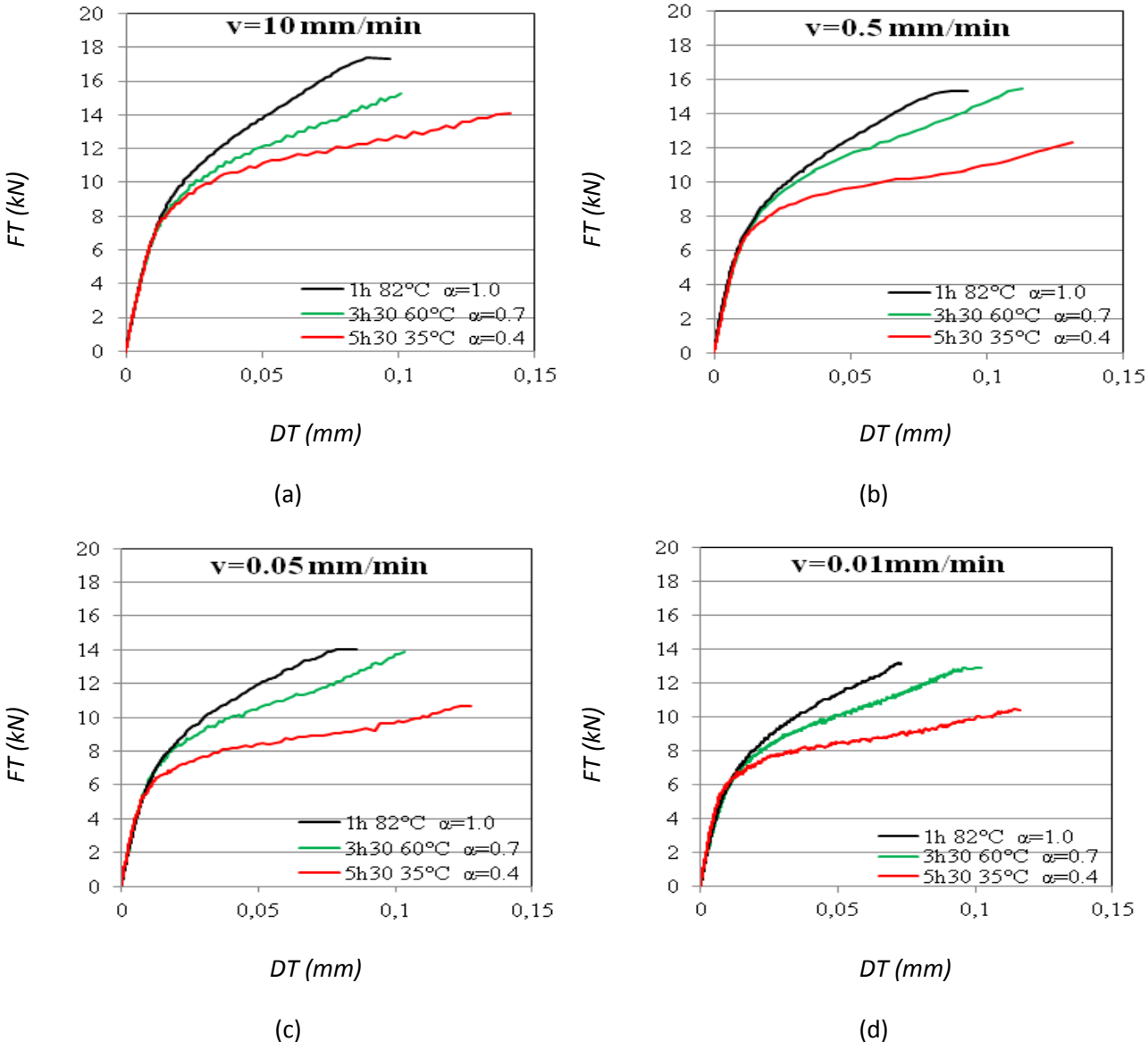

Figure 138. Influence of the curing degree on the strain-rate responses for Arcan Evolution specimens tested in compression-shear (γ=135°): (a) v=10 mm/min, (b) v=0.5 mm/min, (c) v=0.05 mm/min and (d) v=0.01 mm/min

For compression-shear configuration (Figure 138), similar conclusions to those reflected for shear loading can be made. In fact, the curves are moved up and the loads and displacements at failure are reduced when increasing curing degree. On the contrary to shear responses, the three specimens do not exhibit exactly similar behaviors in the non-linear part. For low curing states, an inflection point followed by a slope increase is observed around a tangential displacement of half of the non-linear part. This slope recovery attenuates with increasing of the curing state. For instance, at a strain-rate of 0.01 mm/min for α= 0.4, (Figure 138 (b)), this inflection point is located at around 0.064 mm.

3.4. Conclusions

In this chapter, the influence of the curing degree of the adhesive Hysol EA-9321 was experimentally investigated through the Arcan Evolution device. This one is an improvement of the modified Arcan fixture from a manufacturing point of view. Further, the surface of bonded specimens is twice lower than previous pieces used in modified Arcan device. Thus, more tests can be performed. It is very interesting for test repeatability.

The influence of the curing conversion was investigated by applying three different curing cycles to Arcan Evolution specimens: 1h at 82°C, 3h30 at 60°C and 5h30 at 35°C. The chemical state of the adhesive reached after each curing process induced different mechanical responses. Moreover, the temperature effects on the curing behavior of the adhesive in a bonded assembly were accounted for. This was based on the applying of the thermo-kinetic FE model established in chapter 2 to an Arcan Evolution specimen in order to provide the temperature and curing degree distribution in the adhesive during each curing process.

Considering the influence of the curing degree on the mechanical behavior of the adhesive Hysol EA-9321, monotonic loadings, such tension (γ=0°), tension-shear (γ=45°), shear (γ=90°) and compression-shear (γ=135°) were firstly considered at a crosshead speed of 0.5 mm/min for each curing state of the adhesive. Then, rate effects were investigated on shear and compression-shear loadings at traverse speeds of 10 mm/min, 0.5 mm/min, 0.05 mm/min and 0.01 mm/min. The purpose was to analyze correctly the viscous effects. For each loading ration, only two or three specimens were tested since very low scatter was observed. Careful consideration was given to the measurement set-up and post-processing method. A 3D full field measurement enabled to analyze accurately the adhesively bonded joint behavior during testing.

Similar conclusions were drawn when investigating the influence of adhesive state on monotonic and strain-rate loads. At first, the curing degree had almost no effects in tensile (γ=0°) and tensile-shear (γ=45°) loadings. This was mainly due to the brittleness of this adhesive. For shear (γ=90°) and compression-shear loadings (γ=135°), the loads at failure occurred for smaller tangential displacements when increasing the curing state of the adhesive. Further, the responses were shifted up with the increase of curing state. A major explanation was the decrease of mobility with the increase of curing degree. As a result, the bonded assembly was more resistant and the adhesive layer deformed with more difficulties. With regard to the adhesive behavior, an inflection point followed by an apparent increase in the stiffness was observed at low curing states. This phenomenon was attenuated with the increase of curing degree.

∞

In the following, we will focus on the prediction of the 3D behavior of the adhesive Hysol EA-9321 in an assembly by including polymerization effects. The experimental database establishes in this chapter will be used to correctly identified the model parameters through an inverse identification strategy.

3.5. References

[ARC 87] Arcan L, Arcan M, Daniel L. SEM fractography of pure and mixed mode interlaminar fracture in graphite/epoxy composites ASTM Tech. Publ. ASTM. Philadelphia, 948:41-67, 1987.

[ARN 14] Arnaud N., PhD Thesis : Analyse de l'effet du vieillissement en milieu humide sur le comportement mécanique d'adhésifs en assemblages sous sollicitations multiaxiales, 2014.

[AVI 10] Avitabile P., Niezrecki C., Helfrick M., Warren C., Pingle P., Noncontact Measurement Techniques for Model Correlation, Sound & vibration, Vol. 44, pp. 8-13, 2010.

[ETA 99] ETAG 002. Guideline for European technical approval for structural sealant glazing system (SSGS) part 1 supported and unsupported systems. EOTA, Kunstlaan, Brussels, Belgium; 1999.

[COG 05] Cognard J.Y., Davies P., Gineste B., Sohier L., Development of an improved adhesive test method for composite assembly design. Compos Sci Techno, 65:359-68, 2005.

[COG 08] Cognard JY, Numerical analysis of edge effects in adhesively-bonded assemblies. Application to the determination of the adhesive behavior. Computers and Structures, 86:1704-17, 2008.

[CRE 15] Créac'hcadec R., Sohier L., Cellard C., Gineste B., A Stress Concentration-Free Bonded Arcan Tensile Compression Shear Test Specimen for the Evaluation of Adhesive Mechanical Response, 2015.

[DEV 15] Devaux O., Créac'hcadec R., Cognard J.Y, Lavelle F. FE simulation of the curing behavior of the epoxy adhesive Hysol EA-9321, International Journal of Adhesion and Adhesives, 2015.

[FAZ 10] Fazzini M., Mistou S., Dalverny O., Robert L., Study of image characteristics on digital image correlation error assessment, Optics and Lasers in Engineering, Vol. 48 (3), pp. 335-339, 2010.

[GOM] Gom documentation, GOM France SAS, (www.gom.com), Ris Orangis, France.

[IWA 10] Iwamoto T., Nagai T., Sawa T., Int. J. Solids Structures, Vol. 47, p. 175, 2010.

[KOK 13] Kok CK, Ooi CC, Ng JJ, Liew KW., Experimental study and modelling of an adhesive bonded polycarbonate assembly for application in consumer electronics. J Adhes, 89:247-263, 2013.

[LI 11] Li C., Strachan A., Molecular dynamics predictions of thermal and mechanical properties of thermoset polymer EPON862/DETDA, Polymer, Vol. 52, pp. 2920-2928, 2011.

[MAR 98] Martinez M.A., Chocron I.S., Rodriguez J., Sanchez Galvez V., Sastre A., Int. J. Adhesion and Adhesives, Vol. 18, p. 375, 1998.

[MAU 12] Maurice J., PhD Thesis: Characterization and modeling of the 3D elastic-plastic

behavior of structural adhesive films for aeronautical applications, 2012.

[MAU 13] Maurice J, Créac'hcadec R, Cognard JY, Davies P, Meirinhos G, Mahdi S. 3D modeling of the elastic-plastic behavior of thin aeronautical adhesive films suited for a wide range of tensile/compression-shear loads. J Adhes, 89:727-51, 2013.

[MCG 05] McGinnis M.J., Pessiki S., Turker H., Application of Three-dimensional Digital Image Correlation to the Core-drilling Method, Experimental Mechanics, Vol. 45 (4), pp.350-367, 2005.

[PAN 09] Pan B., Qian K., Xie H., Asundi A., Two-dimensional digital image correlation for in-plane displacement and strain measurement: a review. Measurement Science and Technology, Vol. 20(6), 062001, 2009.

[RIC 06] Richeton J., Ahzi S., Vecchio K.S., Jiang F.C., Adharapurapu R.R., Influence of temperature and strain rate on the mechanical behavior of three amorphous polymers: Characterization and modelling of the compressive yield stress, International Journal of Solids and Structures, Vol. 43, pp. 2318-2355, 2006.

CHAPTER 4:

CONSTITUTIVE IDENTIFICATION BEHAVIOR

Résumé

Ce chapitre s'attache à modéliser le comportement mécanique d'un adhésif non totalement polymérisé dans un assemblage, notamment l'adhésif Hysol EA-9321. Cette démarche s'appuie sur les données expérimentales collectées dans le chapitre précédent, à savoir la sollicitation d'éprouvettes Arcan Evolution en traction (0°), cisaillement (90°), traction-cisaillement (45°) et compression-cisaillement (135°) pour différentes vitesses de traverse, ces essais étant réalisés pour divers cycles de cuisson. Plusieurs modèles prenant en compte l'effet de cuisson sur le comportement mécanique d'un tel adhésif ont été présentés dans cette étude. Ceux-ci sont généralement découpés en deux étapes : la détermination du comportement de l'adhésif totalement polymérisé et l'intégration du taux de polymérisation dans ce comportement. Un modèle élasto-plastique de type Mahnken-Schlimmer a tout d'abord été modifié puis employé dans le but de prédire le comportement 3D de l'adhésif totalement cuit en assemblage. Ce comportement a été dit « de référence ». L'effet du taux de polymérisation a ensuite été intégré dans ce modèle de comportement. Une méthode d'identification globale basée sur un couplage entre calculs élements-finis et routine d'optimisation a permis de prendre en compte les effets de cuisson. Ensuite, un modèle elasto-viscoplastique de type Mahnken-Schlimmer prenant en compte les effets de cuisson a été développé. Il est basé sur le premier modèle décrit en y introduisant les effets de vitesse. La dépendance des paramètres visqueux au taux de polymérisation a été déterminée selon les deux étapes définies précédemment. Enfin, une extension purement numérique de ce modèle elasto-viscoplastique à la visco-élasticité a été proposée.

Summary

This chapter consists in modeling the mechanical behavior of an uncured adhesive, such the cold-curing adhesive Hysol EA-9321, in a bonded assembly. This approach is based on experimental mechanical tests under tension/compression-shear loadings for several traverse speeds investigated for several curing cycles in the previous chapter. Multiple cure-dependent models are developed and split in two steps: a first characterization of the totally cured adhesive behavior and the integration of cure-dependent parameters in such model. An elasto-plastic model based on the Mahnken-Schlimmer model is firstly developed and applied to a totally cured adhesive. Then, the cure-dependency of the model is integrated to that model by using inverse identification techniques. The latter are based on a coupling between FE simulations and an optimization process. Next, a cure-dependent elasto-visco-plastic model is developed. It is built on the previous cure-dependent elasto-plastic model by integrating strain-rate effects. At last, a purely numerical extension of this model to viscoelasticity is proposed.

Contents

4.1. Constitutive behavior of a fully cured adhesive Hysol EA-9321

4.1.1. Mahken-Schlimmer elastic-plastic model (MS-Model)

As detailed in chapter 1, epoxy adhesives generally exhibited an elastic-plastic behavior which was very sensitive to the hydrostatic pressure. It appeared that the model proposed by Mahnken was well suited to describe the non-linear behavior of such adhesive [COG 10][CRE 09][JOU 10][MAH 05].

The yield surface was given by:

$$F = f_p - Y_0 \tag{4.1}$$

$$f_p = \sqrt{J_2 + a_1 I_1 Y_0 + a_2 {I_1}^2} \tag{4.2}$$

where a_1 and a_2 were material parameters, Y_0 the initial yield stress before plasticity, I_1 and J_2 were the first stress invariant and the second deviatoric stress invariant defined as:

$$J_2 = \frac{3}{2}\underline{\underline{S}} : \underline{\underline{S}} \qquad ; \qquad I_1 = \frac{1}{3}\mathrm{trac}\left(\underline{\underline{\sigma}}\right) \tag{4.3}$$

where $\underline{\underline{\sigma}}$ was the stress tensor decomposed into a deviatoric part $\underline{\underline{S}}$ and a hydrostatic part P_h:

$$\underline{\underline{\sigma}} = \underline{\underline{S}} + p\underline{\underline{I}} \qquad ; \qquad P_h = I_1 \tag{4.4}$$

The hardening function was given by the relation:

$$Y = Y_0 + q\left(1 - e^{-be_v}\right) + He_v \tag{4.5}$$

where e_v was the equivalent plastic strain defined as follows:

$$\dot{e}_v Y_0 = \underline{\underline{\sigma}} : \underline{\underline{\dot{\varepsilon}}}^{pl} \tag{4.6}$$

The flow potential was given by:

$$g = \sqrt{J_2 + a_1^* I_1 Y_0 + a_2^* {I_1}^2} - Y \tag{4.7}$$

where *a1** and *a2** were material parameters to determine. A non-associated flow rule was chosen. Hence, $a_1^* \neq a_1$ and $a_2^* \neq a_2$ since the flow rule and the yield function may not be the same.
The evolution of the plastic flow and the definition of its direction were defined by a classical normal rule between the plastic strain tensor $\underline{\underline{\varepsilon}}_p$ and the stress tensor $\underline{\underline{\sigma}}$:

$$d\underline{\underline{\varepsilon}}_p = d\lambda \frac{\partial g}{\partial \underline{\underline{\sigma}}} \tag{4.8}$$

where $d\lambda$ was the plastic multiplier.
This model was called “MS-Model” was ruled by 10 parameters:

- Elastic parameters: the Young modulus *E* and the Poisson's ratio *v*
- Model parameters: a_1, a_2, a_1^*, a_2^*, Y_0, q, b and H

4.1.2. Model implementation

The previous equations were transformed to an incremental form using an implicit backward Euler method divided in an elastic predictor phase and a plastic corrector phase [SIM 00], as shown in section 1.4 of chapter 1.

At first, null plastic flow was assumed. Thus the yield criterion defined at increment *n+1* is equal to zero and a trial elastic stress tensor $\underline{\underline{\sigma}}^{trial}$ can be defined as:

$$F\left(\underline{\underline{\sigma}}_{n+1}, Y_{n+1}\right) = 0 \tag{4.9}$$

$$\underline{\underline{\sigma}}_{n+1}^{trial} = \underline{\underline{\sigma}}_{n+1} + \underline{\underline{\underline{\underline{C}}}}_e : \underline{\underline{\Delta\varepsilon}} \tag{4.10}$$

When the trial elastic stress tensor $\underline{\underline{\sigma}}_{n+1}^{trial}$ violated the yield criterion, i.e. F>0, the plastic flow must be considered and the plastic corrector step of the algorithm must be defined to get an admissible stress state. It came the updated stress:

$$\underline{\underline{\sigma}}_{n+1}^{trial} = \underline{\underline{\sigma}}_{n+1} + \underline{\underline{\underline{\underline{C}}}}_e : \left(\underline{\underline{\Delta\varepsilon}} - \underline{\underline{\Delta\varepsilon}}^p\right) = \underline{\underline{\sigma}}_{n+1} + \Delta p \underline{\underline{\underline{\underline{C}}}}_e : \left(\frac{\partial g}{\partial \underline{\underline{\sigma}}}\right)_{n+1} \tag{4.11}$$

Where $\underline{\underline{\underline{\underline{C}}}}_e$ was the elastic constitutive matrix and Δp the plastic multiplier.

The trial stress tensor and the tangent matrix can be decomposed into two parts, one deviatoric $\underline{\underline{S}}$ I and another one spherical P_h:

$$\underline{\underline{\sigma}}^{trial} = \underline{\underline{S}}^{trial} + \frac{1}{3} P_h^{trial} \underline{\underline{I}} \tag{4.12}$$

$$\underline{\underline{\underline{\underline{C}}}}_e = 2\mu_{rev} \underline{\underline{I}} + \lambda_{rev} \underline{\underline{I}} \otimes \underline{\underline{I}} \tag{4.13}$$

It came:

$$\begin{cases} \underline{\underline{S}}_{n+1} = \underline{\underline{S}}_{n+1}^{trial} - 2\mu_{rev}\Delta p \underline{\underline{S}}_{n+1} \\ P_{h,n+1} = P_{h,n+1}^{trial} - 3\left(3\lambda_{rev} + 2\mu_{rev}\right)\Delta p \frac{1}{3}\left(a_1^* Y_0 + 2a_2^* P_{h,n+1}\right) \end{cases} \tag{4.14}$$

$\underline{\underline{S}}_{n+1}$ and $\underline{\underline{S}}_{n+1}^{trial}$ being proportional, it can be written as:

$$\begin{cases} \underline{\underline{S}}_{n+1} = \underline{\underline{S}}_{n+1}^{trial}\left(1 - 2\mu_{rev}\Delta p\right) \\ P_{h,n+1} = \dfrac{P_{h,n+1}^{trial} - 3\left(3\lambda_{rev} + 2\mu_{rev}\right)\Delta p \dfrac{1}{3} a_1^* Y_0}{1 + \left(3\lambda_{rev} + 2\mu_{rev}\right)\Delta p 2a_2^*} \end{cases} \tag{4.15}$$

The updating of the stress depended on the computation of the incremental multiplier which is calculated with a Newton method:

$$\Delta p^{i+1} = \Delta p^{i} - \frac{1}{J^{i}} R_{p}\left(\Delta p^{i}\right) \qquad i = 1..n, \text{ where} \qquad J = \frac{\partial R_{p}}{\partial \Delta p} \tag{4.16}$$

After determining the multiplier *Δp*, the final stress tensor was obtained as

$$\underline{\underline{\sigma}}^{trial} = \underline{\underline{S}}^{trial} + P_{h}^{trial}\underline{\underline{I}} \tag{4.17}$$

The algorithmic tangent modulus necessary for applying a Newton method for iterative solution of the global equilibrium problem requires the derivative of the stress tensor $\underline{\underline{\sigma}}$:

$$\underline{\underline{\underline{\underline{C}}}} = \frac{\partial \underline{\underline{\sigma}}}{\partial \underline{\underline{\varepsilon}}} \tag{4.18}$$

Straightforward differentiation renders the following result:

$$\underline{\underline{\underline{\underline{C}}}} = \frac{\partial}{\partial \underline{\underline{\varepsilon}}}\left(\underline{\underline{S}} + \frac{1}{3}P_{h}\underline{\underline{I}}\right) \tag{4.19}$$

$$\underline{\underline{\underline{\underline{C}}}} = \frac{2\mu_{rev}}{\left(1-2\mu_{rev}\Delta p\right)}\left(\underline{\underline{I}} - \frac{1}{3}\underline{\underline{I}} \otimes \underline{\underline{I}}\right) + \underline{\underline{S}}^{trial} \otimes \left(\frac{2\mu_{rev}}{\left(1-2\mu_{rev}\Delta p\right)^{2}}\right)\frac{\partial \Delta\lambda}{\partial \Delta\varepsilon} + \frac{3\lambda_{rev}+2\mu_{rev}}{1+\left(3\lambda_{rev}+2\mu_{rev}\right)\Delta p 2a_{2}^{*}}\underline{\underline{I}} \otimes \underline{\underline{I}} \tag{4.20}$$

4.1.3. Identification strategy of the MS-Model

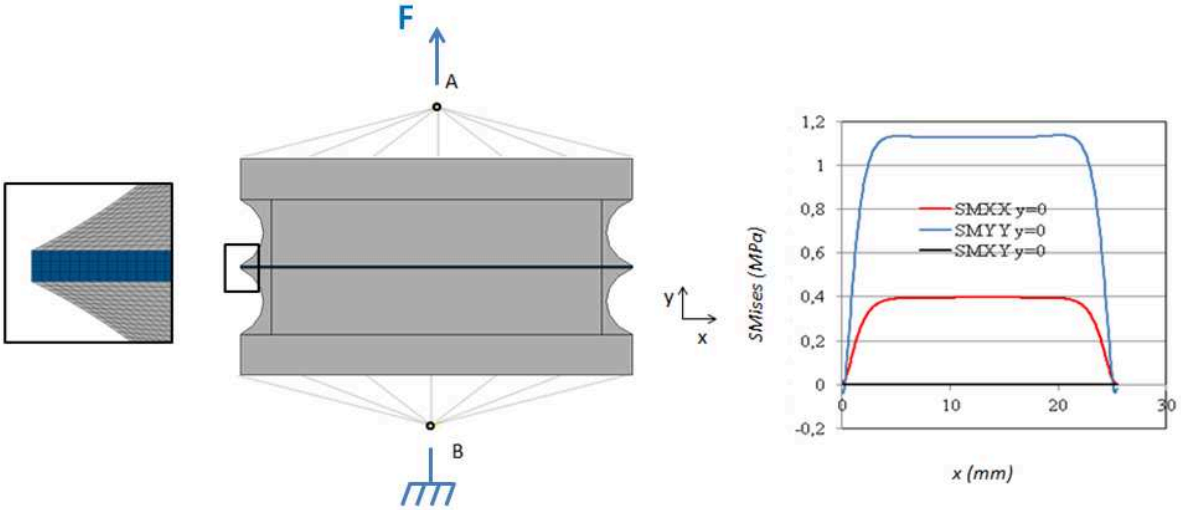

(a) (b)

Figure 139. Arcan Evolution specimen under traction (γ=0°): (a) FE model with boundary conditions and focus on the beak at the end of the overlap, (b) stress distribution results along the overlap length and in the mid-plane of the adhesive layer.

The MS-Model was implemented in a user-material subroutine (UMAT) in the FE code Abaqus/standard using a return mapping algorithm, as noted below. On the one hand, this model required establishing elastic parameters such as the Young modulus E and the Poisson's ratio ν, and on the other, the 8 following parameters *a1*, *a2*, *a1**, *a2**, *Y0*, *q*, *b* and *H* must also be identified. All parameters were identified using Arcan Evolution tests.

As explained in chapter 1, a direct stress-strain relation cannot be directly derived from the experimental load-displacement curves obtained due to the non-uniform stress state within the adhesive layer. Indeed, as shown in Figure 139, the simple case of an Arcan Evolution specimen loaded in tension, the stress distribution within the adhesive layer is non-uniform.

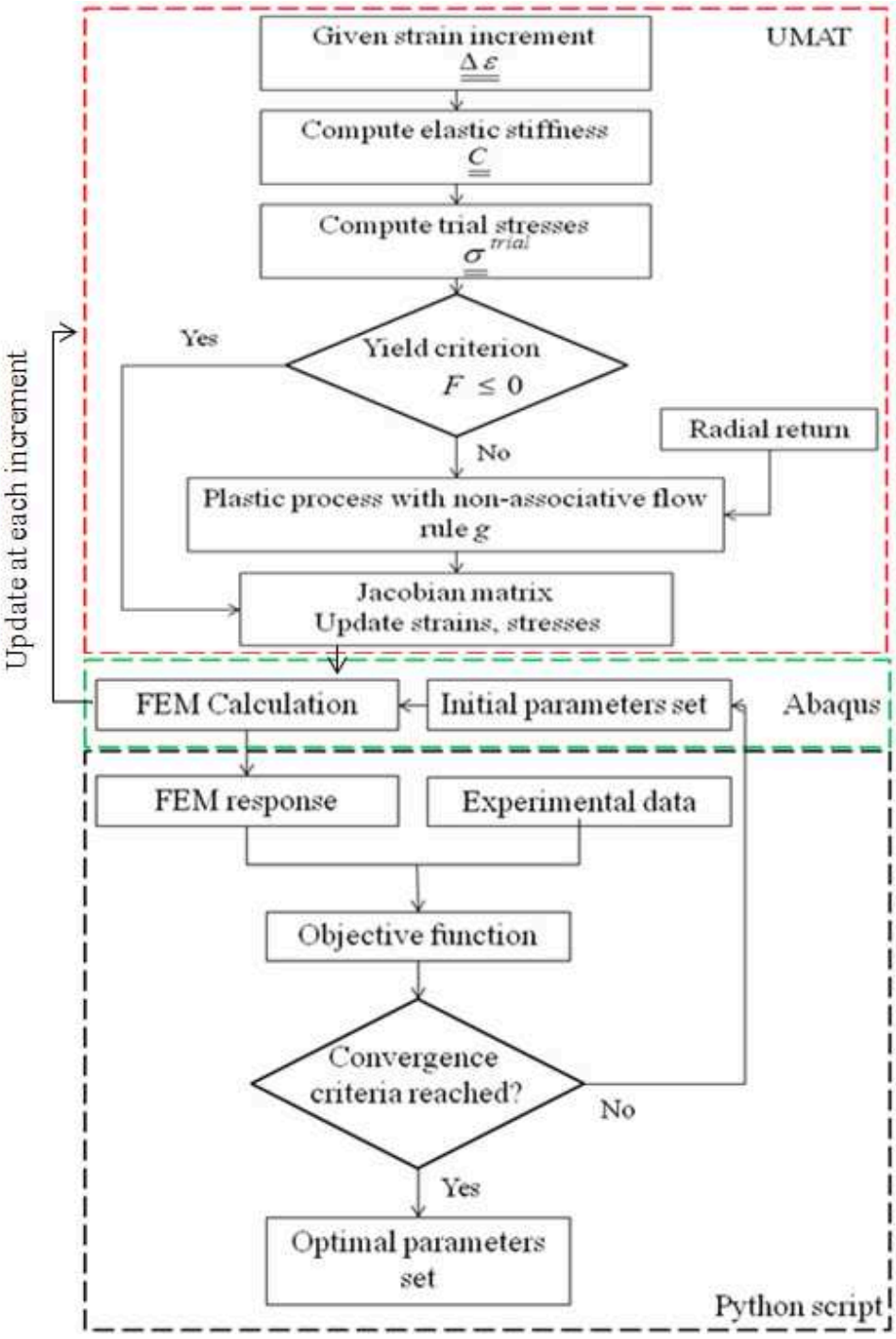

Figure 140. Flow chart of the inverse identification procedure.

Thus, an inverse identification was required to find a suitable set of parameters in such a manner that the numerical response calculated matches with the constitutive model the corresponding experimentally measured response. Some authors proposed inverse identification strategies of the elastic-plastic model of Mahnken-Schlimmer [JOU 10][MAH 05][MAU 12][MAU 13] to identify material parameters. Mahnken et al. [MAH 05], Jousset et al. [JOU 10] based their identifications on tension-torsion tests, Maurice et al. [MAU 12][MAU 13] and Arnaud et al. [ARN 14] used modified Arcan tests. Given the number of parameters to identify and complexity of constitutive model, a step-by-step identification was proposed to obtain a converged solution.

A fully automated procedure was proposed to simulate the whole material model and to find the best set of material parameters. This procedure links Abaqus to a Fortran user-subroutine UMAT through a python script and is summarized in Figure 140.

The available pre-processor to the FE software Abaqus was used to create the model, i.e. geometry, mesh and to generate the input data file for the analysis. The subroutine UMAT was developed to take into account the mechanical behavior of the adhesive. It allowed implementing the constitutive equations defined in section 4.1.2 with a radial return method [SIM 00]. The equivalent stress, the plastic strain, the stress tensor and the elastic constitutive tensor were updated at the end of each increment.

The python script was used to find a suitable set of parameters such that the numerical response calculated with the constitutive model matches the corresponding experimentally measured response. This optimization problem used a least square cost function to minimize with respect to the material parameters such as:

$$f = \sum_{i=1}^{n} \left[F_{FEM,i}(u) - F_{EXP,i}(u) \right]^2 \tag{4.21}$$

where $F_{FEM,i}(u)$ and $F_{FEM,i}(u)$ are the finite element force computed and the force experimentally measured, respectively. The problem is solved iteratively using local methods such as gradient algorithms or global methods such as genetic algorithms.

Maurice et al. [MAU 12] proposed an identification of model parameters into three steps. Arnaud et al. [ARN 14] slightly modified this proceeding which is defined as follows:

- Step 1: It consisted in identifying the initial yield surface with the parameters *a1*, *a2* and *Y0*. Finite element calculations under elastic assumption were performed for a shear-loading. Knowing the young modulus for the adhesive, the initial yield stress *Y0* was determining by comparing the non-linear point on the load-displacement experimental and simulation curves. Regarding the parameters *a1* and *a2*, the von Mises and hydrostatic stresses were numerically determined for tension (γ=0°), shear (γ=90°), tension-shear (γ=45°) and compression-shear (γ=135°) loadings at the non-linear point determined from the load vs. relative displacement curve. From these data, the initial yield surface was plotted in the Mises-hydrostastic stress plane and the function was identified thanks to a least-squares error method.
- Step 2: Parameters of the hardening function *q*, *b* and *H* were identified. It can be showed that flow rule parameters *a1* and *a2* had no influence on the identification of the hardening function for a shear-loading. Hence, only the result in shear was considered. An inverse identification was used to identify the hardening parameters coupling FE model with the software Abaqus and an optimization algorithm which has been developed in a python script, the minimization being applied to the least squares error between simulation and experimental results.
- Step 3: Flow rule parameters *a1** and *a2** are identified with results in tension-shear (45°) and compression-shear (135°) thanks to an inverse identification similar to that of the previous step.

4.1.4. Finite Element Analysis

4.1.4.1. Finite Element model

Two 3D FE models were used to identify material parameters:

- A first one was created with a single element in the width in the $\vec{y}$ direction (Figure 141 (a)). A relatively coarse mesh made of 11468 elements in the entire model and 128 elements for the adhesive layer was chosen. These elements are 8-node trilinear reduced integration brick elements including hourglass control and 10-node quadratic tetrahedral elements, C3D8R and C3D10 elements in ABAQUS notation [ABA 10], respectively.
- A second one included the entire shape of an Arcan Evolution specimen. It was assumed that the geometry widthwise was negligible (Figure 141 (b)). Only half of the specimen was represented due to the symmetry in the transverse direction. This model contained a mesh sufficiently refined: 1380586 elements in the whole model and 597600 elements in the adhesive layer (40 elements in the thickness). As for the reduced FE model, this mesh was made of 8-node trilinear reduced integration brick elements including hourglass control and 10-node quadratic tetrahedral elements.

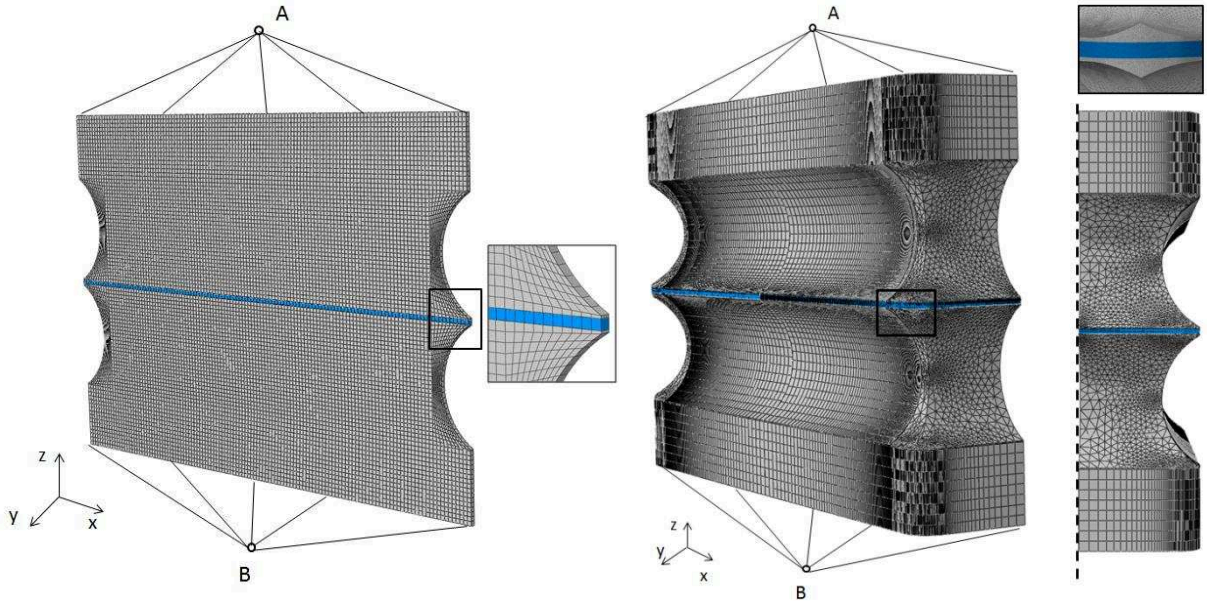

(a) (b)

Figure 141. Details of the Finite Element models used for the inverse identification: (a) 3D model with a single element in the width and (b) 3D complete model with symmetry plane.

For each of them, only the bonded specimen was considered. Its clamping with the Arcan Evolution device was considered perfect and the boundary conditions were represented by kinematic couplings between driving points A, B and the driven surfaces of the bonded specimen. The MS-Model was firstly identified on the 3D model with a single element in the width. Starting from this first identification, a second one was investigated on the 3D complete model. The latter increased the computational time. However, as it will be showed in the section 4.2, this model was required to consider the curing degree gradients within the adhesive layer following the curing cycle applied.

Special care was drawn to the post-processing of the relative displacements. In fact, the position of the points where the relative displacements were computed must be accurately known to avoid discrepancies between experimental and numerical curves. Thus, as shown in Figure 142 (a)-(b), the coordinates of measurement points were exactly known experimentally and were used in the numerical model to compute normal and tangential relative displacements of the substrates.

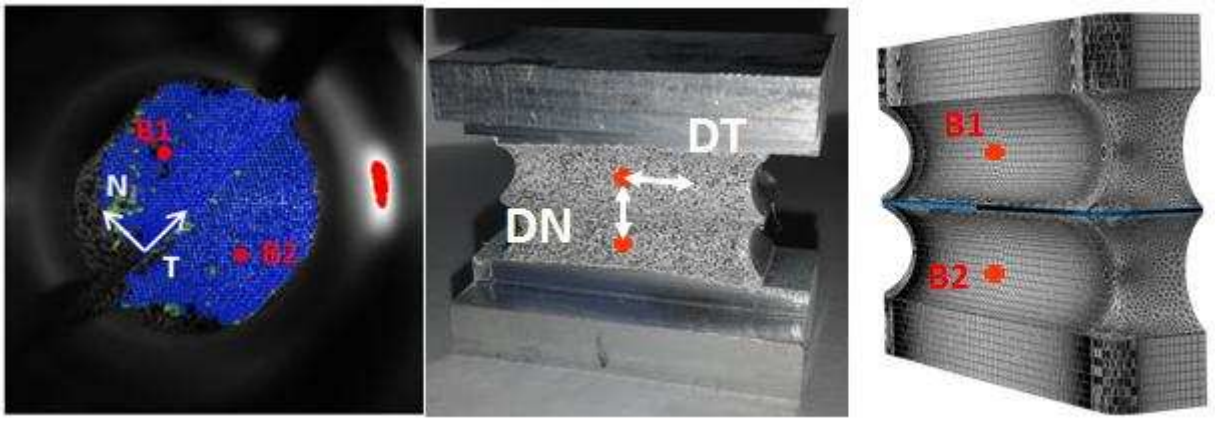

(a) (b) ©

Figure 142. Arcan Evolution specimen: (a), (b) points of experimental measurement of relative displacements and (c) numerical estimate of relative displacements.

4.1.4.2. Inverse identification results

The identification of parameter set was made using Arcan Evolution specimens cured 5h30 at 35°C. Figure 143 presents the results of the identification of the yield surface, yield functions and flow functions in the Mises stress – Hydrostatic pressure plane for several equivalent plastic strains: e_v = 0.0, 0.05, 0.5, 0.8 and 1.0. This gave full account of such functions from their initial values (e_v = 0). The experimental values at the elastic limit for the four loading cases represented in the Mises stress – Hydrostatic stress plane in Figure 143 (b) enabled to identify the initial yield function. Considering this last one, the dependence on the hydrostatic stress component was clearly demonstrated. Thus, the Mises stress at the elastic limit increased with the compressive hydrostatic stress: It goes from 18 MPa in tension (γ=0°) to 59.5 MPa in compression-shear (γ=135°), as shown in Figure 143 (b). The initial yield function fits reasonably the experimental points. The slight difference observed at γ=0° may come from the ductile nature of such adhesive.

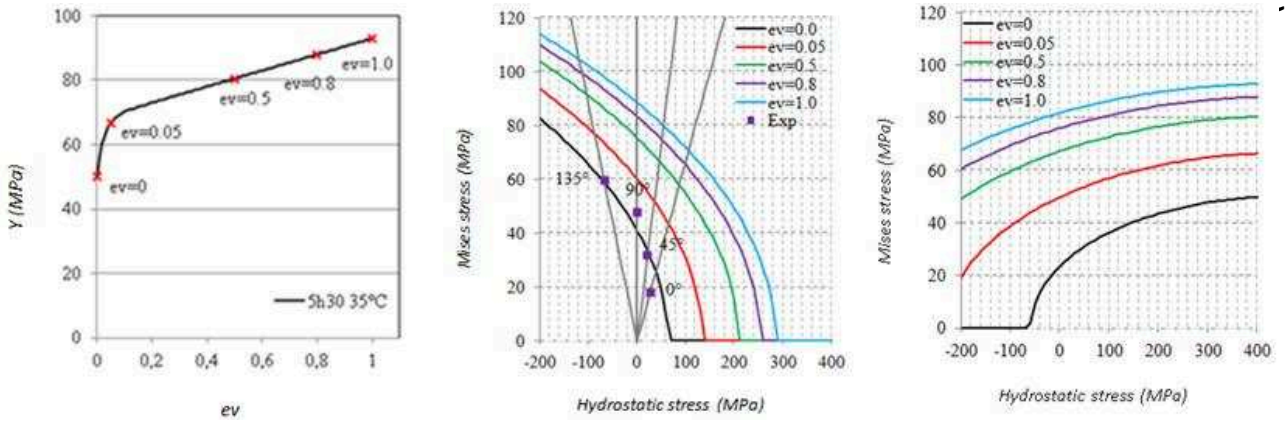

(a) (b) (c)

Figure 143. Arcan evolution specimen cured 5h30 at 35°C for several equivalent plastic strains: (a) hardening function, (b) yield functions and (c) flow functions.

Parameters	E	ν	Y_0	a_1	a_2	a_1^*	a_2^*	q	b	H
Unit	Mpa	-	Mpa	-	-	-	-	Mpa	-	Mpa
5h30 35°C	3480	0.369	50	0.6	0.1	0	0.24	18	38	25

Table 17. Material parameters identified for the MS-Model for a curing cycle of 5h30 at 35°C.

Table 17 shows elastic constants and material parameters issued from the inverse identification process for a curing cycle of 5h30 at 35°C and the correlation between experiments and results predicted by the MS-Model defined previously is presented in Figure 144.

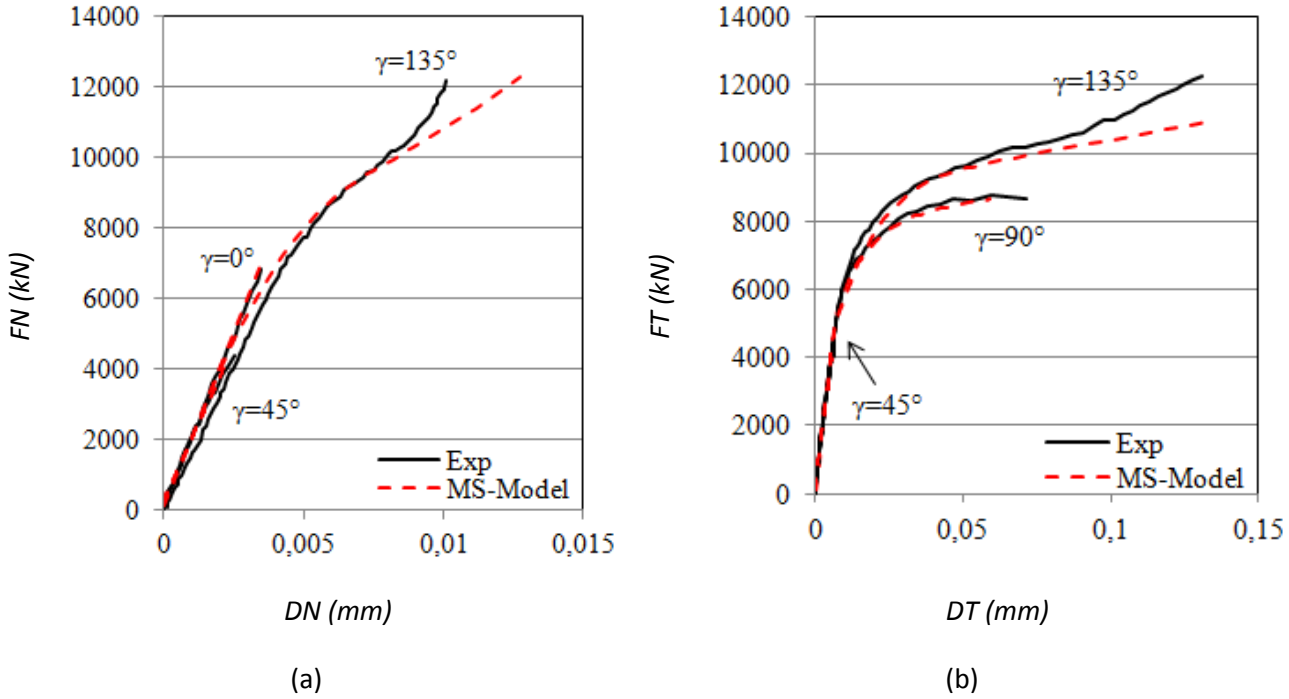

Figure 144. Comparisons of experimental and numerical results for the curing cycle of 5h30 at 35°C under tensile (γ=0°), shear (γ=90°), tensile-shear (γ=45°) and compression-shear (γ=135°): FN vs. DN and (b) in tangential direction: FT vs. DT.

The results predicted by the identification process fit the experimental results accurately except in compression-shear. Indeed, the experimental curve in compression-shear (γ=135°) exhibit an inflexion point at around a displacement of 0.075 mm in tangential direction (Figure 144 (b)) followed by a slope increase. The predicted result at 135° does not consider this strength recovery. A similar phenomenon is observed in normal direction.

Considering the results in compression-shear (γ=135°), main changes occur in the non-linear part. Moreover, the change slope at the half of the curve leads to a modification of the hardening function. In addition, some adjustments must be brought on the identification strategy of material parameters to take better account of this change.

4.1.5. Modification of the MS-Model

As noticed in the previous section, this curves predicted by the MS-Model does not consider the entire behavior of the adhesive for compression-shear (γ=135°) result. In fact, regarding Figure 145 (a), the non-linear behavior domain is restricted to tangential forces ranging up to 10.5 kN. However, experimental investigations from a previous work on another epoxy adhesive showed experimentally that the remaining section curve must be taken into account in the non-linear behavior of the adhesive since it is an adhesive contribution and does not totally come from the interfaces. Further, this kind of behavior is characteristic of that of numerous polymers, an adhesive being a polymer [LAF 04]. Figure 145 (b) shows the behavior of the epoxy adhesive Araldite® 420 A/B under monotonic and cyclic loadings with modified Arcan test in compression-shear (γ=135°). Under monotonic loading and for the applied load rate, a non-linear behavior was observed for shear loads higher than 12 kN and maximum relative displacement was at 0.288 µm. Regarding cycling loading, the cumulative displacement DT at failure in the bonded joint was measured for similar magnitudes. This experimental analysis under various types of compression-shear loadings

underlines that failure was reached for similar maximum relative displacement, maximum cumulative displacement. This result does not depend on loading amplitude or mean load and seems to constitute a suitable criterion under compression-shear loadings. This was not observed for monotonic and cycling tensile loading. Further, cohesive failure and adhesive failure had been observed under tensile and compression-shear loadings, respectively. Therefore, bonding mechanisms involved are load-dependent. It can be assumed that interfaces are less stressed under compression-shear loading than for others loadings and provide almost no contribution to the mechanical behavior of the adhesive. Thus, the curve predicted in Figure 145 (a) shows the non-linear behavior of the adhesive over its entire section.

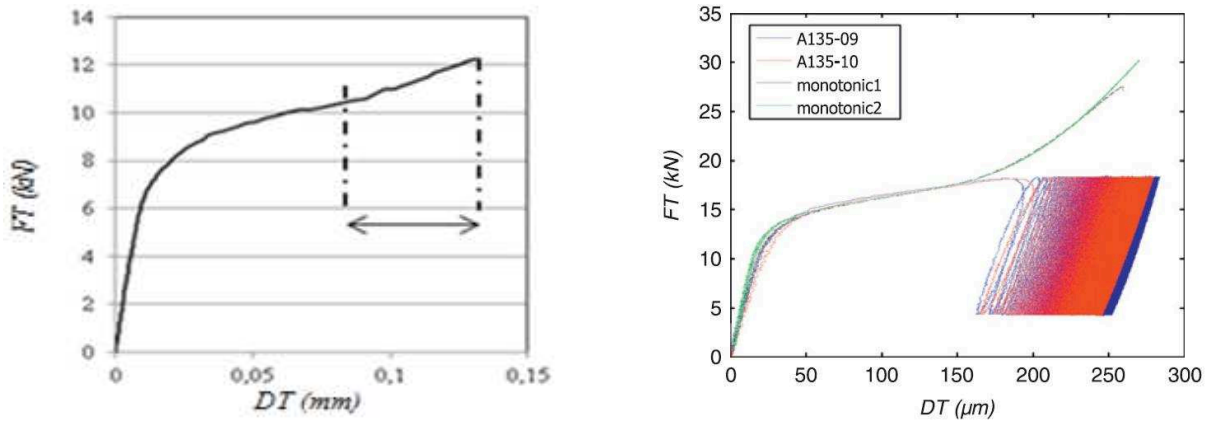

(a) (b)

Figure 145. (a) Arcan Evolution test: experimental result in the tangential direction for compression-shear loading for a curing history of 5h30 at 35°C and (b) Modified Arcan test : influence of load amplitude on the cyclic behavior of the epoxy adhesive Araldite® 420 A/B in the tangential direction in compression-shear [THE 13].

The MS-Model proposed previously was therefore slightly modified to take into account the entire non-linear behavior occurring under compression-shear loading. The change arose in the hardening function such as:

$$Y = Y_0 + q\left(1 - e^{-be_v}\right) + He_v + a_3\left(e^{ce_v} - 1\right) \qquad (4.22)$$

This added term was generally used in the definition of the yield function of polymers [LAF 04].
This modified model was called “modified MS-Model”.

Since the results under compression-shear loadings exhibited mainly the non-linear behavior of the adhesive with almost no contribution of surfaces or interfaces, a modification in the inverse identification steps must be provided, namely in the second stage. Thus, the modified steps of the inverse identification were redefined as follows:

- Identification of the yield surface (Y_0, a_1 and a_2) using elastic FE simulations
- Identification of the hardening function (q, b, H and a_3, c) using results in compression-shear (γ=135°)
- Identification of flow rule parameters (a_1^* and a_2^*) using compression-shear (γ=135°) results

Figure 146 shows the comparison between experimental result and predicted result by both MS-Model and modified MS-Model in the tangential direction for compression-shear (γ=135°) loading.

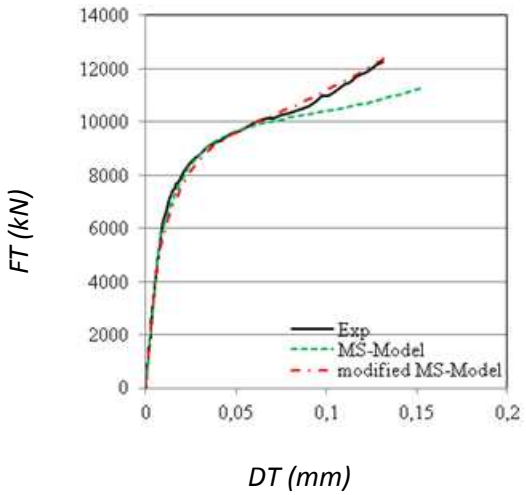

Figure 146. Predicted vs. Experimental result in the tangential direction for compression-shear loading for a curing history of 5h30 at 35°C

The numerical result predicted by the "modified MS-Model" at γ=135° in tangential direction is in good agreement with the experimental curve.

Figure 147 shows the comparison between experiment and numerical results predicted by the modified MS-Model for the four types of loads (γ=0°, γ=45°, γ=90°, γ=135°). An excellent agreement between the measurements and the predictions is observed, particularly in compression-shear (γ=135°). Hence, this modified model will be considered in the following.

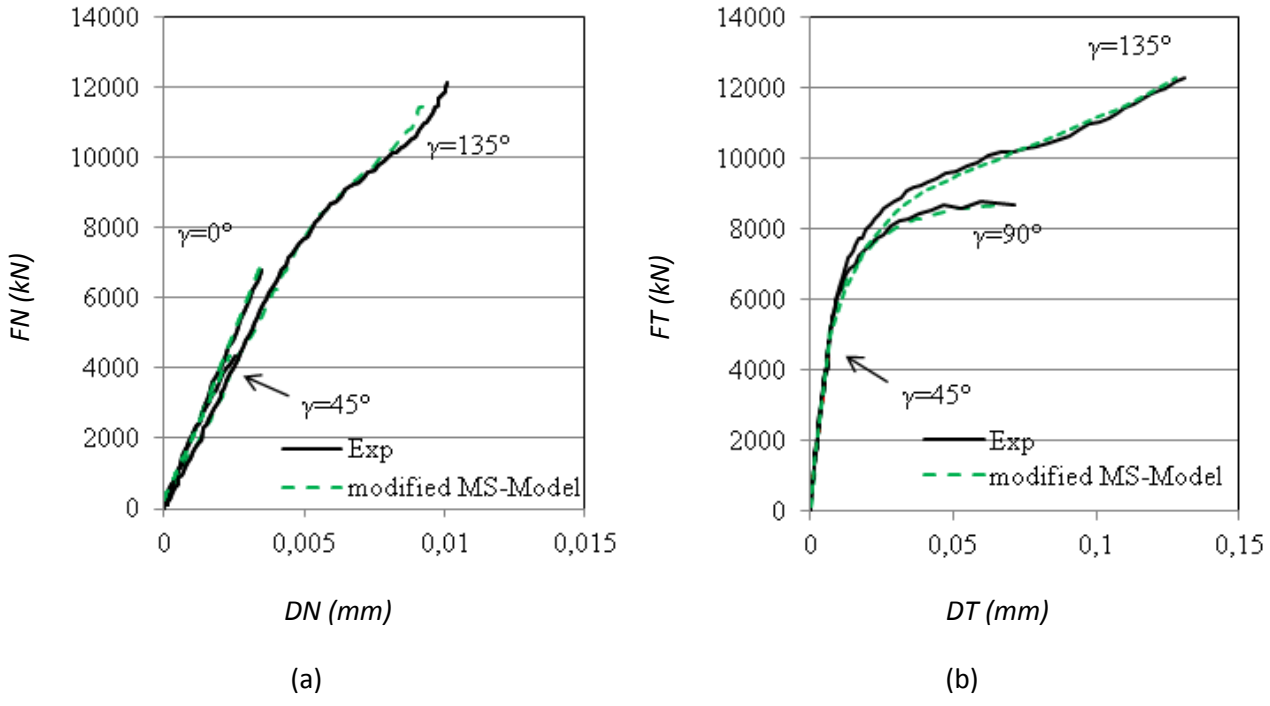

Figure 147. Experimental vs. Predicted results for the modified MS-Model for: (a) tensile loading (γ=0°), (b) shear loading (γ=90°), tensile-shear loading (γ=45°) and compression-shear loading (γ=135°).

4.2. Cure-dependent modified Mahnken-Schlimmer elastic-plastic model

In chapter 3, the influence of the curing cycle, i.e. the curing state of the adhesive Hysol EA-9321 on its mechanical properties under tension/compression-shear loadings was experimentally investigated. Those data underlined a strong influence of the curing state of the adhesive on its mechanical response. In the course of this study, a constitutive model was proposed for modeling the cure-dependent properties of such adhesive. This model was based on the modified MS-Model detailed in the previous section and was validated by comparing predictive responses with experimental results of chapter 3. The identification of such model for the three curing cycles defined, i.e. 5h30 at 35°C (α=0.4), 3h30 at 60°C (α=0.7) and 1h at 82°C (α=1.0), was performed using the same approach defined previously. The values of the material parameters identified for the three remaining curing cycles are presented in Table 18.

Parameters	**E**	**ν**	**Y_0**	**a_1**	**a_2**	**a_1^***	**a_2^***	**q**	**b**	**H**	**a_3**	**c**
Unit	**Mpa**	**-**	**Mpa**	**-**	**-**	**-**	**-**	**Mpa**	**-**	**Mpa**	**Mpa**	**-**
5h30 35°C – α=0.4	3480	0.369	50	0.6	0.1	0	0.24	18	38	25	30	0.75
3h30 60°C – α=0.7	3480	0.369	50	0.6	0.1	0	0.24	23	66.5	42	30	1.5
1h 82°C – α=1.0	3480	0.369	50	0.6	0.1	0	0.24	28	95	60	30	2.0

Table 18. Material parameters identified for the three specific cured specimens.

For each curing cycles, identical parameters are identified for elastic properties (*E*, *ν*), yield surface (Y_0, a_1, a_2) and flow rule parameters (a_1^*, a_2^*). Main changes occur for the hardening function. Further, those parameters can be relied to the curing degree, such as:

$$Y = Y_0 + q(\alpha)\left(1 - e^{-b(\alpha)e_v}\right) + H(\alpha)e_v + a_3\left(e^{c(\alpha)e_v} - 1\right)$$

$$\begin{cases} q(\alpha) = \sqrt{\alpha}\cdot q_{max} \\ b(\alpha) = \alpha\cdot b_{max} \\ c(\alpha) = \alpha\cdot c_{max} \\ H(\alpha) = \alpha\cdot H_{max} \end{cases} \quad \text{with} \quad \begin{cases} q_{max} = 28 \\ b_{max} = 95 \\ c_{max} = 2.0 \\ H_{max} = 60 \end{cases} \qquad (4.23)$$

4.2.1. 3D-chemo-thermo-mechanically coupled model including curing behavior of adhesives and elastic-plasticity: finite element model

On the contrary to the first identification (section 4.1.4.1), only the 3D complete FE model was used. Indeed, this last one was necessary to take into account the curing state of the adhesive layer in the bonded assembly. The finite element model used is almost the same as that used in Figure 141 (b) and appears in Figure 148.

The main difference was the inclusion of a film condition applied on the external faces of the Arcan Evolution specimen exposed to the oven environment during the curing stage to model the thermal loading, using a heat transfer coefficient characteristic of forced convective heating. For the same reason as mentioned above, the numerical points using for the measurement for relative displacements of the substrates coincided with those used experimentally.

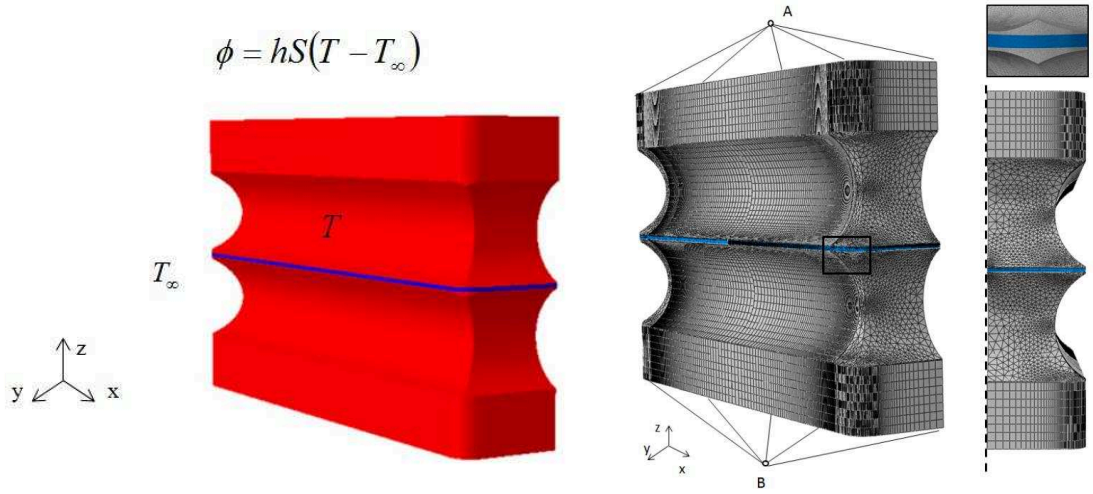

Figure 148. Details of the Finite Element model used for the inverse identification: (a) film convection on external surfaces of the bonded assembly and (b) boundary conditions overview with symmetry plane.

4.2.2. 3D-chemo-thermo-mechanically coupled model including curing behavior of adhesives and elastic-plasticity: inverse identification strategy

The whole material model can be considered as a coupling between a transient heat-transfer analysis by taking into account the effect of the adhesive curing in a bonded assembly, as studied in section 3.2.2 of chapter 3 and a mechanical analysis by considering the mechanical behavior of the adhesive Hysol EA-9321 as a function of its curing state.
A fully automated procedure was proposed to simulate the whole material model and to find the best set of material parameters. This procedure links Abaqus to fortran subroutines through a python script and is summarized in Figure 149.

The available pre-processor to the FE software Abaqus was used to create the model, i.e. geometry, mesh and to generate the input data file for the analysis. Some subroutines were developed to take into account problems generated by the whole coupled model. Two main problems were identified:

- The adhesive curing: as explained in section 3.2.2 of chapter 3, the subroutine SDVINI was used to define initial material values of adhesive such as curing degree α, specific heat $C_p(0,T)$ and conductivity $\lambda(0,T)$. Then, the subroutine HETVAL was used for determining the heat produced at each Gauss point, by the curing reaction and the curing degree by solving the kinetic equation of Kamal & Sourour with diffusion (Eq.(2.15) of chapter 2) with parameters identified in chapter 2. The subroutine USFLD enabled the cure-dependent parameters such as specific heat or conductivity to be updated at each increment. This allowed predicting the curing state of the adhesive in a bonded assembly regardless of the curing cycle applied.

- The mechanical behavior of the adhesive: the subroutine UMAT allowed implementing the cure-dependent constitutive equations defined in the previous sections with a radial return method [SIM 00]. The equivalent stress, the plastic strain, the stress tensor and the elastic constitutive tensor were updated at the end of each increment.

In the same manner as in section 4.1.3, the python script was used to find a suitable set of parameters such that the numerical response calculated with the constitutive model matches the corresponding experimentally measured response.

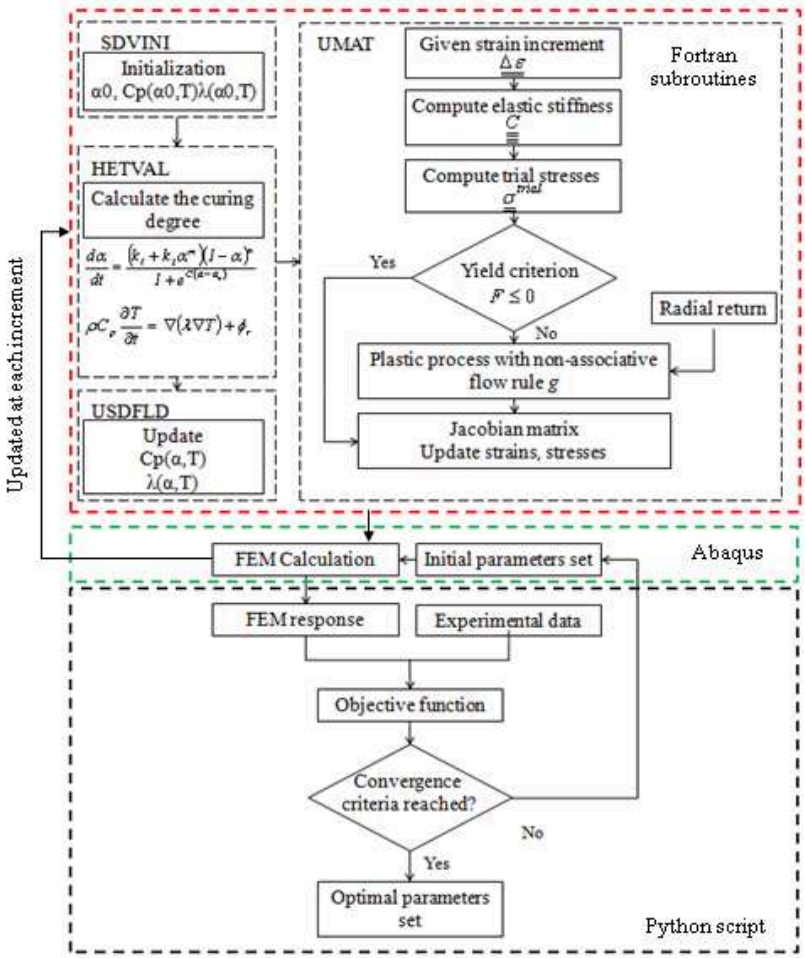

Figure 149. Principe of the inverse identification process used in the 3D coupled chemo-thermo-mechanical model.

4.2.3. 3D-chemo-thermo-mechanically coupled model including curing behavior of adhesives and elastic-plasticity: Inverse identification results

The identification of parameter set was made using experimental data from chapter 3, i.e. Arcan Evolution specimens cured 1h at 82°C (α=1.0), 3h30 at 60°C (α=0.7) and 5h30 at 35°C (α=0.4). Figure 150 presents the results of the identification of the yield surfaces, yield functions and flow functions in the Mises stress – Hydrostatic pressure plane for several equivalent plastic strains: e_v = 0.0, 0.05, 0.5, 0.8 and 1.0 for both curing cycles. This gave full account of such functions from their initial values (e_v = 0). The initial yield function was identified thanks to the experimental values at the elastic limit for each load in the Mises stress – Hydrostatic stress plane, as shown in Figure 150 (b). As for the fully cured adhesive, the Mises stress at the elastic limit increases with the compressive hydrostatic stress for each load. The yield function parameters (*Y0*, *a1* and *a2*) and the flow rule parameters (a_1* and a_2*) being the same for all curing cycles, the initial yield and flow functions are identical and the initial yield function fits well with the experimental points (Figure 150 (b)). The curing state of the adhesive strongly affects each function. Considering the yield and flow functions, the elliptic shape increases with the curing state of the adhesive for identical equivalent plastic strains (with $e_v > 0$).

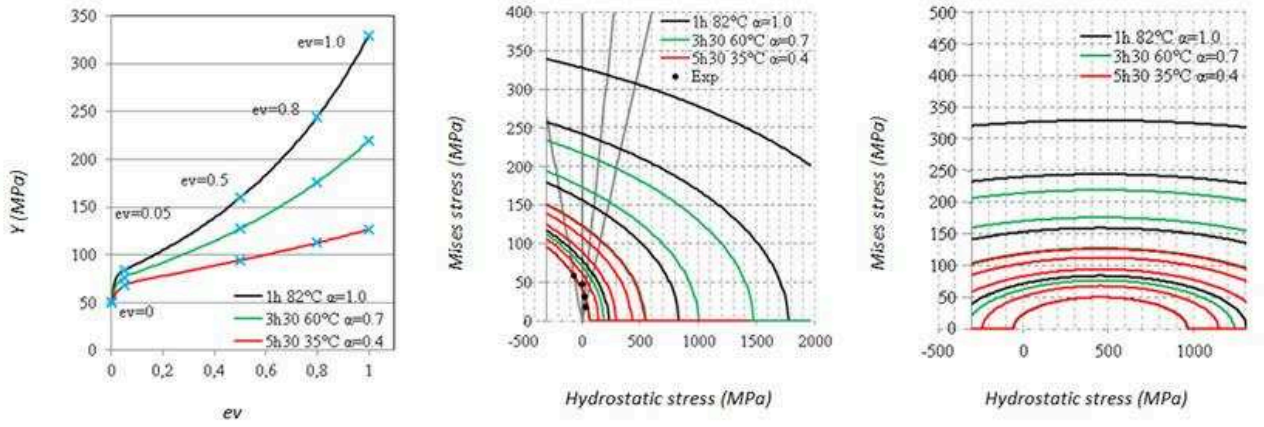

(a) (b) ©

Figure 150. Arcan evolution specimens cured 1h at 82°C, 3h30 at 60°C and 5h30 at 35°C for several equivalent plastic strains: (a) hardening functions, (b) yield functions and (c) flow functions.

Figure 151 shows the correlation between experiments and results predicted by the cure-dependent modified MS-Model defined previously. The identification for the cured specimens fit the experimental results accurately and underlines the good quality of the identification procedure.

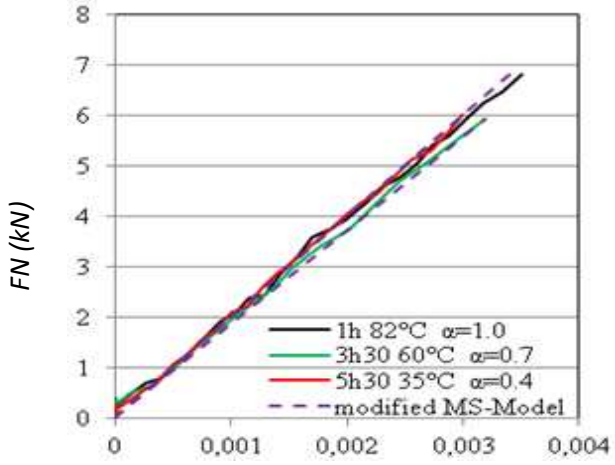

(a)

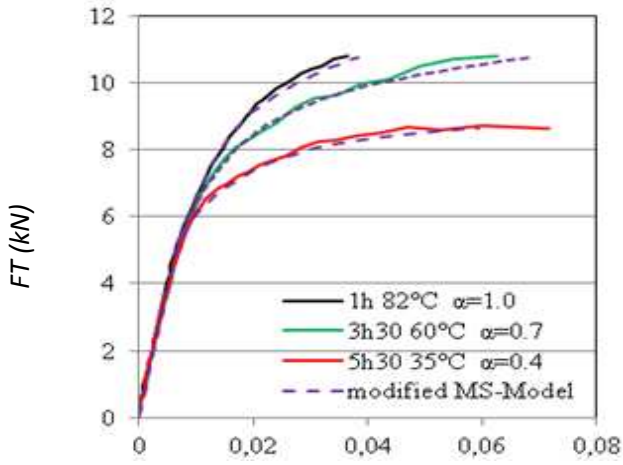

(b)

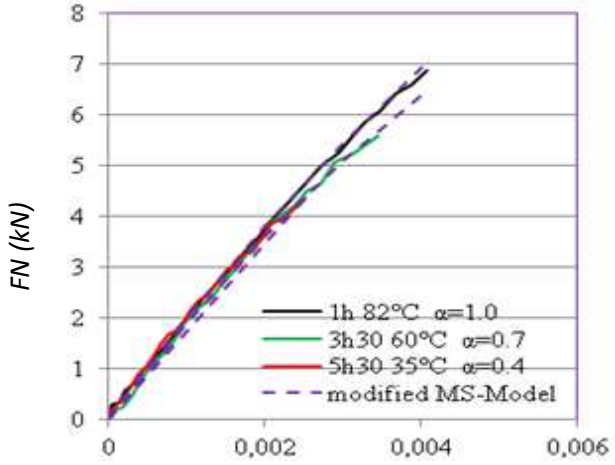

©

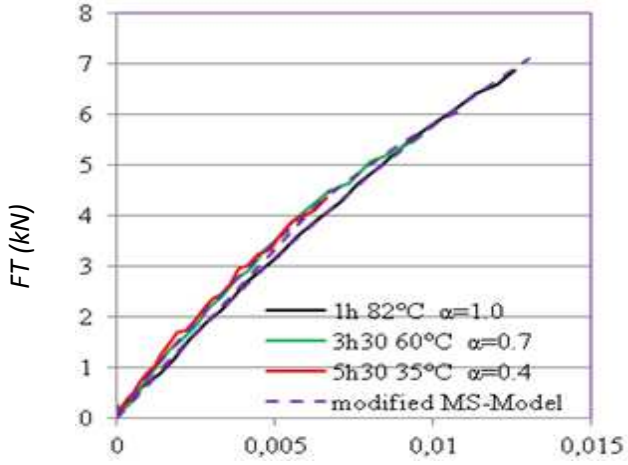

(d)

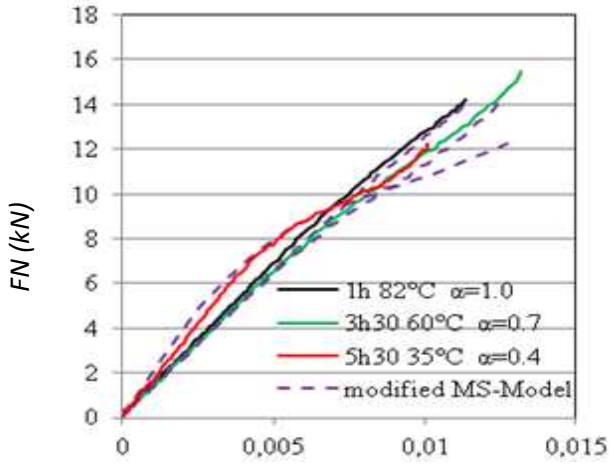

(e)

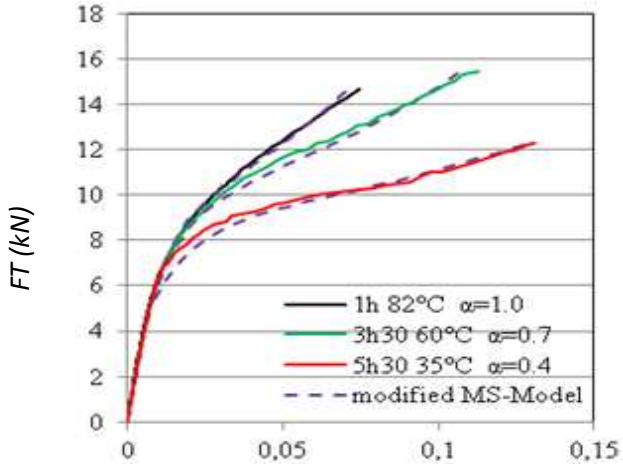

(f)

Figure 151. Experimental vs. Predicted results for the three curing states specimens for: (a) tensile loading (γ=0°), (b) shear loading (γ=90°), tensile-shear loading (γ=45°) and compression-shear loading (γ=135°).

4.3. Cure-dependent modified Mahnken-Schlimmer elastic-visco-plastic model

In this section, the cure-dependent elastic-plastic model developed previously was extended to viscous effects in order to investigate the influence of curing degree of the cold-curing adhesive Hysol EA-9321 on its viscous properties. Only viscosity in terms of rate effects was treated in this part.

4.3.1. Constitutive equations

Figure 152 presents experimental responses for pure shear (γ=90°) and compression-shear (γ=135°) tests for four crosshead displacement rates of tensile testing machine: 0.01 mm/min, 0.05 mm/min, 0.5 mm/min and 10 mm/min. An increase of the "yield stress" is observed with an increasing strain rate. Thus, an extension of the cure-dependent modified model of Mahnken-Schlimmer was developed to consider such effects.

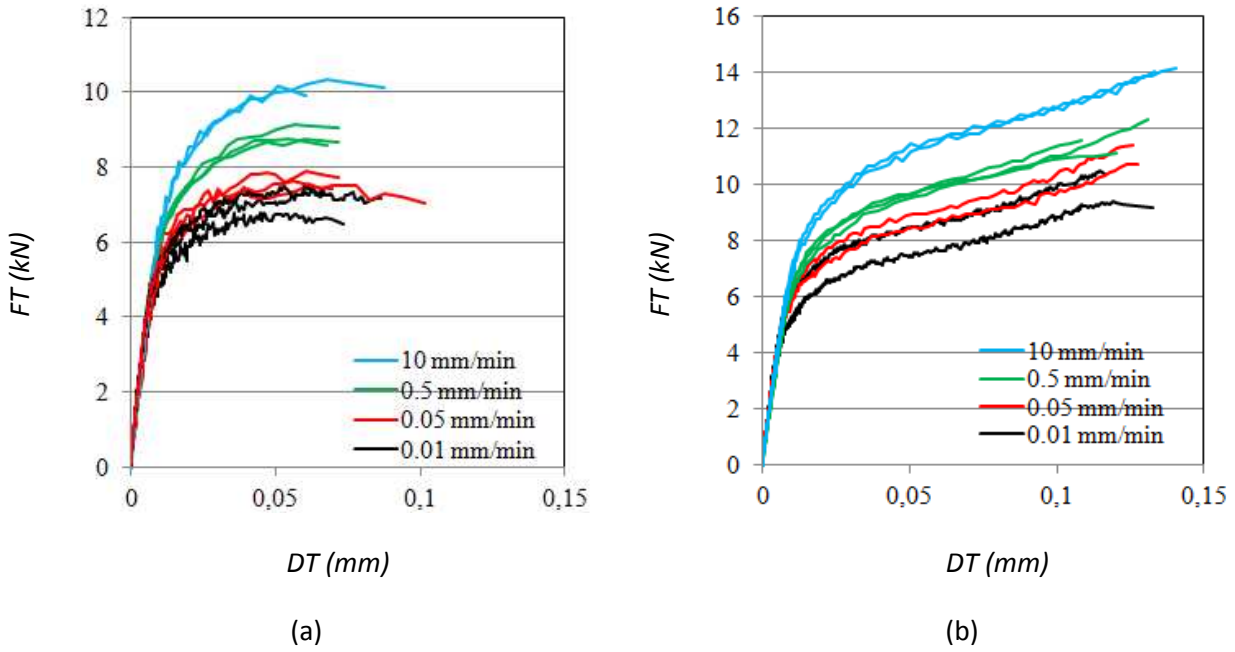

Figure 152. Strain-rate effects using the Arcan Evolution specimen for a curing cycle of 5h30 at 35°C under: (a) shear (γ=90°) loading and (b) compression-shear (γ=135°) loading.

The definition of the model is similar to the one developed previously. The yield surface was given by:

$$F = f_p - Y_0 \tag{4.24}$$

$$f_p = \sqrt{J_2 + a_1 I_1 Y_0 + a_2 I_1^{\,2}} \tag{4.25}$$

The hardening function was defined as follows:

$$Y = Y_0 + q(\alpha)\left(1 - e^{-b(\alpha)e_v}\right) + H(\alpha)e_v + a_3\left(e^{c(\alpha)e_v} - 1\right)$$

$$\begin{cases} q(\alpha) = \sqrt{\alpha}\cdot q_{max} \\ b(\alpha) = \alpha \cdot b_{max} \\ c(\alpha) = \alpha \cdot c_{max} \\ H(\alpha) = \alpha \cdot H_{max} \end{cases} \quad \text{with} \quad \begin{cases} q_{max} = 28 \\ b_{max} = 95 \\ c_{max} = 2.0 \\ H_{max} = 60 \end{cases} \tag{4.26}$$

The flow potential was given by:

$$G = \sqrt{J_2 + a_1^* I_1 Y_0 + a_2^* I_1^2} - Y \tag{4.27}$$

where *a1** and *a2** were material parameters to determine. A non-associated flow rule was chosen. Hence, $a_1^* \neq a_1$ and $a_2^* \neq a_2$ since the flow rule and the yield function may not be the same.

The rate effects were described through a Nouailhas viscoplastic potential [CRE 08][NOU 89]:

$$\Omega = \frac{K_V}{\alpha(n+1)} \exp\left(\alpha \left\langle \frac{F}{K_V} \right\rangle^{n+1} \right) \tag{4.28}$$

where *F* was the yield surface defined in equation 4.14, *n* was the viscoplastic yield surface exponent, K_v was the initial factor for the normalization of the yield surface and α is the viscosity parameter.
The exponential potential of Nouailhas was used for the implementation of the adhesive behavior. The plastic multiplier was defined as:

$$\dot{p} = \left\langle \frac{F}{K_V} \right\rangle^{n} \exp\left(\alpha \left\langle \frac{F}{K_V} \right\rangle^{n+1} \right) \tag{4.29}$$

Those equations were grounded on 15 material parameters:

- Elastic parameters: the Young modulus *E* and the Poisson's ratio *v*
- Cure-dependent modified MS-Model: a_1, a_2, a_1^*, a_2^*, Y_0, *qmax*, *bmax*, a_3, *cmax* and *Hmax*
- Visco-plastic flow parameters: K_v, *n* and α

4.3.2. Computational algorithm

In the same way as for the computation of the previous model of section 4.1.2 (MS-Model), the return-mapping algorithm [SIM 00] was used for the implementation of the cure-dependent modified Mahnken-Schlimmer elastic-viscoplastic model.

The first step consisted in assuming an elastic behavior for a given time increment. Thus, a trial stress tensor at increment n+1 was defined as:

$$\underline{\underline{\sigma}}_{n+1}^{trial} = \underline{\underline{\sigma}}_{n+1} + \underline{\underline{\underline{\underline{C}}}}_e : \underline{\underline{\Delta\varepsilon}} \tag{4.30}$$

When the trial elastic stress tensor $\underline{\underline{\sigma}}_{n+1}^{trial}$ was located outside the yield surface, the behavior was no longer elastic. Consequently, the plastic flow must be considered and the plastic corrector step of the algorithm must be used in order to get an admissible stress state. In such case, the trial stress tensor at increment *n+1* was defined as follows:

$$\underline{\underline{\sigma}}_{n+1}^{trial} = \underline{\underline{\sigma}}_{n+1} + \underline{\underline{\underline{\underline{C}}}}_e : \left(\underline{\underline{\Delta\varepsilon}} - \underline{\underline{\Delta\varepsilon}}^p \right) \tag{4.31}$$

A combination of the plastic strain tensor with the flow rule gave:

$$\underline{\underline{\sigma}}_{n+1}^{trial} = \underline{\underline{\sigma}}_{n+1} + \Delta p \underline{\underline{\underline{\underline{C}}}}_{e} : \left(\frac{\partial g}{\partial \underline{\underline{\sigma}}} \right)_{n+1} \tag{4.32}$$

A decomposition of the trial stress and the elastic constitutive matrix into their spherical and deviatoric part gave:

$$\begin{cases} \underline{\underline{S}}_{n+1} = \underline{\underline{S}}_{n+1}^{trial} - 2\mu_{rev}\Delta p \left(\frac{\partial g}{\partial \underline{\underline{\sigma}}} \right)_{n+1} \\ P_{h,n+1} = P_{h,n+1}^{trial} - \frac{1}{3}\Delta p \lambda_{rev} \left(\underline{\underline{I}} \otimes \underline{\underline{I}} \right) : \left(\frac{\partial g}{\partial \underline{\underline{\sigma}}} \right)_{n+1} \end{cases} \tag{4.33}$$

The determination of the stress at each increment depended on the resolution of the following final return-mapping scalar equation:

$$R_p(\Delta p) = \Delta p - \Delta t \left\langle \frac{F}{K_V} \right\rangle^n \exp\left(\alpha \left\langle \frac{F}{K_V} \right\rangle^{n+1} \right) \tag{4.34}$$

The incremental multiplier Δp^{i+1} was computed with a Newton method:

$$\Delta p^{i+1} = \Delta p^i - \frac{1}{J^i} R_p(\Delta p^i) \quad i = 1..n \text{, where } J^i = \left. \frac{\partial R_p}{\partial \Delta p} \right|_i \tag{4.35}$$

Where *J* is calculated with the following equation:

$$J = 1 - \frac{\Delta t}{K_V} \exp\left(\alpha \left\langle \frac{F}{K_V} \right\rangle^{n+1} \right) \left(n \left\langle \frac{F}{K_V} \right\rangle^{n-1} + \alpha(n+1) \left\langle \frac{F}{K_V} \right\rangle^n \right) \left(\frac{\partial J_2}{\partial \Delta p} - \frac{1}{3} \frac{\partial \varphi}{\partial \Delta p} \right) \tag{4.36}$$

Once *Δp* was determined, the final stress tensor can be computed thanks to the following equation:

$$\underline{\underline{\sigma}}^{trial} = \underline{\underline{S}}^{trial} + P_h^{trial} \underline{\underline{I}} \tag{4.37}$$

where $\underline{\underline{S}}^{trial}$ was the deviatoric part of the trial stress tensor $\underline{\underline{\sigma}}^{trial}$ and P_h^{trial} was its hydrostatic part.

The algorithmic tangent modulus necessary for applying a Newton method for iterative solution of the global equilibrium problem was computed as:

$$\underline{\underline{\underline{\underline{C}}}} = \frac{\partial \underline{\underline{\sigma}}}{\partial \underline{\underline{\varepsilon}}} \tag{4.38.}$$

$$\underline{\underline{\underline{\underline{C}}}} = \frac{2\mu_{rev}}{(1 - 2\mu_{rev}\Delta p)} \left(\underline{\underline{I}} - \frac{1}{3} \underline{\underline{I}} \otimes \underline{\underline{I}} \right) + \underline{\underline{S}}^{trial} \otimes \left(\frac{2\mu_{rev}}{(1 - 2\mu_{rev}\Delta p)^2} \right) \frac{\partial \Delta\lambda}{\partial \Delta\varepsilon} + \frac{3\lambda_{rev} + 2\mu_{rev}}{1 + (3\lambda_{rev} + 2\mu_{rev})\Delta p 2a_2^*} \underline{\underline{I}} \otimes \underline{\underline{I}} \tag{4.39}$$

4.3.3. Inverse identification

The inverse identification of this model took place in two main procedures:

- The parameters of the cure-dependent modified MS-Model were determined without rate effects. This identification was detailed in section 4.2.
- The visco-plastic parameters were identified with the experimental responses of chapter under shear (γ=90°) and compression-shear (γ=135°) loadings for the four strain rates for all curing cycles applied. For each curing cycle, the identification was firstly realized and validated in shear (γ=90°). Then, the identified parameters were applied to an Arcan Evolution specimen loaded in compression-shear (γ=135°). From this step, it was possible to establish the cure-dependency between all material parameters: such parameters were known for each curing cycle applied, i.e curing state of the adhesive. Those parameters can be written as a function of the curing degree. At last, the constitutive model was implemented with the cure dependency of visco-plastic flow parameters and an identification procedure such as that proposed in Figure 149 was performed to find the best set of parameters.

4.3.4. Finite Element Analysis

The FE model used for the identification of the model detailed previously was identical to that presented in Figure 148 of section 4.2.1. After identification on each curing cycles applied, i.e. 5h30at 35°C (α=0.4), 3h30 at 60°C (α=0.7) and 1h at 82°C (α=1.0), the values of the visco-plastic flow parameters are presented in Table 19.

Parameters	K_v	**n**	**α**
Unit	**MPa**	**-**	**MPa**
5h30 35°C – α=0.4	23700	2.7	4000
3h30 60°C – α=0.7	42800	2.7	4000
1h 82°C – α=1.0	60000	2.7	4000

Table 19. Visco-plastic flow parameters identified for the three specific cured specimens.

The parameter *Kv* can be relied to the curing degree, such as:

$$K_v(\alpha) = \alpha \cdot K_{v0} \quad \text{with} \quad K_{v0} = 60000 \quad \text{MPa} \tag{4.40}$$

Once this link was established, a global identification that considers this equation was investigated following the procedure defined in Figure 149 of section 4.2.2. Figure 153 and Figure 154 show the comparison between experimental measurements of chapter 3 and numerical predictions coming for the three curing cycles in shear (γ=90°) and compression-shear (γ=135°).

The curves predicted by the identification procedure correlate well with the experimental results in shear (γ=90°), as shown in Figure 153 (a), (b) and (c). In compression-shear (γ=135°), the numerical results fit the experiment accurately until the strength recovery occurring in the second part of the non-linear curve portion (Figure 154). Nevertheless, it seems that the model fits better the first part of the non-linear curve for low curing degrees in tangential direction than for others curing states, namely for the curing cycle of 5h30 at 35°C (curing degree of α=0.4) as shown in Figure 154 (f). It may be come from the fact that the inflexion point is located at higher displacements for low curing degrees: for instance, Figure 154 (b) shows an accurate fit for tangential displacements going from DT= 0 to 4.13e-2 mm (curing degree of α=1.0) and

Figure 154 (f) provide good correlation for tangential displacements within a range from DT= 0 to 9.9e-2 mm (curing degree of α=0.4). The problem of the strength recovery occurs later for such curing states. The elasto-visco-plastic modified model of Mahnken-Schlimmer erased the hardening modification brought to consider the inflexion point in the non-linear behavior at 135°.

Based on the latter observation, one solution could be to add an identification step on results in compression-shear (γ=135°) on the hardening parameters, particularly on parameters a_3 and c introduced in section 4.1.5, to take into account again the strength recovery. In fact, an increase of the hardening stress for displacements starting around the inflexion point must be provided.

Figure 155 shows the comparison of experiment and numerical curves after this identification step for a curing cycles of 5h30 at 35°C in compression-shear (γ=135°). The numerical results are in good agreement with the experimental curves.

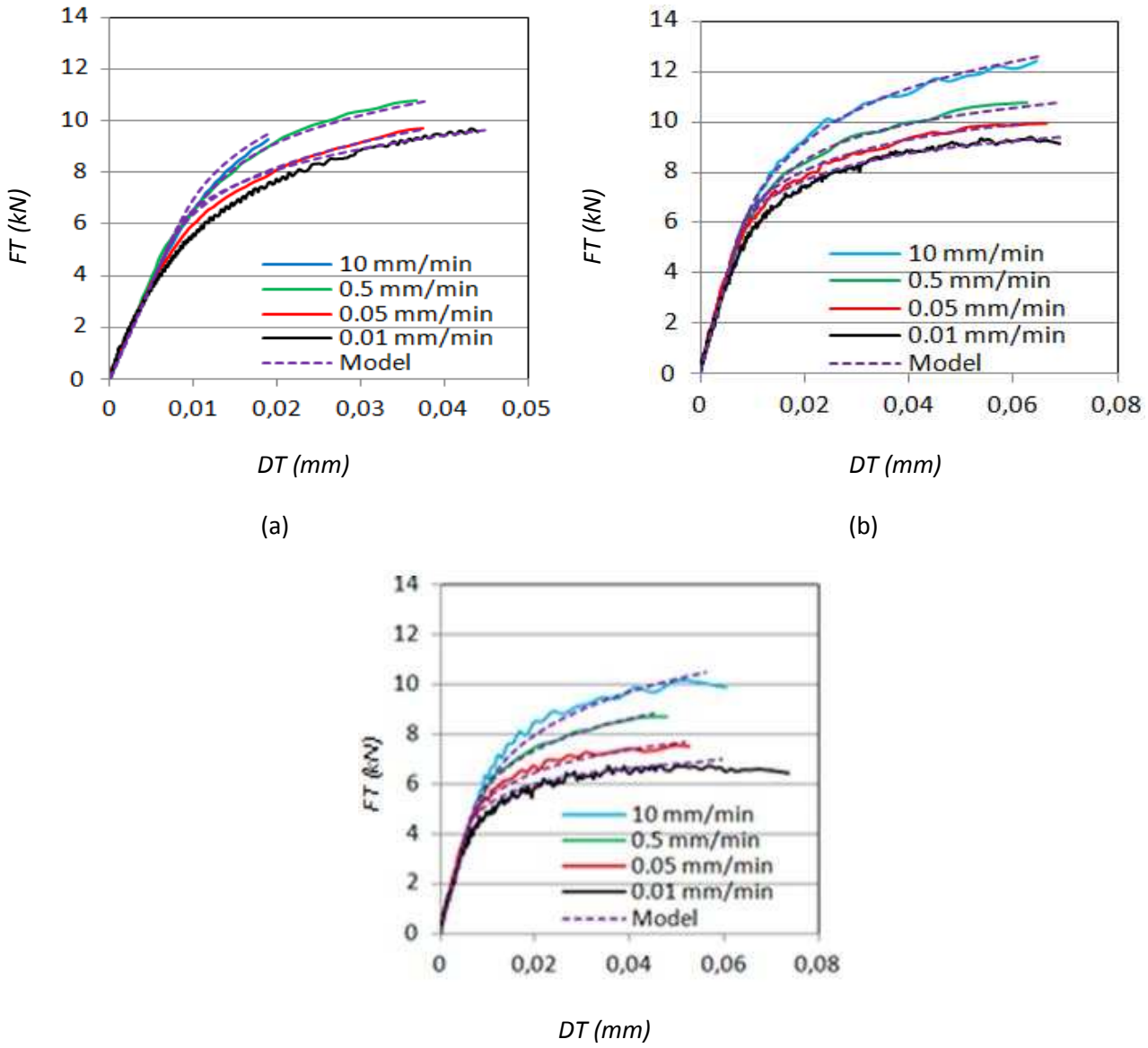

Figure 153. Experimental vs. Predicted results for the four loading rates: loaded in shear (γ=90°): cured (a) 1h at 82 °C, (b) 3h30 at 60°C, (c) 5h30 at 35°C.

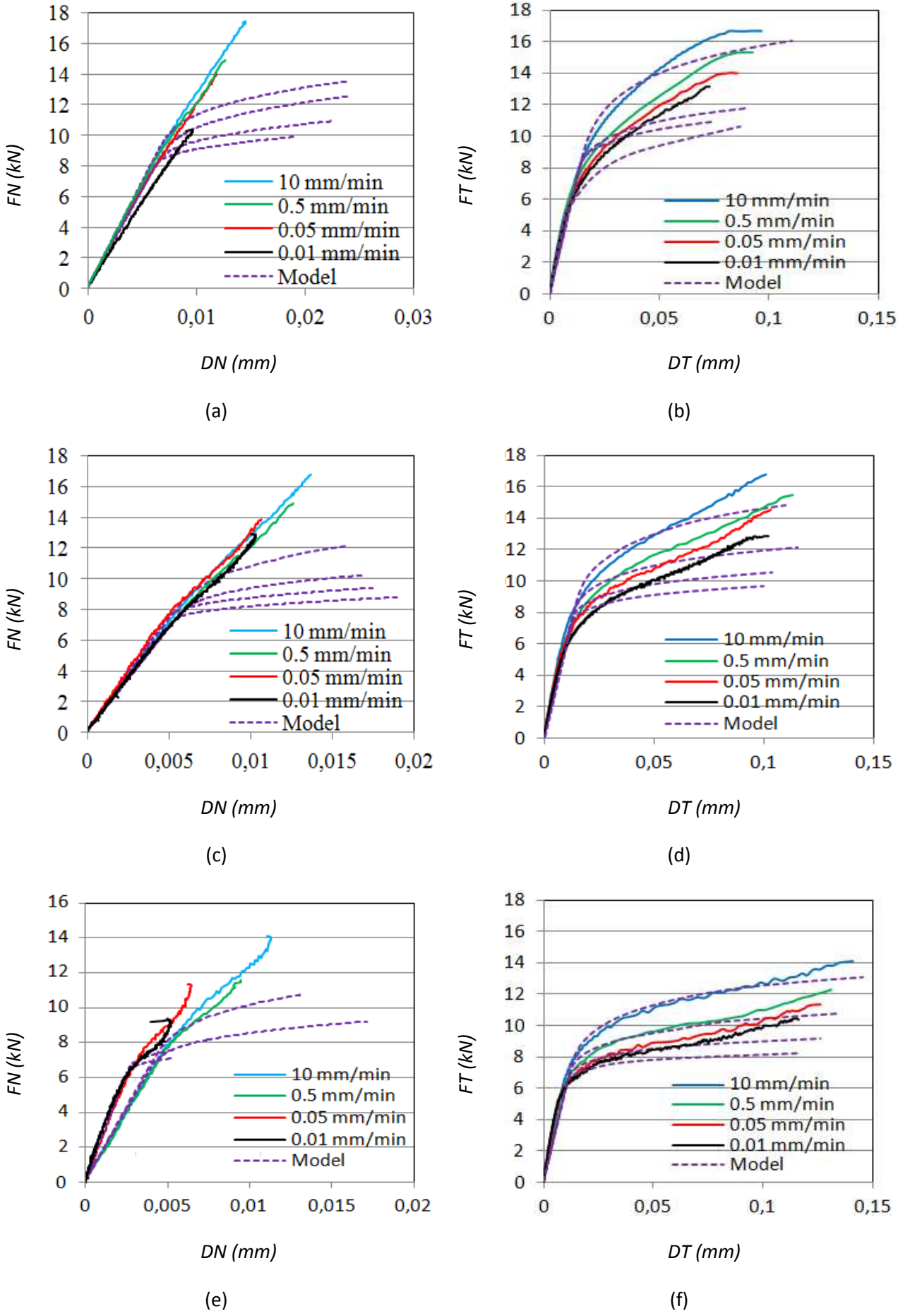

Figure 154. Experimental vs. Predicted results for the four loading rates: loaded in compression-shear (γ=135°): cured (a)-(b) 1h at 82 °C, (c)-(d) 3h30 at 60°C, (e)-(f) 5h30 at 35°C.

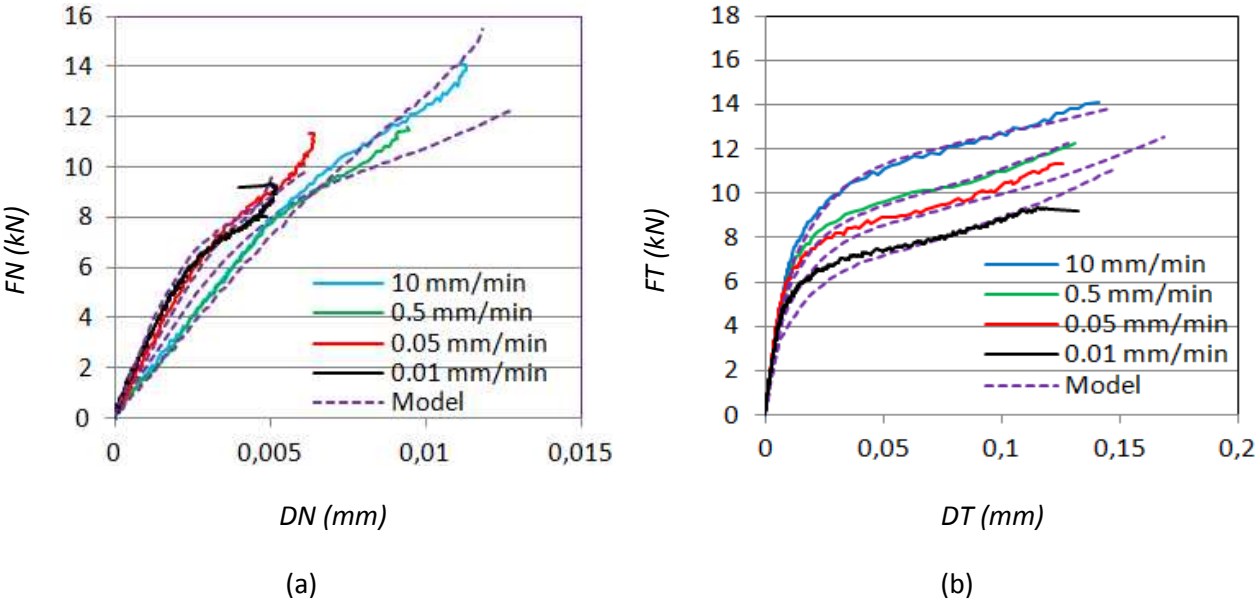

(a) (b)

Figure 155. Predicted vs. Experimental result for compression-shear loading for a curing history of 5h30 at 35°C for several heating rates: (a) in the tangential direction and (b) in the normal direction.

Table 20 shows the hardening parameters obtained after the latter identification step applied on compression-shear (γ=135°) results. This parameter adjustment gave good predictions but it led to a physical nonsense. In fact, the hardening function obtained (Figure 156) reaches extreme high values compared to those of first identification results (Figure 150). This demonstrates the limits to the applicability of the inverse identification process. This may generate parameters that allows a best fit of experimental curves but does not necessarily lead to a scientifically reliable solution.

Parameters	**a_3**	**c**
Unit	**MPa**	**-**
5h30 35°C – α=0.4	2200	4.2

Table 20. Modified hardening parameters for a curing cycle of 5h30 at 35°C.

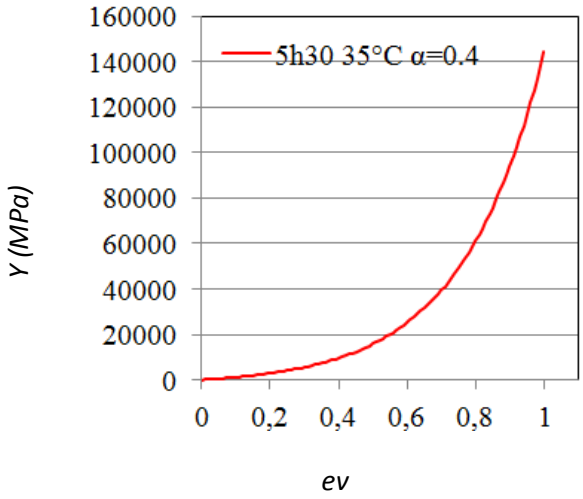

Figure 156. Hardening function established after the latter identification step for a curing cycle of 5h30 at 35°C.

4.4. Cure-dependent modified Mahnken-Schlimmer visco-elastic-visco-plastic model

A purely numerical concept was brought in this section which presents an extension of the cure-dependent modified Mahnken-Schlimmer elasto-visco-plastic model to visco-elasticity in order to describe every aspects of the viscous behavior of an adhesive: creep/recovery response, cyclic behavior. This approach was particularly interesting for cold-curing adhesives such as that used in this study. Indeed, since they are not totally cured, viscous phenomena occurring in bonded assembly may be important [BID 14].

Considering the SYLDA structure, viscous effects are particularly in evidence during the transport stage.

4.4.1. Constitutive equations

A strain rate definition was used and the additive strain rate decomposition was assumed as:

$$\dot{\underline{\underline{\varepsilon}}} = \dot{\underline{\underline{\varepsilon}}}_{\mathrm{el}} + \dot{\underline{\underline{\varepsilon}}}_{\mathrm{v1}} + \dot{\underline{\underline{\varepsilon}}}_{\mathrm{v2}} + \dot{\underline{\underline{\varepsilon}}}_{\mathrm{vp}} \tag{4.41}$$

The Hooke law gave:

$$\dot{\underline{\underline{\sigma}}} = \underline{\underline{\underline{\underline{\mathrm{C}}}}}_{\mathrm{e}} : \dot{\underline{\underline{\varepsilon}}}_{\mathrm{el}} \tag{4.42}$$

The following equations allowed computing the stress state:

$$\dot{\underline{\underline{\varepsilon}}}_{\mathrm{v1}} = \frac{1}{\tau_1}\left(\underline{\underline{\underline{\underline{\mathrm{S}}}}}_{\mathrm{v1}} : \underline{\underline{\sigma}} - \underline{\underline{\varepsilon}}_{\mathrm{v1}} \right) \tag{4.43}$$

$$\dot{\underline{\underline{\varepsilon}}}_{\mathrm{v2}} = \frac{1}{\tau_2}\left(\underline{\underline{\underline{\underline{\mathrm{S}}}}}_{\mathrm{v2}} : \underline{\underline{\sigma}} - \underline{\underline{\varepsilon}}_{\mathrm{v2}} \right) \tag{4.44}$$

$\underline{\underline{\underline{\underline{\mathrm{S}}}}}_{\mathrm{v1}}$ and $\underline{\underline{\underline{\underline{\mathrm{S}}}}}_{\mathrm{v2}}$ were the isotropic compliance tensors. τ_1 and τ_2 were the characteristic creep time associated with $\underline{\underline{\varepsilon}}_{\mathrm{v1}}$ and $\underline{\underline{\varepsilon}}_{\mathrm{v2}}$.

Yield, hardening functions and flow rules were the same as those defined previously:

The yield surface was given by:

$$\mathrm{F} = \mathrm{f_p} - \mathrm{Y_0} \tag{4.45}$$

$$\mathrm{f_p} = \sqrt{\mathrm{J_2} + \mathrm{a_1 I_1 Y_0} + \mathrm{a_2 I_1}^2} \tag{4.46}$$

The hardening function was defined as follows:

$$\begin{gathered} \mathrm{Y} = \mathrm{Y_0} + \mathrm{q}(\alpha)\left(1 - \mathrm{e}^{-\mathrm{b}(\alpha)\mathrm{e_v}}\right) + \mathrm{H}(\alpha)\mathrm{e_v} + \mathrm{a_3}\left(\mathrm{e}^{\mathrm{c}(\alpha)\mathrm{e_v}} - 1\right) \\ \begin{cases} \mathrm{q}(\alpha) = \sqrt{\alpha} \cdot \mathrm{q_{max}} \\ \mathrm{b}(\alpha) = \alpha \cdot \mathrm{b_{max}} \\ \mathrm{c}(\alpha) = \alpha \cdot \mathrm{c_{max}} \\ \mathrm{H}(\alpha) = \alpha \cdot \mathrm{H_{max}} \end{cases} \quad \text{with} \quad \begin{cases} \mathrm{q_{max}} = 28 \\ \mathrm{b_{max}} = 95 \\ \mathrm{c_{max}} = 2.0 \\ \mathrm{H_{max}} = 60 \end{cases} \end{gathered} \tag{4.47}$$

The flow potential was given by:

$$g = \sqrt{J_2 + a_1^* I_1 Y_0 + a_2^* I_1^2} - Y \tag{4.48}$$

The following equation gave the viscoplastic potential:

$$\Omega = \frac{K_V}{\alpha(n+1)} \exp\left(\alpha \left\langle \frac{F}{K_V} \right\rangle^{n+1} \right) \tag{4.49}$$

Such model was ruled by 21 parameters:

- Elastic parameters: the Young modulus *E* and the Poisson's ratio *v*
- Visco-elastic parameters: (E_1, v_1, τ_1) and (E_2, v_2, τ_2)
- Cure-dependent modified MS-Model: a_1, a_2, a_1^*, a_2^*, Y_0, *qmax*, *bmax*, a_3, *cmax* and *Hmax*
- Visco-plastic flow parameters: K_v, *n* and α

4.4.2. Computational algorithm

A return mapping algorithm [SIM 00] was also used to implement those constitutive equations.

When assuming an elastic behavior for a given time increment, it came:

$$\underline{\underline{\Delta\varepsilon_{el}}}^{trial} = \underline{\underline{\Delta\varepsilon}} - \underline{\underline{\Delta\varepsilon_{v1}}} + \underline{\underline{\Delta\varepsilon_{v2}}} \tag{4.50}$$

$$\underline{\underline{\Delta\varepsilon_{el}}}^{trial} = \underline{\underline{M}}^{-1} \left(\underline{\underline{I}} - \frac{\Delta t}{\Delta t + \tau_1} \left(\underline{\underline{\underline{\underline{S_{v1}}}}} : \underline{\underline{\sigma}}_n - \underline{\underline{\varepsilon_{v1}}}_n \right) - \frac{\Delta t}{\Delta t + \tau_2} \left(\underline{\underline{\underline{\underline{S_{v2}}}}} : \underline{\underline{\sigma}}_n - \underline{\underline{\varepsilon_{v2}}}_n \right) \right) \tag{4.51}$$

$$\underline{\underline{\underline{\underline{M}}}} = \underline{\underline{I}} - \frac{\Delta t}{\Delta t + \tau_1} \underline{\underline{\underline{\underline{S_{v1}}}}} . \underline{\underline{\underline{\underline{C_e}}}} - \frac{\Delta t}{\Delta t + \tau_2} \underline{\underline{\underline{\underline{S_{v2}}}}} . \underline{\underline{\underline{\underline{C_e}}}} \tag{4.52}$$

The trial stress tensor was given by:

$$\underline{\underline{\sigma}}_{n+1}^{trial} = \underline{\underline{\sigma}}_{n+1} + \underline{\underline{\underline{\underline{C_e}}}} : \underline{\underline{\Delta\varepsilon}}^{trial} \tag{4.53}$$

Where $\underline{\underline{\underline{\underline{C_e}}}}$ was the elastic constitutive matrix.

The consistent tangent matrix was expressed as follows:

$$\underline{\underline{\underline{\underline{L}}}} = \underline{\underline{\underline{\underline{C_e}}}} . \underline{\underline{\underline{\underline{M}}}}^{-1} \tag{4.54}$$

When the yield criterion was no longer verified, the assumption of elastic and visco-elastic behavior was rejected and a plastic correction must be required. The updating trial stress was defined as:

$$\underline{\underline{\sigma}}_{n+1}^{trial} = \underline{\underline{\sigma}}_{n+1} + \Delta p \underline{\underline{\underline{\underline{C_e}}}} \underline{\underline{\underline{\underline{M}}}}^{-1} : \left(\frac{\partial g}{\partial \underline{\underline{\sigma}}} \right)_{n+1} \tag{4.55}$$

$$\underline{\underline{\sigma}}_{n+1}^{trial} = \underline{\underline{\sigma}}_{n+1} + \Delta p\left(2\mu_{rev}\underline{\underline{I}} + \lambda_{rev}\underline{\underline{I}} \otimes \underline{\underline{I}} \right) : \left(\frac{\partial g}{\partial \underline{\underline{\sigma}}} \right)_{n+1} \tag{4.56}$$

The trial stress tensor and the tangent matrix can be decomposed into two parts, one spherical and another one deviatoric:

$$\underline{\underline{\sigma}}^{trial} = \underline{\underline{S}}^{trial} + \frac{1}{3} P_h^{trial} \underline{\underline{I}} \tag{4.57}$$

$$\underline{\underline{\underline{\underline{C}}}}_e = 2\mu_{rev}\underline{\underline{I}} + \lambda_{rev}\underline{\underline{I}} \otimes \underline{\underline{I}} \tag{4.58}$$

It came:

$$\begin{cases} \underline{\underline{S}}_{n+1} = \underline{\underline{S}}_{n+1}^{trial} - 2\mu_{rev}\Delta p \underline{\underline{S}}_{n+1} \\ P_{h,n+1} = P_{h,n+1}^{trial} - 3(3\lambda_{rev} + 2\mu_{rev})\Delta p \frac{1}{3}\left(a_1^* Y_0 + 2a_2^* P_{h,n+1} \right) \end{cases} \tag{4.59}$$

$\underline{\underline{S}}_{n+1}$ and $\underline{\underline{S}}_{n+1}^{trial}$ being proportional, it can be written as:

$$\begin{cases} \underline{\underline{S}}_{n+1} = \underline{\underline{S}}_{n+1}^{trial}\left(1 - 2\mu_{rev}\Delta p\right) \\ P_{h,n+1} = \dfrac{P_{h,n+1}^{trial} - 3(3\lambda_{rev} + 2\mu_{rev})\Delta p \frac{1}{3} a_1^* Y_0}{1 + (3\lambda_{rev} + 2\mu_{rev})\Delta p 2a_2^*} \end{cases} \tag{4.60}$$

The stress at each increment depended on the resolution of the following final return-mapping scalar equation:

$$R_p(\Delta p) = \Delta p - \Delta t \left\langle \frac{F}{K_V} \right\rangle^n \exp\left(\alpha \left\langle \frac{F}{K_V} \right\rangle^{n+1} \right) \tag{4.61}$$

where Δp^{i+1} was computed with a Newton method:

$$\Delta p^{i+1} = \Delta p^i - \frac{1}{J^i} R_p\left(\Delta p^i\right) \quad i = 1..n \text{, where } J^i = \left.\frac{\partial R_p}{\partial \Delta p}\right|_i \tag{4.62}$$

$$J = 1 - \frac{\Delta t}{K_V} \exp\left(\alpha \left\langle \frac{F}{K_V} \right\rangle^{n+1} \right)\left(n\left\langle \frac{F}{K_V} \right\rangle^{n-1} + \alpha(n+1)\left\langle \frac{F}{K_V} \right\rangle^n \right)\left(\frac{\partial J_2}{\partial \Delta p} - \frac{1}{3}\frac{\partial \varphi}{\partial \Delta p} \right) \tag{4.63}$$

After determining *Δp*, the final stress tensor can be calculated as:

$$\underline{\underline{\sigma}}^{trial} = \underline{\underline{S}}^{trial} + P_h^{trial}\underline{\underline{I}} \tag{4.64}$$

The algorithmic tangent modulus necessary for applying a Newton method for iterative solution of the global equilibrium problem was determined as follows:

$$\underline{\underline{\underline{\underline{C}}}} = \frac{\partial \underline{\underline{\sigma}}}{\partial \underline{\underline{\varepsilon}}} \tag{4.65}$$

$$\underline{\underline{\underline{\underline{C}}}} = \frac{2\mu_{rev}}{(1-2\mu_{rev}\Delta p)}\left(\underline{\underline{\underline{\underline{I}}}} - \frac{1}{3}\underline{\underline{I}} \otimes \underline{\underline{I}}\right) + \underline{\underline{S}}^{trial} \otimes \left(\frac{2\mu_{rev}}{(1-2\mu_{rev}\Delta p)^2}\right)\frac{\partial \Delta\lambda}{\partial \Delta\varepsilon} + \frac{3\lambda_{rev}+2\mu_{rev}}{1+(3\lambda_{rev}+2\mu_{rev})\Delta p 2a_2^*}\underline{\underline{I}} \otimes \underline{\underline{I}} \quad (4.66)$$

4.4.3. Finite Element Analysis

For a given set of visco-elastic parameters (E_1, v_1, τ_1, E_2, v_2, τ_2), the simulations were performed using FE model loaded in shear (γ=90°) presented in section 4.2.1 (Figure 148). Two curing cycles were applied: 1h at 82°C (α=1.0) and 5h30 at 35°C (α=0.4). The values of cure-dependent modified MS-Model parameters (*a1*, *a2*, *a1**, *a2**, *Y0*, *qmax*, *bmax*, *a3*, *cmax* and *Hmax*) and visco-plastic flow parameters (K_v, n and α) were those determined in section 4.3.

Figure 157 (b) displays the tangential displacement *DT* during a cyclic creep/recovery instruction under shear for the two curing cycles applied.

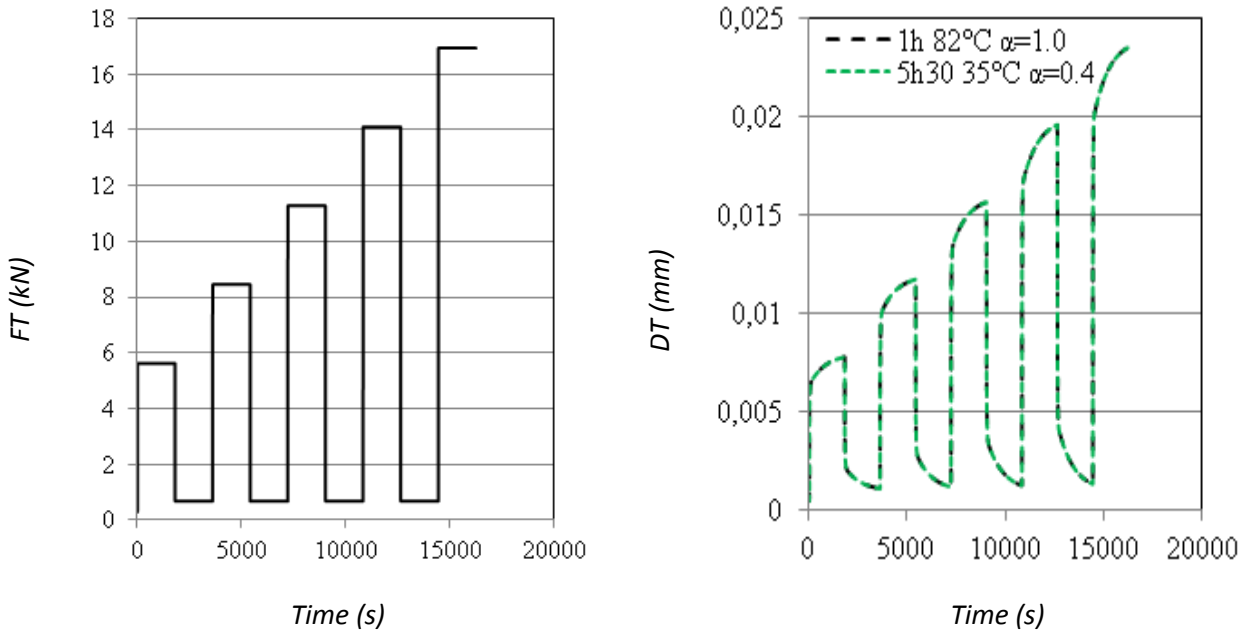

Figure 157. Cyclic shear creep/recovery simulation for two curing cycles: 1h at 82°C (α=1.0) and 5h30 at 35°C (α=0.4): (a) FT. Vs Time and (b) DT vs. Time.

For the different loads applied, creep occurred and the tangential displacement was not fully recovered. It can be showed that tangential displacements are similar for a fully-cured adhesive than for an adhesive polymerized at α=0.4. It is not surprising because no dependency of visco-elastic parameters to the curing degree has been provided.

A sensitivity analysis on visco-elastic parameters, i.e. (E_1, v_1, τ_1) and (E_2, v_2, τ_2) on a fully cured adhesive was realized to better understand the constitutive behavior proposed, as shown in Figure 158. The curves for a partially cured adhesive were not considered. Since as visco-elastic parameters are not cure-dependent in the model proposed, the resulting curves will present the same trend as those obtained for a fully cured adhesive. Those results show that only the instantaneous modulus E_1 has an influence on the creep/recovery response. In addition, it can be assumed that such parameter varies significantly according to the adhesive curing state and thus, has a direct impact on mechanical responses.

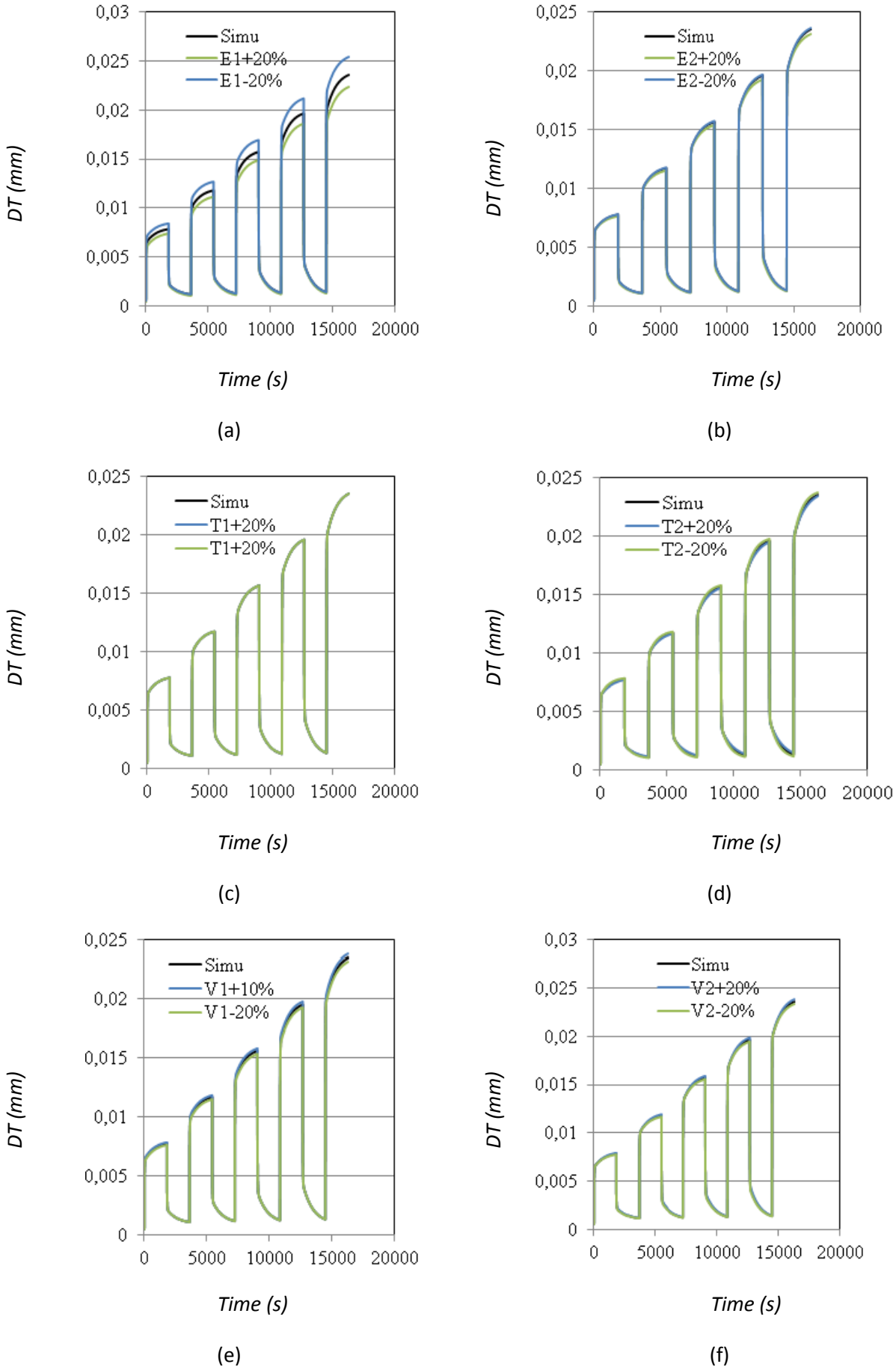

Figure 158. Cyclic shear creep/recovery for a fully cured adhesive (α=1.0), sensitivity analysis of visco-elastic parameters: (a) E1, (b) E2, (c) τ_1, (d) τ_2, (e) ν_1 and (f) ν_2.

4.5. Conclusions

In this chapter, three cure-dependent constitutive models, based on Mahnken-Schlimmer elasto-plastic model, were implemented: an elasto-plastic model, an elasto-visco-plastic model and a visco-elasto-visco-plastic model. Regarding the first two models, the approach was split in two steps. The first one consisted in determining the mechanical behavior of the fully cured adhesive. The second one involved integrating the curing behavior of the adhesive Hysol EA-9321 identified in chapter 2.

Regarding the elasto-plastic model, the fully cure constitutive behavior was considered as a reference. This was built on the model of Mahnken-Schlimmer but slightly modified to consider the strength recovery exhibited on the non-linear part of the compression-shear (135°) response. The parameters were defined by using a sequential identification strategy coupling FE simulations and optimization process. The numerical responses obtained showed that the modified MS-Model gave good results for the three curing cycles considered separately. A global identification procedure was then set up to relied the parameters of the modified Mahnken-Schlimmer model to the curing degree. A good correlation was obtained between experimental and predictive curves.

The elasto-visco-plastic model was built on the cure-dependent modified Mahnken-Schlimmer model by integrating strain-rate effects. As previously, cure-dependent visco-plastic parameters were determined through a global identification procedure. This model gave good predictions in shear (90°). However, responses predicted in compression-shear (135°) correlated well with experiment until an inflexion point for the strength straightened. An additional identification of some hardening parameters led to good predictions. However, these values greatly exceeded their initial values and as a consequence, were not acceptable. This pointed to serious limitations in the inverse identification process. Indeed, it conducted to a better set of parameter to reach a best fit between experiment and numerical results but did not consider its physical sense.

The numerical study on the cure-dependent visco-elasto-visco-plastic underlined the possibility of describing the viscous behavior of a partially cured adhesive in a bonded assembly, namely the creep/recovery and cyclic behavior. However, a dependency of visco-elastic parameters must be introduced in the model proposed to better consider the viscous behavior of the adhesive.

∞

The cure-dependent modified MS-Model accurately predicted the mechanical behavior of the cold-curing adhesive Hysol EA-9321. Besides, this model must be validated on a representative structure of the intended industrial application, i.e. the mechanical responses predicted by the SYLDA structure during its life course.

4.6. References

[ABA 10] Abaqus Analysis User's Manual version 6.10. Simulia, Providence, RI, USA, 2010.

[ARN 14] Arnaud N., PhD Thesis : Analyse de l'effet du vieillissement en milieu humide sur le comportement mécanique d'adhésifs en assemblages sous sollicitations multiaxiales, 2014.

[BID 14] Bidaud P., PhD Thesis: Analysis of the cyclic behavior of an adhesive in an assembly for offshore windmills applications, 2014.

[COG 10] Cognard J.Y., Créac'hcadec R., Maurice J., Davies P., Peleau M., Da Silva LFM, Analysis of the influence of hydrostatic stress on the behavior of an adhesive in a bonded assembly. Journal of Adhesion Science and Technology, pp. 24-1977, 2010.

[CRE 08] Créac'hcadec R, Cognard JY, Heuzé T. On Modelling the Non-linear Behavior of Thin Adhesive Films in Bonded Assemblies With Interface Elements. Journal of Adhesion Science and Technology. Vol. 22, pp. 1541-1563, 2008.

[CRE 09] Créac'hcadec R., Cognard J.Y., 2-D modelling of the behavior of an adhesive in an assembly using a non-associated elasto-visco-plastic model. Journal of Adhesion, pp. 85-239, 2009.

[JOU 95] Jousset P., Rachik M., Pressure-dependent plasticity for structural adhesive, Journal of Adhesion Science and Technology, pp.24-1995, 2010.

[LAF 04] Lafarge M., PhD Thesis : Modélisation couplée comportement endommagement et critères de rupture dans le domaine de la transition du PVDF, 2004.

[MAH 05] Mahnken R., Schlimmer M., Simulation of strength difference in elasto-plasticity for adhesive materials. International Journal for Numerical Methods in Engineering, pp. 63-1461, 2005.

[NOU 89] Nouailhas D. International Journal of Plasticity. Vol. 5, pp. 501-520, 1989.

[SIM 00] Simo J.C, Hugues T.J.R, Computational Inelasticity, Springer 2000.

[THE 13] Thevenet D., Créac'hcadec R., Sohier L., Cognard J.Y., Experimental analysis of the behavior of adhesively bonded joints under tensile/compression-shear cyclic loadings, Int. J. Adhes. Adhes., Vol. 44, pp. 15-25, 2013.

CHAPTER 5:

NUMERICAL STUDY OF AN APPLICATION CASE AND PROPOSAL FOR A REPRESENTATIVE SYLDA MINI STRUCTURE

Résumé

Dans le chapitre précédent, la mise en place d'une procédure d'identification du comportement mécanique de l'adhésif Hysol EA-9321 sur des essais Arcan Evolution avec intégration du taux de polymérisation a été présentée. Ce chapitre a pour but de proposer un essai représentatif du comportement de l'adhésif sur la structure spatiale collée SYLDA 5. La structure SYLDA 5 est volumineuse. Elle mesure plusieurs mètres de diamètre. La réalisation de tests sur une telle structure est donc coûteuse. Pour des contraintes d'intégration des satellites dans le lanceur Ariane 5 à l'aide d'une structure SYLDA 5, il est nécessaire que cette structure permette d'adapter son diamètre à l'aide de réductions de section. Cette réduction de section est actuellement réalisée par des géométries coniques collées. Il est ainsi primordial de pouvoir caractériser et tester ce type de géométrie expérimentalement. L'approche proposée dans ce chapitre a donc consisté à comparer numériquement les sollicitations d'une liaison type SYLDA 5 dite « Joint SSS » et d'un assemblage conique basé sur une modification d'un essai de traction / compression – torsion développé par Arnaud et al. [ARN 14a][ARN 14b]. L'objectif est de comparer ces deux types d'assemblages collés pour analyser l'influence de l'utilisation des résultats expérimentaux pour des essais type liaison conique pour le dimensionnement d'assemblages coniques collés tels que ceux du SYLDA 5. Cette approche offre des perspectives intéressantes pour la validation de l'influence du taux de polymérisation sur la tenue mécanique de la structure SYLDA 5.

Summary

In the previous chapter, an identification strategy was developed to predict the mechanical behavior of the cold-curing adhesive Hysol EA-9321 with integration of the curing degree. Such procedure was applied on Arcan Evolution specimens. The purpose of this chapter is to provide a test representative of the adhesive behavior in the SYLDA 5 structure. This consistent structure has several meters in diameter. Thus, conducting some experiments on such structure represents a substantial cost. In addition, such structure must accept lower and upper satellites and, as a consequence, requires a diameter adjustment through section reductions. This means introducing conical bonded geometries. Characterizing and testing such large-scale geometries is then essential. Therefore, this chapter aims to estimate and compare numerically the solicitations encountered by a SYLDA 5 connection called "Joint SSS" with those sustained by a conical bonded joint based on a modified tension / compression - torsion test developed by Arnaud et al. [ARN 14a][ARN 14b]. The purpose is to analyze the influence of the use of a classical conical bonded joint for the dimensioning of conical joints similar to those of the SYLDA 5 structure. This provides attractive prospects to validate the cure-dependent constitutive models developed.

Contents

5.1. Introduction

The aim of this chapter is to study a typical case of a structural bonded spatial part, namely a conical bonded joint similar to that present in the SYLDA 5 structure. The global strategy consists in suggesting a simple test representative of the stresses sustained by this spatial structure in order to validate an application of the cure-dependent modified Mahnken-Schlimmer elasto-plastic model identified on the Arcan Evolution specimen.

This is a purely numerical study that compares the stress distribution within the adhesive layer for a SYLDA 5 type bonded joint called “joint SSS” and a conical bonded joint loaded in tension.

The support of this study is the Ariane 5 SYLDA 5 structure which is contained inside the launcher Ariane 5 fairing, as shown in

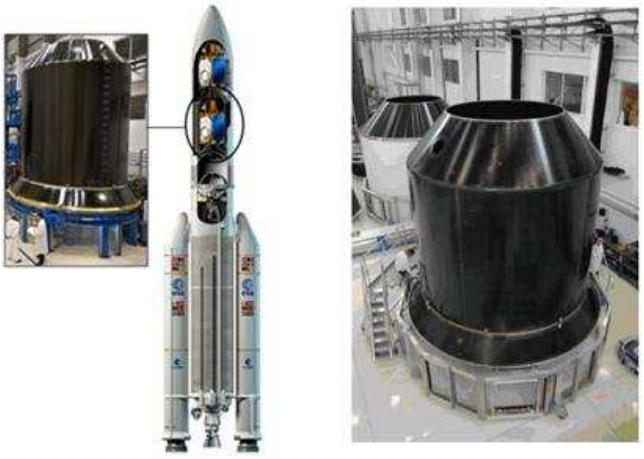

(a) (b)

Figure 159 (a) and allows carrying several payloads on a single flight. Such structure is an assembly of cones with a cylindrical part made of expanded aluminium honeycomb core and covered by carbon fiber/resin skins. The Figure 159 (a) details the localization of the SYLDA 5 structure at the head of the launcher Ariane 5. The Figure 159 (b) points out the storage environment of these kinds of structures waiting for being send to the French Guyana.

(a) (b)

Figure 159. Ariane 5 and SYLDA 5 structure. (a) Localization of the SYLDA 5 structure in the launcher and (b) Storage of the SYLDA 5 Structure.

The connection between those different assemblies is done by different rings. The geometries of such sets are presented in Figure 160. All these geometries are axisymmetric. These connecting elements include titanium bolts and CFRP straps, known as lashings. The load transfer in the connection between the sandwich panel and the metal part is carried out by the cold-curing adhesive Hysol EA-9321.

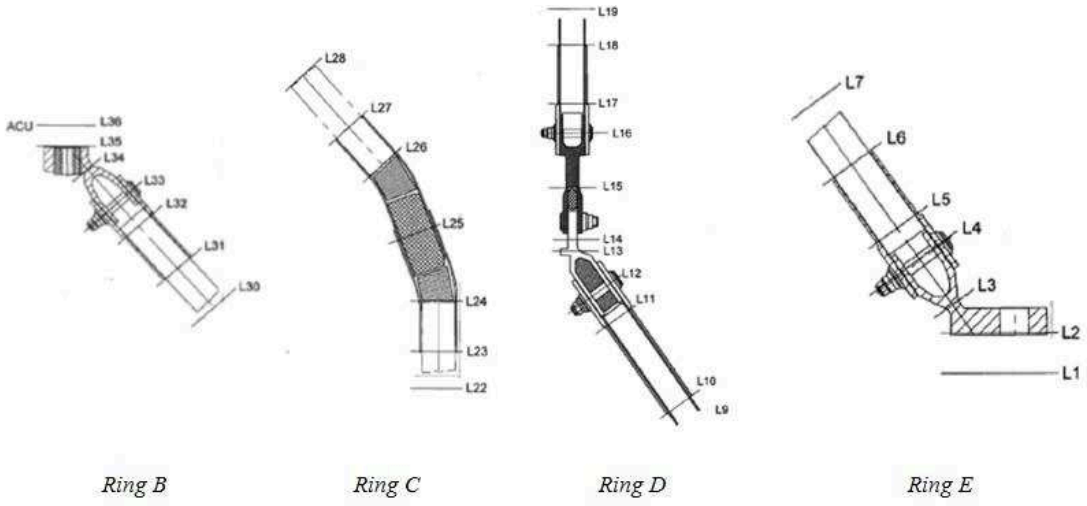

Figure 160. Geometries of connections called "Ring" available on the SYLDA 5 structure.

The connection called "Ring D" is that associated with the bonded joint "Joint SSS" which links the SYLDA 5 structure to remaining launcher. Such connection is bolted in its center to allow a pyrotechnic cordon entry necessary to separate the launcher payloads (Figure 161).

Figure 161. Connection Ring D called « Joint SSS ».

We focus on this connection "Joint SSS". The industrial objective is to achieve a conical connection that replaces bolts by structural adhesive bonding. The purpose is:

- To limit the stress concentrations produced by mechanical fasteners such as bolting or drilling adhesive bonding allows a more homogeneous/uniform stress distribution.

- A significant reduction of labor costs and time production. Indeed, mechanical fastening such as bolting, riveting or drilling are time-consuming processes resulting in additional production costs
- To lighten structures and then being more efficient

- To integrate specific adhesive functions such as depreciation, thermal isolation

The study of such joint requires the examination of stresses sustained by the whole SYLDA 5 structure. Such a structure is subjected to various loads during its lifespan, i.e. from its manufacturing to the Ariane 5 launching:

- Thermal loads associated with the storage environment and the transport step
- Mechanical loads associated with transportation and maintenance
- Thermal, mechanical and thermo-mechanical loads during the Ariane 5 flight stages

The combination of thermal and mechanical loadings encountered during the flight of Ariane 5 is defined by flight times. Three time periods are identified, as suggested in Table 21.

First phase	Important mechanical and low thermal loadings
Second phase	Low mechanical and important thermal loadings
Third phase	Exclusively thermal loadings

Table 21. Global loadings during the Ariane 5 flight.

As shown in Table 22, the bonded structure SYLDA 5 is subjected to 304 loading cases during the flight times detailed above.

Load Case	Event	Description
1 - 216	Wind and gust	18 basic cases times 12 rotated positions (0°±45°, 90°±45°,180°±45°,270°±45°)
217	EAP cut-off	1 basic case (0°)
218 – 225	Lift-off	8 basic cases(0°)
226 – 227	EPC cut-off	2 basic cases(0°)
228 – 241	EPC cut-off	7 additional rotated positions (45°, 90°, 135°, 180°, 225°, 270°, 315°)
242 – 297	Lift-off	7 additional rotated positions (45°, 90°, 135°, 180°, 225°, 270°, 315°)
298 - 304	EAP cut-off	7 additional rotated positions (45°, 90°, 135°, 180°, 225°, 270°, 315°)
temp		Min./max thermal environment

Table 22. Description of the 304 loading cases sustained by the SYLDA 5 structure during the flight.

Some additional local loadings must be considered:

- Pre-load of separation springs which are used to force away the spacecraft from the launch vehicle

- Engagement and disengagement of local connectors

As detailed above, the mechanical behavior of the bonded/bolted connection Ring D called “Joint SSS” is studied. Thus, only the flight time for which the mechanical loadings are predominant, i.e. the first time period according to Table 21, will be investigated in this study.

As shown in Figure 162, the SYLDA 5 structure is submitted to a uniaxial compressive strength F_X applied on its upper part. Table 23 gives orders of magnitude of such a load. *LC 257_c* and *LC 259_t* are the compressive, the tension loadings cases used to sizing the SYLDA 5, respectively. For each loading pattern, *F_spr* and *F_S/S* are the pre-loads associated with the separation system SYLDA 5/launcher and

electrical connectors. Both pre-loads are neglected in this study.

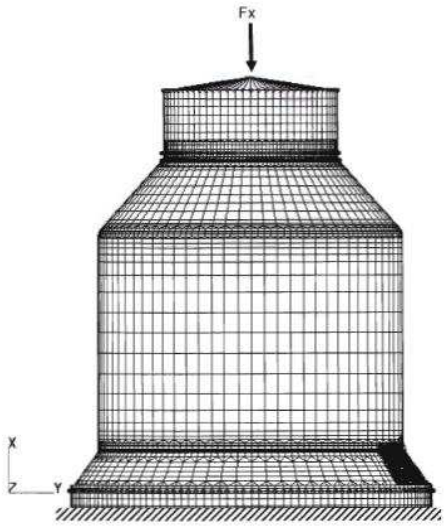

Figure 162. SYLDA 5 structure: configuration considered for the first flight period.

Description	Item	LC 257_c	LC 259_t
axial force	F_X [N]	-1402000	1226000
Pre-comp. force of Sep. Spr.	F_spr [N]	F_spr_c	F_spr_t
Pre-comp. force of S/S bracket	F_S/S [N]	F_S/S_t	F_S/S_t

Table 23. Strengths applied on the SYLDA 5 structure for the first flight period.

5.2. Connection Ring D called "Joint SSS": Issue

Figure 163 presents the elements which constitute the connection Ring D and its dimensions.

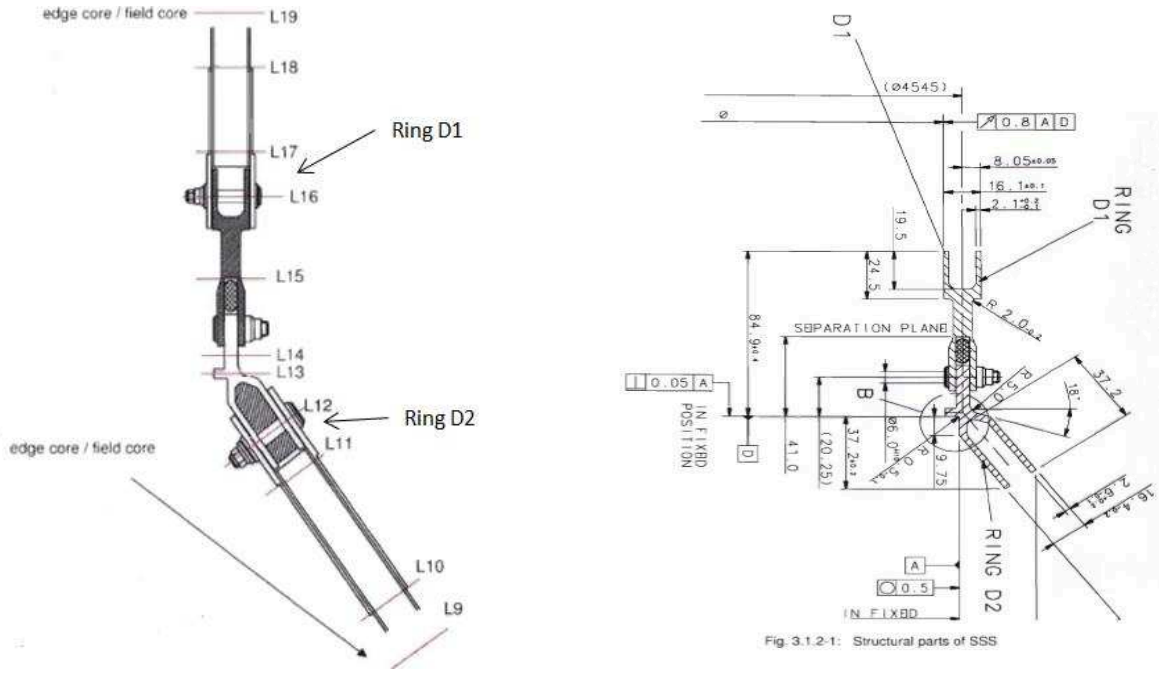

(a) (b)

Figure 163. (a) Ring D called « Joint SSS » and (b) Dimensions of Ring D.

As shown in Figure 163, the Ring D is composed of two bonded/bolted connections Ring D1 and Ring D2. Both are linked together with a bolt crossed by a pyrotechnic cordon, as noticed in Figure 161. When the SYLDA 5 structure is sustained to a tension loading, Ring D1 and Ring D2 behave differently. Thus, it seems necessary to consider separately each bonded/bolted connection to predict properly the global mechanical behavior of the Ring D when it is submitted to such loading. In addition, it is interesting to associate those bonded/bolted connections to classical tests in order to size the "Joint SSS".
When the SYLDA structure is sustained to a tension loading, the Ring D1 can be referred to a double lap joint [AST 96] (Figure 164).

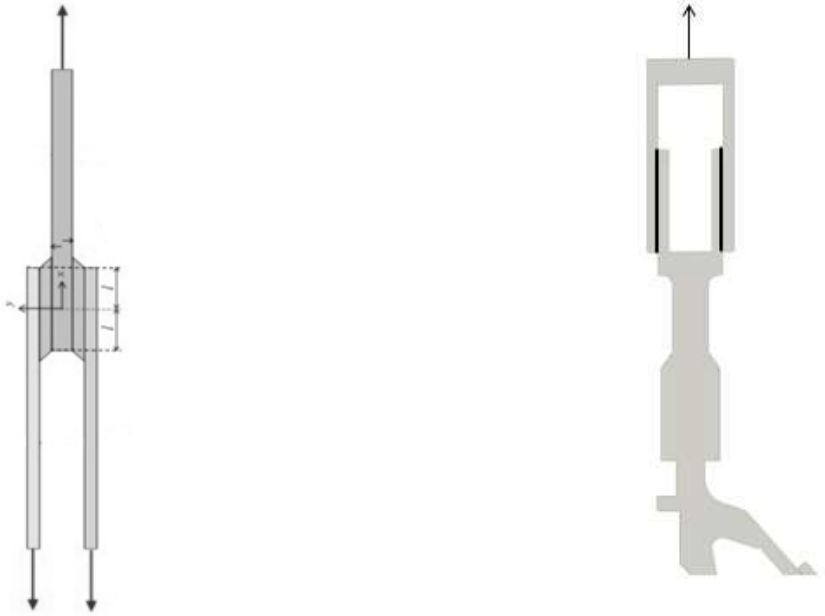

(a) (b)

Figure 164. (a) Double lap joint and (b) Ring D1 loaded in tension.

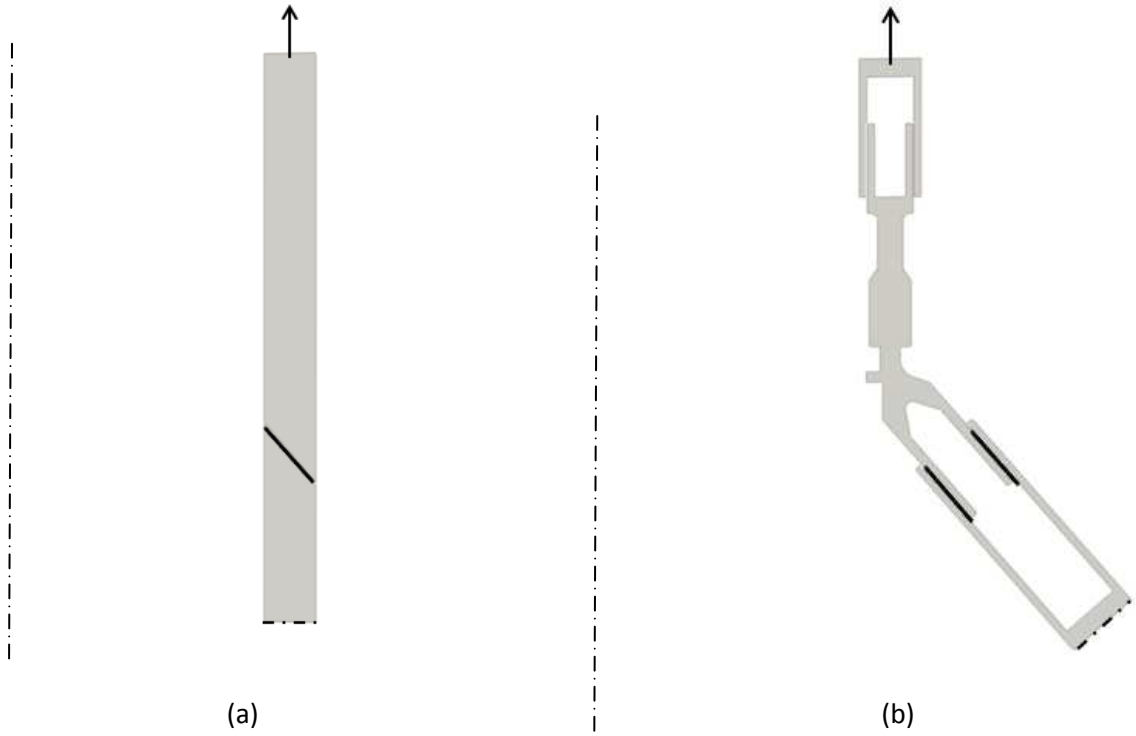

(a) (b)

Figure 165. Comparison of two tests: (a) Conical bonded joint and (b) Ring D2 loaded in tension.

A study on such loading and the analogy of this ring with the double lap joint has already been done by the CNES [INT]. Thus, this review is limited to the analysis of Ring D2.

Similar reasoning to that made previously with the Ring D1 leads to associate the Ring D2 to a kind of double conical connection. The purpose is to show that the stresses sustained by the bonded joint in the Ring D2 are similar to those seen in a conical bonded joint (Figure 165).

5.3. Strategy overview

The SYLDA structure was not entire considered but locally studied. The aim was only to characterize the adhesive Hysol EA-9321 for loading similar to that encountered on the Ring D2. The bonding aluminium/composite was not regarded but only a bonding aluminium/aluminium. Thus, the studied structure was made of two aluminium/adhesive interfaces.

The load imposed by the SYLDA structure led to complex solicitations of the two bonded joints. Therefore, it was necessary to develop a test representative of the mechanical behavior of the adhesive on the connection Ring D2. This test will validate and optimize the mechanical behavior of such bonded assemblies.

5.4. Numerical comparison between the Ring D2 and a conical bonded joint

The stress distribution within the adhesive layer for a conical bonded joint and a Ring D2 were investigated. The aim was to compare the numerical responses of both connections in order to determine if the conical bonded joint can be used to design bonded assemblies such as Ring D2 type.
3D FE model were introduced in the software Abaqus. Figure 166, respectively Figure 167, presents the FE model of a conical bonded joint, respectively a Ring D2 joint.

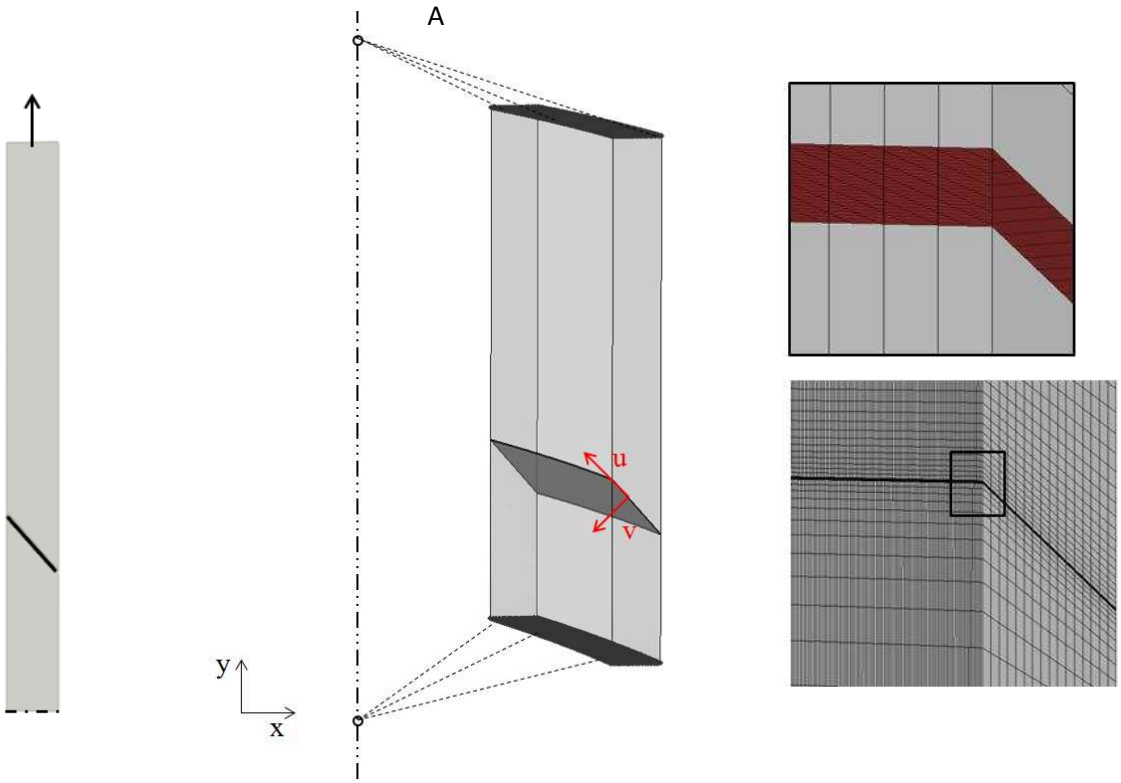

Figure 166. FE model of a conical bonded joint: (a) and (b) Boundary conditions, (c) mesh.

Finite Element studies were undertaken under elastic assumption, for a bonding between aluminium

(Young's modulus E = 70 GPa, Poisson's ratio ν = 0.30) and epoxy adhesive Hysol EA-9321 (Young's modulus E_A = 3480 MPa, Poisson's ratio ν_A = 0.369). For each model, the boundary conditions were represented by a kinematic coupling between driving points A, B and the driven surfaces of the bonded joint. Only a slice of the bonded assembly was represented to reduce time calculation. Good numerical results were obtained using meshes with 40 8-node trilinear reduced integration brick elements including hourglass control (C3D8R in the software Abaqus [ABA 10]) in the adhesive thickness (adhesive thickness of 0.2 mm).

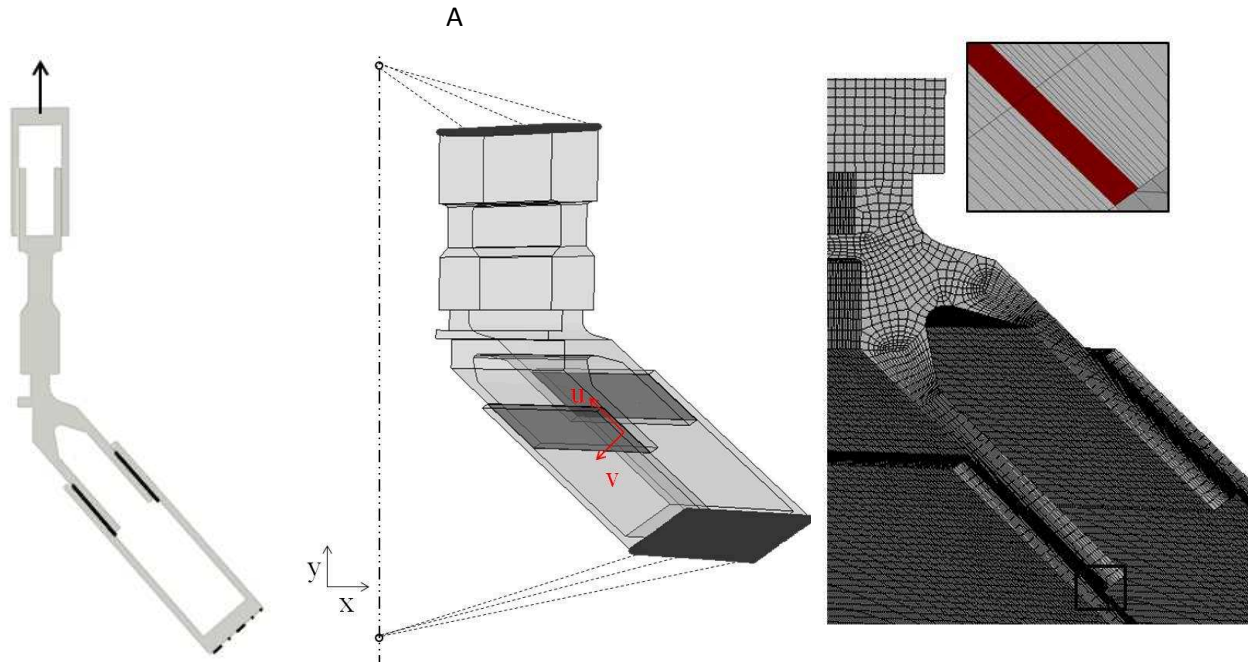

(a) (b) (c)

Figure 167. FE model of the Ring D2: (a) and (b) boundary conditions, (c) mesh.

The base (*u*, *t*, *v*) was used to facilitate the analysis of the adhesive behavior. In this base, the stress components are denoted by: σ_u, σ_v, σ_t et τ_{uv} ; where σ_v is the peel stress and τ_{uv} is the shear stress.

Figure 168 and Figure 169 present the evolution of the von Mises equivalent stress, the peel stress and the shear stress in the mean plane of the adhesive layer along the overlap of the joint for both conical bonded joint and Ring D2 for a compression loading. The peel and von Mises stresses values predicted for both connections are closed in the middle area of the overlap of the adhesive layer (4 mm < x < 16 mm). Those stresses differ from each other when approaching the free edges of the bonded joint. This can be the cause of edge effects or stress heterogeneities due the geometry of the Ring D2.

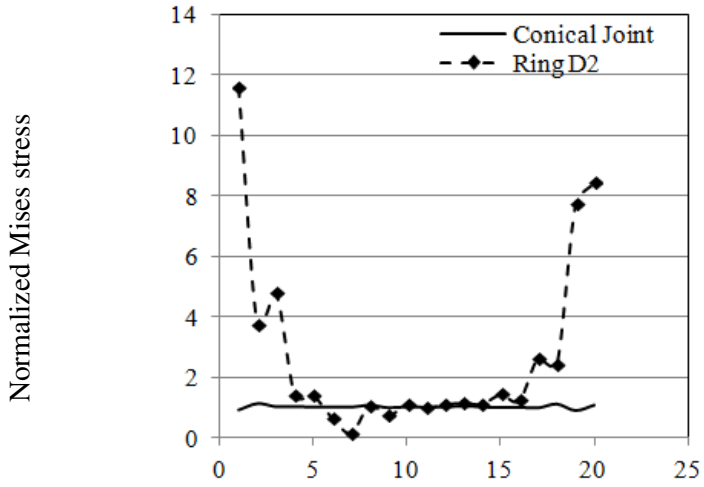

x (mm)

Figure 168. Influence of the connection type on the normalized von Mises stress response along the overlap of the adhesive layer.

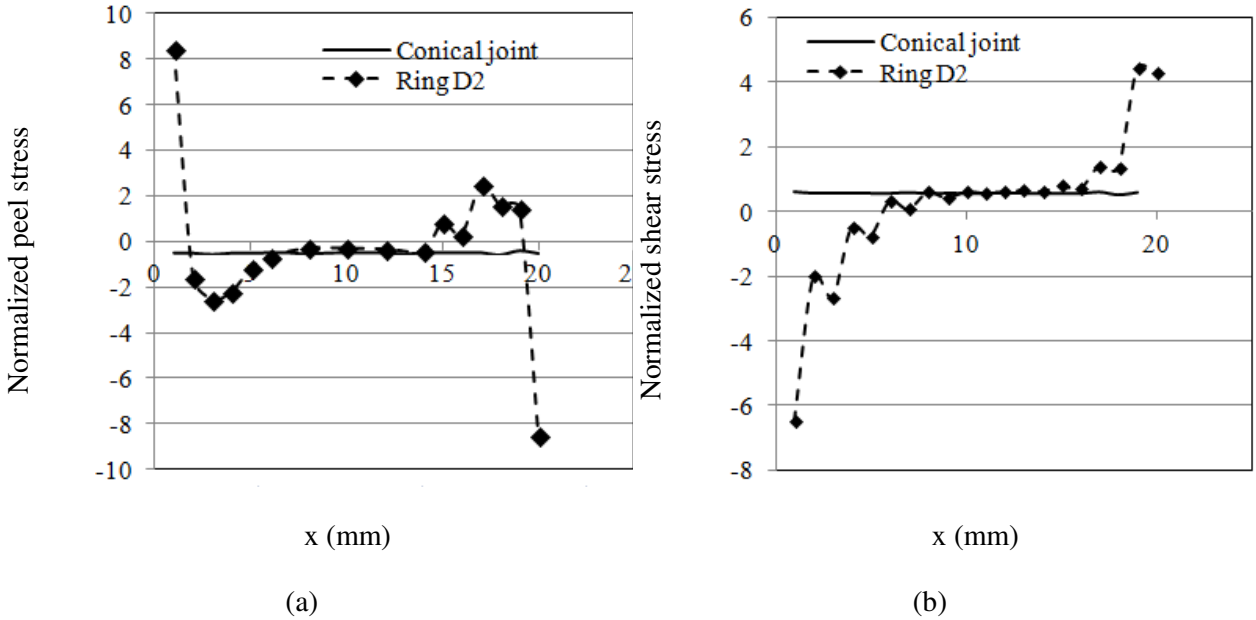

Figure 169. Influence of the connection type along the overlap of the adhesive layer on: (a) normalized peel stress and (b) normalized shear stress.

Cognard et al. [COG 12] studied the influence of the angle of coaxial joints on numerical responses in compression, tension and showed that an angle of 40° strongly limited edge effects. The FE model used above presented an angle close to 40°. Thus, edge effects were almost inexistent for the conical bonded joint. It can be deduced that the divergent results close to the free edges for the Ring D2 were mainly due to high stress concentrations due to such geometry.

Figure 170 and Figure 171 show the evolution of the von Mises equivalent stress, the peel stress and the shear stress in the mean plane of the adhesive layer along the overlap of the joint for the Ring D2 joint for a compression loading throughout the adhesive thickness (thickness of 0.2 mm) (e = 0 was the middle line of the adhesive and e = h/2 was the upper adhesive-substrate interface).

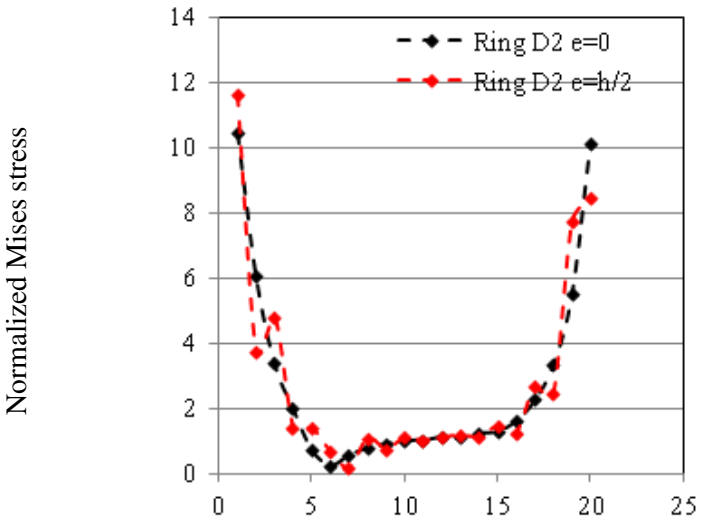

x (mm)

Figure 170. Normalized von Mises stress throughout the thickness of the adhesive with respect to overlap length for Ring D2.

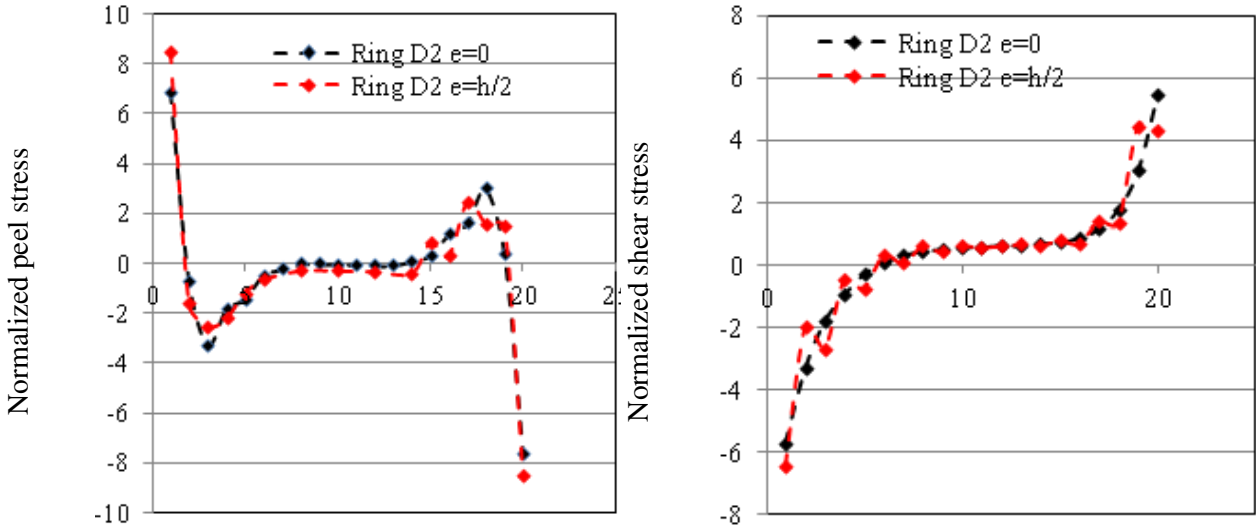

x (mm) x (mm)

(a) (b)

Figure 171. Normalized von Mises stress throughout the thickness of the adhesive with respect to overlap length for Ring D2.

For all stress components, stress concentrations are present in the middle line of the adhesive layer and at the interface adhesive/substrate. Thus, it was assumed that those stress peaks were caused by Ring D2 geometry.Those stress concentrations should be minimized by modifying geometry of the bonded joint. For instance, it must be interesting to add beaks close to the free edges or modify the angle of the bonded assembly.

The influence of the angle on the Ring D2 strength is showed in Figure 172 and Figure 173. Mesh sufficiently refined meshes such that used for previous investigations were used to obtain good results. In the same way, the three stress components were computed in the base (*u*, *t*, *v*).

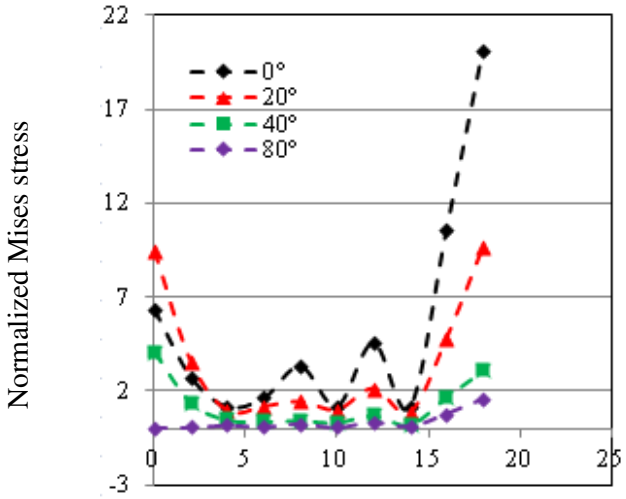

x (mm)

Figure 172. Ring D2 : Influence of the angle of the bonded assembly on the normalized von Mises stress along the overlap length.

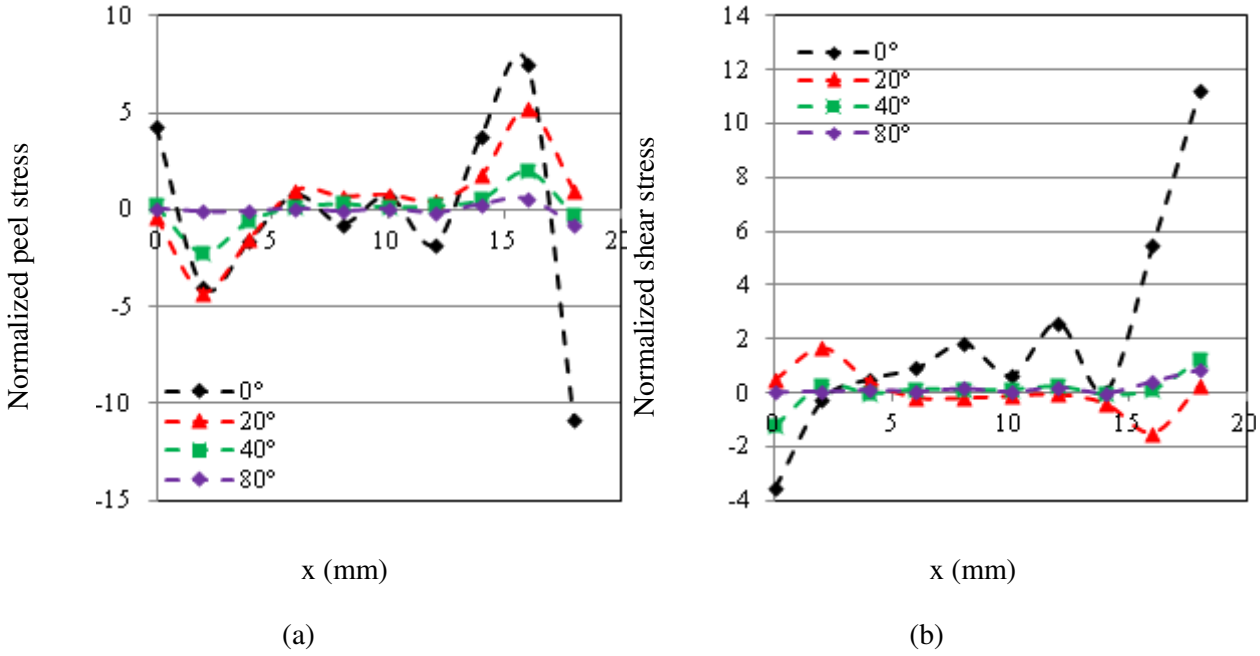

Figure 173. Ring D2: Influence of the angle of the bonded assembly along the overlap length on: (a) the normalized peel stress and (b) the normalized shear stress.

Those results highlight the strong influence of the Ring D2 geometry, namely the angle of the bonded assembly, on the stress concentrations close to the free edges of the adhesive. The latter decreased for angles of 40° and 80°. Similar results were obtained for the conical bonded joint studied by Cognard et al. [COG 10] since, in that study, he showed that stress concentrations are neglected for an angle of 40°.
The stress distribution within the adhesive layer was similar for both bonded joints, i.e. a conical bonded joint and a Ring D2 joint. In addition, stress concentrations near the free edges were minimized for an angle of the bonded assembly of 40° for both bonded joints. Thus, the Ring D2 joint can be associated with a conical bonded joint with an angle of 40°.

5.5. Prospects using the Tensile / Compression – Shear test developed by Arnaud et al. [ARN 14a] [ARN 14b]

The characterization of the adhesively bonded joint such that of the connection Ring D2 can be realized by using a Tensile / Compression – Shear test. Such test was developed by Arnaud et al. [ARN 14a] [ARN 14b] and was best suited to analyze the mechanical behavior of adhesives under non-proportional loadings and in compression. Tests are realized on tubular bonded specimens, as shown in Figure 174. In the same manner as for Arcan Evolution specimens, classical edge effects occur in bonded assemblies resulting in premature failures and high scatter in experimental results. Thus, a particular geometry containing beaks with cleaned edges close to the adhesive layer was used to reduce edge effects and to limit scatter in results. Such specimens have a bonded area of 452 mm² and an adhesive thickness of 0.4 mm. An adhesive thickness of 0.2 mm will be used for this study in order to remain in the same conditions such that of the Ring D2 bonded joint. Particular attention was paid to the specimen preparation. Indeed, a special bonding system was designed to realize reliable bonding. This system allowed ensuring a suitable adhesive thickness, a well positioning of substrates and an easy access to the adhesive spew fillet to clean edges, as detailed by Arnaud et al. [ARN 14a][ARN 14b].

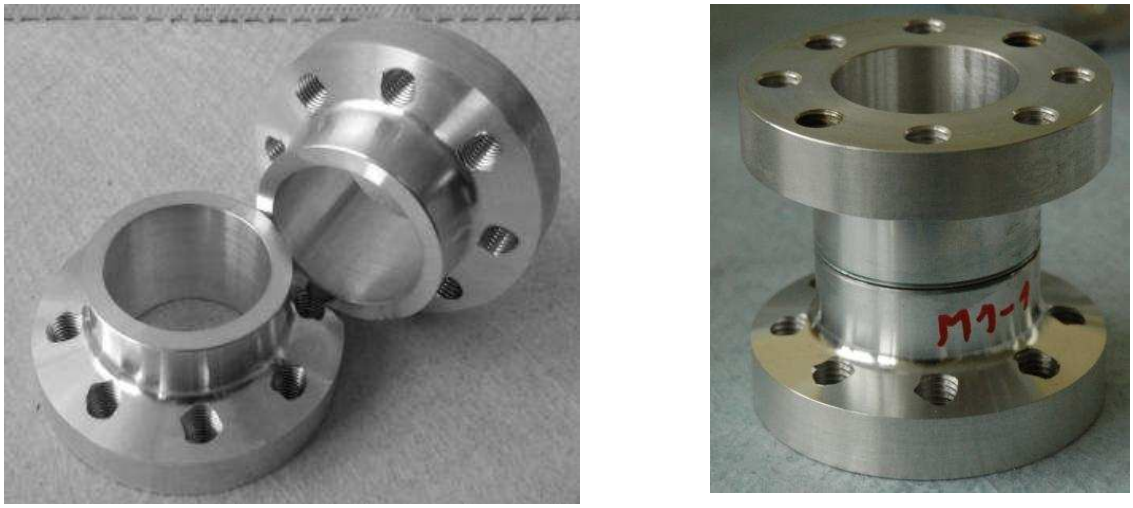

(a) (b)

Figure 174. Tension/Compression – Torsion specimen: (a) Substrates before bonding and (b) Specimen bonded and cured.

The testing device appears in Figure 175. As shown in Figure 175 (a), the bonded specimen (in red) is placed on two supports (in grey). The screws are tightened to insure a high pressure contact to avoid every movement of the bonded specimen. Then, the testing device is placed in the tension-torsion machine through two interface parts that offset any misalignment in the fixture.Figure 176 shows both configurations obtained after screwing the interface parts. Mixed loadings including tension are realized using the configuration illustrated in Figure 176 (a). Those including compression are effected using the setup detailed in Figure 176 (b). During the loading, the loads pass through the paths represented by the white arrows on such figures.

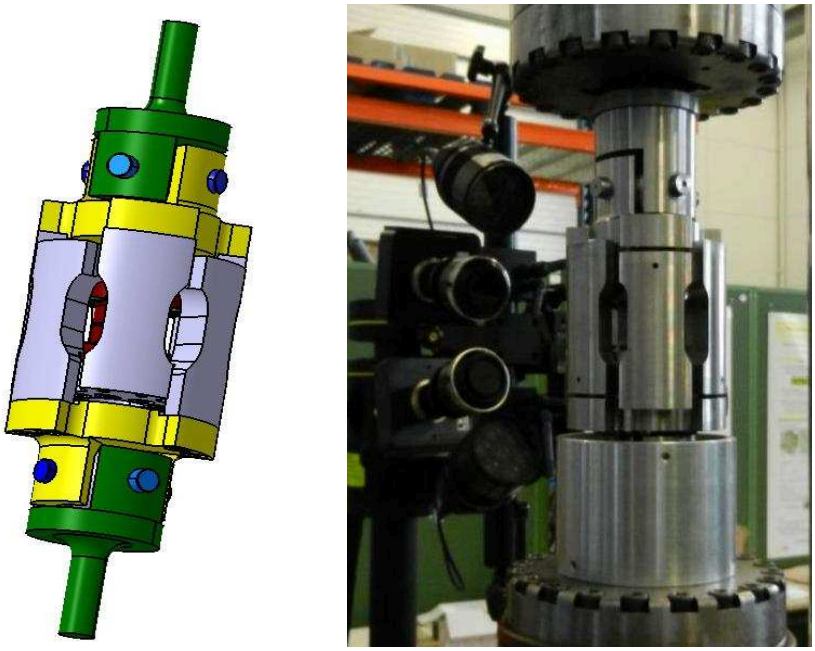

(a) (b)

Figure 175. Tension/Compression-Torsion device: (a) Description of the device with the different colored parts (the test specimen is in red) and (b) Experimental tensile configuration.

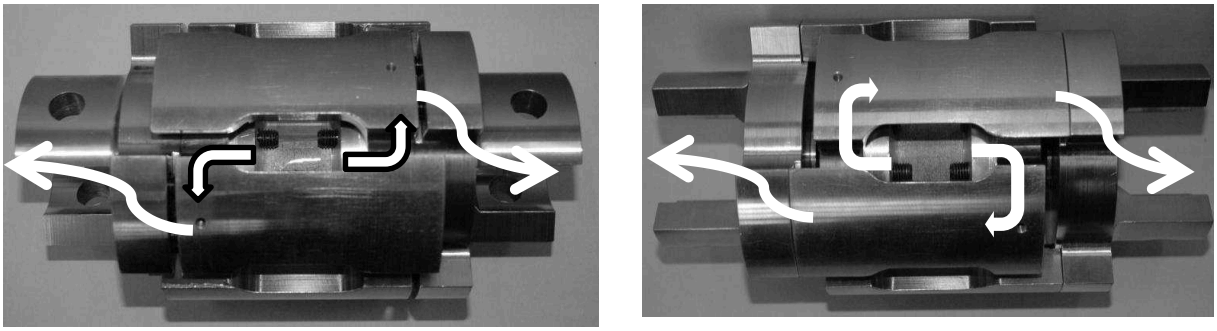

(a) (b)

Figure 176. Tension/Compression-Torsion device: (a) Tension configuration and (b) Compression configuration.

Using Tension / Compression – Torsion test in this study is very interesting. Indeed, this test was firstly realized on tubular joints but it can be adjusted to conical bonded joint such that presented in Figure 177. The latter shows conical bonded joints with several angles. It underlines the possibility to characterize a wide range of conical bonded joints that differ in geometries, namely angle values, and then to provide more solutions for designing the Ring D2 bonded joint.

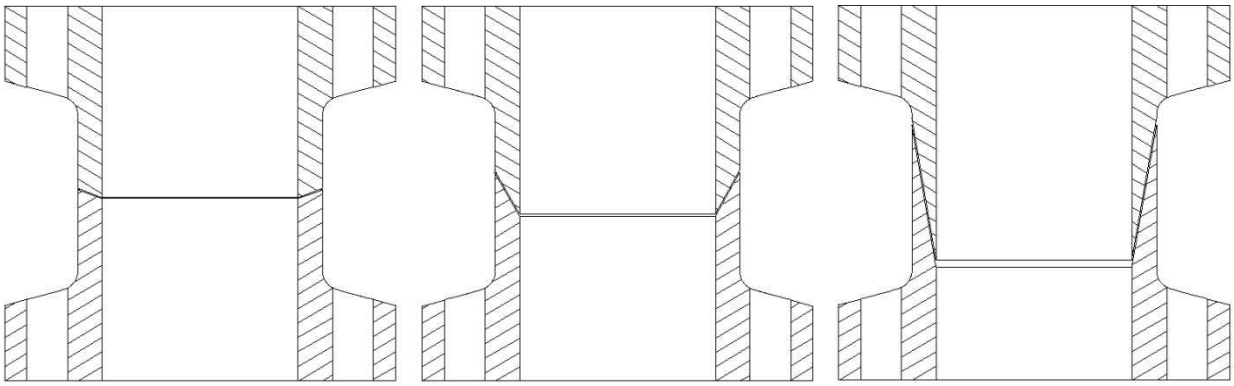

(a) (b) (c)

Figure 177. Conical test specimens with different angles: (a) 20°, (b) 60° and (c) 80°.

Conical test specimens with different geometries, namely several angles, will be tested in the future via the Tension / Compression – Torsion test and for several curing states of the adhesive. This will provide a strong database to choose an optimized geometry that reduce edge effects, increase bonded assembly resistance and to validate the cure-dependent constitutive models established earlier.

5.6. Conclusion

The integration of lower and upper satellites in the large-scale SYLDA 5 structure required the use of conical bonded joints to adjust its diameter. During the flight, such structure is submitted to complex loadings such thermal, mechanical or coupled thermo-mechanical loadings. In addition, these loadings have a different importance according to the flight time period, the magnitude or the direction of structure during the flight. Thus, characterizing and testing such large-scale geometries thanks to classical and representative tests is essential to better understand the behavior of such bonded assemblies.

The numerical study presented in this chapter allowed reconciling the bonded joints of the SYLDA structure, namely those of the Ring D called “Joint SSS”, by standard tests. The Ring D1 was easily associated with a double lap joint. However, the association of the bonded joint Ring D2 with a conical joint was less apparent and a finite element analysis was required to compare both joints. The numerical solicitation of a Ring D2 joint and a conical joint with an angle of 40° in tension showed similar mechanical responses. Nevertheless, stress concentrations close to the free edges of the adhesive were observed for the Ring D2 and sensitivity analysis to the angle of the joint showed that those concentrations were the results of the Ring D2 geometry. Conical bonded joints with an angle of 40° can therefore be used for dimensioning of bonded joints such the Ring D2.

From this numerical analysis, a complementary study must be realized. This will involve an experimental stage and a numerical step:

- Experimentally, non-proportional loadings must be explored on conical bonded joints with an angle of 40° via a tension/compression-torsion test developed by Arnaud et al. [ARN 14a] [ARN 14b] for an aluminium/adhesive Hysol EA-9321 bonding. Stress relaxation and creep recovery tests must also be initiated to highlight the viscous effects .The three curing cycles used for the determination of mechanical properties under proportional loadings via the Arcan Evolution device must be applied to study the influence of the curing state of the adhesive on non-proportional and viscous responses. This step will constitute an experimental database to validate the constitutive models presented in chapter 4, mainly cure-dependent elasto-plastic, elasto-visco-plastic and visco-elasto-visco-plastic modified Mahnken-Schlimmer models.

- Numerically, a detailed study of the influence of the geometry (for instance, the influence of the adhesive thickness, the cone section, beaks geometry) on the bonded assembly strength must be realized under elastic assumptions to provide an optimized conical joint. Then, the constitutive models identified in chapter 4 must be introduced to the FE model containing the optimized geometry.

The purpose of this additional study will be to validate the identification strategy of constitutive laws developed on proportional loadings in Chapter 4. Indeed, a good correlation between experimental and numerical responses predicted by such constitutive models for non-proportional loadings will validate the mechanical behavior of such adhesive since it will be not influenced by the type of effort.

5.7. References

[ABA 10] Abaqus Analysis User's Manual version 6.10. Simulia, Providence, RI, USA, 2010.

[ARN 14a] Arnaud N., PhD Thesis : Analyse de l'effet du vieillissement en milieu humide sur le comportement mécanique d'adhésifs en assemblages sous sollicitations multiaxiales, 2014.

[ARN 14b] Arnaud N., Créac'hcadec R., Cognard J.Y., A tension/compression-torsion test suited to analyze the mechanical behavior of adhesives under non-proportional loadings, International Journal of Adhesion and Adhesives, Vol. 53, pp. 3-14, 2014.

[AST 96] ASTM D3528-96, American Society for Testing and Materials, Philadelphia, 1996.

[COG 12] Cognard J.Y., Sohier L. ,Créac'hcadec R., Lavelle F., Lidon N., Influence of the geometry of coaxial adhesive joints on the transmitted load under tensile and compression loads, Internaltional Journal of Adhesion and Adhesives, pp. 37-49, 2012.

[INT] Internal document referenced "A5-CT-1640000-X-001-CNES".

CONCLUSIONS AND PERSPECTIVES

Structural adhesive bonding is of great and still increasing industrial importance in the spatial industry, namely in design concepts. However, large-scale bonded assemblies, such the SYLDA structure, are associated with some constraints like a manufacturing/storage stage in outdoor conditions that has a significant impact on the SYLDA resistance. In fact, Low temperature-curing leads to an incompletely polymerized adhesive which exhibit a wide range of mechanical properties depending on its curing state. This unsteady state of the adhesive and thus of the bonded assembly makes manufacturers confused. Therefore, the development of numerical tools must be necessary to design industrial parts to better understand the behavior of such bonded assemblies. The establishment of such a tool requires a specific strategy in which each step must be validated.

The first part of this work was dedicated to the numerical prediction of the curing behavior of an adhesive, namely the cold-curing epoxy adhesive Hysol EA-9321, in a bonded assembly regardless of the thermal loading applied. At first, the evolution of the cross-linking reaction under different thermal conditions, i.e. isothermal and dynamic loadings, was monitored through a Differential Scanning Calorimeter Analysis. Since the chemical composition of the adhesive constituents was unknown, mechanistic models could not be applied to study the cure kinetics of the adhesive. However, it appeared that phenomenological models such as the autocatalytic model likeKamal & Sourour were best suited to model the curing process of the adhesive Hysol EA-9321 under dynamic loadings, isothermal loadings, respectively. Drawing on this and assuming that dynamic loadings can be considered as a series of isothermal heating with a small period of time, a modified model of Kamal & Sourour with temperature dependency of parameters was proposed. The main interest was clearly in the use of a single model for both dynamic and isothermal loadings. Particular attention was paid to the inverse identification strategy use to determine model parameters. In fact, the identification process used several experimental measurements that considered the global kinetic behavior of the adhesive unlike most works that did not consider experiment dispersion. Then, the kinetic model identified for the adhesive Hysol EA-9321 was implemented in the software Abaqus® via fortran subroutines to predict the distribution couple (curing degree α – temperature T) in a bonded assembly whatever the thermal load applied. The applicability of this FE model was verified by comparing predicted temperature profiles and curing degree profiles within a cylindrical block of adhesive. Good results obtained highlighted the relevance of such models to predict the thermo-physical behavior of an adhesive, particularly the adhesive Hysol EA-9321, in a bonded assembly during curing. A sensitivity analysis to kinetic parameters and measurement point locations exhibited temperature and curing degree gradients. Hence, an accurate knowledge of these data must be required to properly predict the curing behavior of an adhesive in a bonded assembly. This finite element procedure is particularly interesting for large-scale structures that are erected and stored in outdoor conditions such the SYLDA structure. It allows knowing the temperature and curing degree profiles at each location of the bonded area at any time of the life course of the structure.

The second part consisted in characterizing and modeling the cure-dependent 3D constitutive behavior of the adhesive Hysol EA-9321. This involved in several steps:

The influence of the cross-linking of this adhesive on its mechanical properties was experimentally investigated through the Arcan Evolution device. To that end, three curing cycles were applied to Arcan Evolution specimens, i.e. 1h at 82°C, 3h30 at 60°C and 5h30 at 35°C. The idea was to reach a curing state sufficiently stable to predict the mechanical properties that goes with it. The FE thermo-kinetic model developed in the first part was applied to an Arcan Evolution specimen loaded with the three curing cycles chosen in order to provide the temperature and curing degree distribution within the adhesive layer during each curing process. Considering each curing state, Arcan Evolution tests under tension, shear, tension-shear and compression-shear were investigated at several traverse speeds. A post-processing procedure by 3D-Digital Image Correlation was set-up. It allowed verifying that there was no misalignment in the testing device and knowing the exact position where the relative displacements were measured. The latter was critically important in the identification strategy process to rightly determine material parameters of the mechanical model. Mainly changes occurred in shear and compression-shear results. The responses were moved up and the load failure was reduced with an increasing curing degree. A changing behavior in the non-linear part was observed in compression-shear since a slope modification was observed when decreasing of the curing states.

An elasto-plastic model such as the Mahnken-Schlimmer one was identified on a fully polymerized Arcan Evolution specimen. However, the hardening function was slightly modified to consider the strength recovery exhibited on the non-linear part of the compression-shear response. The constitutive parameters were identified using a sequential identification strategy that coupled finite element computations and an optimization process. The application of this procedure to each curing cycles responses allowed relying the parameters of the Mahnken-Schlimmer model to the curing degree and led to good predictions. Considering this cure-dependent model, a global identification strategy was developed to indentify material parameters on all experiment responses, i.e. without taking each curing case separately. Then, this model was extended to strain-rate effects with a Nouailhas visco-plastic potential type. The visco-plastic parameters were identified in the same way as the firstly parameters identified. It rested to a first identification on each curing case followed by another global that also integrated the curing step. This model gave good results in shear and did not take into account the strength straightened in the non-linear part of the compression-shear response. An additional identification of hardening parameters to fit experiment pointed the limits of the inverse identification process since it conducted to a best fit but a physical nonsense due to high numerical values for some parameters of the law behavior. An extension of this last model to visco-elasticity offered the possibility to describe the creep/recovery or cyclic behavior of a partially cured adhesive in a bonded assembly.

The last part of this work studied especially the bonded joints of the SYLDA structure, namely those of the Ring D called “Joint SSS”. The purpose of this numerical study was to reconcile such connection by standard or simple tests. This connection was made of two sub-assemblies. One of these was loaded in the same way as a double lap joint. The other one called Ring D2 composed the main part of the numerical study. The stress distribution within the adhesive layer for a Ring D2 and a conical bonded joint were compared. Finite element analysis were undertaken under elastic assumptions for a bonding aluminium/adhesive Hysol EA-9321 under tension loading. Numerical predictions underlined similar responses for both connections even if in regions close to the free edges. In fact, it was showed that stress concentrations were due to the particular geometry of this joint. However, a sensitivity analysis to the angle of such bonded assembly underlined a minimization of stress concentrations near to the free edges for an angle of 40°. Single lap joint and conical joint can thus be used to design the bonded connection Ring D on SYLDA structure.

Finally, this study provides a numerical tool that is able to predict the temperature and curing

degree distribution whatever the thermal load applied and the resulting mechanical properties.

As a perspective, a complementary study to that realized on the bonded joint Ring D on the SYLDA structure may be provided. Experimentally, it will consist in loading conical bonded joints with an angle of 40° through a tension/compression test for the three curing cycles identified in the study, namely 1h at 82°C, 3h30 at 60°C and 5h30 at 35°C. Numerically, the constitutive model identified, mainly the cure-dependent elasto-plastic modified Mahnken-Schlimmer model must be introduced to the FE model of a conical joint to validate the identification strategy of such constitutive law developed on the Arcan Evolution device on proportional loadings.

Another perspective should be the entire determination of a visco-elasto-visco-plastic constitutive law. This will require the definition of specified creep/recovery, cyclic tests to access numerically to viscous parameters. A strong identification procedure must be established to determine all parameters.